

Research on Powering a Personal Heating Garment with a Hybrid Power Supply



Zohreh Soleimani

*A submission in partial fulfilment of the requirements of the University of
Derby for the award of the degree of Doctor of Philosophy*

College of Science and Engineering

August 2021

Content

Content	i
List of Figures	vii
List of Tables	xiii
List of Publications	xvi
Nomenclature	xix
Author’s Declaration	xxii
Acknowledgments	xxiv
Thesis Summary	xxviii
1. Introduction	1
1.1 Background.....	2
1.2 Research aim and objectives.....	7
1.3 Research questions	8
1.4 Research Significance	8
1.5 Thesis outline.....	9
1.5.1 The literature review	9
1.5.2 The research methodology	10
1.5.3 The numerical modelling	10
1.5.4 The laboratory study	11
1.5.5 The field study	11
1.5.6 The thesis conclusions	12
2. Thermal Comfort	14
2.1 Introduction.....	15
2.2 Predicted mean vote (PMV).....	15

2.3 Acceptable PMV	18
2.4 Adaptive PMV	19
2.5 Distribution of thermal sensitivity	21
2.6 Summary	24
3. Personal Heating Systems.....	26
3.1 Introduction.....	27
3.2 Heating chairs	27
3.3 Heating floor /desktop mats	31
3.4 Heating garments	34
3.5 Summary	37
4. Principles of Thermoelectric Generators.....	39
4.1 Introduction.....	40
4.2 Basic principles of TEGs	40
4.2.1 The Seebeck coefficient (α)	42
4.2.2 Electrical conductivity (σ)	42
4.2.3 Thermal conductivity (λ)	43
4.2.4 Energy conversion efficiency	44
4.3 Different types of TE materials.....	45
4.4 Inorganic thermoelectric materials	46
4.4.1 <i>P</i> -type inorganic TE materials	48
4.4.2 <i>N</i> -type inorganic TE materials	51
4.5 Organic thermoelectric materials	53
4.5.1 Polymer-based TE material.....	54
4.5.2 Carbon-based TE materials.....	60
4.6 Hybrid thermoelectric materials	65
4.6.1 <i>P</i> -type hybrid TE materials.....	66
4.6.2 <i>N</i> -type hybrid TE materials.....	69
4.7 Summary	71
5. Different Configurations of TEGs.....	74
5.1 Introduction.....	75
5.2 Wearable TEGs.....	75
5.3 Configurations of wearable TEGs	76
5.4 Ingot-shaped thermocouples	78
5.4.1 Inorganic TE materials.....	78

5.4.2 Hybrid TE materials.....	82
5.5 Film-shaped thermocouples.....	85
5.5.1 Inorganic TE materials.....	85
5.5.2 Organic TE materials.....	87
5.5.3 Hybrid TE materials.....	90
5.6 Yarn-shaped thermocouples.....	94
5.6.1 Inorganic TE materials.....	94
5.6.2 Organic TE materials.....	95
5.6.3 Hybrid TE materials.....	98
5.7 Summary.....	102
6. Research Methodology.....	104
6.1 Introduction.....	105
6.2 Literature Review.....	105
6.3 Numerical experiment.....	106
6.4 Laboratory experiment.....	109
6.5 In-field experiment.....	113
6.6 Summary.....	114
7. The Life Cycle Impact Assessment.....	117
7.1 Introduction.....	118
7.2 Life cycle impact assessment stages.....	120
7.3 Goal and scope of the assessment.....	121
7.4 Life cycle inventory.....	124
7.5 Results.....	127
7.5.1 Input-output mass flow.....	127
7.5.2 Primary energy demand.....	130
7.5.3 Global warming potential (GWP).....	133
7.5.4 Ozone depletion potential (ODP).....	136
7.5.5 Human toxicity potential (HTP).....	139
7.6 Summary.....	142
8. The Lightweight Integrating Substrate.....	146
8.1 Introduction.....	147
8.2 Device overview.....	149
8.3 Numerical modeling.....	151
8.3.1 Governing equation.....	152

8.3.2	Physic 1: Heat transfer in solids.....	152
8.3.3	Physic 2: Heat transfer in porous media	153
8.3.4	Physic 3: Electric currents	154
8.3.5	Coupling multiphysics: thermoelectric effect.....	155
8.3.6	Boundary and initial conditions	156
8.3.7	Grid independence test and solution convergence analysis.....	157
8.3.8	Results of the numerical simulation.....	159
8.4	Validation of the numerical modeling	162
8.4.1	Fabrication procedure	162
8.4.2	Equipment and testing condition	165
8.4.3	Results of the experiments	168
8.5	Comparison of the numerical modelling and the experiments	178
8.6	Summary	182
9.	The Lightweight Heatsink	185
9.1	Introduction.....	186
9.2	Fabrication procedure	194
9.3	Equipment and testing conditions.....	196
9.4	Results of the experiments	197
9.4.1	Electrical current.....	197
9.4.2	Electric potential	198
9.4.3	Output power	199
9.5	Summary.....	201
10.	Fabricating the Heating Armbands.....	203
10.1	Introduction.....	204
10.2	Fabrication procedure	204
10.2.1	Coupling the TEGs	204
10.2.2	Fabricating the hybrid power supply	206
10.2.3	Checking the thermal performance of the PDMS substrate.....	212
10.2.4	Fabricating the armbands	213
10.3	Testing conditions	216
10.3.1	The experimental room	216
10.3.2	Description of the subjects.....	218
10.3.3	The experimental procedure	219
10.4	Measurements	220

10.4.1 Objective measurements	220
10.4.2 Subjective questionnaire survey	221
10.5 Results of the objective measurements	222
10.6 Results of the subjective questionnaire survey	225
10.6.1 Thermal sensation and comfort of body parts.....	225
10.6.2 Whole-body thermal sensation and comfort	239
10.6.3 Whole-body thermal acceptability	241
10.6.4 Whole-body preferred thermal sensation.....	242
10.7 Discussion	244
10.8 Summary	247
11. Conclusions and Future Works	250
11.1 Conclusions.....	251
11.2 “State of the art”	251
11.3 Contributions.....	253
11.4 Limitations	255
11.5 Future works	257
11.5.1 Applying external heat sources	257
11.5.2 Applying hybrid energy harvesters	259
References.....	261
Appendix A: First Questionnaire (Background Questions)	288
Appendix B: Second Questionnaire (Environmental Condition at the Time)	292
Appendix C: Request for ethical approval.....	297
Appendix D: Ethics_application_ETH1819-0044_Decision	308

List of Figures

Fig. 1: a) Global primary energy consumption by end-use sector from 1970 to 2040; and b) final energy consumption in buildings by fuel from 2000 to 2040 [3].	2
Fig. 2: Whole-body thermal sensitivity and thermal sensation mapping [14].	4
Fig. 3: The intensity of the conditioning area as it gets closer to the human body [30].	6
Fig. 4: The metabolic rates according to the activity [46].	16
Fig. 5: The thermal insulation values for clothing [47].	17
Fig. 6: The seven-point thermal sensation scale [48].	18
Fig. 7: Content removed due to copyright reasons	19
Fig. 8: Local and overall thermal sensation and comfort in: a) a uniform/cold; and b) a uniform/warm environment [84].	22
Fig. 9: Temperature of different body parts at varying ambient temperature, adapted from [31].	23
Fig. 10: Content removed due to copyright reasons.	28
Fig. 11: Content removed due to copyright reasons	29
Fig. 12: The design and the thermal image of the heating chair [95].	30
Fig. 13: The developed foot warmer [97].	31
Fig. 14: Combination of the developed foot warmer and palm warmer [98].	32
Fig. 15: Sketch of the tested heating systems consisting of a convection-heated chair (HC), an under-desk radiant heating panel (UD RHP), and a floor radiant heating panel (FL RHP) [99].	33
Fig. 16: The fabricated personalized heating systems: a) a heated chair; b) a heated desk mat; and c) a heated floor mat [10].	33
Fig. 17: The heating strategies used in this study: a) HB1: a radiant heating panel with a heated table pad; b) HB2: a heated chair with a heated floor mattress; and c) EHC: a heated jacket with heated trousers [22].	34
Fig. 18: The personal heating devices: a) the heating chair; b) the leg warmer; and c) a subject using the devices [104].	36
Fig. 19: The schematic diagram of a conventional TEG and its components.	42
Fig. 20: Content removed due to copyright reasons.	45
Fig. 21 : Temperature dependencies of : a) the electrical resistivity; b) the Seebeck coefficient; c) the thermal conductivity; and d) the ZT values of $f(\text{CuInTe}_2)/\text{BST}$ ($f= 0, 0.1, 0.2$ and $0.3\text{wt.}\%$) [137].	49
Fig. 22: Temperature dependence of: a) the electrical resistivity; b) the Seebeck coefficient; c) the power factor; and d) the figure of merit of $\text{Mg}_{1-x}\text{Li}_x\text{Ag}_{0.97}\text{Sb}_{0.99}$ [133].	50

Fig. 23: The temperature dependence of: a) the electrical resistivity; b) the Seebeck coefficient; c) the total thermal conductivity; and d) the ZT values of MgAg _{0.97} Sb _x (x= 0.99, 0.9925,0.995, and1.00) [148].	51
Fig. 24: Temperature dependent TE properties of the dense pellet Bi ₂ Se ₃ along different directions: a) the electrical resistivity; b) the Seebeck coefficient; c) the thermal conductivity; and d) the ZT values. The inset to panel c shows the lattice thermal conductivity [153].	52
Fig. 25: Temperature dependences of TE properties parallel to the crystal growth direction for sample A and B: a) the electrical conductivity; b) the Seebeck coefficient; and c) the thermal conductivity; and d) the ZT values [155].	53
Fig. 26: Thermoelectric properties of the H ₂ SO ₄ -treated PEDOT:PSS films at various NaOH treatment conditions: a) dependences of the Seebeck coefficient and electrical conductivity of the PEDOT:PSS films on NaOH concentration; and b) dependence of the power factor of the PEDOT:PSS films on NaOH concentration [169].	55
Fig. 27: Thermoelectric properties of the FeCl ₃ /nitromethane solutions doped PDPP3T [172].	56
Fig. 28: The temperature-dependence of the TE properties for a–c) DDQ-doped polymer films and d–f) F4TCNQ-doped polymer films [177].	57
Fig. 29: Chemical structures of NTCDI2DT-2T (N1) and NTCDI-AF4A (N2) polymers [185].	58
Fig. 30: The electrical and the TE properties of the (RuCp*mes) ₂ -, N-DMBI-H-, and (N-DMBI) ₂ -doped FBDPPV at varying dopant concentrations: a) the electrical conductivity; b) the Seebeck coefficient; and c) the power factor [180].	59
Fig. 31: Thermoelectric performance characterization: a) Electrical conductivities; b) Seebeck coefficients; and c) PFs (circular points indicate positive Seebeck coefficients) for different N-DMBI mass ratios [184].	60
Fig. 32: Top view (left) and side view (right) of the partial chain segment conformation of: a) PANi; b) PPy; and c) PANiPy under the lowest energy state [189].	62
Fig. 33: Content removed due to copyright reasons.	63
Fig. 34: Schematic illustration of the preparation procedure of the P/RTG hybrid films [202].	64
Fig. 35: Transition between the p-type and n-type Seebeck coefficient. Different CNT weight loadings in PVDF show that the transition is dependent on the mass ratio between PEI dopant and CNT matrix [203].	65
Fig. 36: The thermoelectric properties of the Te-PEDOT:PSS thin films with different contents of PEDOT:PSS [206].	67
Fig. 37: Schematic illustrations of the fabrication and post-treatment of the composite films [207].	68
Fig. 38: The schematic illustration of the thin film growth: a) as-deposited composited thin film; b) annealing process; and c) cooling process [217].	69
Fig. 39: The influence of the PEG content on the TE properties of the melt mixed composites containing the fixed CNT (2 wt%) and CuO (5 wt%) concentrations [225].	70
Fig. 40: The schematics of: a) the cross-plane; b) the in-plane; and c) the combined configurations [255].	78
Fig. 41: a) The schematic drawing of the flexible TEG; b) photo of the actual fabricated TEG [258].	79

Fig. 42: a) Photo of the fabricated TEG; b) the obtained open circuit voltage at the room temperature [259].	80
Fig. 43: The fabricated TEG with the FPCB substrate and the PDMS filler [260].	81
Fig. 44: The designed flexible TE system consisted of a flexible holder [248].	82
Fig. 45: The schematic diagram of the fabrication processes of the proposed TEG [251].	83
Fig. 46: The fabrication process of the flexible TE films [278].	86
Fig. 47: a) Schematic illustration; and b) the photo of the fabricated TEG [279].	86
Fig. 48: a) Photo of the fabricated flexible SnTe–PbTe based TEG; b) Photo of the TEG placed on the arm as the power source of an LED [280].	87
Fig. 49: a) Illustration of roll to roll printing of the flexible TE devices; b) UV treated plastic substrate; c) Plasma-treated plastic substrate [283].	88
Fig. 50: Demonstration of the applied roll to roll and inject printing techniques to fabricate the film-shaped TEG [284].	88
Fig. 51: Photograph of the devices with 5, 10, 15 and 30 PN pairs. Demonstration of the TE bracelet wrapped around the wrist [285].	89
Fig. 52: a) The schematic of the 3D printed PDMS grid; b) Photo of the fabricated grid-based TEG; and c) Schematic design of integrating 7 units of the developed grid-based TEGs together [286].	90
Fig. 53: Images of the flexible and twistable TE generator comprising 240 legs arranged in four rows [287].	90
Fig. 54: A photo of the developed TEG and the 4.5 mV voltage created at 3.5 °C temperature difference [289].	91
Fig. 55: Photos of the fabricated TEG and its open-circuit voltage after being placed on the arm [290].	92
Fig. 56: Photo of the fabricated TEG and its mounting position on the human body [291].	92
Fig. 57: The schematic of the fabrication for the CNF@PP (p-type) and the PEI treated CNT (n-type) fibres [306].	96
Fig. 58: Photographs of the embroidered textile thermopile [307].	96
Fig. 59: All-organic in-plane embroidered textile TE device with 38 n/p elements [308].	97
Fig. 60: The schematic of the fabrication procedure of the TE fiber [309].	98
Fig. 61: a) Schematic illustration of the fabrication processes of the TE fibers; b) photos of the TE fiber; c) the TE fabric; and d) the application demo [310].	99
Fig. 62: a) The schematic illustration of the doping process; b) photo of the fabricated TEG [311].	100
Fig. 63: The defined flows and their connections in GaBi to produce Bi ₂ Te ₃ .	107
Fig. 64: COMSOL setup for the heat flux of the samples at 1.2 m/s air speed.	109
Fig. 65: The fabricated samples in the lab to validate the computational simulations.	111
Fig. 66: The schematic configuration of the proposed hybrid power supply.	113
Fig. 67: The research methodology flowchart.	115
Fig. 68: The different stages and sub-stages of the life cycle of the TE materials [322].	122
Fig. 69: Comparing the environmental input and outputs of different types of TE materials: a) inorganic; b) organic; and c) hybrid TE materials.	129

Fig. 70: The contribution of the three sub-stages of the production stage to primary energy demand: a) inorganic; b) organic; and c) hybrid TE materials.	132
Fig. 71: The share of different phases of the TE materials production in the impact category of GWP: a) inorganic; b) organic; and c) hybrid TE materials.	135
Fig. 72: The share of different phases of the TE materials production in the impact category of ODP: a) inorganic; b) organic; and c) hybrid TE materials.	138
Fig. 73: The share of different phases of the TE materials production in the impact category of HTP: a) inorganic; b) organic; and c) hybrid TE materials.	141
Fig. 74: The schematic of the two stage cascaded TEG fabricated for this chapter.	150
Fig. 75: The schematic diagram of the four specified models in COMSOL Multiphysics.: Model 1 (the reference model); Model a (the top stage coated); Model b (the bottom stage coated); and Model c (both stages coated).	150
Fig. 76: The specified boundary conditions for the modelled samples in COMSOL.	156
Fig. 77: a) Mesh sensitivity analysis results for the reference model; b) meshing the models with medium size grid.	158
Fig. 78: The convergence monitoring of the electric potential and temperature (created automatically in COMSOL).	159
Fig. 79: Changes in the output currents of the simulated samples concerning different air flow conditions.	160
Fig. 80: Changes in the output voltage of the simulated samples concerning different air flow conditions.	161
Fig. 81: Changes in the output power of the simulated samples concerning different air flow conditions.	162
Fig. 82: Different stages and sub-stages of the fabrication procedure.	163
Fig. 84: Photographs of the thirteen prepared samples.	165
Fig. 85: Top: different views of the wind tunnel: a) the top view; b) the side view; and c) the perspective view; Bottom: d) the assembled wind tunnel.	167
Fig. 86: Test-setup at 1.2 m/s air velocity.	167
Fig. 87: Changes in the output current of the samples regarding different air flow conditions: covering a) the top; b) the bottom; and c) both stages.	171
Fig. 88: Temperature profiles of the samples at 1.2 m/s air flow derived from COMSOL simulation.	172
Fig. 89: Changes in the average output voltage of the samples regarding different air flow conditions: covering a) the top; b) the bottom; and c) both stages.	175
Fig. 90: Changes in the output powers of the samples regarding different air flow conditions: covering a) the top; b) the bottom; and c) both stages.	178
Fig. 91: Comparison between the experimental results and the simulation outcomes: a) average output amperes; b) average output voltages; and c) average output powers.	181
Fig. 92: The schematic of the modelled heatsinks in COMSOL: a) straight fins; b) perforated fins; c) T-shape fins; d) trapezium fins; and e) wavy fins [336].	187
Fig. 93: a) Schematic of the developed TEG; b) the experimental setup of the TEG on the wrist [243].	188

Fig. 94: a) The fabrication process of the TEG; b) photo of the TEG fabricated with copper sheet as the heatsink [269].	189
Fig. 95: Fabrication process of the flexible heatsink [271].	190
Fig. 96: Fabricated wearable TEGs: a) without heat sink; b) with copper-foam heat sink; and c) with plate-fin heat sink [272].	191
Fig. 97: Schematic of the design and structure of the fabricated TEG and its gel-based heatsink [273].	192
Fig. 98: The flexible hydrogel-based heatsink fabricated onto the TEG [274].	193
Fig. 99: a) Schematic of the fabrication process and the components of the TEG; b) the fabricated device on the human wrist [275].	193
Fig. 100: Photographs of the three prepared sample concerning the determined configurations for the heatsink.	195
Fig. 101: Schematic of the fabrication procedure of the a) bumpy-shaped heatsink and b) the fin-shaped heatsink.	195
Fig. 102: The complete test set-up for pin-shaped heatsink.	196
Fig. 103: Changes in the output current of the samples regarding different air flow conditions.	198
Fig. 104: Changes in the output voltage of the samples regarding different air flow conditions.	199
Fig. 105: Changes in the output power of the samples regarding different air flow conditions.	200
Fig. 106: The schematic procedure of integrating the TEGs.	205
Fig. 107: a) The integrated TEGs with the PDMS substrate and the pin-shaped heatsinks; b) covering only the top half of the TEGs with the PDMS substrate.	206
Fig. 108: Fabrication process of the benchtop power supply.	208
Fig. 109: Photo of the PFM control DC/DC booster and blueprint of its internal circuitry [337].	209
Fig. 110: Integrating the benchtop power supply with a current source (a rechargeable battery).	211
Fig. 111: Schematic of measuring temperature at different levels of the PDMS substrate.	213
Fig. 112: Variation of temperature at different levels of the integrated TEGs.	213
Fig. 113: Fabricating procedure of the heating armband: a) Adafruit electrical heating pad; b) sewing the heating fabric onto a polycotton fabric; c) sewing the polycotton fabric onto a commercial armband; and d) sticking a copper foil tape onto the heating fabric.	215
Fig. 114: The fabricated heating armband connected to the benchtop power supply.	216
Fig. 115: Location and building of the experimental room.	217
Fig. 116: Photo and layout of the experimental room.	218
Fig. 117: Photos of the experimental (left) and the control (right) groups in one of the experiments.	219
Fig. 118: The experimental procedure of this study.	220
Fig. 119: Variation in the room's temperature at different heights.	223
Fig. 120: Variation in the skin's temperature of the subjects at the back of their hands and arms.	224

Fig. 121: a) The armbands worn by an experimental participant; b) the thermal image of the hands and armbands (FLIR T660).	224
Fig. 122: Forehead’s thermal sensation (a) and comfort (b).	226
Fig. 123: Front torso’s thermal sensation (a) and comfort (b).	228
Fig. 124: Back torso’s thermal sensation (a) and comfort (b).	230
Fig. 125: Sitting behavior of the participants at the 25 and 35 min of the experiments.	231
Fig. 126: Hand’s thermal sensation (a) and comfort (b).	233
Fig. 127: Front thigh’s thermal sensation (a) and comfort (b).	235
Fig. 128: Back thigh’s thermal sensation (a) and comfort (b).	237
Fig. 129: Feet’s thermal sensation (a) and comfort (b).	239
Fig. 130: Whole-body thermal sensation (a) and comfort (b).	241
Fig. 131: Whole-body thermal acceptability.	242
Fig. 132: Whole-body preferred thermal sensation.	243
Fig. 133: The modelled concept in COMSOL Multiphysics.	259

List of Tables

Table 1: Summary of the main categories of TE materials usable in wearable TEGs.....	46
Table 2: Summary of the properties of most typical inorganic TE materials at 26 °C room temperature.	47
Table 3: Summary of the TE properties of some typical polymer based TE materials at 26 °C... ..	54
Table 4: Summary of the TE properties of some typical carbon based TE composites at 26 °C.. ..	60
Table 5: Summary of the TE properties of some typical inorganic/organic TE composites at 26 °C.	66
Table 6: Potential energy sources of the human body and the associated energy harvesters	76
Table 7: Summary of the recently developed wearable TEGs comprising the ingot-shaped thermocouples.	84
Table 8: Summary of the recently developed wearable TEGs comprising film-shaped thermocouples.	93
Table 9: Summary of the recently developed wearable TEGs comprising the yarn-shaped thermocouples.	101
Table 10: Inventory data list on the raw materials of the TE materials derived from CES EduPackTM 2018	124
Table 11: Inventory data list on the manufacturing processes of the inorganic TE materials.	125
Table 12: Inventory data list on the manufacturing processes of the organic TE materials.	126
Table 13: Inventory data list on the manufacturing processes of the hybrid TE materials.....	126
Table 14: Summary of the environmental input and outputs of the TE materials at the production stage.	130

Table 15: Summary of the total primary energy demand of the TE materials at the production stage.	133
Table 16: Summary of the equivalent CO ₂ emission of the TE materials at the production stage.	136
Table 17: Summary of the ozone depletion potential of the TE materials at the product stage.	139
Table 18: Summary of the human toxicity potential of the TE materials at the product stage.	142
Table 19: Details regarding material's parameters used in the manufacturing and analysis.	151
Table 20: The codes of the prepared samples based on the coating region and the added filler.	151
Table 21: Summary of the physical specification and output power of the TEGs consisted of ingot-shaped legs.	181
Table 22: Scales of the subjective responses.	222

List of Publications

Part of the work presented in this thesis has been published and presented in the references listed below.

- **Journal Papers**

- J1:** Z. Soleimani, S. Zoras, B. Ceranic, Y. Cui, and S. Shahzad, “A comprehensive review on the output voltage/power of wearable thermoelectric generators concerning their geometry and thermoelectric materials,” *Nano Energy*, vol. 89 (Part A), pp. 106325, **2021. (IF: 17.881)**
- J2:** Z. Soleimani, S. Zoras, B. Ceranic, S. Shahzad, and Y. Cui, “The cradle to gate life-cycle assessment of thermoelectric materials: A comparison of inorganic, organic and hybrid types,” *Sustain. Energy Technol. Assessments*, vol. 44, p. 101073, **2021. (IF: 5.353)**
- J3:** Z. Soleimani, S. Zoras, B. Ceranic, S. Shahzad, and Y. Cui, “A review on recent developments of thermoelectric materials for room-temperature applications,” *Sustain. Energy Technol. Assessments*, vol. 37, pp. 100604, **2020. (IF: 5.353)**

- **Conference Papers**

- C1:** Z. Soleimani, S. Zoras, Y. Cui, B. Ceranic, and S. Shahzad, “Design of heat sinks for wearable thermoelectric generators to power personal heating garments: A numerical study,” in *IOP Conference Series: Earth and Environmental Science*, vol. 410, no. 1, pp. 012096, **2020.**
- C2:** Z. Soleimani, S. Zoras, B. Ceranic, S. Shahzad, and Y. Cui, “Optimization of a wearable thermoelectric generator encapsulated in polydimethylsiloxane (PDMS): A numerical modelling,” in *2019 IEEE 2nd International Conference on Renewable Energy and Power Engineering (REPE)*, pp. 212–215, **2019.**

• Posters & Presentations

- P1:** **Z. Soleimani**, S. Zoras, and B. Ceranic, “Research on the development of a personal heating system with a thermoelectric generator as one of the energy supplies”, in *2021 Environmental Sustainability Research Centre Conference*, June 21st **2021**, University of Derby, UK.
- P2:** **Z. Soleimani**, S. Zoras, and Y. Cui, “Performance assessment of a cavity wall for generating electricity: a novel 3D model”, in *the 4th International Conference on Changing Cities*, June 24th - 29th **2019**, Chania, Crete Island, Greece.
- P3:** **Z. Soleimani**, S. Zoras, B. Ceranic, and S. Shahzad, “Thermoelectric generators: personal comfort systems powered by body heat”, *RIBA research matters*, October 19th **2018**, Hallam Hall, Sheffield Hallam University, UK.
- P4:** **Z. Soleimani**, S. Zoras, B. Ceranic, and S. Shahzad, “Harvesting body heat as a renewable energy source to introduce a self-powered personalised heating system”, *University of Derby’s annual PGR student Conference*, April 23rd **2018**, University of Derby, UK.

Nomenclature

Symbols		Acronyms	
μ_e	Electron mobility	Al_2O_3	Aluminium oxide
μ_h	Hole mobility	ASHRAE	American Society of Heating, Refrigerating and Air-Conditioning Engineers
Ah	Capacity of the battery (mAh)	Bi_2Te_3	Bismuth telluride
c	Specific heat capacity (J/K)	CHP	Combined heat and power
c_p	Specific heat at a constant pressure (J/kg K)	Clo	Clothing insulation
E_b	The energy stored in the battery (Wh)	CNTs	Carbon nanotubes
E_c	The energy stored in the capacitor (J)	CO_2	Carbon dioxide
F	Capacitance of the capacitor (F)	FPCB	Flexible printed circuit board
f_{cl}	The clothing surface area factor	Gt	Gigatonnes
h_c	The convective heat transfer coefficient (W/m ² K)	GWP	Global warming potential
I_{cl}	The clothing insulation (m ² K/W)	HTP	Human toxicity potential
J	Electrical current density (A / m ²)	HVAC	Heating ventilation and air conditioning
K	Thermal conductivity W/(m·K)	IEQ	Indoor environmental quality
M	The metabolic energy production (W/m ²)	ISO	International organization for standardization
n	Electron concentration	LCIA	life cycle impact assessment
p	Hole concentration	LDPE	polyethylene
P	Peltier coefficient (J/C)	Mtoe	Million tonnes of oil equivalent
p_a	The water vapour partial pressure (Pa)	MWCNTs	Multi-walled carbon nanotube
Q	Heat source (J)	ODP	Ozone depletion potential
q	Generated heat (J)	PANI	Polyaniline
q_x	The heat flux (W/m ²)	PCM	Phase change material
T	Absolute temperature (K)	PCSs	Personal comfort systems
t_a	The ambient air temperature (°C)	PDMS	polydimethylsiloxane
T_C	Temperature of the cold reservoirs (K)	PEDOT	Poly (3,4-ethylenedioxythiophene)
t_{cl}	The clothing surface temperature (°C)	PEDOT:PSS	Poly (3,4-ethylenedioxythiophene): poly (styrenesulfonate)
T_H	Temperature of the hot reservoirs (K)	PF	Power factor
t_r	The mean radiant temperature (°C)	PMV	Predicted mean vote
V	The Seebeck voltage (V)	PPY	Polypyrrole

V_b	Voltage of the battery (V)	SWNTs	Single walled nanotubes
V_c	Voltage of the capacitor (V)	TE	Thermoelectric
W	The rate of mechanical work (W/m ²)	TEGs	Thermoelectric generators
$Z\bar{T}$	The figure of merit		
α	The Seebeck coefficient ($\mu\text{V}/\text{K}$)		
ΔT	The temperature difference (K)		
η_{max}	Heat-to-power conversion efficiency		
λ	The thermal conductivity (W/mK)		
ρ	Density(kg/m ³)		
σ	The electrical conductivity (S/cm)		

Author's Declaration

I, Zohreh Soleimani, declare that the work outlined in this thesis was carried out in the College of Engineering and Technology, University of Derby, UK under the supervision of Prof. Stamatis Zoras and Dr. Boris Ceranic. Furthermore, I declare that this thesis has been composed solely by myself and that it has not been submitted, in whole or in part, in any previous application for a degree. I confirm that due references have been provided on all supporting literatures and resources, and parts of this work have been published in the papers listed under List of Publications. No animal but human participation has been included in this research, thus the research presented in this thesis has been ethically approved.

Zohreh Soleimani

University of Derby

16th August, 2021

Acknowledgments

First and foremost, I would like to thank God Almighty for giving me the opportunity, strength, knowledge, and ability to start and complete this research.

I would like to express my sincere thanks to my patient and supportive Director of Studies and mentor, Prof. Stamatis Zoras, for his expert guidance, encouragement, support, and friendly supervision throughout my PhD journey. Meanwhile, profound appreciation would be delivered to my second supervisor, Dr Boris Ceranic, who provided me with technical supervision over the last years. Furthermore, I would like to extend my gratitude to Dr. Sally Shahzad. Her support and motivations encouraged me to think beyond, work harder, and look for opportunities to grow.

Then, I would like to express my appreciation and gratitude to my parents for all they have done for me. Thank you for all your supports.

A big thanks goes to my beloved husband. Dearest Sina, thank you for always believing in me, supporting me to fulfil my dreams, being patient, caring, and cheerful. I credit a lot of my success to having you by my side during this period. Without you, I do not think I would have had the confidence to reach for the things I really wanted. Thank you for being beside me when I was unable to stand on my own. This achievement would not have been possible without your support. I will never forget all your kindness before and during my PhD.

I also would like to thank my mother-in-law for her continuous love and support. Dear Maman Parvin, thank you for supporting me spiritually throughout this journey and my life in general. I am so grateful to have you in my life.

Special thanks also goes to my friends in University of Derby, particularly Maham, Hamna, Bilal, Farhan, Sanna, Ade, and Yuanlong. I also want to thank my old friend Fatemeh Jahedpari for all

her supports. Thank you for listening to my worries and bringing joy and happiness to this journey.
I have learnt a lot from each of you.

***To my husband, Sina,
for his love, kindness and never-ending support***

Thesis Summary

Due to the extensive contribution of the fossil fuels' combustion to the global warming, increasing attention has been drawn to reduce the carbon footprint of all sectors by moving toward green technologies. Accordingly, personal comfort systems (PCSs) are considered as a green substitute for the conventional heating, ventilation, and air conditioning (HVAC) systems in the buildings. Precisely, PCSs can address the thermal comfort of each individual in shared spaces, such as office buildings, with remarkably lower energy consumption than the HVAC systems. To clarify, they save energy by conditioning only the air surrounding each individual, leaving the unoccupied points of the buildings unconditioned. However, their main drawback is that they are mostly powered either by a fossil fuel based power supply (i.e. public electricity) or batteries, which to some extent offsets their eco-friendly feature. Regarding batteries, although they are not considered as a fossil fuel based power supply, they can cause negative environmental impact due to their constitutive elements (e.g. cobalt).

Accordingly, in this thesis, it was proposed to develop a hybrid power supply comprising a renewable power source called a thermoelectric generator (TEG) and a rechargeable battery to reduce the carbon footprint of the PCSs. To illustrate, a TEG is considered as a promising thermal energy harvester, which captures the waste ambient heat and converts it into electricity. To put it another way, it employs the temperature difference between a hot and a cold object to generate electricity. In this research, this temperature difference was provided by a candle and the ambient air as the heat and cold sources, respectively. The main reason for using a candle as the heat source was that at room temperature none of the existing internal heat sources (e.g. radiators, hot pipe works) could provide the required temperature difference along the thermoelectric (TE) legs. As a result, the TE legs could not generate enough electricity to power a PCS. Regarding the rechargeable battery, it mainly served as a storage system to store the generated electricity by the

TEG to release it on demand. In fact, this storage system performed a pivotal role between the TEG (as a green energy supply) and the electricity demand. To clarify, the generated electricity by a TEG is variable, depending on the temperature difference along its legs. Thus, to provide a reliable power for the studied PCS, usage of a storage system was inevitable. In addition, due to the low output current of the TEGs at the room temperature, the storage system also performed as a backup power supply to provide a constant current for the PCS.

To develop the TEG part of the hybrid power supply, initially the life cycle impact of 14 thermoelectric materials were numerically studied from cradle to gate (i.e. raw material's extraction to manufacturing the final material). The main aim of this numerical study was to select the most environmental friendly material out of the three TE types of inorganic, organic, and hybrid. The employed software for this life cycle impact assessment (LCIA) was GaBi v.4.4, and the results proved the greatest environmental damage of the inorganic type compared with the other two types. However, Bi_2Te_3 was an exceptional inorganic TE material that its life cycle impact was not only less than that of the other studied inorganic TE materials, but also far less than that of the studied organic and hybrid ones.

According, an off-the-shelf TEG consisted of Bi_2Te_3 was selected for this research, and different integrating patterns were determined to couple six of that together. These patterns were considered based on providing enough temperature difference along the TE legs. Accordingly, three different patterns were developed namely, coating either the top half, or the bottom half, or fully the legs with the integrating substrate. To further improve the temperature difference along the legs, the thermal conductivity of the integrating substrate was manipulated by adding different fillers to it. Then, the thermoelectric effects of all of the developed samples were studied both numerically (i.e. computational modelling by COMSOL) and experimentally (i.e. laboratory tests). Based on the outcomes of both studies, coating only the top half of the legs with a low thermal conductivity substrate called polydimethylsiloxane (PDMS) resulted in the highest output power compared with the other two patterns. Accordingly, the TEG part of the hybrid power supply was fabricated with respect to the achieved optimal integrating substrate. Then, to further improve the temperature difference along the TE legs, two different heatsinks (pin-shaped and bumpy-shaped) were developed, and their performances were studied in the laboratory under three air flow conditions

(0,1.2, and 2.4 m/s). The results proved the superiority of the pin-shaped heatsink to the bumpy-shaped one after being attached to the PDMS-based integrating substrate.

Next, six of the considered off-the-shelf TEG were coupled together from the top half of their legs using the optimal developed PDMS-based integrating substrate. After that, the pre-developed pin-shaped heatsink was attached to the integrating substrate. Then, the integrated TEGs were coupled with a rechargeable battery to heat a pair of pre-developed heating armbands (i.e. the studied PCS). To test the heating performance of the armbands, they were tested in-field on eight subjects served as office workers in the heating season of March in the UK. The results revealed that at roughly 15 °C to 16 °C ambient temperature, 75% of the subjects felt warmer after 30 min of wearing the armbands. To specify, the armbands improved their average comfort level from slightly uncomfortable to slightly comfortable after 30 min of wearing them. Thus, not only this thesis developed a PCS concerning its conditioning performance, but also it addressed the sustainability aspect of its power supply. Accordingly, this thesis paves the way for further research on developing different types of renewable power supplies for any green technologies, including PCSs.

Chapter 1

Introduction

1.1 Background

Driven by the shortage of the fossil fuels reservoirs and the inevitable global warming, extensive attempts have been made to replace the fossil fuel based power sources with the renewable ones. Accordingly, international conventions such as the United Nations Framework Convention on Climate Change (UNFCCC) (1994), the Kyoto Protocol (1997), and the Paris Agreement (forced on 2016) established international emission reduction targets and strengthened the global response to the threat of the climate change. To specify, the Paris Agreement aimed to limit the global warming to well below 2 °C, preferably to 1.5 °C, compared to pre-industrial levels [1]. Consequently, there has been a considerable increase in the national and subnational mitigation plans and strategies, such as the Ten Point Plan for a Green Industrial Revolution in the UK, aiming at net zero emissions by 2050 [2]. Supporting these mitigation plans and strategies, the building sector is one of the main targets due to being accountable for 36% of the global final energy demand [3], as Fig. 1 shows. To clarify, the final energy consumption of the buildings in 2018 was 3050 Million tonnes of oil equivalent (Mtoe). This associated with 3 Gigatonnes (Gt) energy related carbon dioxide (CO₂) emissions, equalling to 39% of the total direct and indirect global CO₂ emissions [4,5].

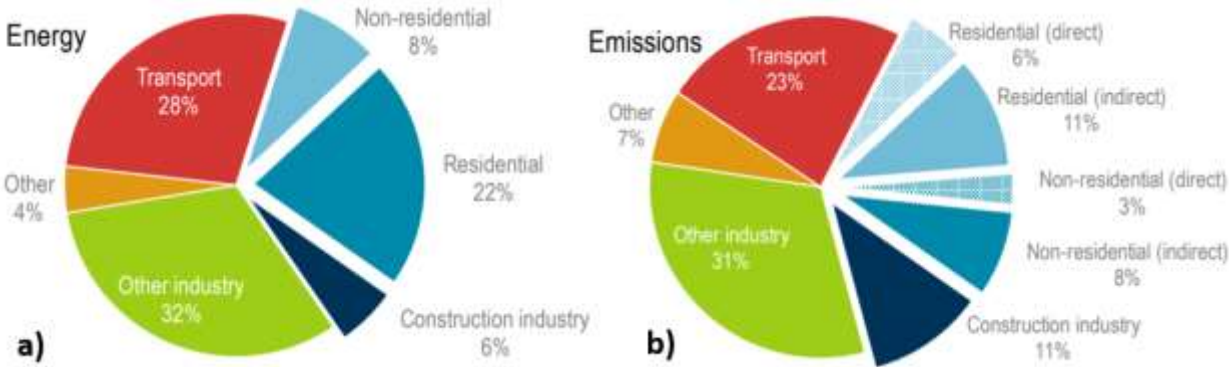


Fig. 1: a) Global primary energy consumption by end-use sector from 1970 to 2040; and b) final energy consumption in buildings by fuel from 2000 to 2040 [3].

Importantly, heating, ventilation, and air conditioning (HVAC) systems are responsible for nearly 50% of the final energy demand of the non-residential buildings [6]. This highlights the importance

of reducing the carbon footprint of the buildings by moving away from the fossil fuel based conditioning systems but towards the renewable ones. Also, the well-managed usage of the conditioning systems is of critical importance to decrease their associated high energy consumption. To specify, the foremost reason of the high energy demand of the HVAC systems is that they waste energy by equally conditioning every point of buildings, regardless of the real occupancy status of the buildings at the time [7]. To put it another way, the control systems of most non-residential buildings condition the ambient air based on their maximum occupancy set-point. This approach suffers from two issues, including the dynamic variation of the buildings' occupancy during weekdays and conditioning the unoccupied points the same as the occupied ones [8]. Therefore, assuming the maximum occupancy status by the control systems causes either overheating or overcooling of the buildings, which inevitably leads to the waste of energy and even the discomfort of occupants [9].

Another reason leading to the high energy consumption of the HVAC systems is that they condition the ambient air regardless of the individuals' thermal preferences. To illustrate, the HVAC systems ignore the fact that the thermal preference of the occupants varies from person to person in the shared spaces, such as office buildings. Therefore, in spite of their high energy consumption for conditioning the office buildings, more than 20% of office workers suffer from thermal discomfort in their office environments [10]. As a result, thermal dissatisfaction is the main reason of complain among the office workers about their office environments, which negatively impacts on their productivity and efficiency [11-13]. Furthermore, the conventional HVAC systems waste energy by uniformly conditioning the whole body. However, it is against the facts that not only different body parts have different thermal sensitivities, but also the rate of their thermal sensitivity varies depending on the ambient temperature [14]. To clarify, there are specific body parts called hot and cold spots that are more sensitive to the hot and cold conditions, respectively. For instance, the skin temperatures of hands, fingertips, and feet have dominant effect on feeling cold, whereas chest, head and back are the most sensitive body parts to warm [15-18], see Fig.2. Therefore, addressing only the thermal satisfaction of these hot and cold spots could reduce the energy load of the HVAC systems.

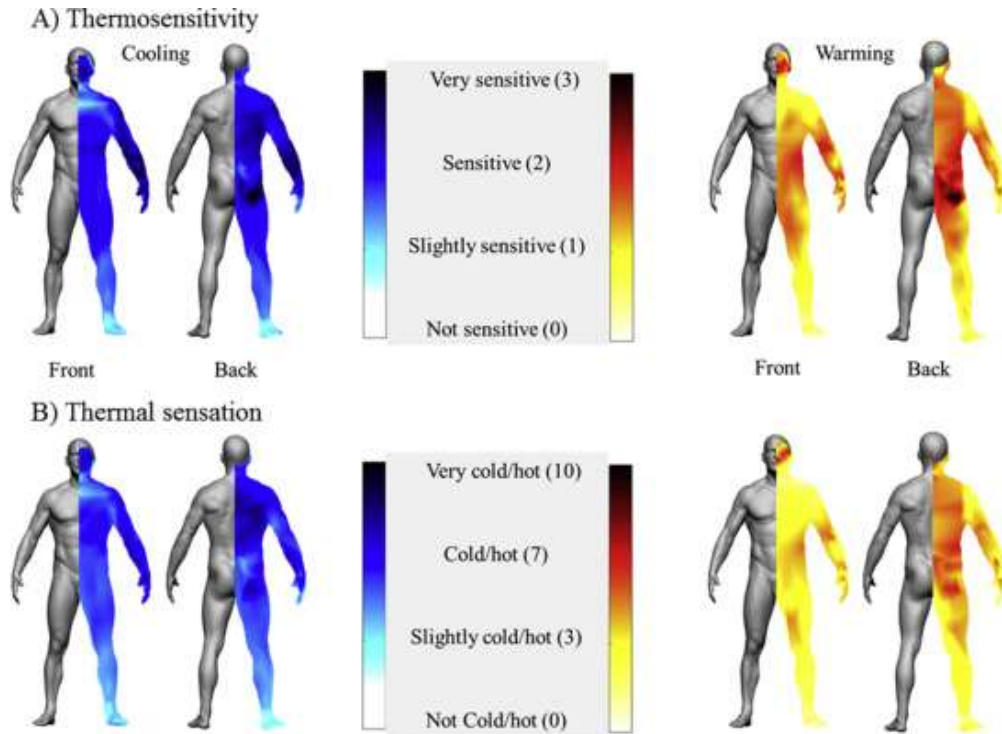


Fig. 2: Whole-body thermal sensitivity and thermal sensation mapping [14].

Accordingly, several research replaced the HVAC systems with the personal comfort systems (PCSs) in the office buildings to tackle both the sustainability-related challenges and the thermal discomfort [19]. To illustrate, the PCSs only condition the air surrounding the body with regard to the thermal expectations of each individual. As a result, they provide higher thermal comfort for the occupants and satisfy a greater number of them compared with the HVAC systems [18]. Precisely, Veselý et al. [20] demonstrated that replacing the HVAC systems with any type of PCS improves both the thermal comfort of the occupants and the energy efficiency of the buildings. Also, Verhaart et al. [21] showed 34% saving in the heating load of a building by replacing its HVAC system with the PCSs. In addition, this replacement also improved the occupants' thermal satisfaction.

Notably, among different types of the PCSs, such as the conditioning chairs, floor/desktop mats, and garments, the latter is most preferred [22]. This is mainly because the conditioning garments have more proximity to the wearers' body surface compared with the other three types as Fig.3 depicts, resulting in greater thermal satisfaction. However, the main drawback of the PCSs, including the conditioning garments, is that they are powered by either public electricity or

batteries [23]. Regarding the public electricity, the number of people without electricity access was 770 million in 2019, and 650 million people (i.e. 8% of the global population) will still lack access to electricity in 2030 [24]. In fact, majority of this population are concentrated in developing countries (e.g. Democratic Republic of the Congo, Nigeria, Uganda, Pakistan, Tanzania, Niger and Sudan) with harsh climatic conditions. Notably, in these countries, PCSs can be considered as a lower cost thermal conditioning system in the buildings compared with the HVAC ones. Whereas, being powered with public electricity, these countries are even deprived from such a low cost service. In addition, 74% of the global electricity generation in 2018 was based on fossil fuels (i.e. coal, oil, and natural gas) combustion [25]. To clarify, the main environmental issue of the combustion-based electricity generation is emitting the main air pollutants, such as sulfur oxides, sulfur dioxide (SO₂), nitrogen oxides (NO_x), and carbon dioxide (CO₂) [26]. Concerning batteries, they cause serious environmental impacts throughout their life cycle, including their raw materials extraction, manufacturing, usage, and recycling/discarding stages [27,28]. Notably, lithium-ion batteries are the most quickly growing form of technology in the battery market. Although there are sufficient reserves of most of the key constituents of these batteries, they cannot be relied on in long term or in case of an extreme and unexpected raise in their demand. Furthermore, there are some concerns about the toxicity and safety of certain components of the batteries, such as the active materials (e.g. cobalt) in their electrodes and electrolytes and the substances that bind their electrodes' materials together [29]. Therefore, it is desirable to develop a PCS with less dependency to these two power supplies (i.e. public electricity and batteries).

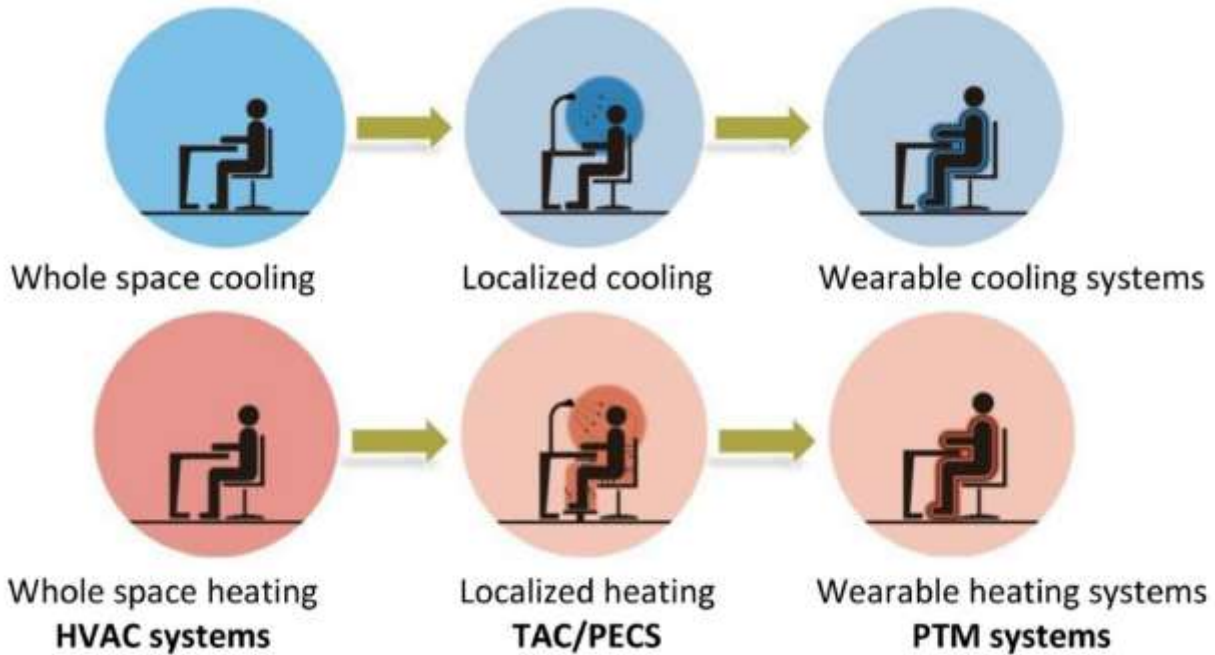


Fig. 3: The intensity of the conditioning area as it gets closer to the human body [30].

To solve these problems, one solution is to move toward eco-friendly power supplies like energy harvesters (e.g. thermoelectric, pyroelectric, and piezoelectric generators) for the PCSs. To illustrate, energy harvesters capture energy either from motion, temperature gradient, light, electromagnetic radiation, or chemical energy and convert them to electricity. Among these various energy sources, temperature gradient is appeared as a promising green and clean energy competitor. This is mainly because, thermoelectric generators (TEGs), which harvest the temperature gradient to generate electricity, benefit from noiseless and maintenance-free operation, no chemical reactions, no moving part, and durability compared with the other energy harvesters. However, the fundamental problem with them to power PCSs is that their generated electricity is not reliable (i.e. insufficient to power the PCSs for a long time). Thus, they are required to be coupled with a rechargeable battery serving both as a backup power supply and a storage system. Splitting the energy generation between an energy harvester and a battery not only decreases the number of the required batteries, but also reduces the discharging rate of the battery. However, so far, no research has applied any type of energy harvesters to power a conditioning garment. Thus, this study aimed to fill this gap by combining a TEG with a rechargeable battery to power a conditioning garment. Due to the highest sensitivity of hands and fingertips to cold

[31], the generated electricity by the developed hybrid power supply was used to heat a pair of heating armbands. Also, owing to the direct relationship between thermal and job satisfactions at office spaces [32-35], the proposed heating armband served to heat office workers in a cold environment.

1.2 Research aim and objectives

The aim of this research is to design a hybrid power supply with a set of optimized integrated TEGs and a rechargeable battery to power a pair of heating armbands:

- i. to reliably satisfy the thermal comfort of office workers in a “cold” environment and diminish their thermal discomfort during the working hours.
- ii. to reduce the dependency of the PCSs to the fossil fuel based power supplies, such as public electricity.

Accordingly, the overall objectives to fulfil the specified aim are as follows:

- Conducting a comprehensive literature review on the principles of thermal comfort, different types of personal heating systems, the properties of different thermoelectric (TE) materials, and different configurations of TEGs.
- Developing the hybrid power supply with a simple, inexpensive, and manual fabricating process. Sub-objectives include:
 - i. assessing the life cycle impact of different TE materials at their production stage to select the most environmental friendly ones.
 - ii. proposing different designs to integrate the TEGs together, and carrying out numerical and laboratory studies to find out the most optimum design
 - iii. developing the hybrid power supply via combining the integrated TEGs with a rechargeable battery.
- Powering a pair of heating armbands using the pre-developed hybrid power supply. Sub-objectives include:

- i. testing the developed heating system in-field by asking some volunteers to wear it in a cold ambient.

1.3 Research questions

- What is the most optimal TE material at room temperature regarding the energy conversion efficiency and the life cycle impact?
- How is it possible to integrate a number of TE legs together with a lightweight substrate that has no or the least negative effects on the efficiency of the legs?
- What is the most appropriate approach to fabricate a lightweight heatsink to improve the efficiency of the integrated TEGs?
- What is the easiest fabrication process to develop the hybrid power supply comprising the integrated TEGs and the rechargeable battery?
- Can the developed hybrid power supply heat the pair of heating armbands?
- Is it possible to improve the thermal comfort of hands and the whole body in a “cold” environment using the powered heating armbands?

1.4 Research Significance

The significances of this research can be summarized as follows:

- **Uniqueness:** the idea of using a renewable power supply (e.g. TEGs) to power a PCS is unique. To the best of our knowledge, it has never been done elsewhere.
- **Sustainability:** powering the proposed PCS (i.e. the heating armbands) with the developed hybrid power supply takes into account the thermal comfort, the energy efficiency, and the carbon footprint of the PCS at the same time. On the contrary, other current PCSs are

mainly powered with a fossil fuel based power supply, which is believed to contribute to higher carbon footprint.

- **Applications:** although the main focus of this research is to satisfy the thermal sensation and comfort of the office workers, but the fabricated personal heating system powered by the developed hybrid power supply is also usable by other individuals having other indoor jobs.

1.5 Thesis outline

The outline of this thesis can be classified into six sections, including the literature review, the methodology, the numerical modelling, the laboratory study, the field study, and the thesis conclusions.

1.5.1 The literature review

The first section of the thesis lays the foundations of this research by including the six following chapters:

- [Chapter 1](#): Introduction
- [Chapter 2](#): Thermal Comfort
- [Chapter 3](#): Personal Heating Systems
- [Chapter 4](#): Principles of Thermoelectric Generators and Thermoelectric Materials
- [Chapter 5](#): Different Configurations of TEGs

[Chapter 1](#) was an introduction to the thesis and included the aim, the objectives, the research questions, the significance, and the outline of the thesis. This was followed by [Chapter 2](#) that explained the principles of the thermal sensation and comfort in indoor environments specially at workplaces. The focus of this chapter was on identifying the most sensitive body parts to cold regarding the overall thermal sensation and comfort. Furthermore, this chapter determined the most essential evaluating factors of the objective measurements and the subjective questionnaire survey concerning the later field study. In [Chapter 3](#), current personal heating systems as well as

their benefits and deficiencies were reviewed. In accordance with [Chapters 2 and 3](#), it was determined to develop a pair of heating armbands to address the thermal sensation and comfort of hands as one of the main cold spots of the body. Also, based on the reviewed literatures in [Chapter 3](#), it was specified to power the heating armbands via a hybrid power supply comprising a rechargeable battery and a renewable power supply (i.e. a set of TEGs). Then, basic principles of TEGs were reviewed in [Chapter 4](#) to determine the most effecting factors on their performance. Accordingly, different TE materials and configurations of TEGs were reviewed in this chapter and 6, respectively. Following the outcomes of [Chapter 4](#), among different types of TE materials, the inorganic type illustrated superior performance than the organic and hybrid types. However, it was demonstrated that the missing point was the environmental impacts of the TE materials, which also should be considered at the time of selection. In accordance with [Chapter 5](#), the ingot-shaped thermocouples comprising inorganic TE materials delivered higher power density than the film- and yarn-shaped ones. However again, it was explained that it was of critical importance to consider the life cycle impact of the TE materials along with the energy conversion efficiency of the TEGs.

1.5.2 The research methodology

This section explains the applied methods to fulfill the research aim, and it consisted of one chapter:

- [Chapter 6](#): Research Methodology

Thus, [Chapter 6](#) illustrated in detail the three applied methods, such as the numerical modelling, the laboratory experiment, and the field study, to fulfill the research aim.

1.5.3 The numerical modelling

This section demonstrates the conducted numerical modelling using GaBi and COMSOL software:

- [Chapter 7](#): The Life Cycle Impact assessment

- [Chapter 8](#): The Lightweight Integrating Substrate

Concerning the outcomes of [Chapters 4](#) and [5](#), the life cycle impacts of different TE materials were analyzed in [Chapter 7](#), using GaBi software. Combining the findings of these three chapters together, a TEG comprising of an inorganic TE material was selected for this research. Accordingly, the aim of [Chapter 8](#) was developing a lightweight integrating substrate to combine a number of the specified TEGs together such that it caused the least negative effect on the efficiency of the TEGs. Thus, several computational simulations were carried out in the COMSOL multiphysics to evaluate the TE performance of the proposed integrating patterns.

1.5.4 The laboratory study

This section clarifies the conducted laboratory tests to optimize the performance of the TEGs:

- [Chapter 8](#): The Lightweight Integrating Substrate
- [Chapter 9](#): The Lightweight Heatsink

Validating the computational modelling, [Chapter 8](#) also fabricated the developed integrating patterns in the COMSOL multiphysics in the laboratory to study their performances in the real-life as well. The results of both the computational and the laboratory studies unanimously revealed the most optimal integrating substrate. Accordingly, in [Chapter 9](#), a lightweight heatsink was developed in the laboratory with regard to the constituent material of the optimal integrating substrate. This was based on this fact that matching the material of the heatsink and the substrate could decrease the thermal resistivity at their junctions.

1.5.5 The field study

This section contains the procedure of fabricating the personal heating system and testing it in the real-life:

- [Chapter 10](#): Fabricating the Heating Armbands

Finally, in [Chapter 10](#), six individual TEGs were integrated together following the optimal integrating substrate developed in [Chapter 8](#). Next, the prepared heatsinks in [Chapter 9](#) were attached to the integrating substrate. After that, the integrated TEGs were coupled with a rechargeable battery to fabricate the hybrid power supply. Next, two heating elements were sewn onto two armbands to be heated by the as-prepared hybrid power supply. To study the heating performance of the developed heating armbands, 8 subjects were recruited to wear the armbands in a cold ambient. The tests were carried out in an office room for 45 min to find out the heating effect of the armbands on the thermal sensation and comfort of different body parts and the whole body.

1.5.6 The thesis conclusions

This section contains the summary of the thesis conclusions, contributions, limitations, and future works:

- [Chapter 11](#): Conclusion and Future Works

Accordingly, [Chapter 11](#) concluded the thesis by presenting a summary of the outcomes of each previous chapter. In addition, this chapter discussed the contributions of this research to the relative studies and highlighted the limitations of this research for future consideration. Last but not least, this chapter demonstrated in detail the future possible works following this research.

Chapter 2

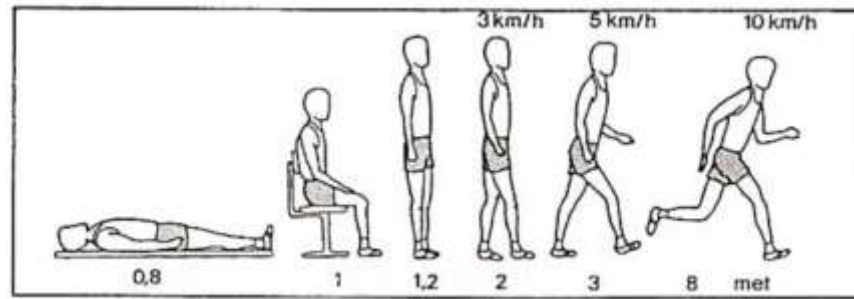
Thermal Comfort

2.1 Introduction

Indoor environmental quality (IEQ) refers to the quality of a building's environment in relation to the health and wellbeing of its occupants. In fact, IEQ depends on several parameters, including indoor air quality, thermal comfort, visual comfort, and acoustic comfort [36]. Among them, the thermal comfort is the most influential and easily defined parameter of IEQ [37,38]. To clarify, satisfying the thermal comfort of the occupants directly impacts on their physical and mental health, productivity, and efficiency in short and long terms [39-41]. Accordingly, the main aim of this chapter is to illustrate the basic principles of thermal comfort, which were considered for preparing the questionnaires of the in-field experiment of this research (i.e. the questionnaires used in Chapter 10).

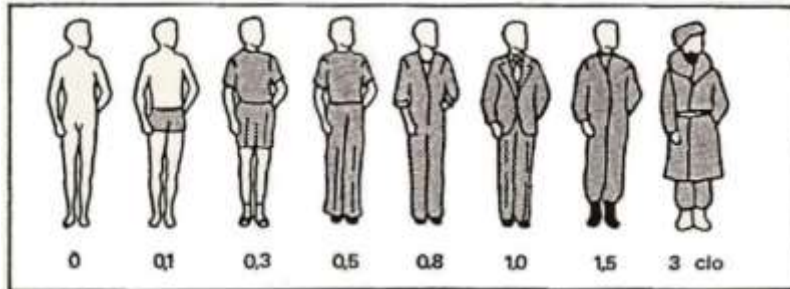
2.2 Predicted mean vote (PMV)

The two globally recognized standards for evaluating indoor environments (i.e. ASHRAE 55 and ISO 7730) define the thermal comfort as “that condition of mind that expresses satisfaction with the thermal environment” [42,43]. To assess this condition, these standards use the seven-point scale of thermal sensation developed by Povl Ole Fanger at Kansas State University and the Technical University of Denmark [44]. To define the seven-point thermal sensation scale, Fanger related the thermal comfort of the occupants to four physical and two personal parameters. The four physical parameters were air temperature, air velocity, mean radiant temperature, and relative humidity. The two personal parameters were physical activity level (i.e. metabolic rate) and clothing insulation (clo), see Fig.4 and Fig.5. Accordingly, Fanger created the predicted mean vote (PMV) model, which is an index to predict the thermal sensation of a group of people based on the mean value of their votes on the seven-point thermal sensation scale [45]. As Fig.6 depicts, the seven-point thermal sensation scale is expressed from -3 to +3 corresponding to the sensations from cold to hot, respectively. Notably, ISO 7730 calculated the PMV based on the metabolic energy production (W/m^2), the rate of the mechanical work (W/m^2), the water vapour partial pressure (Pa), the ambient air temperature ($^{\circ}C$), the clothing surface area factor, the clothing surface temperature ($^{\circ}C$), the mean radiant temperature ($^{\circ}C$), and the convective heat transfer coefficient (W/m^2K) [43].



Activity	Met	$W m^{-2}$
Lying down	0.8	47
Seated quietly	1.0	58
Sedentary activity (office, home, laboratory, school)	1.2	70
Standing, relaxed	1.2	70
Light activity, standing (shopping, laboratory, light industry)	1.6	93
Medium activity, standing (shop assistant, domestic work, machine work)	2.0	116
High activity (heavy machine work, garage work)	3.0	175

Fig. 4: The metabolic rates according to the activity [46].



<i>Clothing ensemble</i>	Clo	$m^2 K W^{-1}$
Naked	0	0
Shorts	0.1	0.016
<i>Typical tropical clothing outfit</i> Briefs (underpants), shorts, open neck shirt with short sleeves, light socks and sandals	0.3	0.047
<i>Light summer clothing</i> Briefs, long lightweight trousers, open neck shirt with short sleeves, light socks and shoes	0.5	0.078
<i>Working clothes</i> Underwear, cotton working shirt with long sleeves, working trousers, woollen socks and shoes	0.8	0.124
<i>Typical indoor winter clothing combination</i> Underwear, shirt with long sleeves, trousers, sweater with long sleeves, heavy socks and shoes	1.0	0.155
<i>Heavy traditional European business suit</i> Cotton underwear with long legs and sleeves, shirt, suit comprising trousers, jacket and waistcoat (US vest), woollen socks and heavy shoes	1.5	0.233

Fig. 5: The thermal insulation values for clothing [47].

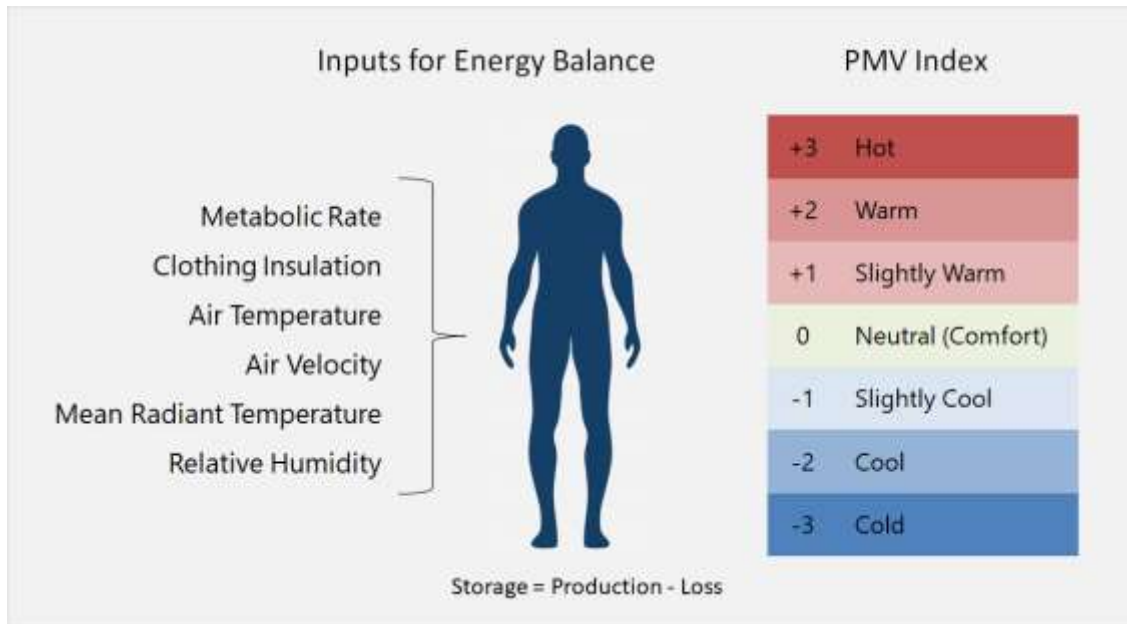


Fig. 6: The seven-point thermal sensation scale [48].

2.3 Acceptable PMV

Considering the PMV index, ASHRAE 55 dictates the thermal comfort zone based on the thermal satisfaction of at least 80% of the occupants. Precisely, the thermal comfort zone is where at least 80% of the occupants are between -0.8 and 0.8 on the PMV scale. Based on ASHRAE 55, the thermal discomfort of the remaining 20% occupants could be acceptable when only 10% of them suffer from whole-body discomfort, and the other 10% bother from partial body discomfort [49]. As Fig.7 shows, at 1.1 metabolic rate and 0.1 m/s air velocity, ASHRAE Standard 55 recommends ~20-24 °C and ~23.5-27 °C as the comfort zone boundaries for winter clothing (1 clo) and summer clothing (0.5 clo), respectively [50].

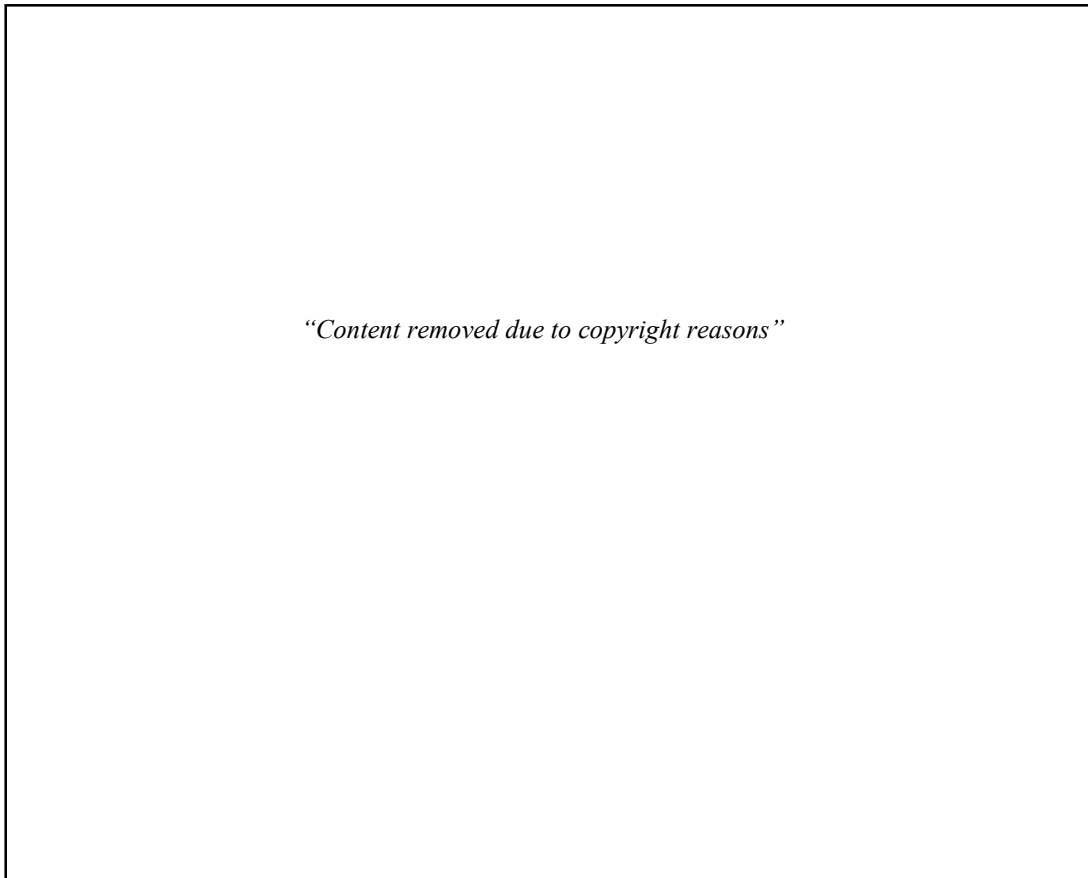


Fig. 7: "Content removed due to copyright reasons"

2.4 Adaptive PMV

Although the PMV model is one of the most widely used index of thermal sensation, several studies indicate that it tends to overestimate or underestimate the actual mean vote of the occupants [51-57]. For instance, Haq Gilani et al. [58] indicates that there is 31% and 33% discrepancy between the predicted (i.e. the PMV model) and the perceived thermal sensation of the occupants in the summer and winter seasons, respectively. This is essentially because the PMV model defines the overall thermal comfort of the human body in a static and inflexible manner. To clarify, the PMV model ignores the occupants' adaptation to thermal conditions, whereas this factor remarkably affects their thermal sensation [59]. To clarify, people implement some corrective actions to retain their comfort in discomfort conditions. Thus, in recent years, the traditional PMV model has been modified by being combined with any type of adaptive PMV model. In fact, the adaptive PMV models determine the thermal comfort of the occupants in a range of possible

temperatures that the occupants are able to adapt themselves to. In particular, there are four widely used adaptive PMV models developed by Yao [51], Dear and Brager [60], Nicol and Humphreys [61], and Fanger –Toftum [62].

Based on all these adaptive models, the thermal sensation not only depends on the six parameters defined by the PMV model, but also it relates to a wider range of contextual factors such as the prior thermal history of the occupants and outdoor temperatures [63]. Accordingly, the occupants' adaptations could be classified into three categories, including physiological, psychological, and behavioural adaptations [64]. The physiological adaptation is part of a systematic thermoregulation process in the body aimed at maintaining a relatively constant body temperature [65]. Accordingly, the brain regulates the body temperature to function within a narrow range (i.e. 3 °C- 4 °C) from 36.8 °C comprising the core (64%) and skin (37%) temperatures [66]. This regulation is achieved by adjusting the physiological activities such as shivering, sweating, vasodilation, and vasoconstriction to produce or dissipate the body heat [67].

The psychological adaptation refers to the occupants' thermal sensation based on their past thermal experiences, contextual factors, and perceived level of control [68]. For example, rather than feeling neutral, people in hot and cold climates may prefer feeling slightly cool or slightly warm to reach the thermal comfort, respectively [69]. Likewise, people prefer feeling warm rather than neutral when it is cool outside and the other way round [70]. Therefore, the defined thermal neutrality by the PMV model is not necessarily the occupants' choice, since their preference for non-neutral thermal sensations is more prevalent. To put it another way, very low and very high PMV values do not necessarily reflect the occupants' thermal discomfort [45]. Another psychological aspect that increases the thermal satisfaction is having access to the thermal controls (i.e. thermostat) even when it is impossible to alter the temperature [71,72]. Alhorr et al. [73] illustrates that when the office occupants have control over the conditioning systems, their satisfaction boosts up to 99%. However, it should be considered that there is a converse relationship between the perceived level of control and the number of occupants in the office [74].

The behavioural adaptation is different from the other two types of adaptation. This is mainly because in this type, the occupants consciously take actions to maintain their own thermal comfort. To specify, the behavioural adjustment can be divided into three main categories, including

personal, technological, and cultural adjustments. The personal adjustment refers to modifying the activity, clothing, posture, eating food or drinking beverages, and changing the place. The technological adjustment includes modifying the environment or surroundings, such as turning the air-conditioners on/off or opening/closing the windows. Finally, the cultural adjustments involves having a siesta on a hot day and scheduling activities accordingly [75]. As a result, ANSI/ASHRAE Standard 55 [50] and European Standard EN 15251 [76] employ the adaptive PMV model instead of the PMV one to evaluate the thermal comfort level of the occupants.

2.5 Distribution of thermal sensitivity

There is a correlation between the thermal comfort of office workers and their efficiency, productivity, and job satisfaction [32-34]. To illustrate, experiencing high thermal satisfaction in the office environment improves the job satisfaction of the office workers [77]. Accordingly, the PMV model indicates that the thermal comfort of the office workers could be satisfied in a range of temperature between 21°C and 25 °C. However, in accordance with the adaptive PMV model, Nicol [57] demonstrated that there is no fixed temperature range for the thermal comfort of the office workers. This was because 80% of the studied occupants were thermally comfortable at 2 °C above and below the predicted comfort temperature range. Notably, the main drawback of both indices is that they consider the same thermal sensitivity for all body parts [78]. Whereas, Fiala et al. [79] demonstrated that the thermal comfort of occupants could not be addressed by providing the same thermal condition for the whole body. This is because the overall thermal discomfort is not driven from the thermal discomfort of a single body part, but it is related to the thermal discomfort of the hot and cold spots owing to the body's thermoregulation process [16,80-84]. To illustrate, not only the skin temperature varies in the cold and warm environments, but also different body parts experience different skin temperatures in each environment. However, in the warm environment, the skin temperatures of different body parts are very similar to each other and their differences are within a 2 °C range. Conversely, in the cold environment, the skin temperature varies widely across the whole body and even within many individual body parts, see Fig.8.

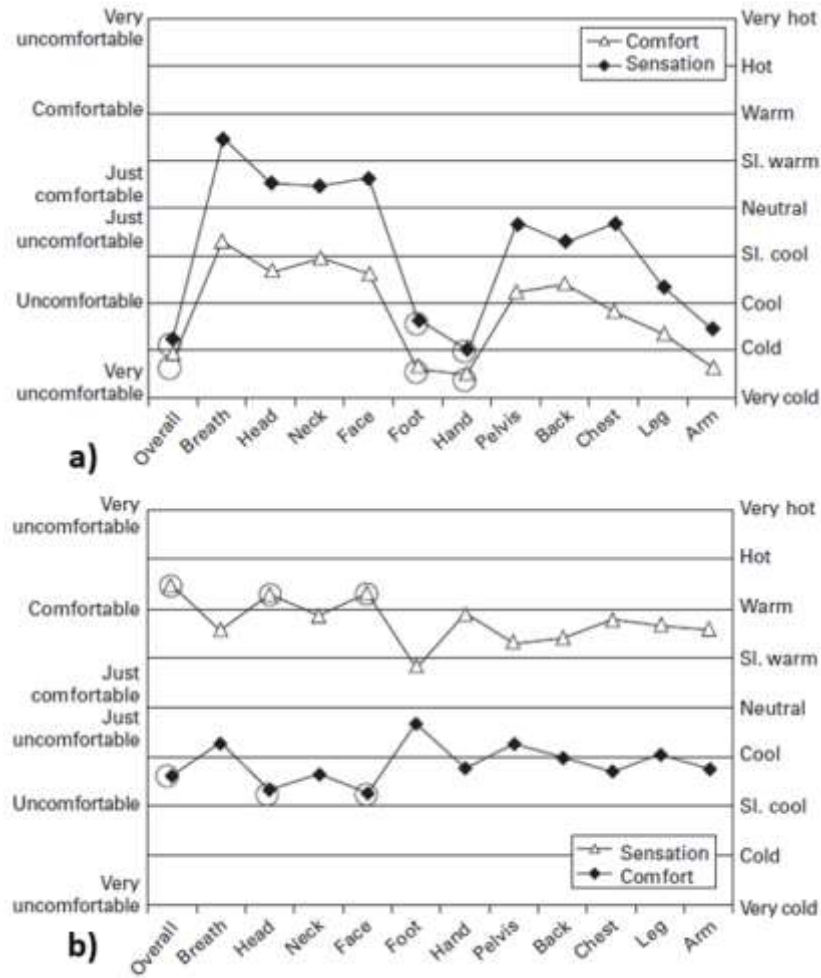


Fig. 8: Local and overall thermal sensation and comfort in: a) a uniform/cold; and b) a uniform/ warm environment [84].

Based on Fig.8 and Fig.9, hands and feet are the most sensitive body parts to cold among all body parts. In the cold environments, the hands and feet reach the lowest skin temperatures among all body parts owing to their fully vasodilation (i.e. blood flow elimination) [84]. A study by Huizenga et al. [85] demonstrated that a few minutes after taking the participants from a warm environment (30 °C) to a slightly cool (22.6 °C) environment, the blood vessels of their hands were well constricted although the temperature of the rest of their upper body was not sensibly changed.

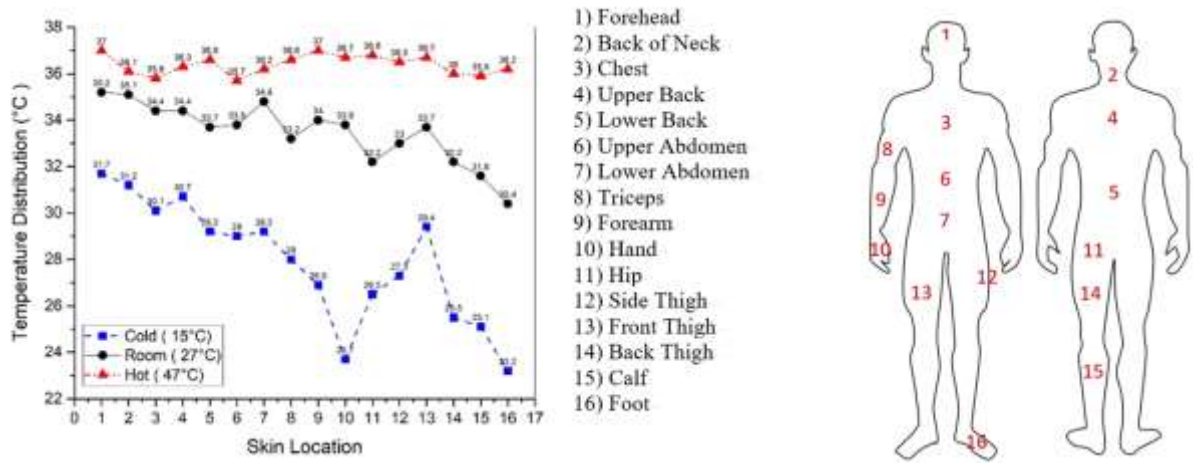


Fig. 9: Temperature of different body parts at varying ambient temperature, adapted from [31].

Accordingly, it is demonstrated that the skin temperature of hands and fingertips dictate the thermal comfort of human body in cold environments [18,86]. Precisely, people feel cold when the temperature of their fingertips falls below 30 °C regardless of the temperature of the other body parts. In addition, these studies showed that when people feel hot, their fingertips’ temperature is in a range of between 36–37 °C. Wang et al. [87] found that there is a correlation between the overall thermal sensation of the participants and the temperature difference between their fingers and forearms. To illustrate, when finger is up to 2 °C warmer than the forearm, people feel either warm or hot. Thus, controlling the fingertips’ temperature in a small bandwidth of 29 °C-31.5 °C satisfies the thermal comfort of the occupants in the cold environments [88]. As a result, the aim of this research is to design a comfortable and an energy efficient heating system that satisfies the thermal comfort of the office workers’ hands. Addressing the thermal comfort of hands is also beneficial because most office workers use computers during the substantial part of their working days. Thus, in the cold environments, it could be difficult to keep writing at keyboards or touching screens, whilst feeling cold in hands. As a result, herein, it is determined to address this issue by fabricating a pair of heating armbands. To study the performance of the developed heating armbands, a set of in-field experiments were carried out while the participants were sitting at an office desk and working with a computer. Then, the effect of wearing the heating armbands was studied on the thermal comfort of their hands, various body parts, and the whole body.

2.6 Summary

This chapter discussed two thermal comfort models (i.e. the PMV and the adaptive PMV models) used to evaluate the thermal sensation and comfort of the occupants in the built environments. It was clarified that along with the PMV model to predict the thermal sensation of the occupants in the buildings, the adaptive PMV models should also be applied to estimate the occupants' thermal comfort. However, the main deficiency of the two models is that they do not prioritize the thermal sensation and comfort of the cold and hot spots. Whereas, addressing the thermal sensation and comfort of these body parts could rigorously decrease the air conditioning load. Accordingly, this research determined to satisfy the overall thermal comfort of office workers in winter time by satisfying the thermal comfort of their hands as one of the most cold-sensitive body parts. Thus, a pair of heating armbands was developed to address the overall thermal sensation and comfort of the wearers.

Chapter 3

Personal Heating Systems

3.1 Introduction

Personal comfort systems (PCSs) (i.e. task/ambient conditioning systems) condition only the air surrounding each individual concerning their thermal preferences [89]. Thus, they reduce the background conditioning (i.e. the HVAC system) load in a range of between 4% and 45% [20,90]. Among different types of PCSs, this chapter focuses only on the personal heating ones in accordance with the aim of this research. In general, the personal heating systems can be classified into three main categories, including heating chairs, heating floor/desktop mats, and heating garments. In fact, the effectiveness of these personal heating systems depends on three main factors, including their surface areas, the density of their power supply, and the body parts exposed to them [91]. Accordingly, the aim of this chapter was to find the most effective personal heating system for this research regarding the differentiation in the thermal sensitivity of various body parts. Thus, various types of personal heating systems and their effect on the thermal comfort of various body parts and the whole body were studied. In addition, this chapter focused on the power supplies of these personal heating systems to illustrate lack of using a renewable power supply for them. This illustration has been added to the introduction section of this chapter.

3.2 Heating chairs

Zhang et al. [92] designed a heating car seat to explore its effect on the thermal perceive of the drivers in the cold environments, as Fig.10 depicts. The tests were conducted in a climate chamber that its temperature was adjusted at three levels, including 15 °C, 18 °C, and 22 °C. To heat the chair, the authors flowed hot water in the tubes fabricated in the seat base. Notably, the hot water was prepared at four different temperatures, including 25 °C, 31°C, 37 °C, and 44 °C. The results revealed that using the heating chair satisfied the thermal comfort of 80% of the 24 subjects even at 9.3 °C lower ambient temperatures.

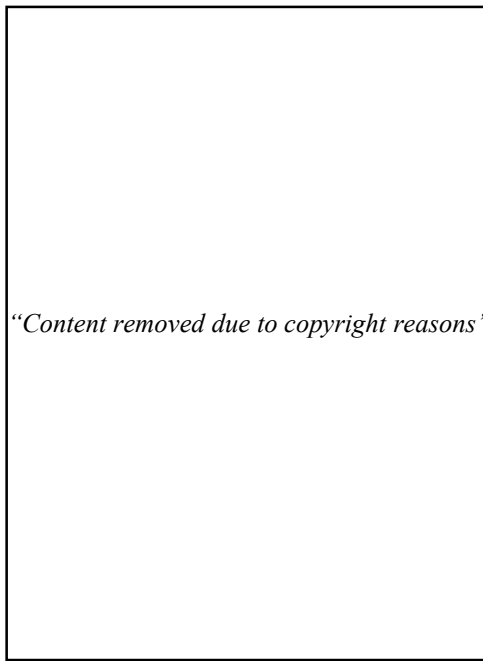


Fig. 10: “Content removed due to copyright reasons”

Pasut et al. [93,94] evaluated the correlation between using the heating chairs and the thermal sensation and comfort of college students. Accordingly, the authors considered two distinct heating elements, including an electrical heating element and a Peltier heater, to individually heat the seat base and backrest of an office chair. Regarding the Peltier module, its performance is exactly the converse of that of a TEG. To specify, applying a voltage across the joined conductors of a Peltier module, heat is removed from one junction (i.e. cooling occurs) and deposited at the other junction (i.e. heating occurs). Thus, one side of the Peltier module is heated, whereas the other side is cooled. Accordingly, two Peltier modules were individually fabricated in the seat base and the backrest of the chair. Heating the chair with an electrical heating element, two electrical heating elements were separately sewn onto the mesh fabric of the seat base and the backrest. Also, three fans were integrated into the seat base and the backrest to adjust the temperature, see Fig.11.

The heating chairs were individually tested in an environmental chamber at 16 °C and 18 °C temperatures to resemble an office environment in the winter time. The results illustrated the extreme positive effect of the heating chairs on the thermal sensation and comfort of the 23 subjects. Precisely, the heating chairs satisfied the thermal comfort of at least 75% of the subjects at 16 °C and more than 80% of them at 18 °C ambient temperature. In addition, the maximum

energy requirement to heat the chair by the electrical heating elements and the Peltier heaters were 16W and 27W, respectively.

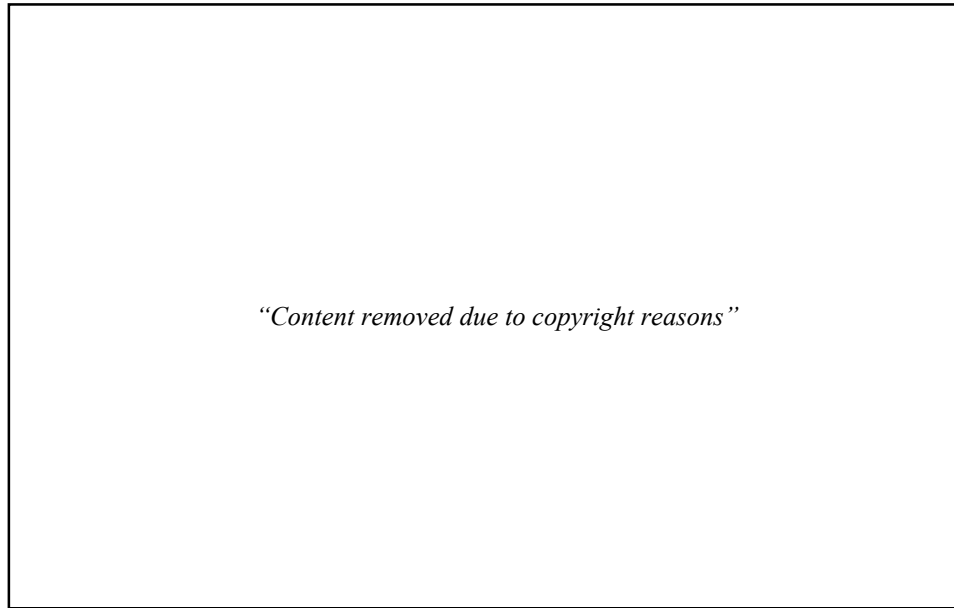


Fig. 11: "Content removed due to copyright reasons"

Shahzad et al. [95] developed a heating chair and investigated its performance on the thermal comfort and sensation of the office workers, as Fig.12 depicts. The authors fabricated the heating pads onto the seat base and the backrest of the chair and covered them with the chair's fabric. Notably, each heating pad used up to 30 W. At the low, medium, and average temperature settings, the surface temperature of the seat base and the backrest reached up to 33 °C, 44 °C, and 53 °C, respectively. The results revealed that using the thermal chair improved the thermal comfort and sensation of the subjects by 20% and 35%, respectively. The authors attributed these low improvements to the overheating of the chair. Precisely, the subjects negatively felt slightly warm and warm at the backrest and the seat base regions.



Fig. 12: The design and the thermal image of the heating chair [95].

Deng et al. [96] investigated the effect of using the heating chairs on the thermal sensation and comfort of people from different genders and ages. The tests were conducted in a single environmental chamber but under two different temperatures, including 18 °C and 16 °C. In total, 36 subjects (i.e. 6 children, 24 young adults, and 6 elderly) were asked to sit on a non-heating and a heating chair separately for 40 min. Notably, the non-heating chair was placed at the 18 °C chamber, and the heating one was placed at the 16 °C chamber. The authors demonstrated that the surface temperature of the heating chair was maintained at 40 ± 1 °C during the tests. Using wireless sensors, the skin temperatures of eight body parts (i.e. forehead, chest, back, pelvis, arms, hands, legs, and feet) were recorded at every 30 seconds during the experiments. The results proved that the subjects experienced greater thermal comfort with the heating chair than the non-heating one. Comparing the impact of the heating chair on the skin temperatures, it significantly increased the mean skin temperature at chest, pelvis, and feet, but decreased it at legs, arms, and hands. In addition, the authors illustrated that the adult female subjects were more sensitive to cold, because the heating chair satisfied their thermal comfort less than the children and the adult male subjects.

3.3 Heating floor /desktop mats

To offset the cold drafts at foot level, Zhang et al. [97] designed a box-shaped foot warmer and placed it on the floor under an office desk. The box was open on one side and its inside was covered with a low emissivity foil. As the heat source, four incandescent reflector bulbs with the total energy consumption of 160W were installed in the box to heat the top of the feet and ankles, see Fig.13. The heating level of the bulbs was controlled by a knob positioned on the desk. The foot warmer was tested on 16 subjects (i.e. 8 females and 8 males) in an office under a range of temperature between 18.9 °C and 21.1 °C. The results showed that although the foot warmer reduced the heating load of the building by 38% and 75%, respectively, 25% of the subjects were not thermally satisfied and required additional foot and leg warmers.

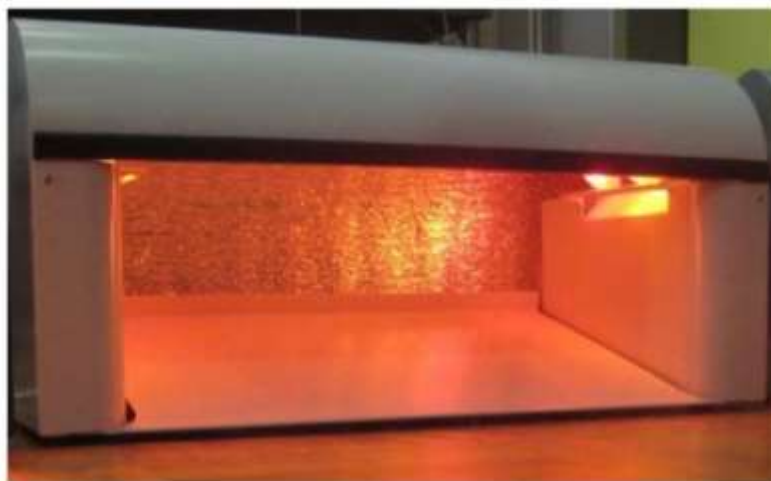


Fig. 13: The developed foot warmer [97].

To solve this issue, Zhang et al. [98] combined the foot warmer with a palm warmer, while the four lamps of the foot warmer was replaced by a 125W reflector heating lamp focused on the top of the feet. The palm warmer was an aluminium curved surface attached to the bottom of the computer keyboards, see Fig.14. Notably, the aluminium curved surface was heated by several electrical heating tapes attached to it. The authors determined both an adjustable and a fixed temperature set-point to study the thermal performance of the coupled heating systems on 18 subjects. The typical surface temperature of the palm warmer was 35 °C with 26W power consumption. Whilst, the maximum temperature of the foot warmer reached 32 °C with an average

radiant flux of 30W. The results proved that when the ambient temperature was 18 °C and below, having control on the temperatures had no privilege over the fixed temperature. This was because, the thermal preferences of the individuals at extreme low temperatures were mostly the same. In addition, it was found that using the palm warmer was thermally inconvenient at 20 °C temperature and higher. Whereas, in general, the coupled personal heating systems maintained the comfort level of acceptable or above at a range of temperature between 18 °C and 20 °C.

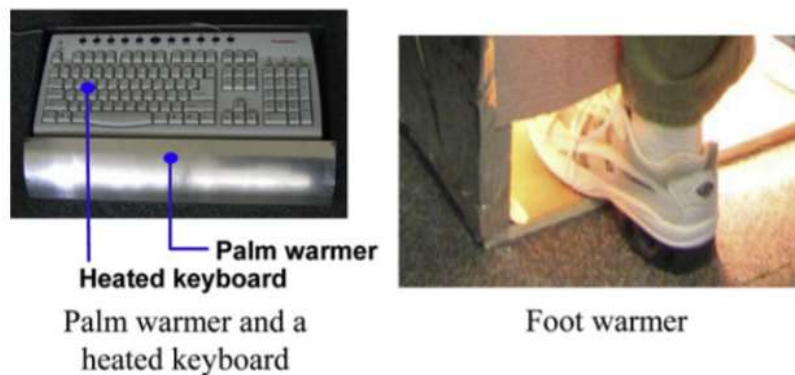


Fig. 14: Combination of the developed foot warmer and palm warmer [98].

Studies by Watanabe et al. [99] and Melikov et al. [100] examined the performance of a personal heating package composed of three separate personal heating systems, including a convective-heating chair, an under-desk radiant heating panel, and a floor -based radiant heating panel. The heating chair was composed of a small heating box attached under the seat base. A fan and an electric heater was installed in the heating box to provide convective heating. Accordingly, the room air was sucked by the fan into the box followed by being heated by the electrical elements and released outside from the backrest, see Fig.15. Regarding the under-desk and the floor radiant heating panels, both of them were composed of a thin heating foil. The results showed that at 20 °C room temperature, the heating chair, the under-desk, and the floor -based radiant heating panels reduced the thermal comfort temperature by 5.2 °C, 2.8 °C, and 2.1 °C, respectively. Whereas, using all the devices at the same time reduced the thermal comfort temperature by 5.9 °C.

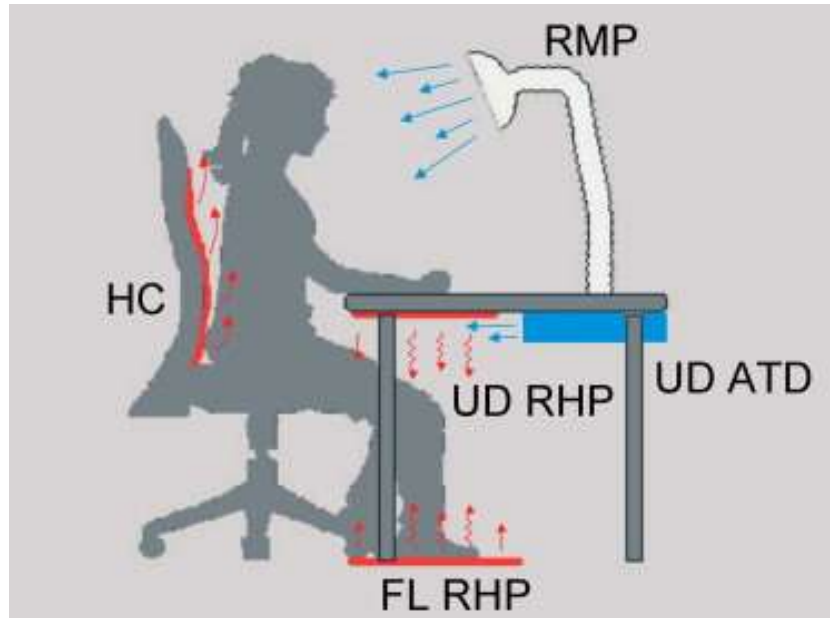


Fig. 15: Sketch of the tested heating systems consisting of a convection-heated chair (HC), an under-desk radiant heating panel (UD RHP), and a floor radiant heating panel (FL RHP) [99].

Likewise, a study by Vesely et al. [10] investigated the thermal performance of a combined personal heating system comprising a heating chair, a heating desk mat, and a heating floor mat, as Fig.16 illustrates. The experiments were conducted on 13 healthy college-aged subjects (i.e. 7 males and 6 females) in an 18 °C climate chamber. The authors demonstrated that using all the heating systems at the same time was superior to using each of them individually. In addition, the heating chair performed better than the other two heating systems concerning the thermal comfort and sensation and the energy efficiency. Also, the study demonstrated that controlling the temperatures by the users can be replaced by the automatic control or the fixed temperatures because the two latter caused no negative effect on the comfort level and the energy consumption.



Fig. 16: The fabricated personalized heating systems: a) a heated chair; b) a heated desk mat; and c) a heated floor mat [10].

3.4 Heating garments

From the beginning of the 19th century, several heating garments have been produced in the form of heating gloves and vests to overcome the cold environments [101]. The heating garments offer significant advantages, such as keeping an even surface temperature in the heating process, flexibility, and structural simplicity [101]. In addition, they results in higher thermal satisfaction compared with the other personal heating systems [22]. To specify, Udayraj et al. [22] compared the thermal comfort and the energy performance of three personal heating systems with each other. The three heating systems were a heating cloth comprising a heating jacket and trousers, a radiant heating panel integrated with a heating desk mat, and a heating chair combined with a heating floor mat. Fig.17 illustrates the schematic of the fabricated personal heating systems. The results showed that the highest thermal satisfaction was achieved when the 14 subjects were heated by the heating cloth. In addition, the energy consumption of the heating cloth (i.e. 15 W) was 4.4% and 14.8% lower than that of the second and third systems, respectively.



Fig. 17: The heating strategies used in this study: a) HB1: a radiant heating panel with a heated table pad; b) HB2: a heated chair with a heated floor mattress; and c) EHC: a heated jacket with heated trousers [22].

The existing heating garments could be divided into four categories, including the electrically, chemically, phase change, and fluid flow heated clothing [23]. The very first heating garment was an electrically heated military uniform consisted of different elements, including some sensors in different places; some textile-based heating elements, a measurement control unit, some humidity sensors, and small batteries [102]. It was revealed that the best heating performance of the uniform

was achieved when its heating element was turned on for a short period of time. This was because keeping the heating element on in a long term raised the temperature quickly and caused overheating.

Wang et al. [103] investigated the thermal performance of an electrically heated vest. The carbon polymer-heating element of the vest consisted of four individual layers, including a protection layer, a heat-insulating layer, a heat generating layer, and a base layer. The tests were conducted separately at 0 °C and -10 °C ambient temperatures. The results showed that the vest provided 34 °C and 38 °C temperatures around the manikin's torso skin and its outside surface, respectively. Also, at 0 °C and -10 °C ambient temperatures, the highest thermal satisfaction was achieved by consuming 5W and 13W, respectively.

He et al. [104] explored the thermal comfort of the occupants under three different heating conditions, namely a non-heating condition, a heating chair, combination of the heating chair with a leg warmer, see Fig.18. To fabricate the heating chair, the leather cushions of the backrest and the seat base of a typical office chair were equipped with the carbon fibres as the heating elements. To fabricate the leg warmer, a pair of heating leg bands was prepared using the carbon fibres, a fire protection layer, and an electric insulation layer. Accordingly, a series of experiments were conducted on 16 subjects (i.e. 8 males and 8 females) at the ambient temperatures of 14 °C, 16 °C, 18 °C, and 22 °C. The results showed that combining the heating chair with the leg warmer was superior to the sole application of the heating chair. To specify, the combination of the heating chair with the leg warmer reduced the thermal comfort temperature to 14 °C. In addition, it resulted in 41.1 W, 34.9 W and 25.4 W energy consumption respectively at 14 °C, 16 °C and 18 °C, saving the total heating load up to 71.0%. It should be noted that since the hands were not directly heated, many subjects touched these devices for a while during the tests to feel warm.



Fig. 18: The personal heating devices: a) the heating chair; b) the leg warmer; and c) a subject using the devices [104].

Taguchi et al. [105] designed a circulating-water garment to cover the entire torso, legs, and upper arms. Precisely, the garment was covering 77.5% of the total surface area of the body. While the circulating-water garment was set at 37 °C, nine subjects were heated by it for 2.5 hrs at 20 °C ambient temperature. The results showed that the core temperature of the body increased from 34 °C to nearly 37 °C after 2.5 hrs warming. Gao et al. [106] designed three heating vests via applying three different phase change materials (PCM) having different phase change temperatures, including 24 °C, 28 °C, and 32 °C. In total, 21 packs of PCM were fabricated in the pockets of the vests. Before starting the tests, the vests were warmed up and the PCMs were melted at about 40 °C. Then at -4 °C air temperature and 0.4 m/s air velocity, the tests were conducted for 4 hrs. The results showed that higher melting temperature of the PCM resulted in greater and longer heating effect of the vest. To specify, using the PCM with the greatest phase change temperature (32 °C) resulted in the longest heating effect (4 hrs) of the vest.

3.5 Summary

This chapter reviewed the three types of personal heating systems, including heating chairs, heating floor/desktop mats, and heating garments. Accordingly, among these three types, personal heating garments are more popular than the other two types owing to providing higher thermal comfort and satisfaction for the users. Precisely, the main complain about the other two types is that they cannot satisfy the thermal comfort of hands and fingertips as the most sensitive body parts to cold (i.e. as explained in [Chapter 2](#)). In addition, regarding the heating chairs, they can cause overheating for the users by captivating the hot air between the skin and the chair. Whereas, this issue could be solved by using heating garments as the heat dissipates into the ambient air from their outmost surface. Accordingly, to both satisfy the thermal comfort of hands and avoid overheating, this work aimed at designing a pair of electrically heated armbands to satisfy the thermal comfort of office workers in heating seasons. In addition, based on the reviewed studies in this chapter, it was proved that there are no previous studies on using any types of renewable power supplies including energy harvesters (e.g. thermoelectric generators) to power personal heating systems.

Chapter 4

TEG Principles and Thermoelectric Materials

4.1 Introduction

As reviewed in [Chapter 3](#), most of the current PCSs are powered with either public electricity or batteries. Whereas, this is in contradiction to their environmental target, which is reducing the carbon footprint of buildings. To specify, although using PCSs can significantly reduce the heating/cooling load of buildings, being powered with either a fossil-fuel based (i.e. public electricity) or an environmental pollutant (i.e. battery) power source offset their environmental mission to some extent. To solve this problem, a promising approach is powering the PCSs with a renewable power supply to entirely fulfill their environmental friendly target. Accordingly, this research aimed at powering the determined heating armbands with a hybrid power supply comprising a rechargeable battery and a set of TEGs as the renewable power supply. To clarify, TEGs are considered as a promising energy harvester, which produce electricity from waste heat. Thus, they would serve as a constant voltage supply for the battery, reducing the number of the batteries required and their discharging rate. Thus, to find out the most efficient TEG for this research, this chapter initially reviewed the main factors affecting their energy conversion efficiency. To specify, since thermoelectric materials are the main element of TEGs, initially their three main thermoelectric features (the Seebeck coefficient, electrical conductivity, and thermal conductivity) affecting the energy conversion efficiency of the TEGs were studied. Then, to find out the most appropriate TE material for this research with respect to its energy conversion efficiency, the three different types (i.e. inorganic, organic, and hybrid) of TE materials were reviewed and compared with each other based on their thermoelectric features. The outcome of this chapter would be used in combination with the results of [Chapters 5](#) and [7](#) to select an appropriate TEG for this research concerning both the efficiency and environmental impact of its thermoelectric material.

4.2 Basic principles of TEGs

Thermoelectric generators (TEGs) are solid-state semiconductor devices that convert waste heat directly into electricity. They are commonly used to convert the heat dissipated from sources such as power plants, factories, motor vehicles, computers, or even human bodies directly into

electricity [107]. The TE theories are based on the Seebeck effect, which was discovered in 1821 by a German physicist called Thomas Johann Seebeck. Based on the Seebeck effect, applying a temperature gradient between the two ends of a thermocouple generates electricity. To clarify, a thermocouple is composed of two electrically different conductors or semiconductors that are contacted together directly or with another electrical conductor. Thus, when a temperature difference occurs between the two ends of the thermocouple, the charge carriers flow between the materials. Precisely, the charge carriers diffuse away from the warmer side of the thermocouple and build up at the cooler end. This movement results in the accumulation of the charge carriers at the colder part, leading to the generation of an open circuit voltage called the Seebeck voltage (V). Following Eq. (1), the Seebeck voltage is directly related to the temperature difference (ΔT) between the junctions of the thermocouple by a proportional factor called the Seebeck coefficient (α).

$$V = \alpha \Delta T \quad (1)$$

Regarding the TEGs, they are composed of an array of p - and n -type TE legs (i.e. semiconductors), having surplus holes and electrons, respectively. Using metal interconnects (i.e. electrodes), the TE legs are connected thermally in parallel and electrically in series to form the thermocouples. A conventional TEG consists of a large number of thermocouples sandwiched between two electrically insulating and thermally conductive substrates. When a temperature gradient occurs along the thermocouples, the free charges (i.e. electrons and holes) in the legs start moving from the hot side to the cold side, converting the thermal energy into the electrical energy. In general, a higher temperature gradient in the thickness direction of the legs leads to a greater energy conversion. Therefore, usually a heatsink (i.e. a radiator) is attached to the cold substrate to accelerate the heat dissipation, resulting in a greater energy conversion [108]. Fig.19 illustrates the standard configuration of a conventional TEG. In what follows, the main factors affecting the conversion efficiency of the TEGs are presented. In general, the TEGs benefit from solid-state operation, easy fabrication, vast scalability, absence of environmentally deleterious wastes, noiseless operation, maintenance-free operation, no chemical reactions, and durability [109-111]. Above all, they are usable for indoor applications.

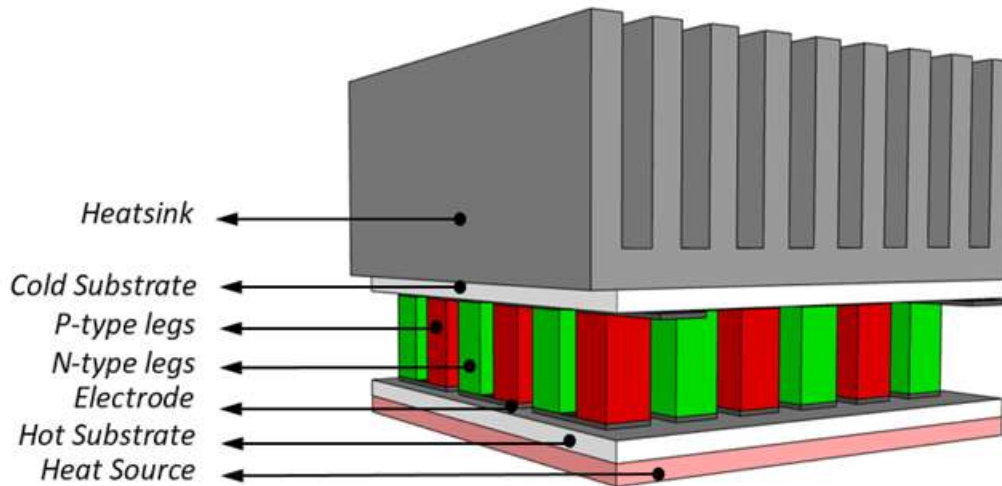


Fig. 19: The schematic diagram of a conventional TEG and its components.

4.2.1 The Seebeck coefficient (α)

In 1821, Thomas J. Seebeck found that there is high potential for generating an electromotive force or a potential difference in a circuit when one junction of two dissimilar conductors or semiconductors is heated. This phenomenon is called the Seebeck effect, and the Seebeck coefficient of a material shows its ability to convert the thermal energy into the electrical energy [112]. Precisely, a higher energy conversion could be achieved via using the materials having greater Seebeck coefficients [113]. It should be noted that the Seebeck coefficient is the intrinsic property of the materials and depends on their molecular structure, charge carrier concentrations, and effective mass [114]. Also, the Seebeck coefficient is a function of temperature, which is linear in the small temperature changes and non-linear in the large temperature changes [115]. Thus, it is of great importance to tune the thermal energy based on the optimal Seebeck coefficient of each material.

4.2.2 Electrical conductivity (σ)

The electrical conductivity is the measure of the materials' ability to transfer an electrical current [114]. Typically, the electrical conductivities of metals, semiconductors, and insulators are in a range of $10^5 (\Omega.m)^{-1}$, $10^{-6} - 10^5 (\Omega.m)^{-1}$, and $10^{-6}(\Omega.m)^{-1}$, respectively. The electrical conductivity

(σ) of a semiconductor depends on the concentration and mobility of the charge carriers as depicted in Eq. (2):

$$\sigma = e(\mu_e \cdot n + \mu_h \cdot p) \quad (2)$$

where μ_e , μ_h , n , and p denote the electron mobility, the hole mobility, the electron concentration, and the hole concentration, respectively. The term carrier (i.e. electron and hole) mobility characterises how quickly the carriers move through metals or semiconductors as they are subjected to an external electric field. There are two basic types of scattering mechanisms that influence the mobility of the electrons and holes, including the lattice vibrations (i.e. phonons scattering) and the impurity scattering. The total mobility then is the sum of the lattice-scattering mobility and the impurity-scattering mobility. Regarding the lattice-scattering, the atomic vibrations increase at higher temperatures, resulting in the higher number of collisions between the electrons and ions. Due to this, the flow of the current carriers is opposed, leading to the greater resistivity of the metals/semiconductors [116]. Hence, the mobility decreases at higher temperatures due to the lattice vibrations. Conversely, the carriers move more slowly at lower temperatures, so they interact more with the charged impurities. As a result, the mobility decreases at lower temperatures due to the impurity scattering [117]. Therefore, preparing a metal/semiconductor with a high electrical conductivity requires to make balance between the lattice-scattering mobility and the impurity-scattering mobility [107].

4.2.3 Thermal conductivity (λ)

From the Fourier's law of heat conduction, the thermal conductivity is the ability of the materials to transfer heat per unit time through a unit area with a temperature gradient of one degree per unit distance. To put it another way, it is expressed as:

$$q_x = -\lambda \frac{dT}{dx} \quad (3)$$

where q_x is the heat flux (W/m^2), λ is the thermal conductivity (W/mK), and $\frac{dT}{dx}$ is the thermal gradient (K). Thus, increasing the thermal conductivity of the materials improves their ability to conduct more heat at a specific temperature. The net thermal conductivity is related to two parameters, including the carrier concentration and the lattice vibrations. Regarding the

semiconductors, they conduct all the heat with the phonons (i.e. lattice vibrations) [118]. Therefore, increasing either the carrier concentration or the lattice vibrations rises the thermal conductivity of the TE materials, which is undesirable for the TE generation.

4.2.4 Energy conversion efficiency

For an ideal TEG with constant thermoelectric properties, the following equation could be used to measure the maximum heat-to-power conversion efficiency (η_{\max}) [119]:

$$\eta_{\max} = \left(\frac{T_H - T_C}{T_H} \right) \cdot \left(\frac{\sqrt{1 + Z\bar{T}} - 1}{\sqrt{1 + Z\bar{T}} + \frac{T_C}{T_H}} \right) \quad (4)$$

where the conversion efficiency (η_{\max}) of a TEG depends on the hot side temperature (T_H), the cold side temperature (T_C), and the figure of merit ($Z\bar{T}$) of the TE materials. Accordingly, the conversion efficiency (η_{\max}) of the TEGs is directly related to the temperature difference between their hot and cold junctions. To put it another way, a higher temperature difference along the legs results in a higher output power. To tune the temperature gradient, one of the most promising approach is manipulating the structural design of the TE legs. As a result, the configuration of the TEGs varies based on the structural design of the TE legs. Regarding the figure of merit ($Z\bar{T}$), it defines how efficiently a TE material can convert the thermal energy into the electrical energy and is expressed as:

$$Z\bar{T} = \frac{(\alpha^2 \sigma T)}{\lambda} \quad (5)$$

where α is the Seebeck coefficient ($\mu\text{V/K}$), σ is the electrical conductivity (S/cm), T is the absolute temperature (K), and λ is the thermal conductivity (W/m K). The numerator, $\alpha^2 \sigma$, is called the power factor (PF). As Eq. (7) illustrates, the $Z\bar{T}$ value can be enhanced by increasing the electrical conductivity and the Seebeck coefficient, but decreasing the thermal conductivity. Therefore, there have been numerous efforts to develop the TE materials with a high power factor but a low thermal conductivity. However, due to the trade-off relationships between these TE properties, it is a big challenge to even slightly enhance the $Z\bar{T}$ value [120]. Precisely, there is an inverse

relationship between the Seebeck coefficient and the electrical conductivity of the materials as the function of the carrier concentration. To illustrate, an increase in the carrier concentration decreases the Seebeck coefficient but increases the electrical conductivity [121]. In addition, as mentioned before, increasing the carrier concentration also rises the thermal conductivity, which is not desirable. As a result, it is too complicated to individually tune one of the TE properties without affecting the others. Currently, the $Z\bar{T}$ values of the commercial TEGs are lower than 1, whilst it is around 2 for some of the developed TE materials in the labs [122,123]. However, as shown in Fig.20, to make the conversion efficiency of the TEGs comparable with that of the other conventional power sources, their target $Z\bar{T}$ values should reach 3 and above [123].



Fig. 20: "Content removed due to copyright reasons"

4.3 Different types of TE materials

As mentioned in Section 4.2.4, the energy conversion efficiency (η_{\max}) of the TEGs depends on two crucial factors, including the operating temperature and the properties of the TE materials. Regarding the latter, it is definitely possible to improve the η_{\max} value of the TEGs by adjusting the properties of the TE materials in different manners, including the point defect engineering, the band engineering, the structural nano crystallization, the interface engineering, and the hierarchical architecturing [125]. In general, the TE materials could be classified into three categories,

including inorganic, organic, and hybrid (inorganic-organic) types. [Table 1](#) summarizes the most common TE materials belonging to each category. As could be seen, the inorganic type consists of the inorganic composites, such as bismuth telluride (BiTe), tin selenide (SnSe), lead telluride (PbTe), and silicon-germanium (SiGe). The organic type is composed of two main compounds, including an active material and an additive. The former is dominantly a conducting polymer such as poly (3,4-ethylenedioxythiophene): poly (styrenesulfonate) (PEDOT: PSS), polyaniline (PANI), and polypyrrole (PPY). The latter (i.e. the additive) is selected based on the required chemical treatments. Ultimately, the hybrid type is composed of an inorganic material (i.e. mostly a metal-based chemical) as an additive and an organic material as a matrix. To illustrate, BiTe – PEDOT: PSS is a hybrid TE material comprised of an inorganic metal compound and a conducting polymer. In what follows, a comprehensive overview of the most recently developed inorganic, organic and hybrid TE materials, and their efficiency at the room temperature (27 °C) are provided.

Table 1: Summary of the main categories of TE materials usable in wearable TEGs.

Inorganic	Organic	Hybrid
Bi ₂ Te ₃	PEDOT: PSS	Te-PEDOT: PSS
Bi _{0.5} Sb _{1.5} Te ₃	PEDOT: S-PHE	SWCNT/PC-Te
Bi ₂ Te _{2.7} Se _{0.3}	PBTTT	Te NWs/PEDOT NWs
Bi _{0.4} Sb _{1.59} Ge _{0.01} Te ₃	PDTDE	Te- MWCNT/PANI
Sb _{1.85} In _{0.15} Te ₃	PBDT-TT-TEO	MoSe ₂ /PEDOT: PSS
Cu _{0.005} Bi _{0.5} Sb _{1.495} Te ₃	PCBM	PEDOT: PSS/ Si-NP
Bi _{0.5} Sb _{1.5} Te _{2.7} Se _{0.3}	CNTs/PANi	PDI-Te
Bi _{0.48} Sb _{1.52} Te ₃ +PbTe composite	PANi/PPy/SWCNT	Ni/PVDF
(BiSbTe _{1.5} Se _{1.5}) _{0.3} Ag _{0.3}	CNT/PEDOT: PSS	NDINE/SWCNT
Bi ₂ Te _{2.38} I _{0.02} Se _{0.6}	PEDOT: PSS /RTCVD graphene CNT/PVDF	PDINE/SWCNT

4.4 Inorganic thermoelectric materials

The inorganic TE materials, specifically Bi₂Te₃, SiGe, and PbTe, are established in 1950 ~1960s (i.e. the early boom of the TE researches) [\[126\]](#). Therefore, the conventional TEGs were mainly composed of the inorganic TE materials, such as bismuth telluride (Bi₂Te₃) and its alloys, Lead telluride (PbTe) and its alloys, silicon-germanium (SiGe) alloys, antimony telluride (Sb₂Te₃), and tin selenide (SnSe) [\[127\]](#). In fact, the main barrier for further improvement of the conventional

TEGs was the low $Z\bar{T}$ values of the inorganic TE materials that were remained close to unity until mid-1990s [128]. However, advances in science and technology and the increased public awareness of the fossil fuels' threats encouraged the scientists to modify the $Z\bar{T}$ values of the inorganic TE materials [129].

To achieve this goal, tremendous efforts have been carried out to improve the Seebeck coefficient and the thermal conductivity of the inorganic TE materials since mid-1990s [126,130]. As a result, Sb_2Te_3 , Bi_2Te_3 , Bi_2Se_3 and their alloys have become the most promising inorganic TE materials for operating at the room temperature (26 °C –126 °C) since 1950s [131,132]. However, the main drawback of using tellurium (Te) as a TE material is that it is one of the rarest elements in the earth's crust with the mass fraction of 0.001 parts per million (ppm) [133]. Thus, MgAgSb has attracted extensive attention as a superb alternative to the tellurium-containing TE materials. This is mainly because the cost, toxicity, and thermal conductivity of MgAgSb is less than those of the Bi_2Te_3 alloys. In addition, the former benefits from higher thermal stability than the latter, which is desirable. In what follows, the applied methods to improve the $Z\bar{T}$ values of different inorganic TE materials are discussed. In addition,

Table 2 summarises the properties of some inorganic TE materials at the room temperature.

Table 2: Summary of the properties of most typical inorganic TE materials at 26 °C room temperature.

Type	TE materials	α [μ V/K]	σ [S/cm]	PF [μ W/mK ²]	λ [W/mK]	$Z\bar{T}$	Ref
	$Sb_{1.85}In_{0.15}Te_3$	124	500	-	0.9	0.27	[131]
	$Mg_{0.995}Li_{0.005}Ag_{0.97}Sb_{0.99}$	200	588	2300	0.9	0.75	[133]
	$Mg_{0.97}Zn_{0.03}Ag_{0.9}Sb_{0.95}$	85	952	690	1.25	0.28	[134]
	$MgAg_{0.97}Sb_{0.985}B_{0.005}$	255	285	1860	0.8	0.7	[135]
	$Bi_{0.38}Sb_{1.62}Te_3 + Ge_{0.5}Mn_{0.5}Te$	194	1100	43	1.28	1.22	[136]
	$CuInTe_2 + Bi_{0.4}Sb_{1.6}Te_3$	175	1250	40	1.1	1.15	[137]
	$Bi_{0.4}Sb_{1.59}Ge_{0.01}Te_3$	207	909	48	1.05	1.36	[138]
	$Cu_{0.005}Bi_{0.5}Sb_{1.495}Te_3$	150	1400	-	1	0.97	[139]
	$Bi_{0.5}Sb_{1.5}Te_{2.7}Se_{0.3}$	109	1250	-	0.96	0.48	[140]
	$Bi_{0.35}Sb_{1.65}Te_3$	270	285	-	0.9	0.8	[141]
	$Bi_{0.48}Sb_{1.52}Te_3 + 0.05\text{wt\% PbTe}$	177	1800	56	1.85	0.9	[142]
	$Bi_{0.4}Sb_{1.6}Te_3$ alloys +5 wt% Te	155	880	21	1.4	0.48	[143]
	$(BiSbTe_{1.5}Se_{1.5})_{0.3}Ag_{0.3}$	200	120	480	0.6	0.25	[144]
	$Bi_{0.8}Sb_{1.2}Te_3$	150	300	-	-	0.58	[145]

	Mg _{0.995} Yb _{0.005} Ag _{0.97} Sb _{0.99}	220	476	2180	0.81	0.8	[146]
	MgAg _{0.97} Sb _{0.99}	170	580	1620	0.8	0.55	[147]
	MgAg _{0.97} Sb ₁	220	476	2280	0.88	0.78	[148]
	Mg _{0.995} Ca _{0.005} Ag _{0.97} Sb _{0.99}	225	416	2080	0.84	0.75	[149]
	Mg _{0.97} Zn _{0.03} Ag _{0.9} Sb _{0.95}	285	166	1250	0.62	1.1	[150]
	Bi _{0.5} Sb _{1.5} Te _{3.2}	224	800	-	0.65	1.2	[151]
N-type	Bi ₂ Te _{2.39} Se _{0.6}	-160	1200	31	1.3	0.7	[152]
	Bi ₂ Se ₃	-105	526	575	1.2	0.14	[153]
	Bi ₂ Te _{2.7} Se _{0.3}	-263	250	-	0.79	0.76	[154]
	Bi ₂ Te _{2.7} Se _{0.3}	-146	2250	49	2.09	0.81	[155]
	Bi ₂ Te _{2.7} Se _{0.3} + 0.3 wt% KI	-135	1350	26	1.45	0.51	[156]
	Bi ₂ Te ₃	-105	1600	17.5	1.65	0.33	[157]
	Bi ₂ Te _{2.7} Se _{0.3}	-168	600	1650	0.73	0.68	[158]

4.4.1 P-type inorganic TE materials

The four most common approaches to raise the $Z\bar{T}$ values of the TE materials are optimizing their carrier concentration, nano-structural engineering them, manipulating their band structure or their defects. Among different inorganic TE materials, (Bi,Sb)₂(Se,Te)₃-based alloys are most popular for operating at the room temperature [159]. To enhance their $Z\bar{T}$ values, the main focus is on optimizing their carrier concentration [141], decreasing their lattice/bipolar thermal conductivity [160], and incorporating a proper second nano-phase [161,162]. For example, Duan et al. [136] added Ge_{0.5}Mn_{0.5}Te to Bi_{0.38}Sb_{1.62}Te₃ alloys to tune the lattice thermal conductivity and the mechanical property of the latter. The four stoichiometric ratios of 0%, 0.5%, 1%, and 1.5% were considered for the (Bi_{0.38}Sb_{1.62}Te₃)_{1-x}(Ge_{0.5}Mn_{0.5}Te)_x composite. The results showed that adding Ge_{0.5}Mn_{0.5}Te improved the carrier concentration and in consequence the Seebeck coefficient of the Bi_{0.38}Sb_{1.62}Te₃ composite. Since this incorporation had no effect on the electrical and thermal conductivities of the composite, the authors proposed to tune the carrier concentration by adding BiCl₃. The results illustrated that adding 1% BiCl₃ reduced the carrier concentration and reached the composite to its lowest lattice thermal conductivity. Notably, adding 1% BiCl₃ also improved the electrical conductivity and the Seebeck coefficient of the composite. As a result, the authors demonstrated that at 26 °C, 1.22 was the optimum $Z\bar{T}$ value of the Bi_{0.38}Sb_{1.62}Te₃ + Ge_{0.5}Mn_{0.5}Te +1% BiCl₃ composite.

There are several high pressure techniques to fabricate the TE materials, including the hot pressing, the spark plasma sintering, the extrusion methods, and the high-pressure synthesis. Among them, Wang et al. [137] applied the hot pressing technique to incorporate $\text{Bi}_{0.4}\text{Sb}_{1.6}\text{Te}_3$ alloys into CuInTe_2 inclusions. The CuInTe_2 and $\text{Bi}_{0.4}\text{Sb}_{1.6}\text{Te}_3$ powders were mixed together with the weight ratios of 0.1, 0.2, and 0.3%. The results illustrated that the hole concentration and phonon scattering of the $\text{Bi}_{0.4}\text{Sb}_{1.6}\text{Te}_3$ alloys improved by adding CuInTe_2 to it. Consequently, a higher electrical conductivity and a lower thermal conductivity were achieved, as Fig.21 illustrates. The study demonstrated 0.2% as the optimal weight ratio of $\text{CuInTe}_2 / \text{Bi}_{0.4}\text{Sb}_{1.6}\text{Te}_3$ to obtain the maximum $Z\bar{T}$ value of 1.15 at 26°C. Notably, the 1.15 $Z\bar{T}$ value was 12% higher than that of the pristine $\text{Bi}_{0.4}\text{Sb}_{1.6}\text{Te}_3$ sample.

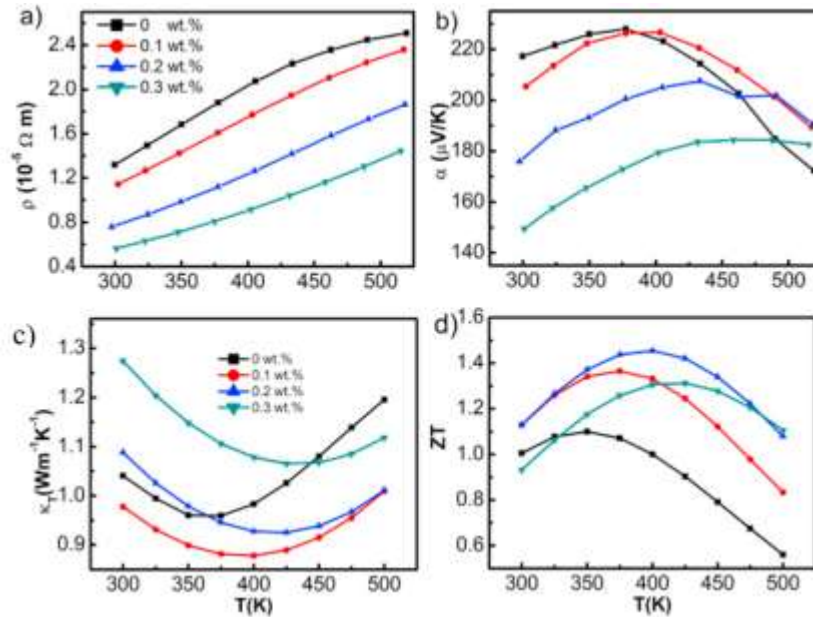


Fig. 21 : Temperature dependencies of : a) the electrical resistivity; b) the Seebeck coefficient; c) the thermal conductivity; and d) the ZT values of $f(\text{CuInTe}_2)/\text{BST}$ ($f= 0, 0.1, 0.2$ and $0.3\text{wt.}\%$) [137].

As mentioned previously, due to the scarcity of the tellurium, MgAgSb has been introduced as a promising substitute for the Bi_2Te_3 alloys at the room temperature. However, there are two barriers for further improvement of the TE properties of MgAgSb . The first one is the difficult synthesis of the pristine MgAgSb [145], and the other is the high electrical resistivity of an undoped MgAgSb attributed to its low carrier concentration. To address these two deficiencies, increasing the carrier concentration with the doping method is a promising solution. Accordingly, Liu et al. [133] tuned the carrier concentration of Mg (Magnesium) by doping Li (lithium) into it.

Then, the nominal composition of $\text{Mg}_{1-x}\text{Li}_x\text{Ag}_{0.97}\text{Sb}_{0.99}$ ($x=0, 0.0025, 0.005, 0.01, 0.02, \text{ and } 0.04$) was prepared by applying two-step ball milling and hot pressing processes. As Fig.22 shows, the results illustrated the positive effect of increasing the Li content up to 2wt% on the electrical conductivity of $\text{Mg}_{1-x}\text{Li}_x\text{Ag}_{0.97}\text{Sb}_{0.99}$ compound. To put it another way, increasing the Li content up to 2wt% increased the carrier concentration of the compound, and ultimately resulted in higher electrical conductivity. Conversely, doping the lithium deteriorated the Seebeck coefficient due to the bipolar effect associated with the decreased MgAgAb band gap. In addition, increasing the lithium concentration led to a higher thermal conductivity of the compound. Consequently, the authors reported that at the room temperature the $Z\bar{T}$ value of the Li doped MgAgAb could be higher than that of an undoped MgAgSb when the Li content was limited up to 1wt% of the composition. Precisely, the highest $Z\bar{T}$ value of the Li doped MgAgAb at the room temperature was 0.75, which was achieved by 0.5wt% lithium content.

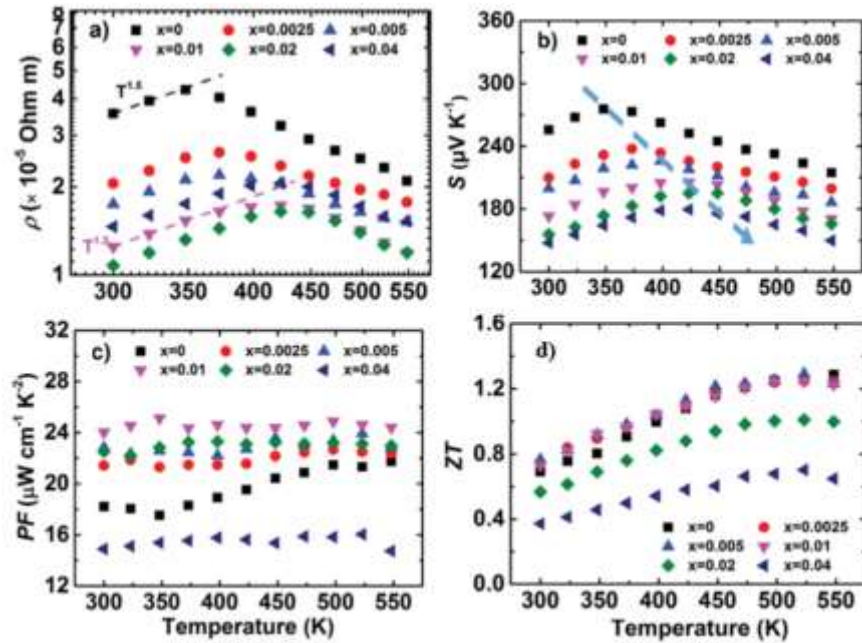


Fig. 22: Temperature dependence of: a) the electrical resistivity; b) the Seebeck coefficient; c) the power factor; and d) the figure of merit of $\text{Mg}_{1-x}\text{Li}_x\text{Ag}_{0.97}\text{Sb}_{0.99}$ [133].

Liu et al. [148] attempted to enhance the Sb content to enhance the $Z\bar{T}$ value of MgAgSb. The authors prepared the nominal composition of $\text{MgAg}_{0.97}\text{Sb}_x$ ($x=0.99, 0.9925, 0.995, \text{ and } 1.00$) by combining ball milling and hot pressing processes together. The results showed that the carrier concentration of the compound gradually increased from $x=0.99$ to 0.995 due to the generation of

Ag and Mg vacancies, but then slightly decreased owing to the very minor Sb impurities. The results showed that increasing the Sb content improved the electrical conductivity, but deteriorated both the Seebeck coefficient and the thermal conductivity, as Fig.23 illustrates. Finally, the work concluded that at 26°C, the highest $Z\bar{T}$ value was achieved by the maximum Sb content ($\text{MgAg}_{0.97}\text{Sb}$), that was 2 times greater than that of $\text{MgAg}_{0.97}\text{Sb}_{0.99}$.

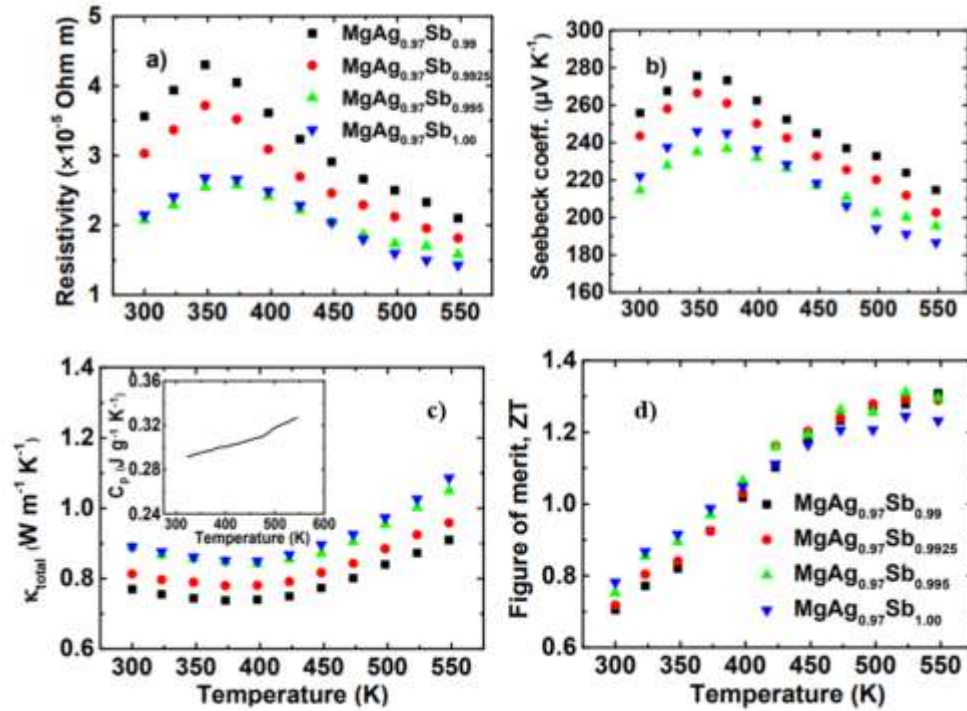


Fig. 23: The temperature dependence of: a) the electrical resistivity; b) the Seebeck coefficient; c) the total thermal conductivity; and d) the ZT values of $\text{MgAg}_{0.97}\text{Sb}_x$ ($x = 0.99, 0.9925, 0.995, \text{and } 1.00$) [148].

4.4.2 N-type inorganic TE materials

In contrary with the p-type Bi_2Te_3 , its n-type alloys suffer from low energy conversion efficiencies at low temperatures. This is primarily attributed to the existence of the excited electron-hole pairs across Bi_2Te_3 band gap, resulting in the extra bipolar thermal conductivity and the low Seebeck coefficient. Kang et al. [153] used high pressure synthesizing method to improve the TE properties of Bi_2Se_3 . Thus, 1 to 6 Gpa were considered as the sintering pressures followed by grinding and spark plasma sintering methods. The authors achieved the highest $Z\bar{T}$ value of 0.14 at the room temperature by sintering the sample at 1Gpa pressure, see Fig.24.

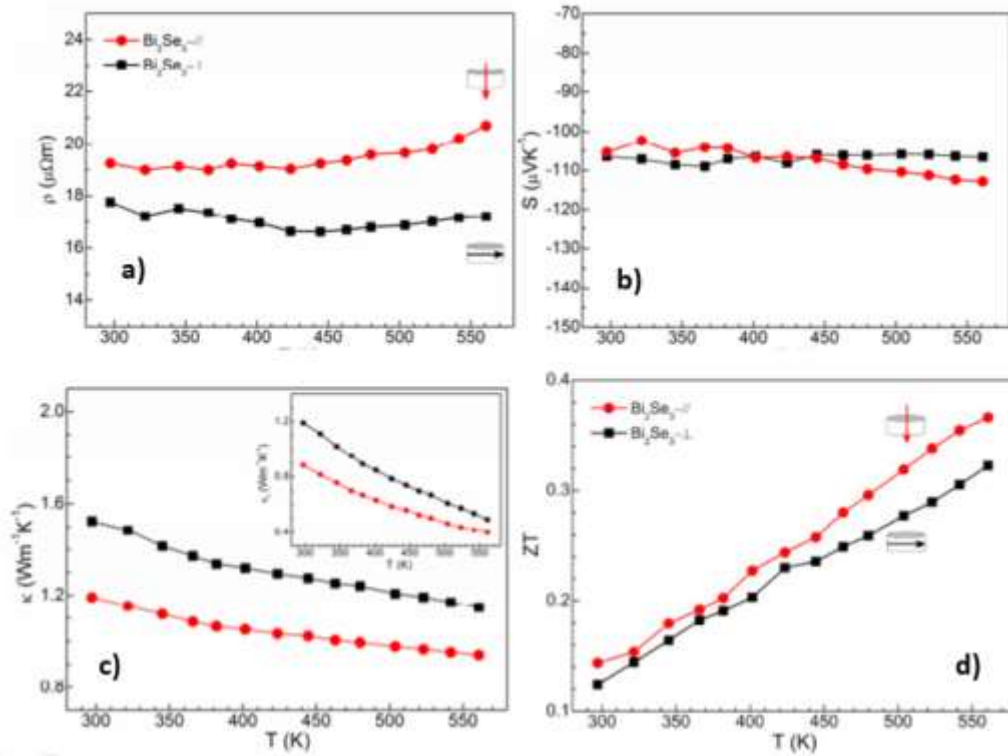


Fig. 24: Temperature dependent TE properties of the dense pellet Bi_2Se_3 along different directions: a) the electrical resistivity; b) the Seebeck coefficient; c) the thermal conductivity; and d) the ZT values. The inset to panel c shows the lattice thermal conductivity [153].

Zhu et al. [155] suggested combining the liquid state manipulating method with the direction solidified texturing to prepare the $\text{Bi}_2\text{Te}_{2.7}\text{Se}_{0.3}$ bulk alloys. As Fig.25 illustrates, there was a remarkable increase in the effective mass after the liquid state manipulation, resulting in a greater Seebeck coefficient. Notably, the texturing structure was reinforced by a high temperature-gradient directional solidification, leading to a higher electrical conductivity. The study concluded that at 26°C , the optimal \overline{ZT} value of 0.81 was achieved after the liquid state manipulation. In fact, this \overline{ZT} value was 35% higher than that of the unexperienced liquid state manipulation sample.

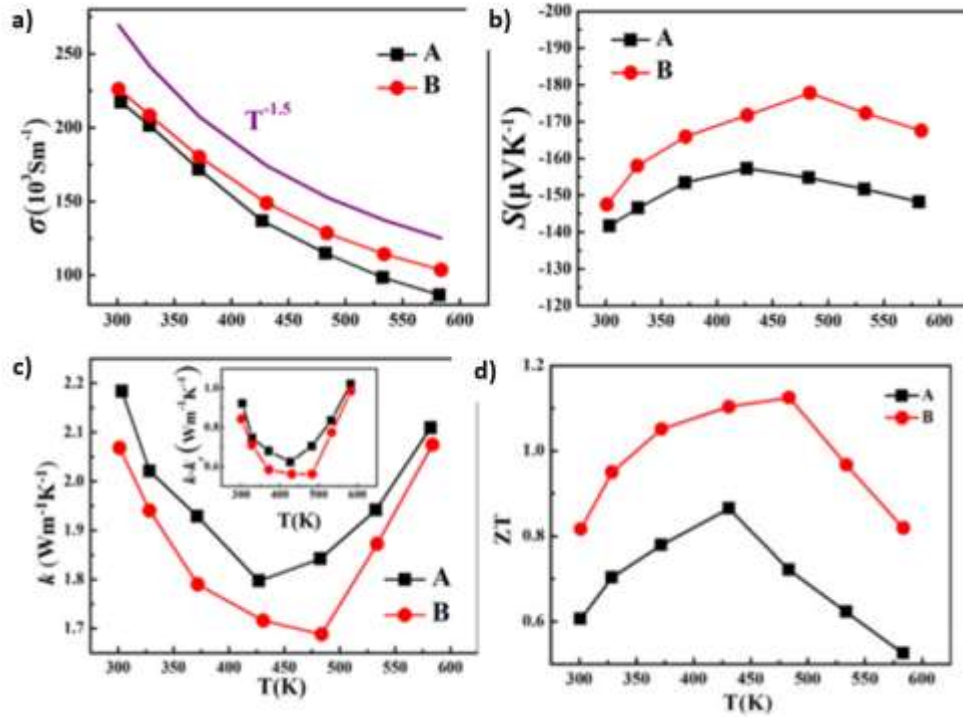


Fig. 25: Temperature dependences of TE properties parallel to the crystal growth direction for sample A and B: a) the electrical conductivity; b) the Seebeck coefficient; and c) the thermal conductivity; and d) the ZT values [155].

4.5 Organic thermoelectric materials

The organic TE materials, including polymers, carbon nanotubes (CNTs), and graphene [163], have been overlooked in the past decades owing to their low $Z\bar{T}$ values and the faster improvement of the inorganic TE materials [164]. Being inexpensive and recyclable, the organic TE materials are the most promising substitute for the inorganic ones [164,165]. In addition, the intrinsic flexibility of the organic TE materials makes them suitable to harvest heat from non-planar heat sources, such as human body [166-168]. In general, the energy conversion efficiency of the organic TE materials could be enhanced by different manners, such as offering a new molecular design, incorporating nanocomposites comprising either conducting polymers or nanomaterials [128]. In fact, the thermal conductivity of the organic type is in a range of between 0.2–0.34 W/mK, which is extremely difficult to be further reduced [169]. Therefore, the $Z\bar{T}$ value of the organic type is mainly dependent on its power factor (PF) [170].

4.5.1 Polymer-based TE material

The polymers of the organic type could be classified into conducting polymers and non-conducting polymers. Since the discovery of iodine- doped polyacetylene in 1977, the conducting polymers have served as the electrodes of the rechargeable batteries [164]. It is noteworthy that due to the intrinsic electrical conductivity of the conducting polymers, they have drawn more attention for the TE power generation than the non-conducting ones. Also, the non-conducting polymers suffer from hindering the bundle-to-bundle hopping, resulting in their lower power factor than the conducting ones [171]. Regarding the non-conducting polymers, the most optimum ones are poly(3-octylthiophene), poly(3-hexylthiophene)(P3HT), and polyvinylidene fluoride [171]. Among different types of the conducting polymers, over the last few years, great efforts have been made to improve the PF of Poly (3,4-ethylenedioxythiophene (PEDOT), Polyaniline (PANI), and Polypyrrole (PPy). These conducting polymers benefit from low thermal conductivities, non-toxicity , and low cost [128]. Table 3 provides the TE properties of some polymer-based TE materials at the room temperature.

Table 3: Summary of the TE properties of some typical polymer based TE materials at 26 °C.

Type	TE materials	α [$\mu\text{V/K}$]	σ [S/cm]	PF [$\mu\text{W/mK}^2$]	Ref
<i>P</i> - type	PEDOT:PSS films treated with H ₂ SO ₄ and NaOH	39.2	2170	334	[169]
	PDPP3T doped with 6mM FeCl ₃ /nitromethane	226	55	276	[172]
	PEDOT:S-PHE films	40	400	7.9	[173]
	PBTTT exposed to FTS vapor	33	1000	110	[174]
	PDTDE12 doped with F4TCNQ	80	75	20	[175]
	PDTDE12 doped with F4TCNQ	30	120	10	[176]
	PBDT-TT-TEO doped with F4TCNQ	190	1.3e-4	0.05	[177]
	C8TBT	60	2.2	1	[178]
	PEDOT:PSS post treated with TFMS–MeOH	21.9	2980	143	[179]
<i>N</i> - type	FBDPPV doped with (N-DMBI) ₂	-80	7.2	7	[180]
	PCBM doped with AOB and N-DMBI	-500	2	1	[181]
	P(PymPh) doped with NaNap	-16.4	18	0.485	[182]
	N-DMBI doped with A-DCV-DPPTT	-575	3.2	110	[183]
	PDPF doped with 5wt% N-DMBI	-235	1.3	4.65	[184]

5.3.1.1 P-type TE polymers

There are different correlations between tuning the electrical conductivity and the Seebeck coefficient of the TE materials to improve their power factors. To make it more clear, decreasing the concentration of the charge carriers improves the Seebeck coefficient but deteriorates the electrical conductivity. However, increasing the mobility of the charge carriers could enhance the the electrical conductivity and the Seebeck coefficient at the same time. Therefore, so far, the most optimal approaches to optimize the power factor of the conducting polymers involve enhancing the mobility of the charges and adjusting the concentration of the carriers. To improve the power factor of the PEDOT:PSS films, Fan et al. [169] sequentially post-treated them by sulfuric acid (H_2SO_4) and sodium hydroxide (NaOH). Initially, the PEDOT: PSS films were washed with sulfuric acid (H_2SO_4) as the oxidization process to increase the charge carriers' mobility of the PEDOT: PSS films. As a result, the electrical conductivity enhanced remarkably, whilst the Seebeck coefficient increased slightly, see Fig.26. To further enhance the Seebeck coefficient, the authors treated the H_2SO_4 -treated PEDOT: PSS films with sodium hydroxide (NaOH) to enhance the carrier concentration of the PEDOT: PSS films. The authors reported that the treated PEDOT: PSS films with H_2SO_4 and NaOH obtained the highest PF of $334 \mu W/mK^2$ at the room temperature.

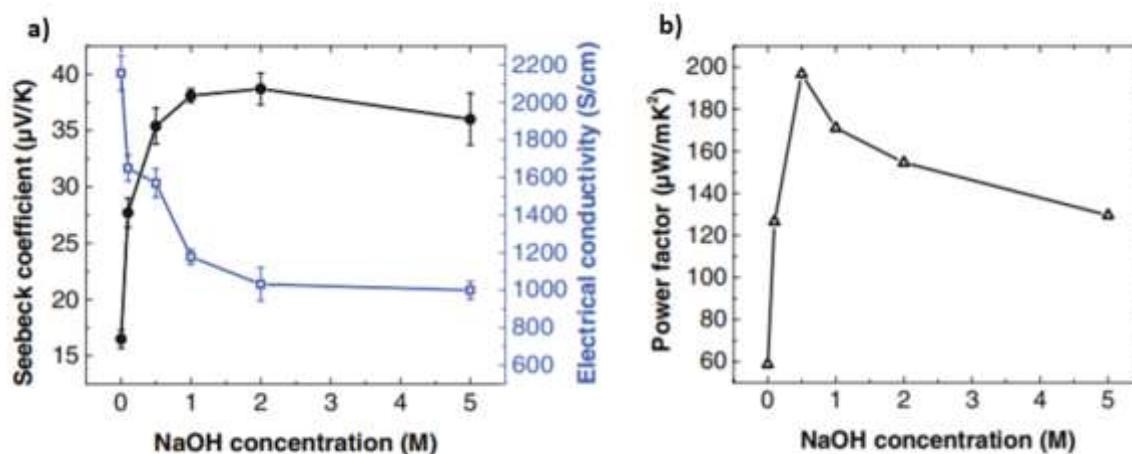


Fig. 26: Thermoelectric properties of the H_2SO_4 -treated PEDOT:PSS films at various NaOH treatment conditions: a) dependences of the Seebeck coefficient and electrical conductivity of the PEDOT:PSS films on NaOH concentration; and b) dependence of the power factor of the PEDOT:PSS films on NaOH concentration [169].

Jung et al. [172] attempted to increase the electrical conductivity and the Seebeck coefficient of PDPP3T as one of the best performing conjugated polymer. Therefore, the authors used the spin-

coating method to dope PDPP3T with FeCl₃/nitromethane solution as a small quantity dopant. The authors indicated that increasing the dopant's concentration from 1 to 9mM improved the electrical conductivity from 0 S/cm to nearly 80 S/cm but decreased the Seebeck coefficient from approximately 1400 $\mu\text{V}/\text{K}$ to 10 $\mu\text{V}/\text{K}$, as Fig.27 exhibits. Therefore, the highest power factors were achieved when the dopant concentration was kept between 3 and 8mM. Precisely, the maximum power factor of 276 $\mu\text{W}/\text{mK}^2$ was recorded for the 6mM FeCl₃/nitromethane doped PDPP3T.

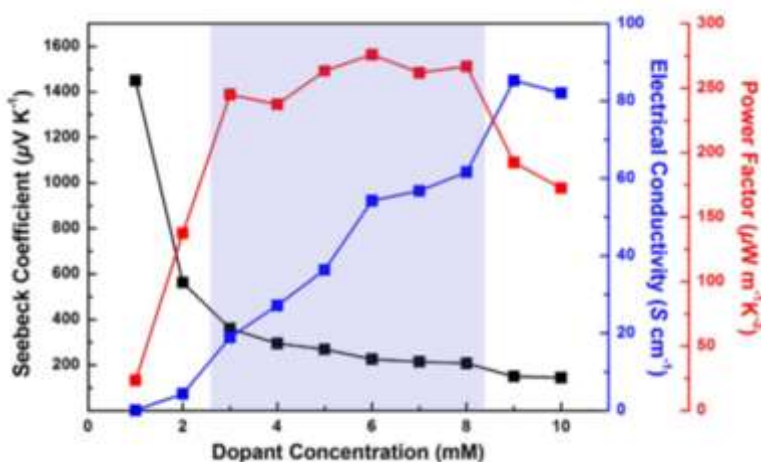


Fig. 27: Thermoelectric properties of the FeCl₃/nitromethane solutions doped PDPP3T [172].

Pan et al. [177] proved that the power factor of the polymers also related to their molecular structure. In particular, the authors focused on the correlation between the polymer side chain and the power factor of the conjugated polymers. Accordingly, two benzo[1,2-b:4,5-b'] dithiophene (BDT)-based conjugated polymers with different side chains were separately doped with DDQ and F4TCNQ. The examined conjugated polymers were PBDT-TT with alkyl side chains and PBDT-TT-TEO with polar side chains. The results confirmed that using either of the dopants, PBDT-TT-TEO achieved higher power factor than PBDT-TT. This was attributed to the polar side chains of the former, which slightly reduced its thermal stability and increased its band gap. As a result, after doping PBDT-TT-TEO with either of those dopants, its polar side chains reduced the clustering of the dopant molecules. Therefore, the electrical conductivity and in turn the power factor of PBDT-TT-TEO was higher than those of PBDT-TT, as Fig.28 shows. Precisely, at the

room temperature, PBDT-TT-TEO obtained the highest power factors of $0.006 \mu\text{W}/\text{mK}^2$ and $0.05 \mu\text{W}/\text{mK}^2$ by being doped with DDQ and F4TCNQ, respectively.

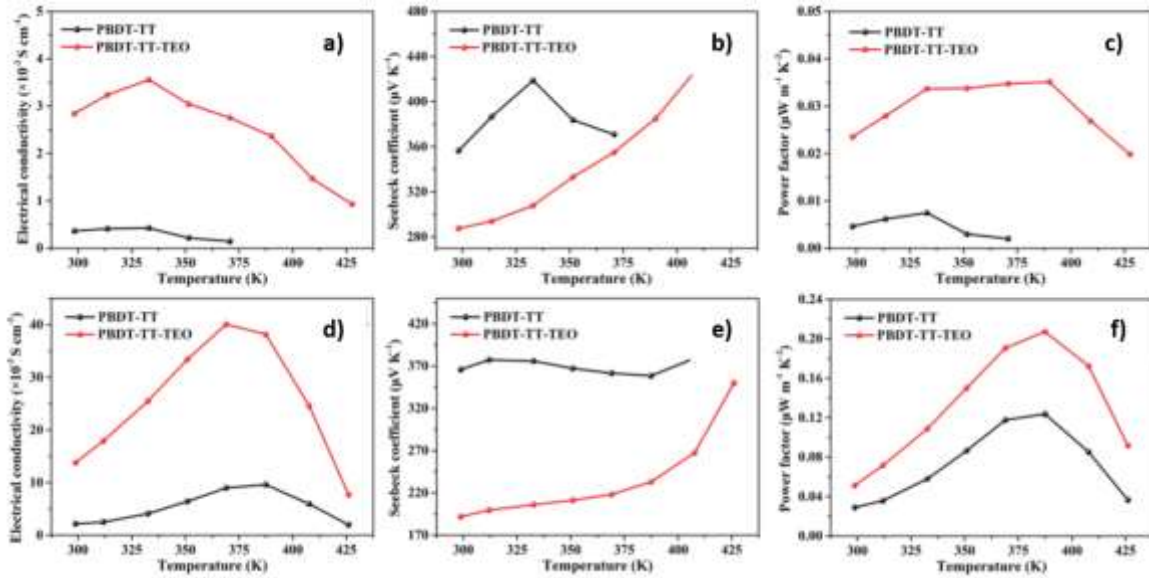


Fig. 28: The temperature-dependence of the TE properties for a–c) DDQ-doped polymer films and d–f) F4TCNQ-doped polymer films [177].

5.3.1.2 N-type TE polymers

P-type polymers have shown tremendous improvement over the last decades due to the development of the solution-processable and air stable TE polymers. Conversely, less attention has been paid to the development of the *n*-type TE polymers owing to their lower air stability, low solubility, and relatively low charge carrier mobility. To improve the electrical conductivity of the *n*-type TE polymers, an appropriate *n*-dopant could be used to directly transfer electrons to the host material. Thus, the extra charge carriers created by the dopant reduce or oxidize the *n*-type organic semiconductors. Putting this principle into practice, Madan et al. [185] employed sodium silica gel (Na-SG) particles as the reducing/doping agent to improve the TE properties of two different *n*-type conjugated polymers, including NTCDI2DT-2T (N1) and NTCDI-AF4A (N2). The chemical structures of these two conjugated polymers are presented in Fig.29 The authors considered four weight percentages (wt%), such as 0, 25, 50, and 75, for doping Na-SG. The results proved that the N2 and N1 films respectively obtained their highest power factors of 0.078

$\mu\text{W}/\text{mK}^2$ and $0.18 \mu\text{W}/\text{mK}^2$ by adding 75wt% Na-SG. The authors attributed this result to the three times higher electrical conductivities of the 75wt% Na-SG doped polymers compared with those of the pristine polymers.

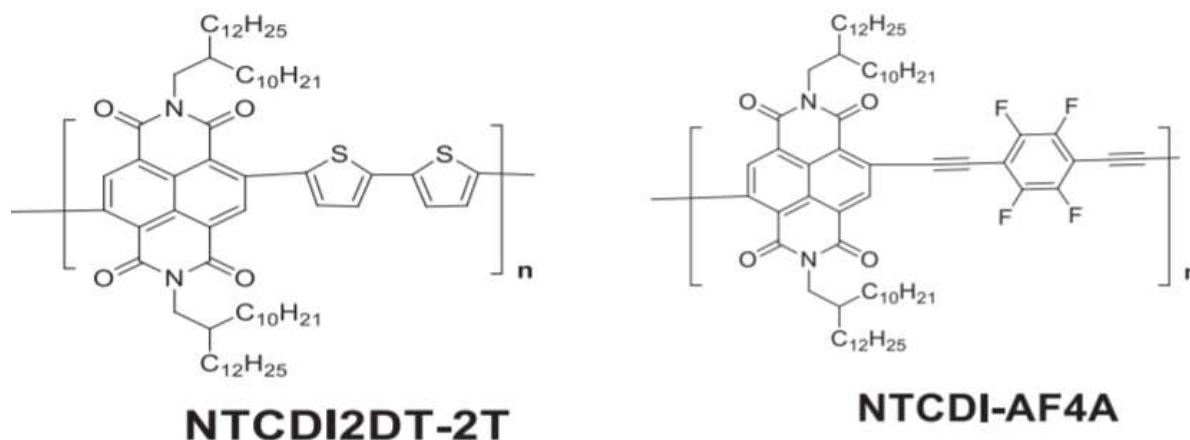


Fig. 29: Chemical structures of NTCDI2DT-2T (N1) and NTCDI-AF4A (N2) polymers [185].

Instead of the polymer type, Un et al. [180] explored the effect of the dopant type on the TE properties of a polymer. Thus, three *n*-type dopants, including $(\text{RuCp}^*\text{mes})_2$, $(\text{N-DMBI})_2$, and N-DMBI-H were specified to be individually doped into FBDPPV as the polymer. As Fig.30 shows, there was a converse relationship between the dopant's mol% and the Seebeck coefficient. Furthermore, the most optimum electrical conductivity was yielded with the $(\text{N-DMBI})_2$ doped FBDPPV $8\text{S}/\text{cm}$, resulting in the highest PF of $7 \mu\text{W}/\text{mK}^2$. Thus, the authors interpreted that a planner shape is the most appropriate molecular shape for the dopants, causing low perturbation of the polymers microstructure. In addition, a high PF could be achieved by the dopants that their molecular possess clean and efficient pathways for the electrons transfer.

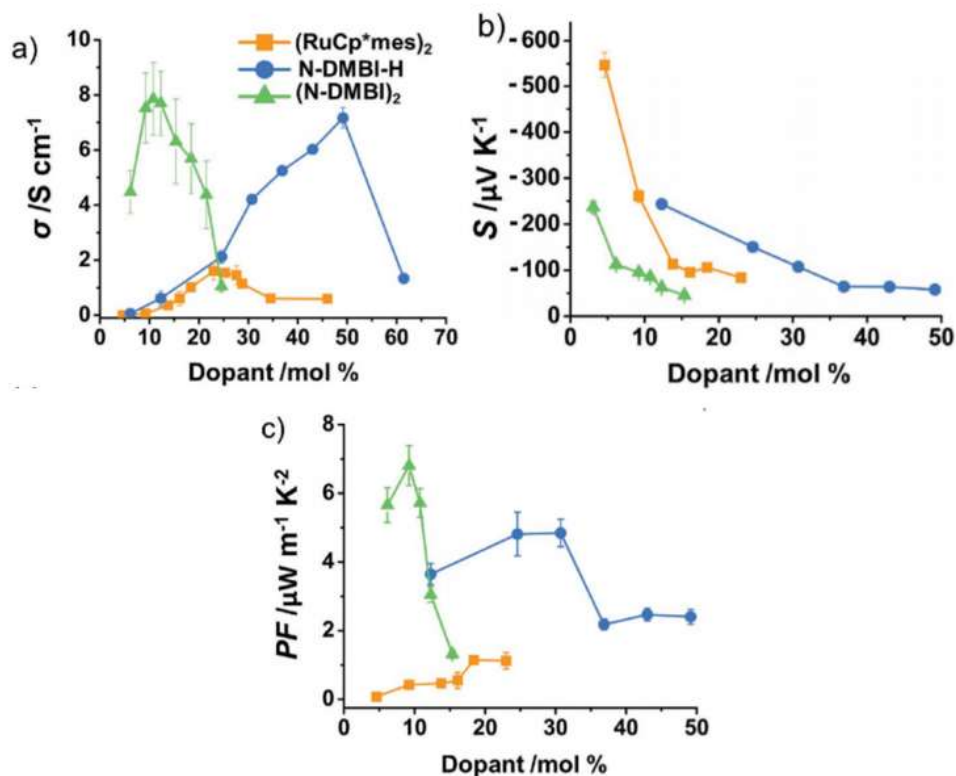


Fig. 30: The electrical and the TE properties of the (RuCp*mes)₂-, N-DMBI-H-, and (N-DMBI)₂-doped FBDPPV at varying dopant concentrations: a) the electrical conductivity; b) the Seebeck coefficient; and c) the power factor [180].

Another fundamental factor that impacts on the TE performance of the *n*-type polymers is their conjugated backbones structures. This is because the conjugated backbones structures determine the carrier mobility, the energy level, the charge transfer efficiency, and the carrier concentration of the doped materials. Yang et al. [184] engineered the donor moiety of the PDPF backbone, which is an *n*-type DPP-based donor–acceptor (D–A) polymer. Then the engineered polymer was doped by N-DMBI in the weight ratios of 2 – 17 wt%. The results indicated that the electron-withdrawing modification of the donor moiety of PDPF improved the electron affinity of the polymer and changed the polymer packing orientation. As a result, the highest PF value of 4.65 $\mu W/mK^2$ was achieved with 5% N-DMBI doped PDPF, as Fig.31 illustrates.

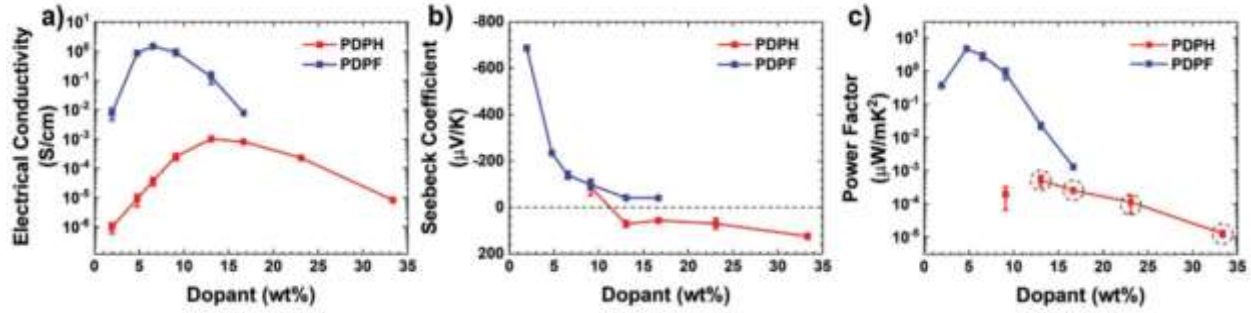


Fig. 31: Thermoelectric performance characterization: a) Electrical conductivities; b) Seebeck coefficients; and c) PFs (circular points indicate positive Seebeck coefficients) for different N-DMBI mass ratios [184].

4.5.2 Carbon-based TE materials

Among different types of carbonic materials, carbon nanotubes (CNT) and graphene are the most promising ones to reinforce polymer nanocomposites [186]. The dominance of CNT and graphene are attributed to four reasons. First, these two carbon based materials possess high electrical conductivities. Second, their large specific surface area in the form of carbon nanomaterials improves their interface with the polymer matrix. Third, it is possible to adjust their high thermal conductivity by embedding them in the polymer matrix. Fourth, they are flexible, low cost, non-toxic, lightweight, and mechanically strong [171]. The TE properties of some carbon based TE composites at room temperature are provided in Table 4.

Table 4: Summary of the TE properties of some typical carbon based TE composites at 26 °C.

Type	TE materials	α	σ	PF	Ref
		[$\mu\text{V/K}$]	[S/cm]	[$\mu\text{W/mK}^2$]	
<i>P-type</i>	SWNTs/PANI composite films	39	1440	217	[187]
	PPy/Graphene/PANi composite	28	500	52.5	[188]
	PANiPy/SWCNT composite	41	425	70	[189]
	CNT/PEDOT:PSS treated with Ethylene glycol	43.7	780	151	[190]
	SWNTs/ PEDOT: PSS treated with DMSO	42.5	500	105	[191]
	Alternate layers of PANi/graphene-PEDOT:PSS/PANi/DWNT-PEDOT:PSS	120	1800	2710	[192]
	PEDOT:PSS /RTCVD graphene composite film	54	193	56.28	[193]
<i>N-type</i>	DWNT-PEI/graphene-PVP nanocomposites	-80	300	190	[194]
	SWNT film doped with PEI solution	-62	3500	1500	[195]

SWCNT doped with PVA	-40	0.66	0.1	[196]
CNT web doped with benzyl viologen (BV)	-120	2200	3103	[197]

5.3.2.1 P-type carbon based TE composites

In recent years, nanocomposites have provided this opportunity to enhance the TE properties of the organic TE materials [198,199]. In general, there are several techniques for preparing the polymer nanocomposites, including the direct mixing, the in situ polymerization, the sol gel process, the melt intercalation, the template synthesis, the solution processing, and the layer-by-layer assembly [200,201]. Wang et al. [187] combined the in situ polymerization with the solution processing to enhance the ordering of the PANi molecular chains in the single walled nanotubes (SWNTs)/PANi composites. The results proved that combining the solution processing and the in suite polarization methods together improved the dispersion of the SWNTs in the composites. Furthermore, this combination created stronger π - π conjugated interactions between PANi and the SWNTs. As a result, a highly ordered structure of PANi was created on the CNTs surface, resulting in greater carrier mobility and electrical transport properties of PANi. The work reported that $217 \mu\text{W}/\text{mK}^2$ was the highest PF of the prepared SWNTs/PANi composite films comprising 65% SWNTs content.

Wang et al. [189] improved the alignment of the PANi molecular chain in the PANi/SWCNT composite by introducing polypyrrole (PPy) onto the PANi backbone. Regarding PPy, it is a well-known aligned polymer. As Fig.32 shows, a strong interaction was formed between the pyrrole and the aniline units on the random copolymer (PANiPy) backbone. The results indicated that the PANiPy/SWCNT composites exhibited the highest power factor of $70 \mu\text{W}/\text{mK}^2$ at $26 \text{ }^\circ\text{C}$, which was by far greater than that of PANi/SWCNT, PPy/SWCNT, and PANi/PPy/SWCNT composites. This higher achievement was associated to the optimum balance between the electrical conductivity and the Seebeck coefficient of the PANiPy/SWCNT composites.

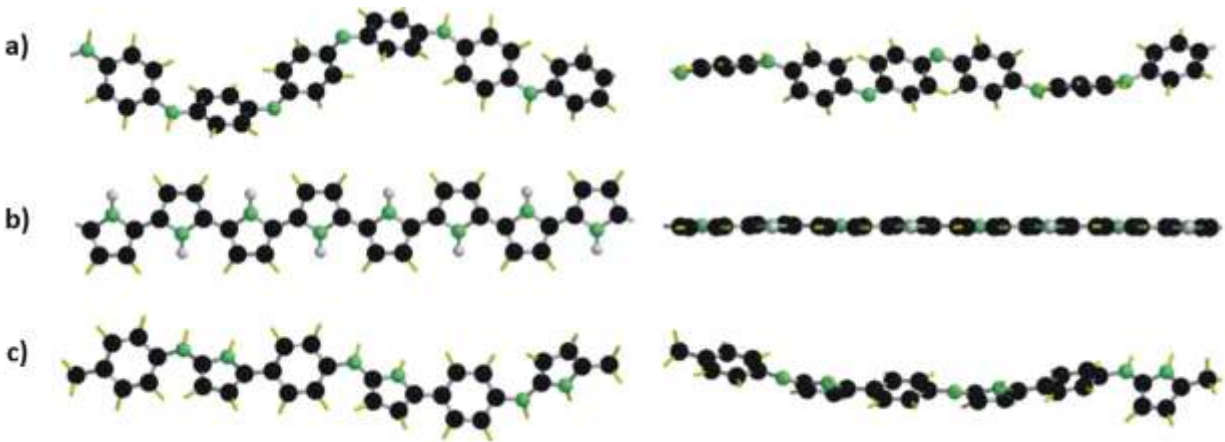
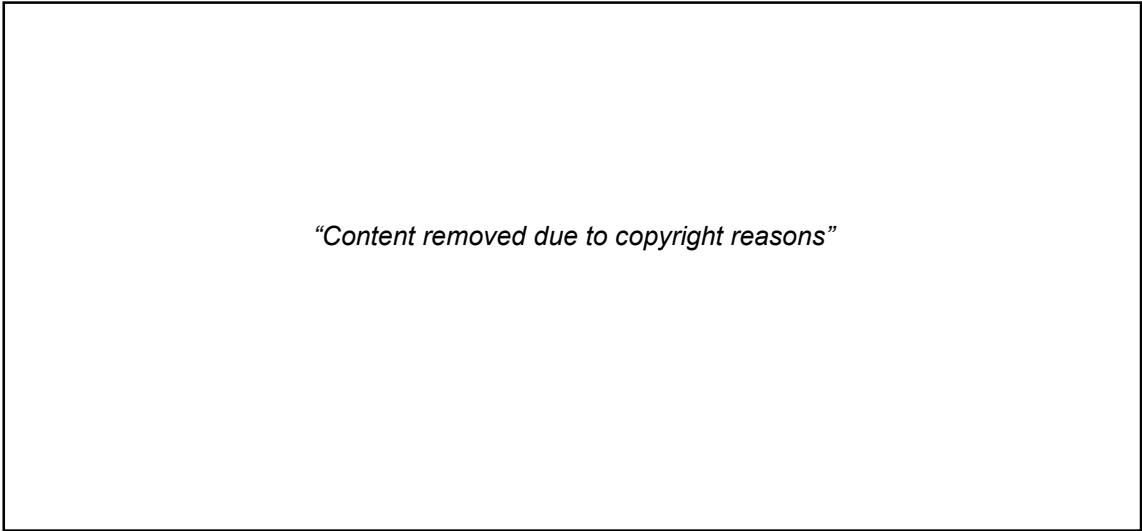


Fig. 32: Top view (left) and side view (right) of the partial chain segment conformation of: a) PANi; b) PPy; and c) PANiPy under the lowest energy state [189].

Cho et al. [192] used the layer by layer disposition process to assemble PANi, graphene, PEDOT:PSS, and DWNT. Fig.33 depicts the fabrication process, while the layering was repeated in a range of between 20 to 80 cycles. The results revealed that 80 cycles of PANi/graphene-PEDOT: PSS/PANi/DWNT-PEDOT: PSS resulted in the maximum PF of $2710 \mu\text{W}/\text{mK}^2$. The authors attributed this high PF to two main reasons. First, improvement in the carrier mobility of the interconnected and layered architecture of the DWNT covered conducting polymer. Second, the bridging between the graphene sheets. Conversely, the lowest PF achieved by an alternate layers of PANi/graphene-PEODT: PSS with $0 \mu\text{W}/\text{mK}^2$.



“Content removed due to copyright reasons”

Fig. 33: “Content removed due to copyright reasons”

The solution based technique could be classified into three categories, including the spin coating, the printing, and the spraying techniques [193]. Park et al. [202] selected the spin coating technique to coat a rapid thermal chemical vapour deposition (RTCVD) graphene surface with PEDOT:PSS solution, as shown in Fig.34. The experiments were conducted at spin rates between 500 and 5000 rpm. The results showed that due to the spin coating, the cracks and the defects on the RTCVD graphene surface minimised, resulting in a higher electrical conductivity. Furthermore, the Seebeck coefficient improved due to the high electron mobility attributed to the pep stacking interaction between the PEDOT: PSS backbone and the RTCVD graphene surface. The authors reported that the PEDOT: PSS /RTCVD graphene composite film obtained the maximum PF of $56.28 \mu\text{W}/\text{mK}^2$ at 5000rpm, while it was only $0.66 \mu\text{W}/\text{mK}^2$ for the pristine PEODT: PSS film.

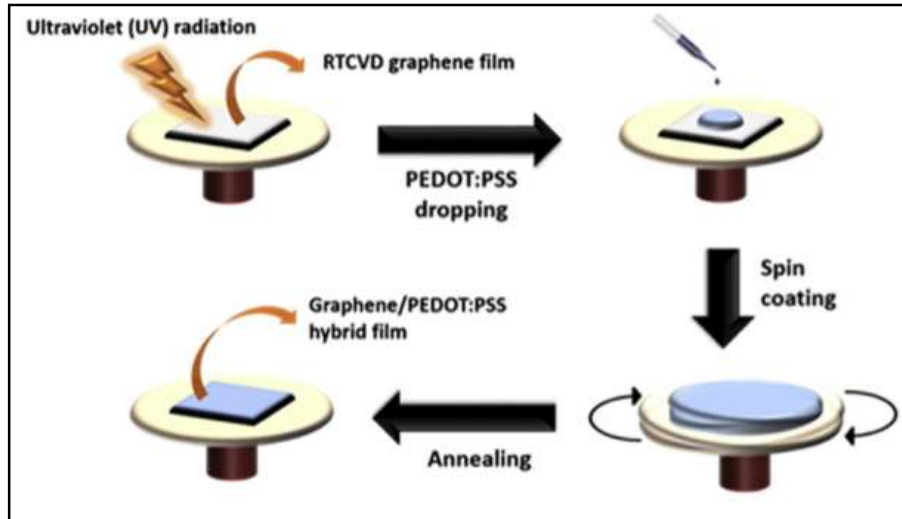


Fig. 34: Schematic illustration of the preparation procedure of the P/RTG hybrid films [202].

5.3.2.2 *N*-type carbon based TE composites

To compete with the *p*-type organic TE films, stable doping is the main challenge that the *n*-type must be overcome. To specify, the negative Seebeck coefficient of the *n*-type TE composites turns into positive when they are exposed to the air. In addition, it is of great importance to develop a homogeneous thin film by controlling the dispersion of the nanoparticles on the polymer substrate. Accordingly, to provide the CNT/polymer composites, the solution doping is the most striking approach to create the *n*-type films. Thus, Montgomery et al. [203] spray doped the *p*-type CNT/PVDF film by the *n*-type PEI/DMF solution. As a result, the *n*-type solution dissolved the surrounding PVDF, resulting in the infiltration of PEI to the CNT network. The results showed that the CNT/PVDF film altered to an *n*-type TE composite after the evaporation of DMF. It is noteworthy that the optimal combination was 10wt% CNT/PVDF with 0.1 mass ratio of PEI/CNT, as Fig.35 shows.

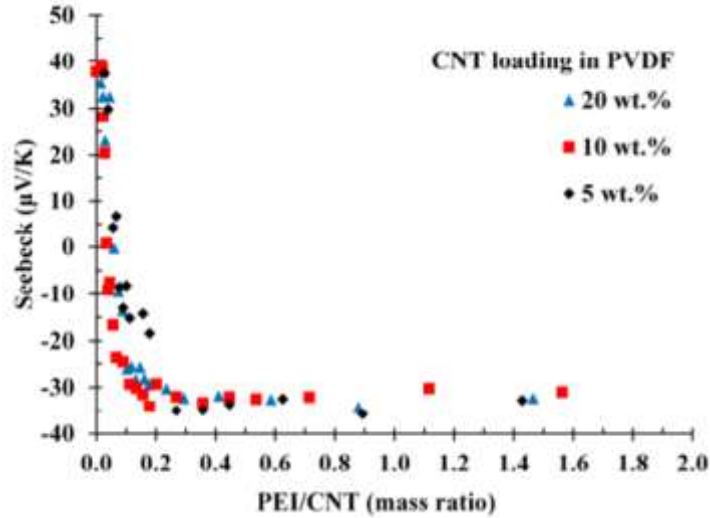


Fig. 35: Transition between the p-type and n-type Seebeck coefficient. Different CNT weight loadings in PVDF show that the transition is dependent on the mass ratio between PEI dopant and CNT matrix [203].

Since the *n*-type films are normally fabricated under the air exposure, the effect of oxygen adsorption should not be undervalued. Zhou et al. [195] drop casted the *n*-type polyethyleneimine (PEI) solution over the *p*-type SWNT film to convert it to an *n*-type film. The results showed that the electrons' concentration increased because the CNT bundles were covered in the amine-rich PEI molecules. In addition, the *n*-type characteristics of the films lasted for over 3 months because the PEI coating deterred the oxygen doping. The authors reported that the prepared *n*-type TE films achieved the highest power factor of $1500 \mu\text{W}/\text{mK}^2$ with 1 wt.% PEI content.

4.6 Hybrid thermoelectric materials

Although massive efforts have been carried out to improve the power factor of organic TE materials, still they cannot compete with their inorganic counterparts in terms of energy conversion efficiency. Precisely, the $Z\bar{T}$ values of the organic TE materials are almost 2 to 3 times lower than that of the inorganic ones [204]. In spite of this, the $Z\bar{T}$ value of the inorganic TE materials is still around unity, whilst it should be 3 or greater to reach widespread acceptance in the market. Apart from the low $Z\bar{T}$ values of the organic TE materials, they benefit from low density, low cost, low environmental impacts, and an appropriate mechanical flexibility [205]. Thus, the inorganic and organic types could be combined together to conjoin the benefits of both, resulting in hybrid TE

materials. In what follow, recent researches on developing hybrid TE materials are summarized. [Table 5](#) presents the TE properties of some hybrid TE materials.

Table 5: Summary of the TE properties of some typical inorganic/organic TE composites at 26 °C.

Type	TE materials	α [$\mu\text{V/K}$]	σ [S/cm]	PF [$\mu\text{W/mK}^2$]	Ref
<i>P</i> -type	Te-PEDOT:PSS thin film	50	100	25	[206]
	PC-Te/PEDOT:PSS treated by H ₂ SO ₄	75	250	141.9	[207]
	PC-Te/PEDOT:PSS treated by H ₂ SO ₄	56	332	104	[208]
	Te-Bi ₂ Te ₃ /PEDOT:PSS treated by H ₂ SO ₄	93.63	70	60.05	[209]
	Te NWs/PEDOT NWs	25	400	28	[210]
	Te- MWCNT/PANI	57.5	130	54.4	[211]
	Bi-Te based alloy nanosheet /PEDOT:PSS	21	1200	53	[212]
	SnSe nanosheets/PEDOT:PSS	100	300	390	[213]
	MoSe ₂ /PEDOT:PSS	21	1000	48.6	[214]
	PEDOT:PSS/ce-MoS ₂	21.9	867	41.6	[215]
	PEDOT:PSS/ Si-NP	24	510	27.5	[216]
	Alternately Sb ₂ Te ₃ /CH ₃ NH ₃ I/ Sb ₂ Te ₃ layers	300	170	1600	[217]
	Graphene nanosheets /Bi _{0.4} Sb _{1.6} Te ₃	177	1428	4600	[218]
	CNTs/Bi _{0.4} Sb _{1.6} Te ₃	180	1000	3200	[219]
	Bi ₂ Te ₃ /PEDOT:PSS	260	67	432	[220]
MgAg _{0.97} Sb _{0.99} /CNTs	183	650	2200	[221]	
<i>N</i> -type	TiS ₂ (TBA) _{0.013} (HA) _{0.019}	-140	450	904	[129]
	SWCNT dipped into KOH and 18-crown-ether	-33	2050	230	[222]
	Te nanowires/PDI	-310	1.6	18.6	[223]
	Ni/PVDF	-20	4500	200	[224]
	PP-CNT-CuO-PEG	-58	0.2	0.78	[225]
	PDINE/SWCNT	-46	500	112	[226]
	NDINE/SWCNT	-55	400	135	[226]
	SWCNT/ADTAb	-44.5	642.4	124	[227]

4.6.1 *P*-type hybrid TE materials

The most optimal hybrid TE materials are composed of the nanostructured inorganics (e.g. tellurium) and the conducting polymers [111]. In fact, this combination benefits from the high electrical conductivity and Seebeck coefficient of the former alongside the low thermal conductivity of the latter. Accordingly, Li et al. [206] drop casted the PEDOT:PSS aqueous

solution with the Te NWs ethanol solution and sonicated the mixture to prepare the Te-PEDOT:PSS thin films. The results revealed that increasing the PEDOT: PSS content up to 10wt% directly improved the power factor. However, more than 10wt% PEDOT: PSS content decreased the power factor up to that of the 5wt% PEDOT: PSS. As a result, the maximum PF of the prepared Te-PEDOT:PSS thin film was $25 \mu\text{W}/\text{mK}^2$ that was achieved by 10wt% PEDOT:PSS concentration, see Fig.36.

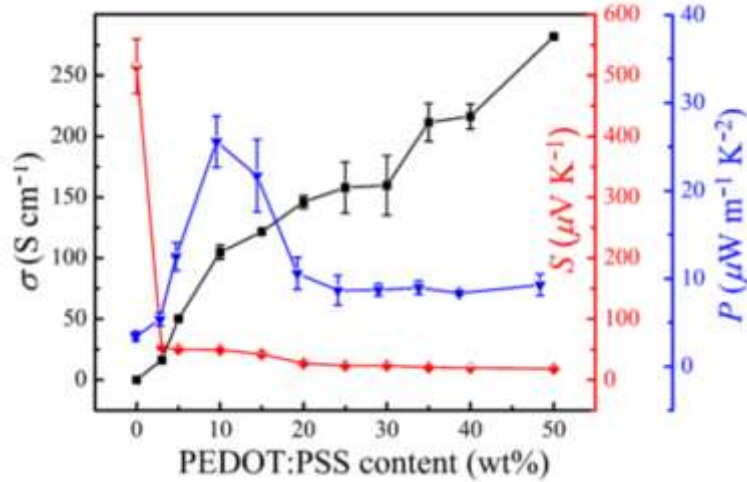


Fig. 36: The thermoelectric properties of the Te-PEDOT:PSS thin films with different contents of PEDOT:PSS [206].

To improve the electrical conductivity of PEDOT: PSS as the organic side of the hybrid TE material, its insulated PSS chains could be removed from its surface via being post treated with either H_2SO_4 , H_3PO_4 , or DMSO. Meng et al. [207] used H_2SO_4 to post treat the PC-Te/PEDOT:PSS composite film, as Fig.37 shows. The results revealed that post treating the prepared composite film with $12\text{M H}_2\text{SO}_4$ resulted in the highest power factor of $141.9 \mu\text{W}/\text{mK}^2$. In fact, this amount was 2.75 times greater than that of an untreated PEDOT: PSS: PC-Te film. The study attributed this optimum power factor to the direct relationship between the post treatment and the electrical conductivity.

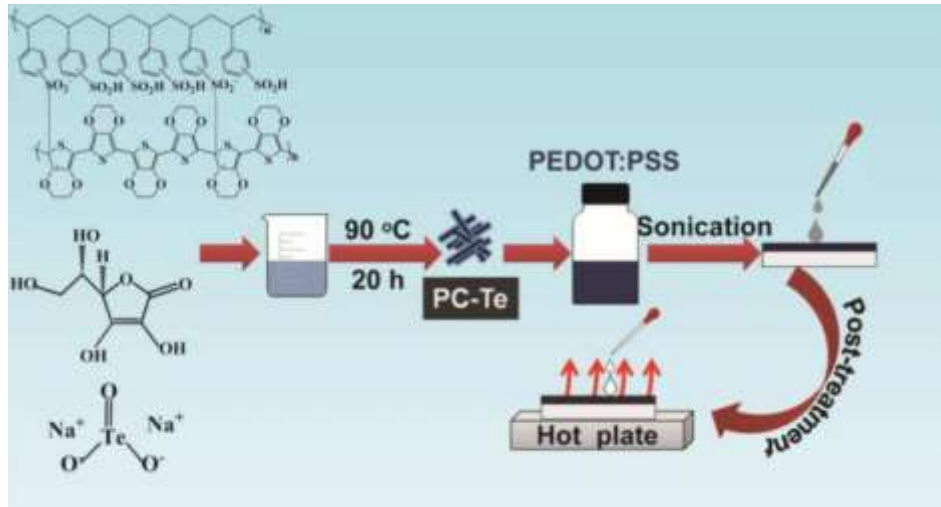


Fig. 37: Schematic illustrations of the fabrication and post-treatment of the composite films [207].

Apart from the conducting polymers, hybrid TE composites also could be prepared with other organic TE materials. For example, Zheng et al. [217] proposed a multilayer hybrid composite using Sb_2Te_3 and $\text{CH}_3\text{NH}_3\text{I}$ as the inorganic and organic TE materials, respectively. To prepare the layers, the thermal evaporation method was employed to encapsulate the $\text{CH}_3\text{NH}_3\text{I}$ layer between two layers of Sb_2Te_3 . Fig.38 shows the schematic illustration of the fabrication procedure. The results proved that the $\text{CH}_3\text{NH}_3\text{I}$ layer improved the electrical conductivity of the composite film by promoting the growth of the organic molecules and the crystallization. Furthermore, the thermal conductivity of the composite decreased via post-annealing the fabricated films, resulting in the enhancement of the phonon scattering. The authors concluded that $1600 \mu\text{W}/\text{mK}^2$ was the highest obtained PF of the composite at the room temperature.

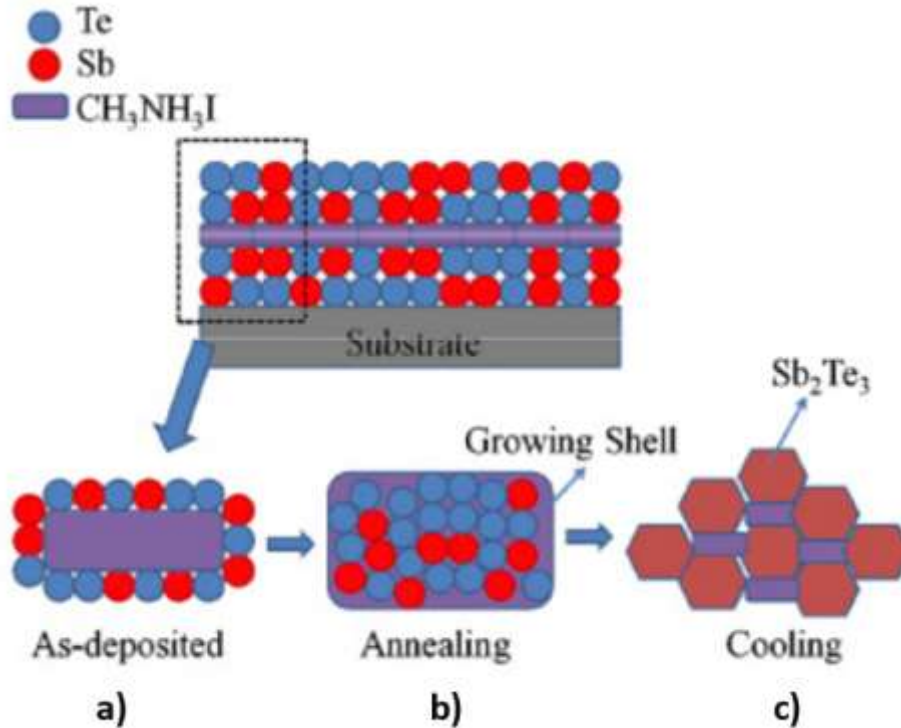


Fig. 38: The schematic illustration of the thin film growth: a) as-deposited composited thin film; b) annealing process; and c) cooling process [217].

4.6.2 *N*-type hybrid TE materials

The hybrid TE materials benefit from the high electrical conductivity and the low thermal conductivity of the inorganic and organic types, respectively. However, the main barrier of generating the *n*-type hybrid TE materials is their instability to the air exposure that turns them back to the *p*-type. Nonoguchi et al. [222] used a series of ordinary salts and crown ethers to enhance the air stability of an *n*-type SWCNT. The studied salts involved sodium chloride (NaCl), sodium hydroxide (NaOH), and potassium hydroxide (KOH). The results revealed that dipping the SWCNT into the stock solution of 0.1 mol/L KOH and 18-crown-ether resulted in an *n*-type composite film with the highest PF of $230 \mu\text{W}/\text{mK}^2$, while its air stability lasted for more than one month. Zaia et al. [223] coated Te nanowires with PDI as an air stable organic component to achieve PDI-Te composite. Different volume ratios of PDI was considered for synthesizing. However, the highest PF of $17.6 \mu\text{W}/\text{mK}^2$ was achieved by 80 vol% PDI concentration.

A simple scale-up fabrication protocols was proposed by Chen et al. [224], who embedded Nickel (Ni) nanowires within PVDF matrix without doping treatment. The authors prepared the *n*-type Ni/PVDF films by mixing the Ni nanowires with PVDF powder using the dimethylformamide (DMF) solution. The results revealed that increasing the concentration of the Ni nanowire from 20 wt% to 80 wt% increased the carrier mobility and led to a higher electrical conductivity, whilst it had no effect on the Seebeck coefficient of the compound. The study concluded that the *n*-type Ni/PVDF films obtained the highest PF of 200 $\mu\text{W}/\text{mK}^2$ with 80 wt% Ni nanowires. Luo et al. [225] converted the *p*-type PP-CNT-CuO composite into an *n*-type by adding polyethylene glycol (PEG) to it. The results revealed that the conversion started from 8 wt% PEG addition, whilst the highest power factor of 0.78 $\mu\text{W}/\text{mK}^2$ was obtained by 10 wt% PEG, as shown in Fig.39.

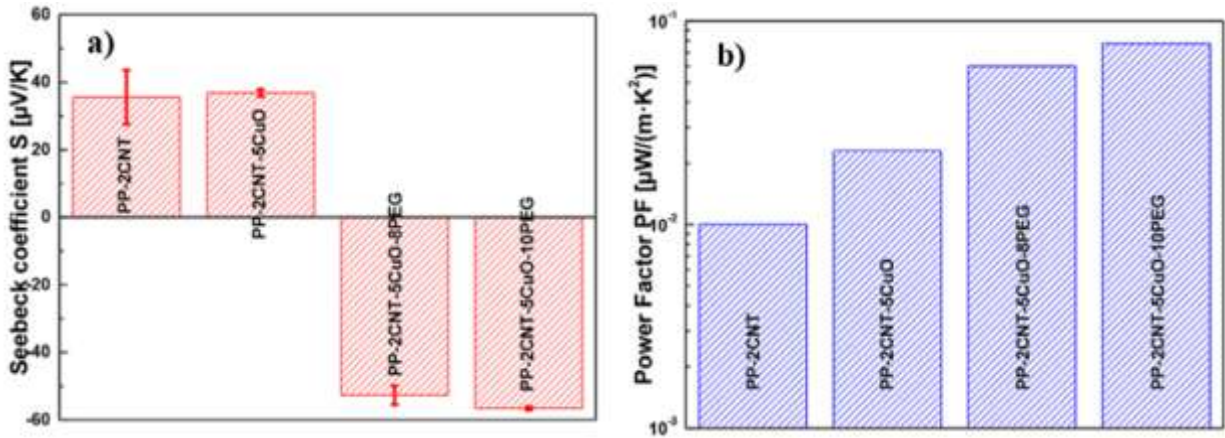


Fig. 39: The influence of the PEG content on the TE properties of the melt mixed composites containing the fixed CNT (2 wt%) and CuO (5 wt%) concentrations [225].

Wu et al. [226] prepared an *n*-type hybrid TE material by taking the benefits of the high electrical conductivity of SWCNT and the large Seebeck coefficient of perylene diimide (PDINE) and naphthalene diimide (NDINE). The experiments were conducted by mixing SWCNT with either PDINE or NDINE. The results showed that the PDINE/SWCNT and NDINE/SWCNT composites achieved the highest power factors of $112 \pm 8 \mu\text{W}/\text{mK}^2$ and $135 \pm 14 \mu\text{W}/\text{mK}^2$, respectively. Gao et al. [227] used a series of terminal tertiary amine groups of ADTA (a-g) to yield *n*-type SWCNT/ADTA composite films. The result showed that two factors were affecting the electrical conductivity and the Seebeck coefficient of the prepared composite films, namely the number of side chains and the type of the terminal amine. As a result, the SWCNT/ADTA composite films displayed the highest PF value of $124.4 \pm 10.5 \mu\text{W}/\text{mK}^2$ at the room temperature.

4.7 Summary

Among different approaches to improve the efficiency of the inorganic TE materials, three of them are the most promising ones, including increasing the holes' concentration, raising the phonon scattering, and decreasing the lattice thermal conductivity. To illustrate, applying each of these three strategies increases the $Z\bar{T}$ values of a *p*-type inorganic alloy called $\text{Bi}_{0.4-x}\text{Sb}_{1.6+x}\text{Te}_3$ to the maximum range of between 1.15 and 1.36. Concerning the *n*-type inorganic TE materials, the highest obtained $Z\bar{T}$ values were in a range of between 0.7 and 0.8, which were obtained by the $\text{Bi}_2\text{Te}_{2.7}\text{Se}_{0.3}$ composite. Concerning different fabrication techniques of the inorganic TE materials, the hot pressing technique was superior to the spark plasma sintering, the ball milling, and the zone melting techniques. From the reviewed organic TE materials, the power factor of the carbon-based ones was greater than that of the polymer-based ones. To fabricate the *p*-type organic TE materials, the layer by layer deposition process was the most striking approach concerning the power factor. Whereas, combining the annealing treatment with the *n*-type doping led to the highest power factors of the *n*-type ones. Likewise, the hybrid TE materials comprising the carbon-based materials illustrated higher power factors than the polymer-based ones. To specify, combining $\text{Bi}_{0.4}\text{Sb}_{1.6}\text{Te}_3$ with either graphene or carbon resulted in the most efficient hybrid TE materials.

Although the inorganic type benefits from the highest *ZT* values (~1) compared with the other two types, it suffers from rigidity, rarity in the earth's crust, and containing toxic elements. On the contrary, the organic type benefits from higher flexibility and absence of toxic elements. However, the organic type suffers from two drawbacks. First, the *n*-type conducting polymers are unstable in the air exposure. Second, the applied methods (such as doping, de doping, post treatment, crystallinity, and alignment) to optimize the power factor of the organic TE materials should be optimized themselves. As a result, solving the rigidity and the low efficiency of the inorganic and organic types, respectively, the hybrid type has attracted more attention in recent years. However, the hybrid TE materials still suffer from containing toxic and rare inorganic elements, lower efficiency compared with the inorganic type, and air instability of their *n*-type. Furthermore, until to date, the TE materials have been examined concerning their efficiency, but not their lifecycle impacts. However, as part of the sustainability criteria for future technologies, the environmental

aspect of any energy technology requires careful attention. This part is heavily neglected in the existing research on the TE materials, but should be addressed in future.

Chapter 5

Different Configurations of TEGs

5.1 Introduction

Based on the reviewed literatures in [Chapter 4](#), inorganic TE materials show superiority to the other two types (i.e. organic and hybrid types) with respect to the energy conversion efficiency. However, not only the efficiency of the TE materials matters in the performance of the TEGs, but also their configuration plays vital role in this manner. Accordingly, herein, different configurations of TE legs, which dictates the ultimate configuration of the TEGs, were studied with regard to their materials to find out their performance under almost the same thermal gradient. It should be noted that TEGs are used to power various applications, including the wearable devices, the wireless sensor networks, the industrial electronic devices, the automobile engines, and the aerospace [\[228\]](#). Thus, the configurations of their TE legs vary in accordance with their applications. To specify, the configurations of the TE legs could be classified into three main categories, including the cross-plane, the in-plane design, and the combination of both. Since each of these three types of TE legs can be used to fabricate a wearable TEG, herein, a comprehensive review on different configurations of wearable TEGs will be presented. Therefore, combining the result of this chapter, with those of [Chapter 4](#) (i.e. the energy conversion efficiency of different TE materials) and [Chapter 7](#) (i.e. life cycle impact of different types of TE materials) pave the way to select the most energy conversion efficient and environmental friendly TEG for this research.

5.2 Wearable TEGs

As the hierarchy in [Table 6](#) shows, the human body is considered as a source of the kinetic energy [\[229-231\]](#), the thermal energy [\[232,233\]](#), the chemical energy [\[234\]](#), and the exhaled air energy [\[235,236\]](#). As the table depicts, to power activity trackers and portable health monitors, each of these energies can be scavenged and converted into the electrical energy with a specific energy harvester. Owing to the metabolic function, the human body is a constant source of the thermal energy in a range of between 100 W and 525 W [\[237\]](#). To illustrate, the body temperature varies in a range of between 23 °C and 37 °C when the room's temperature fluctuates between 15 °C and 47 °C [\[238\]](#), see [Fig.9](#). The wearable TEGs utilize the temperature difference between the body skin and the ambient air to generate a low level of power current [\[125\]](#). Using a wearable TEG

with ~1% conversion efficiency, the whole body should be covered by TEGs to generate an electrical energy in a range of between ~1W to 5.25W [232]. Notably, the conversion efficiency of the wearable TEGs depends on several factors, including the properties of their TE materials [239], the geometry of their TE legs [240,241], the metabolic rate of the wearers (e.g. the resting, walking, or running states) [242], the mounting position of the TEGs (e.g. on the wrist, chest, arm) [242,243], and the thermal conditions (e.g. the dry bulb temperature, the relative humidity, and the air velocity) [244-246]. Therefore, precise considerations are required at the design stage of the wearable TEGs, because any deficiency at this stage impacts the output power of the TEGs.

Table 6: Potential energy sources of the human body and the associated energy harvesters [247-249].

Body energy harvesting			
Biochemical Energy	Thermal Energy	Kinetic Energy	Exhaled Air Energy
Biofuel cells	Thermoelectric	Piezoelectric	Triboelectric
	Pyroelectric	Triboelectric	Piezoelectric
		Electromagnetic	Pyroelectric
			Thermoelectric

5.3 Configurations of wearable TEGs

According to Eq. (6), the conversion efficiency (η_{max}) of the TEGs is directly dependent on the temperature difference between the hot and cold junctions of their TE legs. To specify, a higher temperature difference results in a higher output power. To adjust this temperature difference, one of the main options is manipulating the structural design of the TE legs [244]. The configuration of the TE legs can be classified into three main categories, including the transversal (cross-plane), the lateral (in-plane), and the combination of both. This classification is related to the manner of arranging the legs on the substrate and subsequently to the heat flow direction within them [250]. Regarding the TEGs with a cross-plane configuration as Fig.40a shows, the TE legs are mostly ingot-shaped and perpendicular to the hot and cold substrates. Therefore, the temperature difference along the legs encourages the free holes and electrons to start moving vertically and to generate electricity.

Obviously, it is desirable for a wearable TEG to be lightweight and flexible to take on the shape of the arbitrary surfaces of the body (e.g. wrist) [251]. Whereas, the cross-plane design suffers from rigidity and bulkiness, causing cumbersome for the wearers in long term. Thus, the most promising alternative is the in-plane design comprising film-shaped thermocouples fabricated onto a single substrate, see Fig.40b. Splitting the substrate in half either from the length or width, the opposite halves serve as the hot and cold substrates. As a result, the film-shaped thermocouples merely harvest the parallel temperature gradient between the two halves and rarely capture the vertical temperature difference between the heat source and the ambient air [252]. Accordingly, the in-plane design usually suffers from lower conversion efficiencies than the cross-plane one [113,253]. To solve the rigidity and the efficiency issue at the same time, researchers have suggested to combine these two designs together, resulting in yarn-shaped thermocouples. As Fig.40c shows, the two dimensional and flexible TE yarns (in-plane design) are knitted together or sewn onto a fabric, resulting in a vertical heat flow (cross-plane design) [254]. In what follows, a comprehensive literature review is provided on the energy conversion efficiency of the wearable TEGs concerning the configuration and the material of the thermocouples.

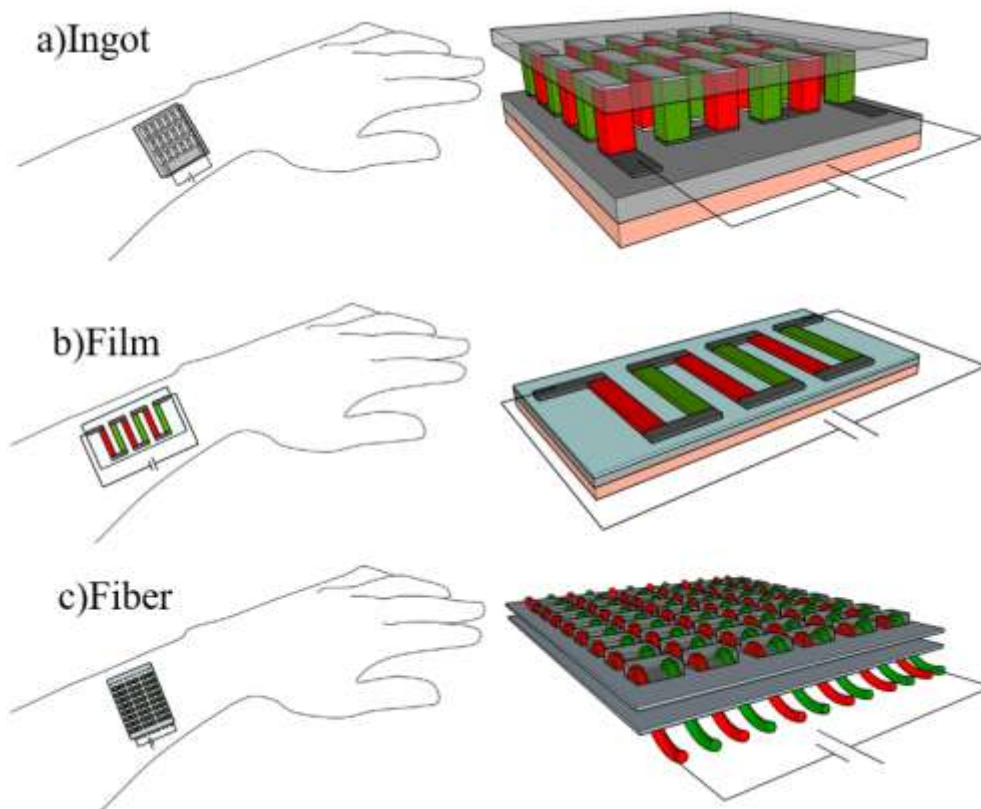


Fig. 40: The schematics of: a) the cross-plane; b) the in-plane; and c) the combined configurations [255].

5.4 Ingot-shaped thermocouples

5.4.1 Inorganic TE materials

The ingot-shaped thermocouples are generated by initially ball milling or melting/heating the TE powders followed by either cold or hot pressing the synthesised powders [256,257]. Then, the obtained TE legs are bonded together by electrical shunts, resulting in the ingot-shaped thermocouples. Following Chapter 4, Bi_2Te_3 -based alloys are the most prevalent materials used for fabricating the inorganic ingot-shaped legs. Precisely, the *p*-type inorganic thermocouples are mostly fabricated via either Bi_2Te_3 or $\text{Bi}_{0.3}\text{Sb}_{1.7}\text{Te}_3$ composites. Whereas, Bi_2Te_3 and $\text{Bi}_2\text{Te}_{2.7}\text{Se}_{0.3}$ composites are the most prevalent *n*-type TE alloys used in the ingot-shaped thermocouples. The privilege of these materials over other inorganic TE materials is their higher energy conversion

efficiencies [122]. To fabricate a wearable TEG using the ingot-shaped thermocouples, the thermocouples could be integrated together using either a flexible or a rigid substrate. In accordance with the recent progresses in the wearable TEGs, using the former have drawn growing attentions compared with the latter. To illustrate, the flexible substrates are composed of either polymers, printed circuit board (FPCB), holders, or fabrics. Whereas, the rigid ones are mainly consisted of a conventional rigid Aluminium Oxide-based substrate.

For example, Kim et al. [258] generated a flexible wearable TEG via encapsulating 72 pairs of ingot-shaped TE legs in a flexible polymer, as Fig.41 shows. Accordingly, the *p*-type ($\text{Bi}_{0.3}\text{Sb}_{1.7}\text{Te}_3$) and the *n*-type ($\text{Bi}_2\text{Sb}_{0.3}\text{Te}_{2.7}$) TE legs each with 1mm^2 covering area were connected together with thin copper films as electrodes. To ensure the mechanical integrity of the structure, the gaps between the legs were filled with a very low thermal conductivity ($0.03\text{ W m}^{-1}\text{K}^{-2}$) polymer. The authors specified different variables for tuning the output power of the fabricated TEG, including the height of the TE legs (i.e. 0.8 mm and 2.5 mm), the fill factor (i.e. 15.1%, 19.8%, and 27.2%), and the air velocity (i.e. 0 m/s-3 m/s with 1m/s interval). The results showed that increasing the legs' height from 0.8 mm to 2.5 mm raised the power density by four times. Furthermore, the authors demonstrated that increasing the fill factor (occupying the area of the legs over the TEG's base area) was more efficient in the higher air velocities. The authors demonstrated that at $8.9\text{ }^\circ\text{C}$ temperature difference and zero air velocity, the maximum obtained output power was $2.5\text{ }\mu\text{W}/\text{cm}^2$, which was achieved by 15.1% fill factor.

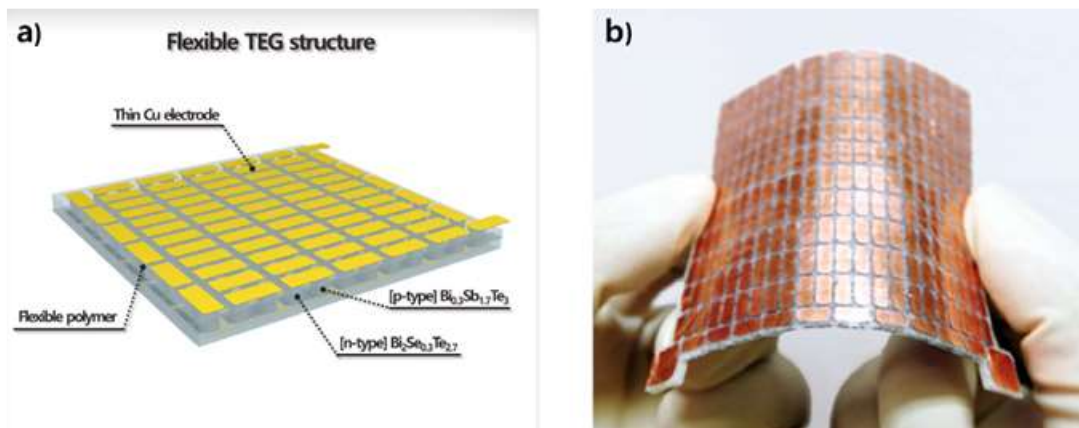


Fig. 41: a) The schematic drawing of the flexible TEG; b) photo of the actual fabricated TEG [258].

Suarez et al. [259] used $\text{Bi}_{0.5}\text{Sb}_{1.5}\text{Te}_3$ (*p*-type) and $\text{Bi}_2\text{Se}_{0.3}\text{Te}_{2.7}$ (*n*-type) solid ingots as the TE legs and electrically bonded them together with EGaIn as the interconnects. Then, 32 thermocouples were fully encapsulated in polydimethylsiloxane (PDMS) as the flexible substrate, resulting in a 4cm^2 flexible TEG, see Fig.42. The results showed that compared with the air layer surrounding the TE legs in conventional rigid TEGs, the PDMS substrate with 0.15 W/mK thermal conductivity performed as a thermal path. To specify, the thermal conductivity of PDMS was 6 times greater than that of the air (0.025 W/m.K). Thus, the heat flew faster in parallel with the TE legs in the former compared with the latter, leading to lower temperature differential and output power. The authors demonstrated that making the PDMS substrate porous could reduce its thermal conductivity down to 0.08 W/mK , resulting in 86% greater output voltage. The paper concluded that when the TEG was worn on the wrist at the ambient temperature of 24°C , the maximum achieved output power was $1\ \mu\text{W}/\text{cm}^2$.

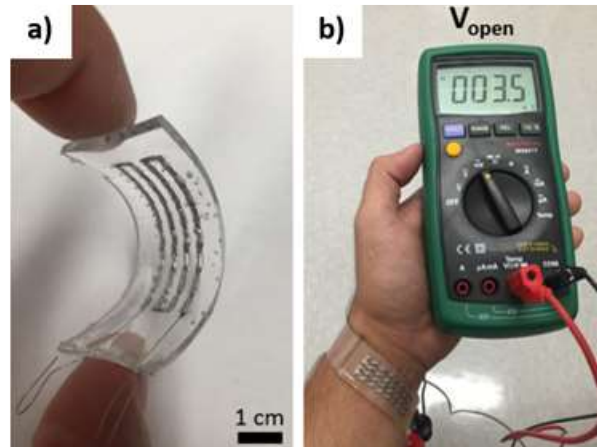


Fig. 42: a) Photo of the fabricated TEG; b) the obtained open circuit voltage at the room temperature [259].

Wang et al. [260] incorporated the polymer-based substrate with a FPCB. Accordingly, 52 pairs of *p*- ($\text{Bi}_{0.5}\text{Sb}_{1.5}\text{Te}_3$) and *n*- ($\text{Bi}_2\text{Se}_{0.5}\text{Te}_{2.5}$) type legs were soldered from their bottom ends to the copper electrodes printed onto the FPCB. It should be noted that the authors cut several holes out of the FPCB to improve its bendability. Next, the upper ends of the legs were electrically connected together using copper strips. Finally, as Fig.43 shows, the spaces between the legs were

fully filled with PDMS to increase the mechanical integrity of the TEG. The results demonstrated that the 11.5cm^2 surface area TEG generated $3.9\ \mu\text{W}/\text{cm}^2$ at $18\ ^\circ\text{C}$ temperature difference.

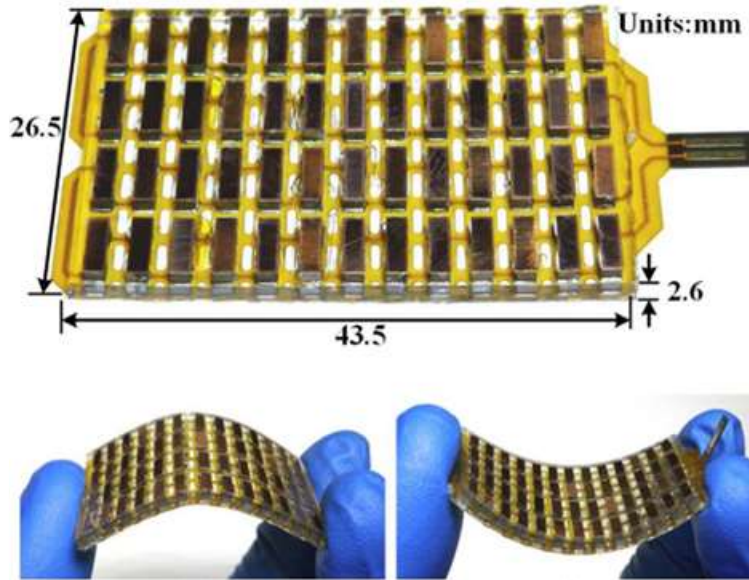


Fig. 43: The fabricated TEG with the FPCB substrate and the PDMS filler [260].

Instead of using a FPCB, Eom et al. [248] developed a flexible holder in the form of a bracelet to put 10 modular TE units together, see Fig.44. Each individual unit was composed of four ingot-shaped TE legs arranged in an array of 2×2 . The *p*- and *n*-type legs consisted of $\text{Bi}_{0.5}\text{Sb}_{1.5}\text{Te}_3$ and $\text{Bi}_2\text{Te}_{2.7}\text{Se}_{0.3}$, respectively. Then, the legs were electrically connected together using copper foils as the electrodes. Finally, the 10 modular units each with the dimensions of $1.4\ \text{cm} \times 1.2\ \text{cm}$ were connected together by passing a shaft through the punched holes in the legs and sides of the units. The results showed that at an ambient temperature of $20\ ^\circ\text{C}$, the highest obtained output powers at rest, walking, and slow running conditions were 2, 2.9, and $4.7\ \mu\text{W}/\text{cm}^2$, respectively.



Fig. 44: The designed flexible TE system consisted of a flexible holder [248].

5.4.2 Hybrid TE materials

Despite the low thermal conductivity and high flexibility of the organic and hybrid TE materials, using them for the preparation of the ingot-shaped TE legs is not prevalent. This is mainly because, there is no privilege in their flexibility when the legs are ingot-shaped. In addition, their low thermal conductivity could be replaced by the high Seebeck coefficient and the electrical conductivity of the inorganic type. In spite of this, Jung et al. [251] generated a flexible hybrid TEG by mixing the hybrid TE materials with PDMS. To prepare the hybrid TE materials, Bi (*p*-type) and Te (*n*-type) were incorporated with carbon nanotubes (CNTs) separately. Next, the hybrid TE powders were mixed with a solution of PDMS as a precursor. Then, as Fig. 45 shows, the *p*- and *n*-type composites were alternately poured into 100 holes of an aluminium stencil followed by being cured for 3 hrs at 90 °C, resulting in the ingot-shaped legs. Then, the 50 pairs of the TE legs were connected together with the aluminium electrodes and the gaps between them were filled with an extra PDMS layer as a flexible substrate. The results showed that the highest output power generated by the prepared flexible TEG was 80 $\mu\text{W}/\text{cm}^2$ at ΔT of 293 °C.

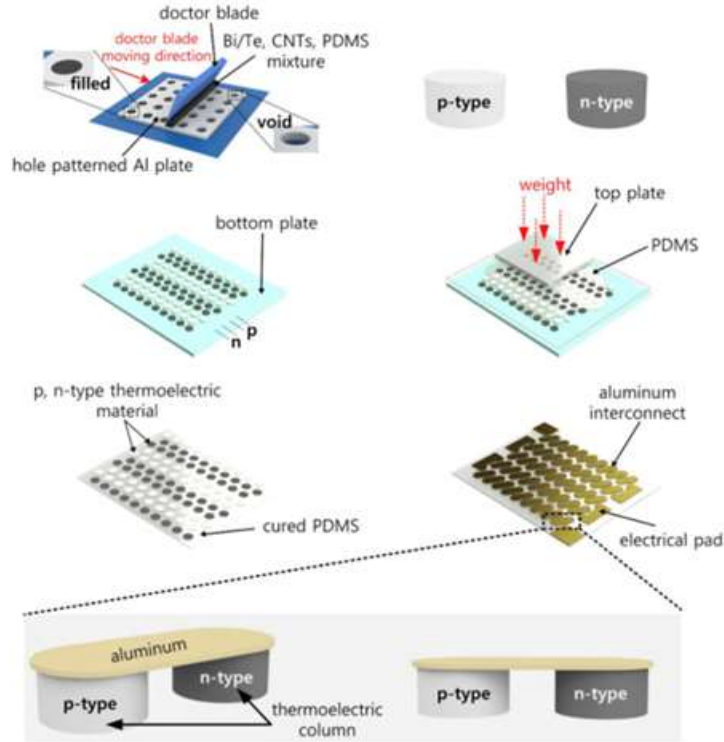


Fig. 45: The schematic diagram of the fabrication processes of the proposed TEG [251].

Instead of preparing a hybrid TE material, Park et al. [261] connected 36 pairs of organic (*p*-type) and inorganic (*n*-type) TE legs together. To prepare the *p*-type legs, a *p*-type polymer film was generated by doping poly(3,4-ethylenedioxythiophene) (PEDOT) in tosylate. Then, the film was cut into smaller area films ($1.8 \times 0.2 \text{ cm}^2$) to be individually rolled up in an elliptical shape. For the *n*-type legs, the Bi_2Te_3 -based powder was ingot-shaped with the dimensions of $2 \text{ mm} \times 2 \text{ mm} \times 0.2 \text{ mm}$. In accordance with the dimensions of the *n*-type legs, the polymer films were rolled up with a 4:1 ratio in the horizontal diameter (0.8 cm) against the vertical diameter (0.2 cm). Preparing the FPCB, a flexible polyimide film was coated with a gold sheet in a specific pattern. After fabricating the 36 thermocouples onto the FPCB, they were soldered to the gold sheet from the bottom and wired by a polytetrafluoroethylene coated wire from the top. The results showed that when the TEG was worn on the wrist, it generated an output voltage of 10.6 mV. Table 7 illustrates the summary of the reviewed ingot-shaped thermocouple.

Table 7: Summary of the recently developed wearable TEGs comprising the ingot-shaped thermocouples.

<i>P</i> -type	<i>N</i> -type	Couple Number	Electrode	Packaging	ΔT (°C)	Output voltage/power	Ref
<i>Inorganic</i>							
Bi_2Te_3	Bi_2Te_3	25	Copper	Rigid ceramic substrates	18	6 $\mu\text{W}/\text{cm}^2$	[243]
$\text{Bi}_{0.5}\text{Sb}_{1.5}\text{Te}_3$	$\text{Bi}_2\text{Te}_{2.8}\text{Se}_{0.2}$	47	Copper	FPCB	14	3.5 $\mu\text{W}/\text{cm}^2$	[247]
$\text{Bi}_{0.5}\text{Sb}_{1.5}\text{Te}_3$	$\text{Bi}_2\text{Te}_{2.7}\text{Se}_{0.3}$	20	Copper	Flexible holder (Bakelite)	20	2 $\mu\text{W}/\text{cm}^2$	[248]
Sb_2Te_3	Bi_2Te_3	12	Silver foils	Silk fabric	35	4.7×10^{-4} $\mu\text{W}/\text{cm}^2$	[249]
$\text{Bi}_{0.5}\text{Sb}_{1.5}\text{Te}_3$	$\text{Bi}_2\text{Se}_{0.5}\text{Te}_{2.5}$	24	Copper	FPCB	35	4.75 $\mu\text{W}/\text{cm}^2$	[252]
$\text{Bi}_{0.3}\text{Sb}_{1.7}\text{Te}_3$	$\text{Bi}_2\text{Sb}_{0.3}\text{Te}_{2.7}$	72	Copper	Flexible polymer	8.9	2.5 $\mu\text{W}/\text{cm}^2$	[258]
$\text{Bi}_{0.5}\text{Sb}_{1.5}\text{Te}_3$	$\text{Bi}_2\text{Se}_{0.3}\text{Te}_{2.7}$	32	EGaIn	PDMS	13	1 $\mu\text{W}/\text{cm}^2$	[259]
$\text{Bi}_{0.5}\text{Sb}_{1.5}\text{Te}_3$	$\text{Bi}_2\text{Se}_{0.5}\text{Te}_{2.5}$	52	Copper	FPCB + PDMS	18	3.9 $\mu\text{W}/\text{cm}^2$	[260]
Bi_2Te_3	Bi_2Te_3	47	Copper	PDMS sponge	8	130 $\mu\text{W}/\text{cm}^2$	[262]
$\text{Bi}_{0.5}\text{Sb}_{1.5}\text{Te}_3$	$\text{Bi}_2\text{Te}_{2.7}\text{Se}_{0.3}$	24	Copper	Flexible polymer	10	4.5 $\mu\text{W}/\text{cm}^2$	[263]
Bi_2Te_3	Bi_2Te_3	18	Silver paste and Copper	FPCB + PDMS	12	3 $\mu\text{W}/\text{cm}^2$	[264]
$(0.25\text{Bi},0.75\text{Sb})_2$ $(0.95\text{Te},0.05\text{Se})_3$	$(0.98\text{Bi},0.02\text{Sb})_2$ $(0.9\text{Te},0.1\text{Se})_3$	12	Silver thread	Polyester fabric	32.9	1×10^{-5} $\mu\text{W}/\text{cm}^2$	[265]
Bi_2Te_3	Bi_2Te_3	6	Gold-coated copper	Rigid ceramic substrates	2.5	34 $\mu\text{W}/\text{cm}^2$	[266]
Bi_2Te_3	Bi_2Te_3	256	Copper	Rigid ceramic substrates and Thermal Insulator	10	28.5 $\mu\text{W}/\text{cm}^2$	[267]
Bi_2Te_3	Bi_2Te_3	8	Gallium-based liquid alloy	Flexible polymer	20	40.6 $\mu\text{W}/\text{cm}^2$	[268]
$\text{Bi}_{0.5}\text{Sb}_{1.5}\text{Te}_3$	$\text{Bi}_2\text{Se}_{0.3}\text{Te}_{2.7}$	32	EGaIn	PDMS	11	5 $\mu\text{W}/\text{cm}^2$	[269]
Bi_2Te_3	Bi_2Te_3	220	Silver-nanowires	PDMS	10	6.96 $\mu\text{W}/\text{cm}^2$	[270]
Bi_2Te_3	Bi_2Te_3	50	Copper	Flexible polymer	3	20 $\mu\text{W}/\text{cm}^2$	[271]
$\text{Bi}_{0.5}\text{Sb}_{1.5}\text{Te}_3$	$\text{Bi}_2\text{Se}_{0.5}\text{Te}_{2.5}$	52	Copper	FPCB + PDMS	3.5	20 $\mu\text{W}/\text{cm}^2$	[272]
$\text{Bi}_{0.5}\text{Sb}_{1.5}\text{Te}_3$	$\text{Bi}_2\text{Te}_{2.7}\text{Se}_{0.3}$	15	Soldered to FPCB	Flexible holder (Bakelite)	9.3	5.6 $\mu\text{W}/\text{cm}^2$	[273]
$\text{Bi}_{0.5}\text{Sb}_{1.5}\text{Te}_3$	$\text{Bi}_2\text{Te}_{2.7}\text{Se}_{0.3}$	15	Soldered to FPCB from	PDMS and resin holder	8	8.30 $\mu\text{W}/\text{cm}^2$	[274]

			bottom and connected with EGaIn from top				
$\text{Bi}_{0.5}\text{Sb}_{1.5}\text{Te}_3$	$\text{Bi}_2\text{Te}_{2.7}\text{Se}_{0.3}$	20	Copper	Flexible holder (Bakelite)	12.5	6.97 $\mu\text{W}/\text{cm}^2$	[275]
$\text{Bi}_{0.5}\text{Sb}_{1.5}\text{Te}_3$	$\text{Bi}_2\text{Te}_{2.7}\text{Se}_{0.3}$	170	Copper	Flexible polymer	12	13 $\mu\text{W}/\text{cm}^2$	[276]
<i>Hybrid</i>							
Bi: CNTs: PDMS	Te :CNTs: PDMS	50	Aluminium	PDMS	293	80 $\mu\text{W}/\text{cm}^2$	[251]
PEDOT doped in tosylate	Bi_2Te_3	36	Gold and Flexible wire	Polyimide film	36	10.6 mV	[261]

5.5 Film-shaped thermocouples

5.5.1 Inorganic TE materials

As mentioned before, the flexible wearable TEGs possess some superiority to the rigid ones, such as being lightweight and conformed to the arbitrary surfaces of the body. Accordingly, as reviewed in [Section 5.4](#), a flexible wearable TEG could be fabricated by encapsulating the ingot-shaped thermocouples in a flexible polymeric substrate. To further increase the flexibility of the wearable TEGs, the ingot-shaped thermocouples could be replaced by the film-shaped ones. To specify, the TE materials can be printed onto flexible substrates, such as plastic films and fabrics. Accordingly, the most common printing techniques to prepare the TE films are dispenser printing, inkjet printing, screen printing, roll to roll printing, and aerosol jet printing [\[277\]](#).

For example, Varghese et al. [\[278\]](#) screen printed an ink-based $\text{Bi}_2\text{Te}_{2.8}\text{Se}_{0.2}$ onto some flexible polyimide substrates. To clarify, the authors initially prepared the $\text{Bi}_2\text{Te}_{2.8}\text{Se}_{0.2}$ nanocrystals using the microwave-stimulated wet-chemical technique. Next, the *n*-type TE ink was screen printed onto the flexible polyimide substrates, generating 5 film-based TE legs each with the dimensions of $10\text{ mm} \times 2\text{ mm} \times 0.01\text{ mm}$. To remove any solvent and binder, the printed films were dried on a $200\text{ }^\circ\text{C}$ hot plate followed by being consolidated with cold compaction. Finally, the films were sintered in vacuum at $430\text{ }^\circ\text{C}$ for 45 min and then electrically connected together with thin copper foils as electrodes, see [Fig.46](#). The results showed that $0.5\text{mW}/\text{cm}^2$ was the greatest obtained output power at a temperature difference of $293\text{ }^\circ\text{C}$.

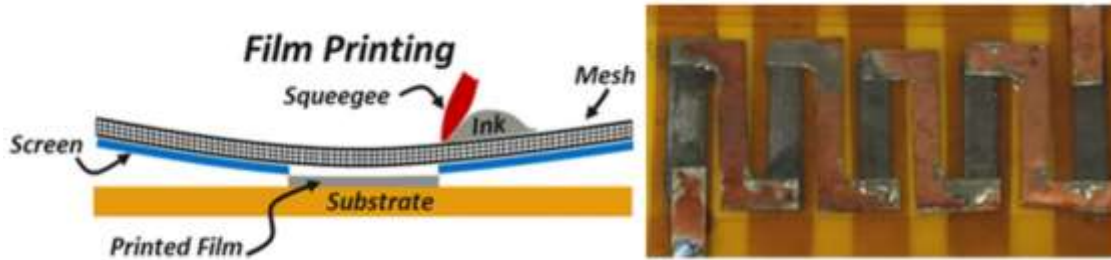


Fig. 46: The fabrication process of the flexible TE films [278].

Wen et al. [279] developed a complementary double-chain thermocouples by screen printing *n*-type $\text{Bi}_2\text{Te}_{2.7}\text{Se}_{0.3}$ and *p*-type Sb_2Te_3 pastes onto a polyimide film. In particular, the *p*- and *n*-type TE pastes were alternately screen printed onto the underlying substrate in two separate complementary chains without an interval, see Fig.47. While each individual TE chain possessed 5 thermocouples, the gap between the two complementary chains was filled by silk fibroin solution. The results demonstrated that one complementary double-chain thermocouple comprising 10 thermocouples achieved the highest output power of $0.095 \mu\text{W}/\text{cm}^2$ at ΔT of $20 \text{ }^\circ\text{C}$.

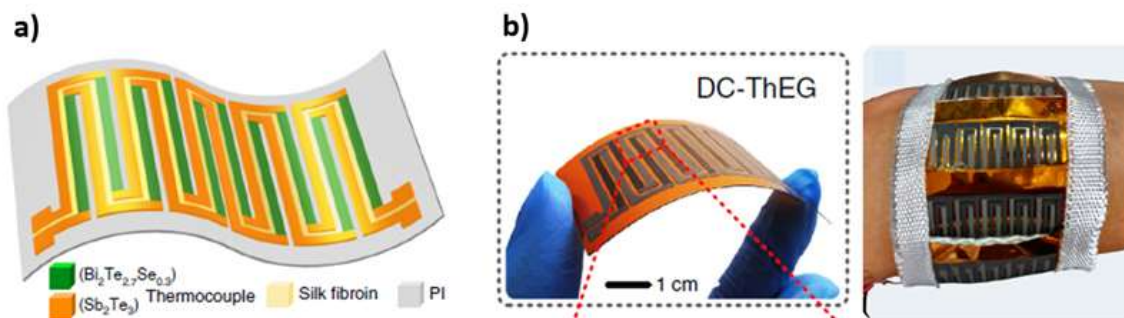


Fig. 47: a) Schematic illustration; and b) the photo of the fabricated TEG [279].

Karthikeyan et al. [280] employed vapour deposition to deposit *p*-type Tin telluride (SnTe) and *n*-type Lead Telluride (PbTe) thin films onto a flexible polyimide substrate. Then, the 32 pairs of the TE legs were interconnected by the aluminium films as the electrodes, as Fig.48 shows. The results showed that the TEG generated $8.4 \text{ mW}/\text{cm}^2$ at ΔT of $120 \text{ }^\circ\text{C}$.

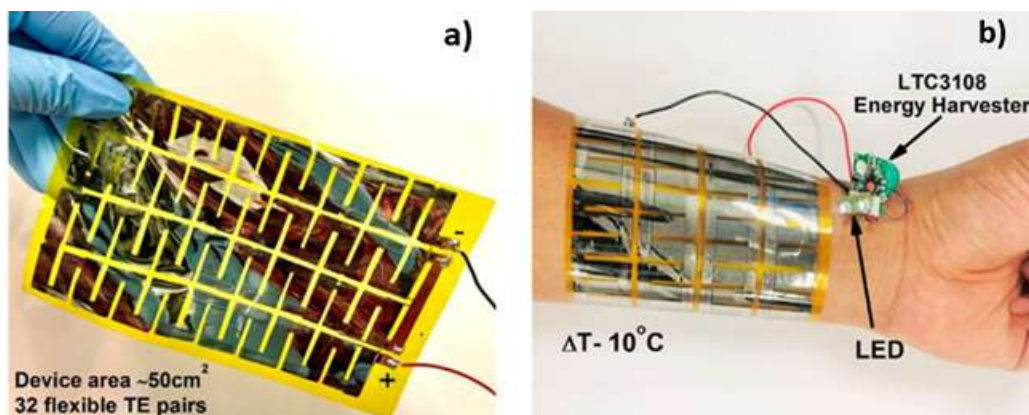


Fig. 48: a) Photo of the fabricated flexible SnTe–PbTe based TEG; b) Photo of the TEG placed on the arm as the power source of an LED [280].

Ren et al. [281] used thermal evaporation to fabricate 14 TE chips comprising p -($\text{Bi}_{0.5}\text{Sb}_{1.5}\text{Te}_3$) and n -($\text{Bi}_2\text{Te}_{2.8}\text{Se}_{0.3}$) type thin films. To generate each TE chip, 4 pairs of p - and n -type films were alternately deposited onto a polyimide film using thermal evaporation. Then, the TE films were connected together with Au-Ge electrodes. To incorporate the 14 modular TE chips into a whole, 14 slots were laser cut on a polyimide substrate as the underlying substrate. Accordingly, the slots were electrically connected together by alternately screen-printing the liquid metal as the electrodes between the two ends of the slots. After that, the chips were inserted into the slots and stiffly bonded with the polyimide substrate by dropping a small amount of the polyimide solution at their junctions. The results proved that at ΔT of 93 °C, the fabricated TEG with 56 thermocouples generated the highest output power of 18.625 $\mu\text{W}/\text{cm}^2$.

5.5.2 Organic TE materials

In spite of the high energy conversion efficiency of the inorganic TE materials, they lack enduring a wide range of dynamic motions. This is mainly attributed to their inadequate elastic limit, tensile strength, and hardness [282]. Accordingly, the organic TE materials show superiority to the inorganic ones concerning the fabrication of the film-shaped TE legs. Using the roll to roll system, Zhang et al. [283] printed the nitrogen-doped graphene (n -type legs) and PEDOT: PSS (p -type legs) inks onto a flexible plastic substrate, as Fig.49 illustrates. The inks were printed onto the substrate with tuneable rotation pressure and speed. Then, the substrate was treated by UV irradiation in the open air for 1 hr followed by being subjected to oxygen plasma treatment for an hour. The authors reported $\sim 0.024 \mu\text{W}/\text{cm}^2$ as the maximum output power at ΔT of 10 °C.

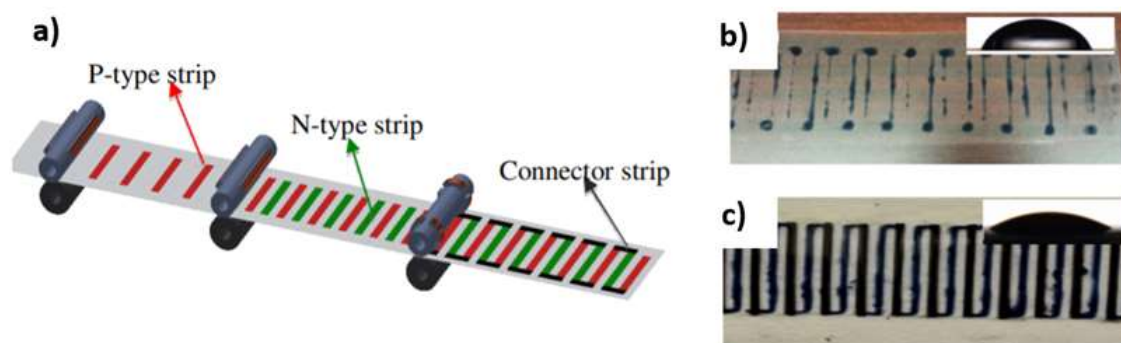


Fig. 49: a) Illustration of roll to roll printing of the flexible TE devices; b) UV treated plastic substrate; c) Plasma-treated plastic substrate [283].

Zhang et al. [284] combined the roll to roll and the dispenser printing techniques together to develop a film-shaped TEG. Accordingly, the authors used SWCNT/PEDOT: PSS composites and SWCNTs/ triphenylphosphine for the *p*- and *n*-type legs, respectively. To generate the electrodes each with 2cm length, the authors used the roll to roll printing to deposit the PEDOT: PSS ink with 2cm intervals onto a polyimide substrate. Then, a pre-prepared PDMS film was pierced with 20 holes with 2cm intervals in accordance with the length and the intervals of the electrodes. Next, the pierced PDMS film was put on the PEDOT: PSS printed substrate, whilst its holes were aligned with the two ends of the electrodes. After that, the holes were alternately filled with the *p*- and *n*-type TE materials followed by being dried on a hot plate. Finally, another PEDOT: PSS printed polyimide substrate covered the holes from the top to connect the legs electrically together, see Fig.50. The results revealed that the fabricated TEG with 10 thermocouples obtained the maximum power density of $0.05 \mu\text{W}/\text{cm}^2$ at ΔT of 20°C .

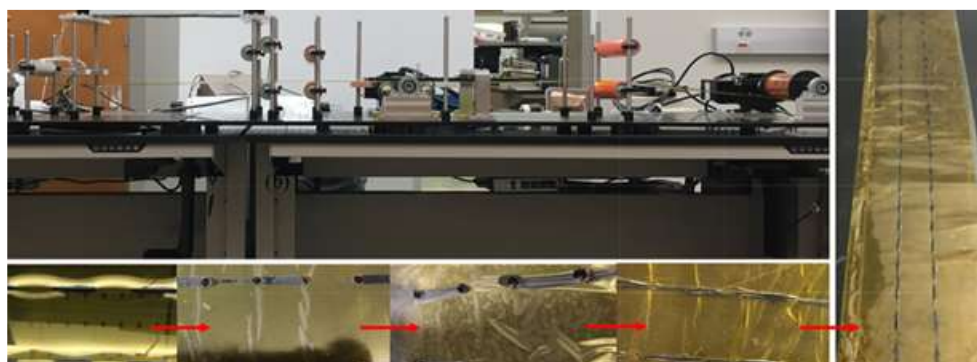


Fig. 50: Demonstration of the applied roll to roll and inject printing techniques to fabricate the film-shaped TEG [284].

Park et al. [285] automate printed the TE inks onto a flexible cable to develop a springy-shaped wearable TEG. To prepare the *p*- and *n*-type inks, the authors doped separately the CNT ink with poly (acrylic acid) (PAA) and poly(ethylenimine) (PEI), respectively. Then, the PAA doped CNT ink was printed in a strip pattern onto one half of a 3mm diameter polyurethane cable, performing as the underlying substrate, see Fig.51. After that, the printed *p*-type ink was dried at 85 °C in the vacuum for 1hr. Following the same pattern, the *n*-type ink was printed onto the other half of the cable and dried overnight under the same condition. Notably, the TE inks were printed onto the cable with 1mm width and 2mm intervals from each other. Finally, the cured *p*- and *n*-type inks were electrically connected together via the dispenser printing of the silver pastes as the electrodes. The results showed that the generated bracelet-shaped TEG comprising 60 thermocouples obtained the maximum output power of 0.2 μW and 1.95 μW at ΔT of 10 °C and 30 °C, respectively.



Fig. 51: Photograph of the devices with 5, 10, 15 and 30 PN pairs. Demonstration of the TE bracelet wrapped around the wrist [285].

As Fig.52 depicts, Zeng et al. [286] developed a 3D grid substrate and coated it with an organic TE material. To clarify, the authors 3D printed the PDMS grid as the underling structure onto a Cu/Ni coated conducting fabric as the bottom electrode. Using the radio frequency sputtering, the PDMS-based grid (10mm×10mm × 2 mm) was coated with a very thin copper film. Then, the coated grid was immersed into the graphene oxide dispersion as the *p*-type TE material. To coat the grid evenly with the TE material, the immersed substrate was coated by the reduced graphene oxide (rGO) Nano sheets. After that, the top side of the developed TEG was covered with another conducting fabric as the upper electrode. The results showed that at ΔT of 50 °C, the fabricated TEG generated the output voltage of 57.33 mV/g. Furthermore, integrating 7 units of the developed TEG in the form of a wristband generated the maximum power density of 4.19 μW/g at ΔT of 15°C.



Fig. 52: a) The schematic of the 3D printed PDMS grid; b) Photo of the fabricated grid-based TEG; and c) Schematic design of integrating 7 units of the developed grid-based TEGs together [286].

5.5.3 Hybrid TE materials

As mentioned before, the hybrid TE materials are a promising candidate to combine the advantages of both the inorganic and organic types. For example, Bae et al. [287] prepared a *p*-type hybrid material called Te-PEDOT: PSS to fabricate a film-shaped TEG. Initially, the Te-PEDOT: PSS hybrid composite was spin-coated onto a 15 cm² area PET (30mm × 10mm) substrate to generate 32 *p*-type legs, see Fig.53. Then, the electrical conductivity of the Te-PEDOT: PSS composite was improved by H₂SO₄ chemical treatment of the composite. Finally, the legs were connected together with conductive silver paste as electrodes. The results showed that 0.7 nW/cm² was the maximum output power delivered from the fabricated TEG at ΔT of 10 °C.

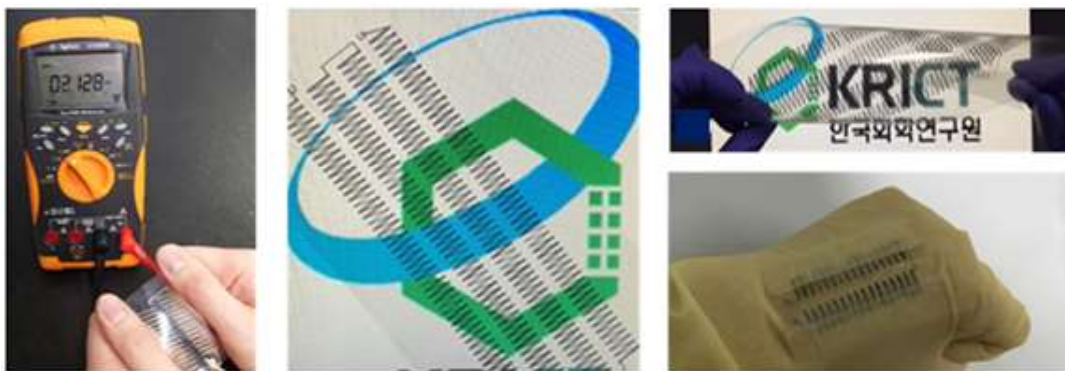


Fig. 53: Images of the flexible and twistable TE generator comprising 240 legs arranged in four rows [287].

Instead of the chemical treatment, Bae et al. [288] used additives in another study to enhance the electrical conductivity of the Te-PEDOT: PSS hybrid composites. Accordingly, the two considered additives were graphene nanoparticles (GNPs) and single-walled CNTs (SSWNTs). Notably, the

additives were added to the Te-PEDOT: PSS composites individually concerning different weight percentages. Then, the optimized Te-PEDOT: PSS samples were spray-printed onto a glass substrate separately to fabricate 14 *p*-type TE legs. Finally, the legs were electrically connected together with silver paste as electrodes. The results showed obtaining the maximum output powers of 1.7 nW/cm² and 31.5 nW/cm² with 8 wt% GNPs and 3wt% SSWNTs addition, respectively. To generate a highly flexible *p*-type composite film, Lu et al. [289] coated polycrystal Cu_xSe_y (PC-Cu_xSe_y) nanowires with PEDOT: PSS. Then, the PEDOT: PSS coated PC-Cu_xSe_y film was cut into 25 legs (25 mm × 5 mm) followed by pasting them with ~5 mm intervals onto a polyimide substrate, see Fig.54. Next, the legs were electrically connected together using silver paste as the electrodes. The results showed that the highest achieved output voltage at ΔT of 6.5 °C was 4.5 mV.

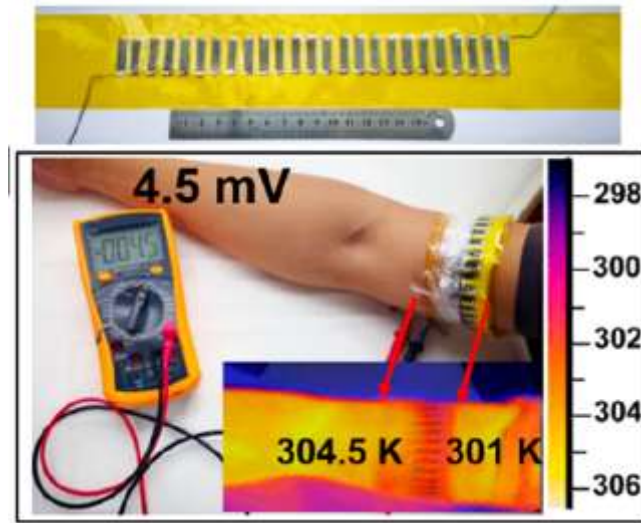


Fig. 54: A photo of the developed TEG and the 4.5 mV voltage created at 3.5 °C temperature difference [289].

Lu et al. [290] prepared a highly flexible *n*-type PEDOT/Ag₂Se/CuAgSe film and cut it into 11 TE legs (25 mm × 5 mm). The legs were pasted with roughly 5 mm intervals onto a polyimide substrate followed by masking the two ends of each leg with a layer of gold evaporation as the junction between the legs and the upcoming electrodes, see Fig.55. After that, the opposite ends (the gold evaporation layers) of the two alternate legs were connected together by painting silver adhesive between them. The authors reported that at ΔT of 36 °C, the highest obtained output power was approximately 840 μW/cm².

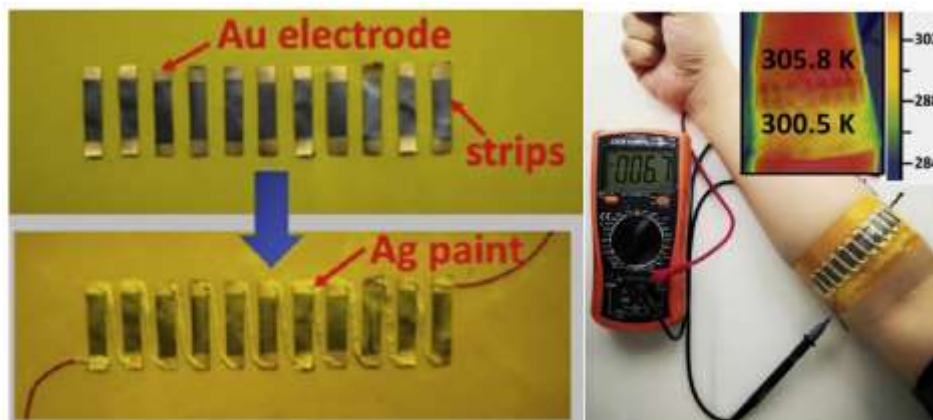


Fig. 55: Photos of the fabricated TEG and its open-circuit voltage after being placed on the arm [290].

Zhao et al. [291] used Cellulose nanofiber (CNF) to fabricate the 6 pairs of CNF/ $\text{Bi}_{0.5}\text{Sb}_{1.5}\text{Te}_3$ (*p*-type) and CNF/ $\text{Bi}_2\text{Se}_{0.3}\text{Te}_{2.7}$ (*n*-type) films. Precisely, the 6 circular film-based thermocouples each with the radius of 5mm were electrically connected together using a silver wire. To reduce the contact resistance between the TE films and the silver wire, a silver paste was deposited at their junctions. Ultimately, a carbon conductive tape was stuck to the junctions to further stuck the wire to the films, see Fig.56. While the TE legs were split in half between the two sides of the arm, the results showed that 6.3mV was the highest output voltage generated at ΔT of 35 °C. Table 8 illustrates the summary of the reviewed film-shaped thermocouples.

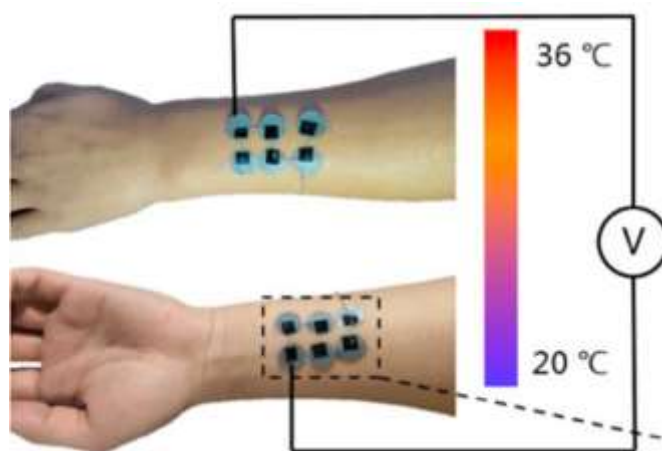


Fig. 56: Photo of the fabricated TEG and its mounting position on the human body [291].

Table 8: Summary of the recently developed wearable TEGs comprising film-shaped thermocouples.

<i>P</i> -type	<i>N</i> -type	Couple Number	Electrode	Substrate	ΔT (°C)	Output voltage/power	Ref
<i>Inorganic</i>							
n/a	Bi ₂ Te _{2.8} Se _{0.2}	5	Copper foils	Polyimide substrate	20	500 $\mu\text{W}/\text{cm}^2$	[278]
Sb ₂ Te ₃	Bi ₂ Te _{2.7} Se _{0.3}	10	n/a	Polyimide substrate	20	0.095 $\mu\text{W}/\text{cm}^2$	[279]
SnTe	PbTe	32	Aluminium films	Polyimide substrate	120	8.5 mW/cm^2	[280]
Bi _{0.5} Sb _{1.5} Te ₃	Bi ₂ Te _{2.8} Se _{0.3}	56	Au-Ge	Polyimide substrate	93	18.62 $\mu\text{W}/\text{cm}^2$	[281]
Bi _{0.5} Sb _{1.5} Te ₃	Bi ₂ Te ₃	5	EGaIn	Polyimide substrate	7	14.1 nW	[292]
Au-MoS ₂ film	n/a	5	Metal yarn	Fabric	5	2.5mV	[293]
Sb ₂ Te ₃	Bi _{1.8} Te _{3.2}	8	SbTe	Polyimide substrate	20	0.016 $\mu\text{W}/\text{cm}^2$	[294]
<i>Organic</i>							
SWNTs/ PANI	n/a	4	Silver paste	Glass substrate	30	0.012 $\mu\text{W}/\text{cm}^2$	[187]
CNT film	polyethylene terephthalate (PET)	3	n/a	Glass substrate	19	0.06 $\mu\text{W}/\text{cm}^2$	[195]
PEDOT: PSS	Nitrogen-doped graphene	18	PEDOT: PSS	Plastic substrate	10	0.024 $\mu\text{W}/\text{cm}^2$	[283]
SWCNT/PEDOT:PSS	SWCNTs/ triphenylphosphine	10	PEDOT: PSS	Polyimide substrate+ PDMS film	20	0.05 $\mu\text{W}/\text{cm}^2$	[284]
poly (acrylic acid) doped CNT	poly(ethylenimine) doped CNT	60	Silver paste	Flexible cable	30	1.95 μW	[285]
Graphene oxide	n/a	7	Cu/Ni coated conducting fabric	PDMS grid	15	4.19 $\mu\text{W}/\text{g}$	[286]
PEDOT: PSS: DMSO	Poly[Na(NiETT)]	16	Silicone-based silver ink	Polyester knitted fabric	3	3mV	[295]
n/a	poly[Kx(Ni-ethylenetetrathiolate)]	108	Gold	PET substrate	12	577.8 $\mu\text{W}/\text{cm}^2$	[296]
PEDOT: PSS	n/a	61	Silver paste	Glass substrate	90	0.025 $\mu\text{W}/\text{cm}^2$	[297]
<i>Hybrid</i>							
Te–Bi ₂ Te ₃ /PEDOT:PSS	n/a	6	Silver paste	Glass substrate	10	1.54 mV	[209]
BiTe /PEDOT:PSS	n/a	5	Silver paint	Polyimide substrate	47.2	16.9 nW	[212]
Te-PEDOT:PSS	n/a	32	Silver paste	PET substrate	10	7e-4 $\mu\text{W}/\text{cm}^2$	[287]
SSWNTs-Te-PEDOT: PSS	n/a	14	Silver paste	Glass substrate	20	0.031 $\mu\text{W}/\text{cm}^2$	[288]
PEDOT: PSS coated PC-Cu _x Se _y film	n/a	25	Silver paste	Polyimide substrate	6.5	4.5 mV	[289]

n/a	PEDOT/Ag ₂ Se/CuAgSe	11	Gold	Polyimide substrate	36	840 μW/cm ²	[290]
CNF/Bi _{0.5} Sb _{1.5} Te ₃	CNF/Bi ₂ Se _{0.3} Te _{2.7}	6	Silver wire	n/a	35	6.3mV	[291]
FeCl ₃ doped CNT	Polyethylenimine doped CNT	9	CNT	PDMS	7	3.4mV	[298]
PEDOT	Bi ₂ Te ₃	5	Gold	Adhesive film substrate	12	0.003 μW/cm ²	[299]
SWCNTs/Sb ₂ Te ₃ film	RGO/Bi ₂ Te ₃ film	10	Silver paste	Polyimide substrate	70	0.7 μW/cm ²	[300]
Bi ₂ Te ₃ /PVDF	Bi ₂ Se ₃ /PVDF	-	Silver paste	Helical polymer substrate	16	8.9mV	[301]
HP-PC-3C1S film	PEDOT/Ag ₂ Se/CuAgSe film	10	Gold	Polyimide substrate	44	0.03 μW/cm ²	[302]

5.6 Yarn-shaped thermocouples

5.6.1 Inorganic TE materials

As reviewed in [Section 5.5](#), the output power of the film-shaped TE legs is considerably lower than the ingot-shaped ones. This is attributed to the higher temperature gradient between the hot and cold junctions of the cross-plane legs than the in-plane ones. Attempting to benefit from the conversion efficiency of the former and the flexibility of the latter, yarn-shaped TE legs have been generated. For example, Lee et al. [303] twisted the thermoelectric-coated nanofibers into yarns to prepare three different TE textiles. To generate the thermoelectric-coated nanofibers, Bi₂Te₃ (*n*-type) and Sb₂Te₃ (*p*-type) were separately deposited onto the highly aligned sheets of electrospun polyacrylonitrile nanofibers using the radio-frequency-magnetron sputtering technique. Then, the thermoelectric-coated nanofibers were separately twisted into *n*- and *p*-type yarns. In addition, the authors developed another TE yarn called the tiger yarn by alternately sputtering the strips of Sb₂Te₃ and Bi₂Te₃ on both sides of the electrospun polyacrylonitrile nanofiber sheet. Connecting the TE strips electrically together, the narrow strips of gold were sputtered onto the gaps between the TE strips. After preparing the yarns, three different weaving patterns, such as zigzag weave, garter-stitch weave, and plain weave, were determined to knit three separate TE textiles. The results demonstrated that the approximate output power of the three weaving patterns were respectively 0.02 W/m², 0.01 W/m², and 0.08 W/m² at ΔT of 20 °C.

Preparing the *p*-type multicore single-crystal SnSe fibres, Zhang et al. [304] clad several single-crystal SnSe rods separately with borosilicate glass and borosilicate glass rods. Then, the 6 obtained TE fibres were weaved into a shirt followed by depositing silver films onto their ends. Using copper wires as electrodes, the fibre legs were electrically connected together. The results illustrated that the TE shirt obtained the highest output voltage of 30 mV at ΔT of 10 °C.

5.6.2 Organic TE materials

Wu and Hu [305] introduced a fibre-shaped TEG by coating the commercial polyester yarns with organic TE composites. For the *p*- and *n*-type TE composites, the authors used the NWPU/PEDOT: PSS/multi-walled carbon nanotube (MWCNT) and the NWPU/nitrogen doped multi-walled carbon nanotube (N-MWCNT), respectively. Then, the TE yarns were embroidered into the lock-nit surface of a spacer fabric, while the *p*- and *n*-type legs were arranged alternatively. Finally, every adjacent *p*- and *n*-type yarns were electrically connected together using silver paint, generating 10 thermocouples in total. Based on the results, the maximum output power of the TE fabric with the dimensions of 6 cm \times 6 cm \times 0.7 cm was 0.21 nW/cm² at ΔT of 66 °C. Lan et al. [306] used the common cotton and the CNT fibres to develop the *p*- and *n*-type fibres, respectively. To prepare the *p*-type fibres, the cotton fibres were treated with absolute ethanol, deionized water, and DMSO followed by being soaked five times in PEDOT: PSS for 24 hrs. To obtain the *n*-type fibres, the *p*-type CNT fibres were treated with PEI. As Fig.57 shows, the silver paste was used as the electrodes to electrically connect the 8 pairs of the TE fibres together. The results revealed that the maximum power density of the fibre TEG was 10 μ W at ΔT of 10 °C.

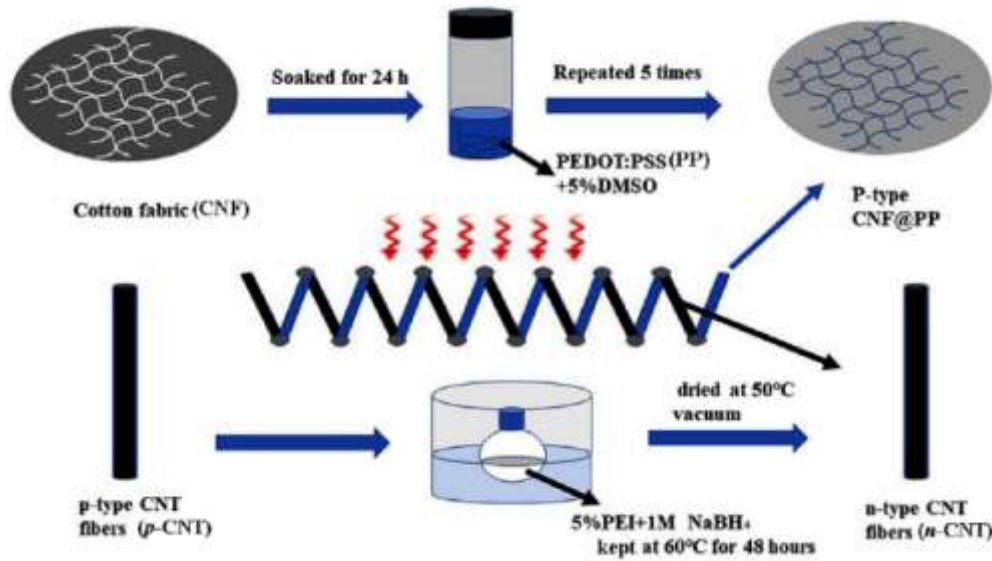


Fig. 57: The schematic of the fabrication for the CNF@PP (*p*-type) and the PEI treated CNT (*n*-type) fibres [306].

To prepare the *p*- and *n*-type threads of a wearable textile, Lund et al. [307] used a PEDOT:PSS coated silk thread and a silver-plated polyamide thread, respectively. To prepare the *p*-type thread, a dye bath comprising aqueous PEDOT: PSS dispersion and ethylene glycol was prepared, and 100m of a silk sewing thread was passed through it. Curing the *p*-type thread, it was dried and treated with dimethyl sulfoxide for 1:20 hrs followed by being dried again at 100 °C with a heat gun. Next, the TE threads were stitched through 9 layers of a felted wool fabric followed by being electrically connected together with the silver paste as the electrodes, see Fig.58. To cure the paste, the TE textile was placed in a 100 °C oven for 10 min. The results revealed that $0.04 \mu\text{W}/\text{cm}^2$ was the maximum output power of the TEG at ΔT of 65 °C.



Fig. 58: Photographs of the embroidered textile thermopile [307].

Ryan et al. [308] fabricated the *n*- and *p*-type yarns separately and sewed them onto a fabric to generate a TE textile. To produce the *n*-type yarns, the commercial PET sewing threads were sequentially coated with poly(N-vinylpyrrolidone), MWNTs, and polystyrene-*b*-polyisoprene-*b*-polystyrene block copolymer as the adhesion layer, the conducting layer, and the protection layer, respectively. To prepare the *p*-type yarns, the commercial silk yarns were dyed by being submerged in poly(3,4-ethylenedioxythiophene): poly(styrenesulfonate) (PEDOT: PSS) solution. Then, as Fig.59 depicts, the 38 pairs of the TE yarns (each was 4cm long) were alternately sewn onto a fabric followed by being electrically connected together with a conducting carbon-based paste. The results depicted that cooling and heating the opposite edges of the TE textile at the same time resulted in the maximum output power of 7.1 nW at ΔT of 80 °C.

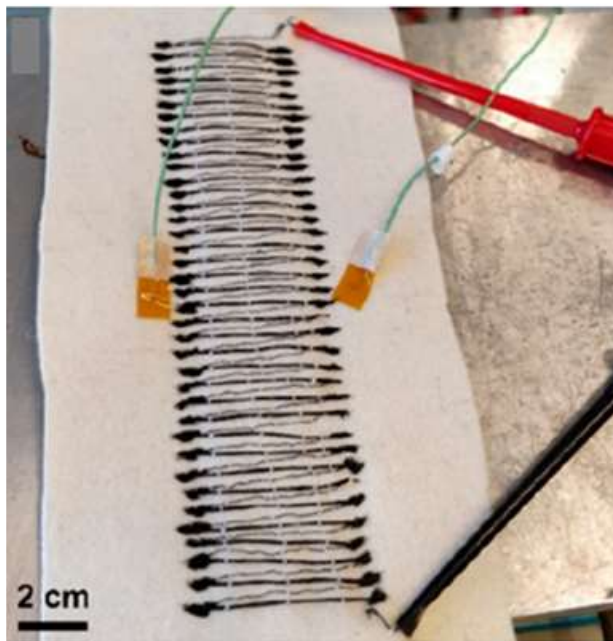


Fig. 59: All-organic in-plane embroidered textile TE device with 38 n/p elements [308].

Sun et al. [309] coated carbon nanotube fibres (CNTFs) with active TE materials to develop a TE fabric. Accordingly, each CNTF was obtained by twisting four CNT films together. To coat the as-prepared CNTFs with active TE materials, each CNTF was divided into three segments alternately, including *p*-hybridized, electrode (un-doped CNTF), and *n*-doped segments. Fabricating the *p*-hybridized segments, the CNTFs were immersed in a commercial poly(3,4-ethylenedioxythiophene): poly(styrenesulfonate) (PEDOT: PSS) solution. Next, both the *p*-hybridized and the un-doped (electrode) segments were mask shaded with polypropylene to

electrospray the *n*-type oleamine solution onto the CNTFs. To avoid any short circuit, ultimately the coated CNTFs were wrapped with acrylic fibres, see Fig.60. To examine the TE performance of the coated fibres, the authors interlocked 15 thermocouples together in two different patterns, including warp knitting and weft knitting. The results showed that at ΔT of 44 °C, the highest output power was 7 $\mu\text{W}/\text{cm}^2$ that was achieved by the warp knitting approach.

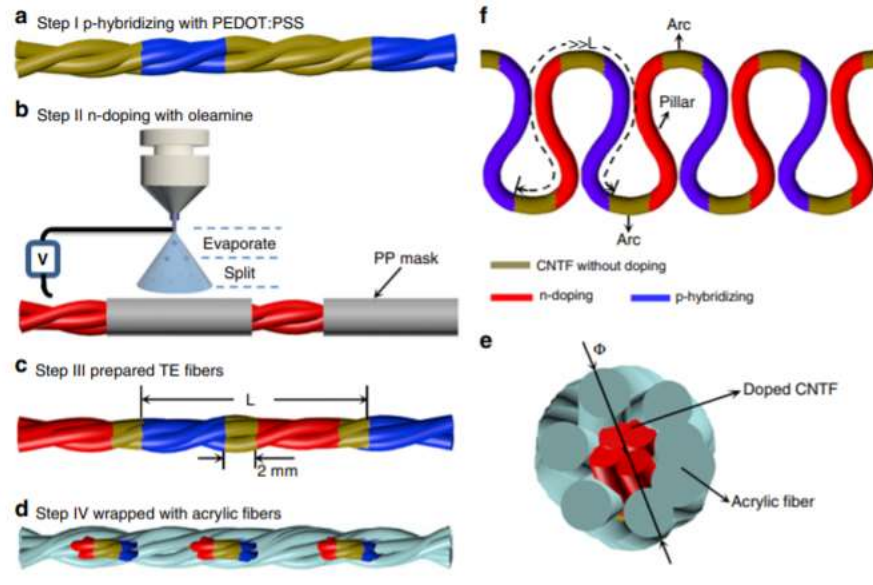


Fig. 60: The schematic of the fabrication procedure of the TE fiber [309].

5.6.3 Hybrid TE materials

To develop a hybrid TE textile, Xu et al. [310] used the wet-spinning process to generate the *p*-type PEDOT: PSS/ Te fibres. Accordingly, the tellurium nanowires were dispersed into the deionized water followed by adding the PEG and PEDOT: PSS pellets to the water, respectively. After collecting the *p*-type PEDOT: PSS/Te fibres, its surface was periodically brushed at 0.65 cm intervals by the conductive silver paste as the electrodes, see Fig.61. Finally, the as-prepared TE fibre was sewn onto a polymer textile and worn on the arm. The authors demonstrated that the highest power density of the developed TEG was 197.9 nW at ΔT of 41 °C.

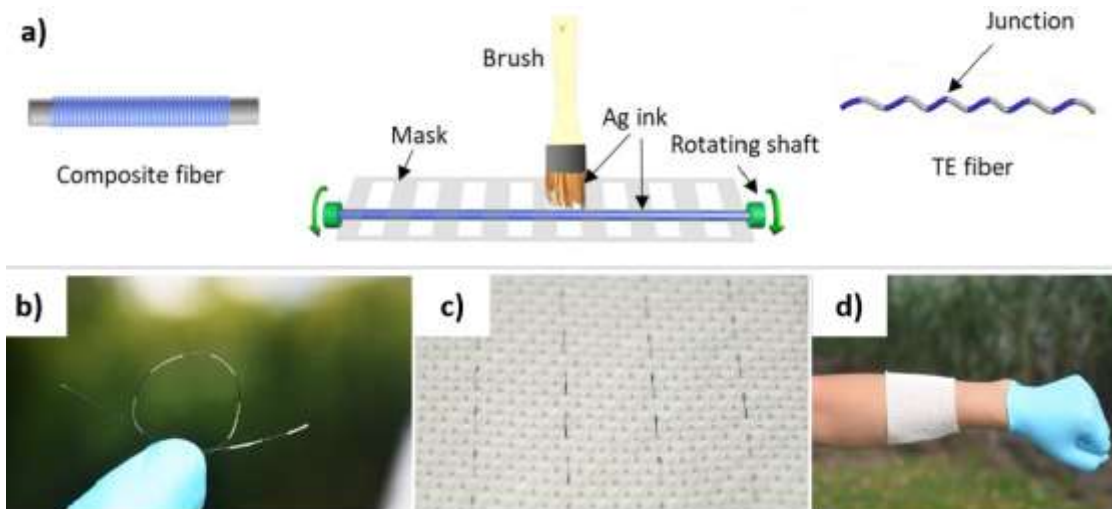


Fig. 61: a) Schematic illustration of the fabrication processes of the TE fibers; b) photos of the TE fiber; c) the TE fabric; and d) the application demo [310].

Choi et al. [311] changed the carbon nanotube yarn (CNTY) into the integral *p-n* type TE material by using a rolling block. Accordingly, the authors wound the CNTY around a PDMS block to dope on one side of the PDMS block in the FeCl_3 ethanol solution as the *p*-type material and the other side in the polyethyleneimine ethanol as the *n*-type. Thus, the un-doped regions of the carbon nanotube yarn on the top and bottom sides of the PDMS block performed as the electrodes, as Fig.62 depicts. The results demonstrated that at ΔT of $65\text{ }^\circ\text{C}$, the output power of the TEG raised from $1.4\text{ }\mu\text{W}$ to $4\text{ }\mu\text{W}$ by increasing the number of thermocouples from 60 to 240. Table 9 illustrates the summary of the reviewed yarn-shaped thermocouples.

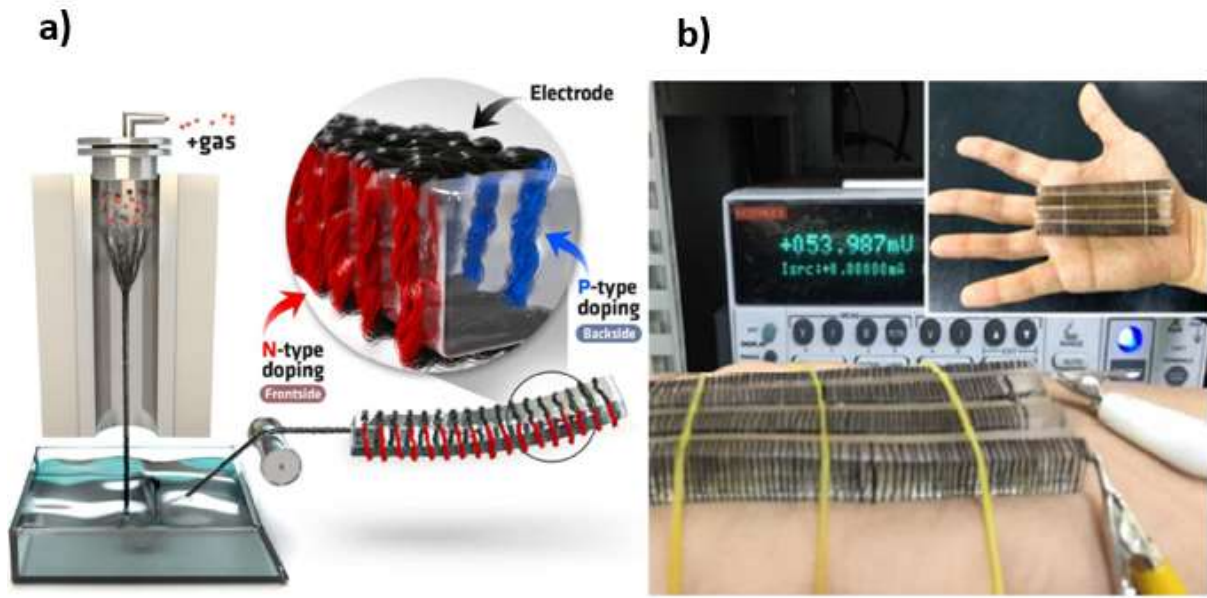


Fig. 62: a) The schematic illustration of the doping process; b) photo of the fabricated TEG [311].

Table 9: Summary of the recently developed wearable TEGs comprising the yarn-shaped thermocouples.

<i>P</i> -type	<i>N</i> -type	Couple Number	Electrode	Substrate	ΔT (°C)	Output Voltage/Power	Ref
<i>Inorganic</i>							
Sb ₂ Te ₃	Bi ₂ Te ₃	30	Gold	Knitting into a textile	20	8 μ W /cm ²	[303]
SnSe	n/a	6	Copper wire	Weaving into a fabric	10	30mV	[304]
<i>Organic</i>							
NWPU/PEDOT: PSS/ MWCNT coated polyester yarn	NWPU/ MWCNT coated polyester yarn	10	Silver paint	Embroidered into the locknit surface of a spacer fabric	66	0.21 nW/cm ²	[305]
PEDOT:PSS coated cotton fabric	Polyethylenimine treated carbon nanotube fabric	8	Silver paste	Connecting with silver paste	10	10 μ W	[306]
PEDOT:PSS coated silk thread	Silver-plated polyamide embroidery thread	8	Silver paste	Stitching through 9 layers of felted wool fabric	65	0.04 μ W/ cm ²	[307]
PEDOT: PSS dyed silk yarns	PVP- MWNTs- SIS coated PET yarns	38	Conducting carbon-based paste	Sewing into a fabric	80	7.1 nW	[308]
PEDOT:PSS doped carbon nanotube fibres	Oleamine solution sprayed carbon nanotube fibres	15	Carbon nanotube fibres	Wrapping with acrylic fibres	44	7 μ W /cm ²	[309]
Hydrazine immersed CNT/PEDOT: PSS composite fibre	PEI infiltrated CNT/PEDOT: PSS composite fibre	12	Silver paste	Sewing into PDMS substrate	10	0.015 μ W /cm ²	[312]
Graphene fibres	PEIE coated graphene fibres	20	n/a	Weaving into PDMS substrate	10	1.3 pW	[313]
P3HT coated cotton thread	Ag pasted P3HT/ cotton thread	13	n/a	Sewing into a fabric	50	1.15 μ W	[314]
CNT/PEG	1-butyl-3-methylimidazolium hexafluorophosphate doped CNT/PEG	-	Silver paste	Sewing into a felt fabric	15	0.125 nW/cm ²	[315]
PEDOT-Cl printed cotton fabric	Carbon fibres	2	Silver-coated nylon	Printing and sewing onto a commercial cotton fabric	30	0.4 nW/ cm ²	[316]
PEDOT: PSS fibres	nickel wires	5	n/a	Sewing into a fabric	3.6	0.72 mV	[317]
Nickle coated carbon fibre	Carbon fibres	105	n/a	Stitching onto	2	0.041 nW/cm ²	[318]

				polyester fabric			
PEDOT: PSS coated CNT yarn	PEI/ethanol coated CNT yarn	966	Pristine CNT yarn	Weaving into a fabric	7	0.14 $\mu\text{W}/\text{cm}^2$	[254]
Hybrid							
PEDOT: PSS coated cotton fabric	Constantan wires	5	Constantan wires	TE-strips attached to a cotton fabric using silver paint	74.3	10.63 nW/cm ²	[168]
PEDOT: PSS/tellurium nanowires	n/a	-	Silver paste	Sewing into a polymer matrix	41	197.9 nW	[310]
FeCl ₃ ethanol doped carbon nanotube yarn	Polyethyleneimine ethanol doped carbon nanotube yarn	240	Un-doped carbon nanotube yarn	Wounding around a PDMS block	65	4 μW	[311]

5.7 Summary

Based on the reviewed papers, the inorganic type is most prevalent in fabricating the ingot-shaped thermocouples, whilst the hybrid and the organic ones are merely and rarely used, respectively. This is mainly attributed to the higher conversion efficiency of the former compared with the two latter. However, to increase the flexibility of the legs at the same time, the researchers suggest replacing the ingot-shaped legs with the film-shaped ones, which could be fabricated with either of the three types of the TE materials. In spite of this, compared with the inorganic ingot-shaped legs, the inorganic film-shaped ones deliver lower power density. As a result, it is suggested to increase the conversion efficiency of the latter by fabricating the two dimensional legs in a three dimensional structure, resulting in the generation of the yarn-shaped legs. Notably, compared with the other two types of the TE materials, using the organic type is more prevalent in preparing the yarn-shaped legs. In addition, compared with the film-shaped ones, the benefit of the three dimensional structure of the yarn-shaped legs is offset by their lower contact surface with the heat source. Consequently, the ingot-, film-, and yarn-shaped legs stand first to third regarding the highest conversion efficiency. However, in accordance with the aim of this study, which is developing a sustainable heating system, it is of critical importance to study the environmental impact of the ingot-shaped legs concerning the life cycle impact of their comprising TE materials.

Chapter 6

Research Methodology

6.1 Introduction

In accordance with the reviewed literatures, the applied methodology to fulfil the aim and objectives of this research was experimental. Accordingly, three types of experiments were developed such as numerical experiment, laboratory experiment, and in-field experiment to address the research questions. Each of these methods were employed to tackle a specific research question. The details of each method and their relative research questions are explained in the following sections.

6.2 Literature Review

In this research, initially a comprehensive literature review was conducted to address the following research question:

- 1) What is the most optimal TE material regarding the energy conversion efficiency?

Regarding this research question, it was studied by reviewing the relevant literatures in [Chapters 4 and 5](#). To clarify, TE materials are the main constitutive element of any TEGs. Accordingly, both their properties and final configuration in the form of TE legs have direct effect on the energy conversion efficiency of the TEGs. Accordingly, [Chapter 4](#) initially illustrated the basic principles of TEGs concerning the properties of the TE materials (i.e. the Seebeck coefficient, electrical conductivity, thermal conductivity, and energy conversion efficiency). Then, the TE properties of several TE materials at room temperature were examined and compared with each other based on the reviewed literatures. To define a benchmark for comparing the TE materials with each other, the materials were classified into three categories (i.e. inorganic, organic, and hybrid) respecting their constitutive materials. Then, the *p*- and *n*- types of each category were segregated from each other due to their intrinsic different TE properties. As a result, the TE properties of the three TE categories were compared with other with regard to their *p*- and *n*-types. Based on the reviewed literatures, the inorganic TE materials are superior to the other two types at room temperature concerning the energy conversion efficiency of the TEGs. However, since the TE materials are used to produce the TE legs, the configuration of the TE legs also influences on the energy conversion efficiency of the TEGs. Therefore, [Chapter 5](#) reviewed the relationship between the configurations of the TE legs and the energy efficiency of the TEGs at room temperature with

regard to their constitutive TE materials. Thus, three different configurations of the TE legs (i.e. ingot-shaped, film-shaped, and yarn-shaped) were reviewed respecting the as three predefined types of the TE materials. Based on the results, the ingot-shaped TE legs consisted of the inorganic TE materials result in the most energy efficient TEGs. Consequently, the first research question was addressed by combining the results of [Chapters 4](#) and [5](#).

6.3 Numerical experiment

After reviewing the relevant literatures, the second step of this research was carrying out several numerical experiments to address the following research questions:

- 2) What is the most optimal TE material regarding the life cycle impact?
- 3) How is it possible to integrate a number of TE legs together with a lightweight substrate, having no or minimum negative effect on the efficiency of the TEGs?

Regarding the second research question, it was required to conduct a numerical experiment on the life cycle impacts of the TE materials reviewed in [Chapters 4](#) and [5](#) to find out the eco-friendliest one for this research. It should be noted that, so far not only no study has comprehensively examined the TE materials from this perspective, but also this consideration has not been of concern to the researchers of this field. Thus, [Chapter 7](#) focused on studying the life cycle impact of the reviewed TE materials at their production stage (i.e. from cradle to gate). Precisely, the environmental impact of some of the reviewed TE materials were examined at their production stage respecting to their TE types. In fact, the production stage of the TE materials could be divided into three main sub-stages, including raw materials extraction, transporting the raw materials to the manufacturing site, and manufacturing the final TE materials. Therefore, the required data on the primary energy demand of the raw materials extraction were collected from CES EduPack™ 2018, which is the world-leading teaching resource for the materials in engineering, science, processing, and design. In addition, the data on the primary energy demand of the manufacturing processes of the TE materials were collected from [Chapters 4](#) and [5](#). Then, the collected data were inserted into a life cycle impact assessment tool called GaBi v.4.4. followed by defining the

relevant flows and connecting them to each other. Fig.63 illustrates the production stage of one of the reviewed TE materials modelled (i.e. Bi_2Te_3) in GaBi.

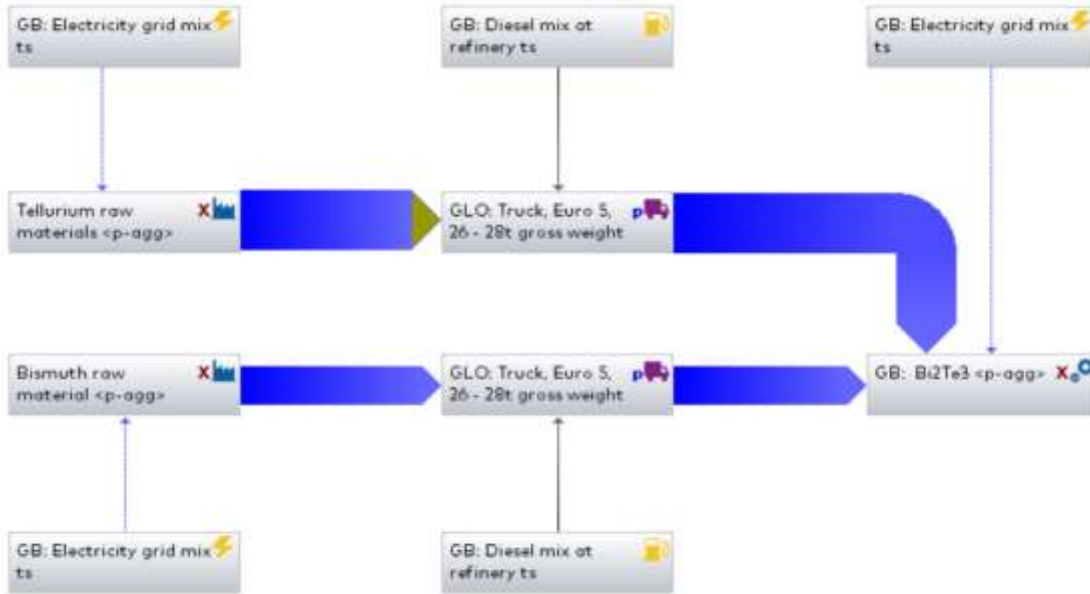


Fig. 63: The defined flows and their connections in GaBi to produce Bi_2Te_3 .

Based on the input data and the defined flows and connections, GaBi assessed the environmental impacts of each TE material from different perspectives, including the primary energy demand, the ozone depletion potential, the human toxicity potential, and etc. Combining the outcomes of Chapters 4, 5, and 7, the most optimal TE material concerning both the energy conversion efficiency and the environmental impact was selected for this research. To clarify, an off-the-shelf TEG composed of the achieved optimal TE material was used in Chapters 8-10.

Concerning the third research question, it was required to integrate several numbers of the selected off-the-shelf TEG together to provide the required voltage for the armbands. Following the reviewed literatures in Chapter 5, this could be achieved by using an integrating substrate. However, still based on the same literatures, the integrating substrate can negatively impact on the energy conversion efficiency of the TEGs. This is mainly because, the TEGs perform based on the temperature difference along the legs. To specify, a higher temperature difference along the legs results in a higher energy conversion efficiency. Whereas, the integrating substrates deteriorate

this temperature difference due to their mostly higher thermal conductivity (U-value) than that of the surrounding air. Accordingly, the aim of [Chapter 8](#) was to develop a non-homogeneous integrating substrate with the least negative impact on the energy conversion efficiency of the TEGs. In this way, not only the required TEGs could be appropriately incorporated into a whole, but also the required temperature difference along the TE legs could be provided.

It should be added that apart from incorporating the TEGs as a whole, another function of this integrating substrate was being a thermal barrier between the heat and cold sources of the TEGs. To illustrate, it was determined to heat up these TEGs from their hot side with a candle and cool them down from their cold side with a fan. Thus, it was of critical importance to consider a thermal barrier between these two sides to avoid cooling down the hot side with the fan. Accordingly, one of the most prevalent lightweight substrate reviewed in [Chapter 5](#) was selected to both integrate the TEGs together and avoid cooling down the hot side of the TEGs with the fan. However, to provide the non-homogeneous boundary condition along the TE legs with the integrating substrate, three different coating patterns with four different thermal conductivities were determined for the integrating substrate. Regarding the integrating patterns, they were coating either the top half, the bottom half, or the full length of the TE legs. Regarding the thermal conductivity of the integrating substrate, two flexible substrates were considered for the integration, namely Polydimethylsiloxane (i.e. PDMS with a U-value of 0.2 (W/mK)) and polyethylene (i.e. LDPE with a U-value of 0.33 (W/mK)). Concerning the PDMS substrate, it was considered to manipulate its thermal conductivity by adding two different fillers to it, namely air bubbles (0.026 W/mK) and Galinstan (16.5 W/mK). Thus, in total, 12 different samples were proposed that their performance should be compared with that of the reference TEG (i.e. the off-the-shelf TEG).

To study the impact of the proposed integrating substrates on the TE performance of the TEG, they were simulated in COMSOL Multiphysics as a cross-platform finite element analysis, solver and multiphysics simulation software. Precisely, to simulate the performance of the determined off-the-shelf TEG under those 12 different integrating patterns, it was required to employ two physics (i.e. *heat transfer* and *electric current*) and one coupling multiphysics (i.e. *thermoelectric effect*) of COMSOL. Regarding the *heat transfer* physics, it computes the heat transfer and distribution in the 12 samples, when a temperature difference occurs along the TE legs. Concerning the *electric*

current, it computes the generated voltage and current in the samples. Thus, to simulate the generated voltage and current based on the distributed heat along the TE legs, it was required to couple these two physics together using a coupling multiphysics called *thermoelectric effect*. Finally, the thermoelectric performances of the 12 samples were compared with that of the reference sample concerning their open circuit currents, voltages, and powers. Fig.64 depicts one of the modelled samples in COMSOL and parts of it setup concerning the *heat transfer* physic. The results proved that covering only the top half of the TE legs with a pristine PDMS substrate results in the most similar TE performance with that of the reference sample. Accordingly, this integrating substrate was nominated for integrating the TEGs in Chapters 9-10. However, it should be noted that to finalize the integrating substrate, its performance should also be validated by an experimental study.

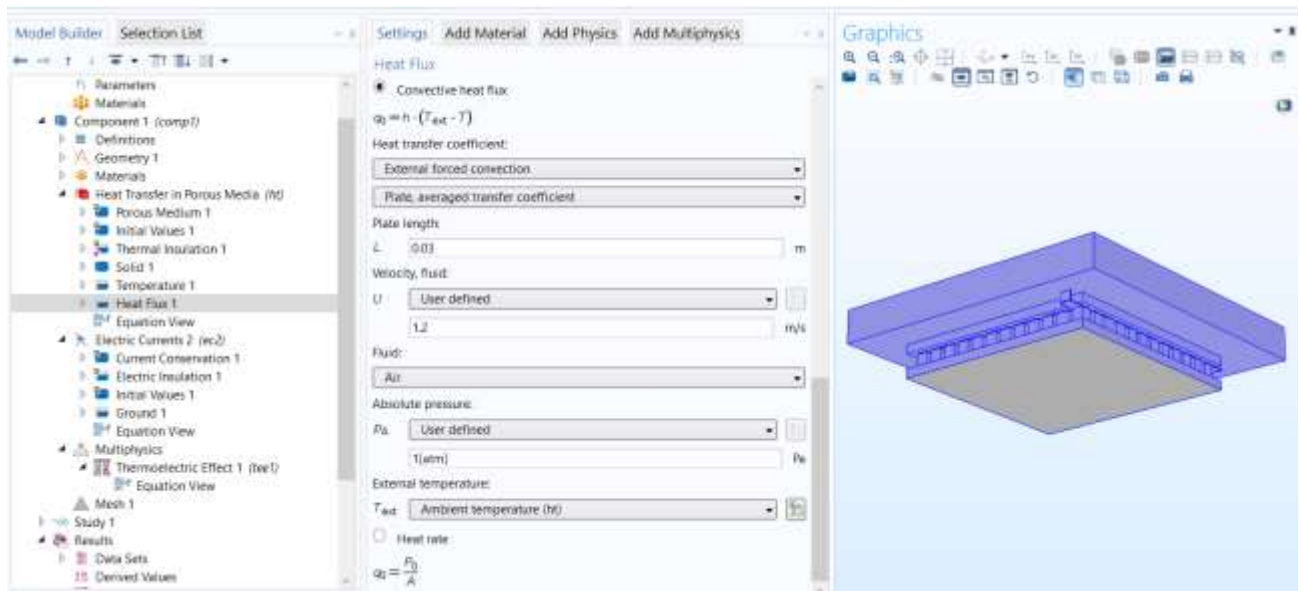


Fig. 64: COMSOL setup for the heat flux of the samples at 1.2 m/s air speed.

6.4 Laboratory experiment

After finding out the appropriate TEG and the nominated integrating substrate, the laboratory experiments were carried out for two reasons. First, to validate the results of the COMSOL

computational modelling and finalize the integrating substrate. Second, addressing the following research questions:

- 4) Is it possible to fabricate a lightweight heatsink to improve the efficiency of a TEG?
- 5) What is the easiest fabrication process to develop the hybrid power supply comprising the integrated TEGs and the rechargeable battery?

To validate the results of the COMSOL modelling, in [Chapter 8](#), all of the 12 modelled integrating samples were developed in the laboratory and tested under the same boundary conditions as the COMSOL simulations. Since the computational modelling was conducted under two different air flow conditions (i.e. 0 m/s and 1.2 m/s), the laboratory experiments were carried out under both air flow conditions. Accordingly, a wind tunnel was designed and fabricated to provide a linear airflow condition for the laboratory experiments. The air velocity in the tunnel and the temperatures inside the wind tunnel and on the hot plate were being checked throughout the experiments using an anemometer and a 4 channel thermometer. Using a multimeter/data logger, the obtained voltage and ampere of each experiment were recorded for 30 min at one second interval. [Fig.65](#) depicts the fabricated samples in the lab, which will be explained in detail in [Chapter 8](#). Comparing the results of the computational modelling and the experimental study, they were aligned with each other. To specify, the results of this experimental study validated that covering only the top half of the legs with a plain PDMS substrate resulted in the greatest output voltage, current, and power. Accordingly, not only the third research question was answered, but also the appropriate integrating substrate was selected for [Chapters 9](#) and [10](#).

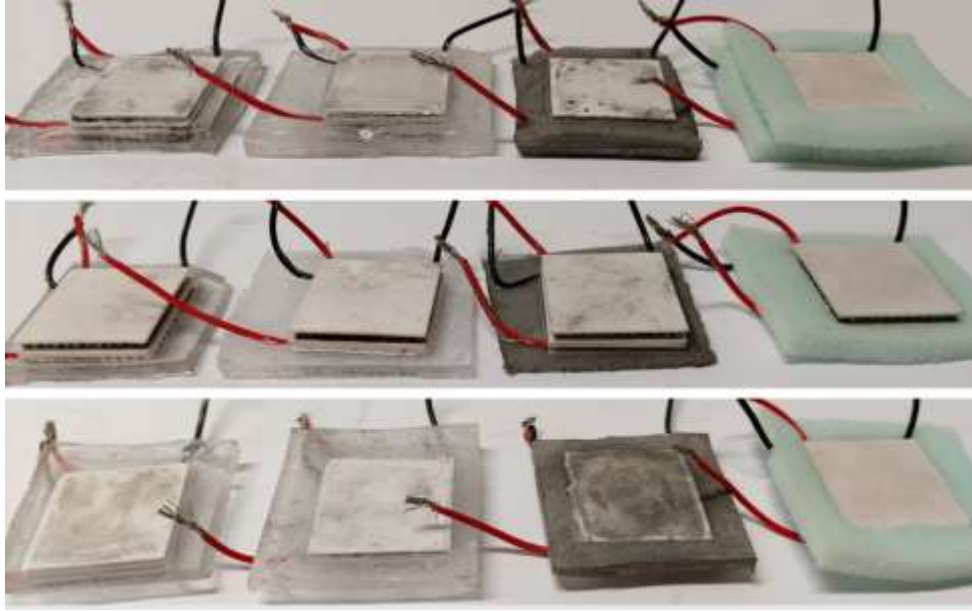


Fig. 65: The fabricated samples in the lab to validate the computational simulations.

Concerning the fourth research question, it should be noted that a heatsink intensifies the temperature difference along the TE legs via accelerating the heat dissipation from the cold side of the legs. Accordingly, in [Chapter 9](#), it was considered to develop a flexible heatsink using the same material used in the fabrication of the flexible integrating substrate (i.e. plain PDMS). It was mainly because matching the materials of the heatsink and the integrating substrate decreases the thermal resistance at their interfaces. Also, it removes the requirement for a structural support to connect them together. Accordingly, two different configurations were considered for the PDMS-based heatsinks, namely semi-spherical PDMS blocks and pin-shaped PDMS blocks. Notably, each of these heatsinks were composed of 44 blocks. Also, their performances were compared with that of the reference model (i.e. the off-the-shelf-TEG that top half of its legs were covered with the plain PDMS integrating substrate) under three different air flow conditions (i.e. 0 m/s, 1.2 m/s, and 2.4 m/s). To test the developed heatsinks under a linear airflow condition, the tests were carried out in the as pre-developed wind tunnel. Based on the achieved results, the optimal heatsink regarding the output current and voltage at different air speeds was the pin-shaped one, which was used for the study in [Chapters 10](#).

The final stage of the laboratory experiment was related to the fifth research question, which was fabricating the hybrid power supply. Accordingly, in [Chapter 10](#), six of the selected off-the-shelf TEGs were integrated together using the optimal integrating substrate (i.e. the plain PDMS substrate covering only the top half of the legs) developed in [Chapter 8](#). Then the optimal heatsink (i.e. 44 pin-shaped PDMS blocks) fabricated in [Chapter 9](#) was attached to the integrating substrate. [Fig.66](#) depicts the schematic of the proposed hybrid power supply. It should be noted that with regard to the required output voltage (i.e. 5V) and current (i.e. 2A) for the heating armbands, a heat source at least the level of a flame was required to heat the TEGs. Since this amount of heat could be provided by none of the internal heat sources (e.g. radiator, hot pipework), it was determined to be provided by a candle. The cold side of the TEGs was cooled down by a fan that was placed above the TEGs.

Checking the outputs of the integrated TEGs, they could provide the required voltage for the armbands, but their total output current was insufficient for this purpose. Thus, they were combined in parallel with a low voltage rechargeable battery (3V) to generate a hybrid power supply for the armbands. To illustrate, the rechargeable battery and the integrated TEGs served as a time-varying voltage source and a constant voltage source, respectively. Thus, coupling them together decreased the discharging speed of the battery, since the integrated TEGs with higher voltage discharged into the battery until they ended up with equal voltages. To put it another way, the battery and the TEGs were connected electrically in parallel during the tests. Due to the voltage difference between the TEGs and the battery, the battery was charged by the TEGs throughout the tests, which were lasting for half an hour. Thus, splitting the provision of the required voltage between the two energy supplies reduced the number of the required batteries and increased the battery's run time. Then, the hybrid power supply was connected to two heating elements that were sewn onto two armbands. To check the surface temperature of the heating armbands, a thermometer was attached to its heating element and its temperature was recorded for 30 minutes at one-minute interval. The highest temperature was recorded in the first 10 min with 41°C, which reduced to 35°C toward the end of the record. Answering the fifth research question, at this stage of the research, the heating armbands and their determined hybrid power supply were fabricated.

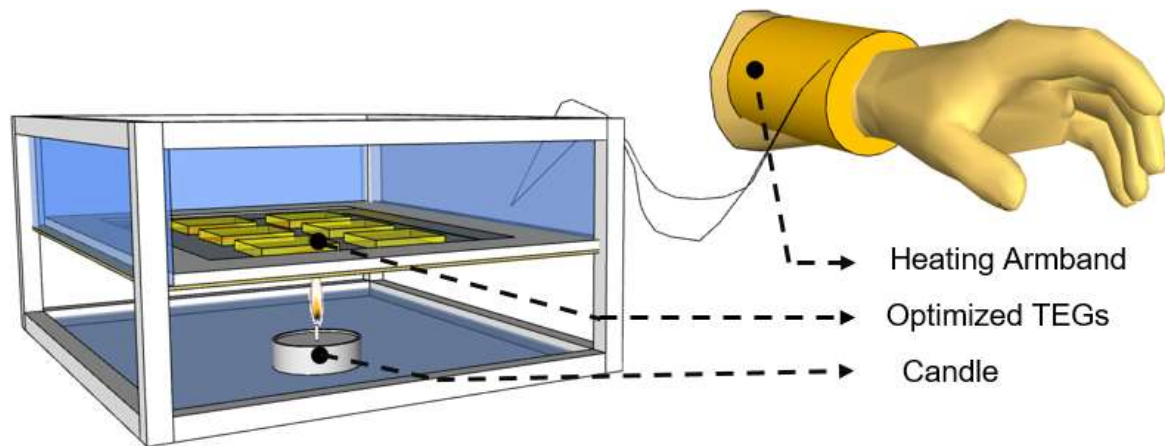


Fig. 66: The schematic configuration of the proposed hybrid power supply.

6.5 In-field experiment

The final stage of this research was addressing the sixth research question, which was fulfilled by an in-field experiment:

- 6) Is it possible to use the designed heating armbands to satisfy both the thermal comfort of the hands and the overall thermal comfort of the office workers in a cold environment?

Accordingly, in [Chapter 10](#), eight participants were recruited to take part in the in-field study carried out in an office room of the University of Derby in the heating month of March. It should be noted that due to the COVID pandemic, a few (i.e. eight participants) people took part in the experiments. Each test was carried out for 1 hr including the preparation (15 min), adaptation (15 min), and experimental (30 min) stages. Each of these stages will explain in details in [Chapter 10](#). During the experimental stage, the participants were divided into two groups, namely the control group and the experimental group. To illustrate, whilst the experimental group was wearing the armbands, the control group was without them as the reference. Each experiment was divided into two parts, including physical measurement at one-minute interval and filling questionnaires at 10 min intervals. Regarding the physical measurements, the temperatures of air and skin (i.e. back of the hand and under the armbands) were measured at one-minute interval. Notably, the room

temperature was kept at 16°C at desk level throughout the experiments. Concerning the questionnaires, they were developed based on the thermal comfort's principles studied in [Chapter 2](#). Accordingly, not only they studied the thermal sensation and comfort of the whole body, but also considered those of the seven different body parts of the participants. To specify, those seven body parts were forehead, torso front and back, hands, thighs front and back, and feet. Collecting the data of the physical measurements and the questionnaires, they were compared with each other to find out the contribution of the armbands to the thermal sensation and comfort of different parts and the whole body. The results of the experiments proved that 50% of the participants felt warmer after 30 min of wearing them. This is mainly because the armbands improved the average comfort level of the participants from less than neutral (i.e. between slightly uncomfortable and neutral) to slightly comfortable.

6.6 Summary

This chapter summarized the different experimental methods used to address the research questions concerning the research aim and objectives. Accordingly, the three employed experimental methods were the numerical experiment, the laboratory experiment, and the in-field experiment. It should be noted that the aim of this chapter was only providing the whole picture of the conducted studies in this research, their sequences, and the applied experiments to accomplish them. Whereas, each study will be discussed in more detail in the relevant chapter. [Fig.67](#) illustrates the research methodology flowchart.

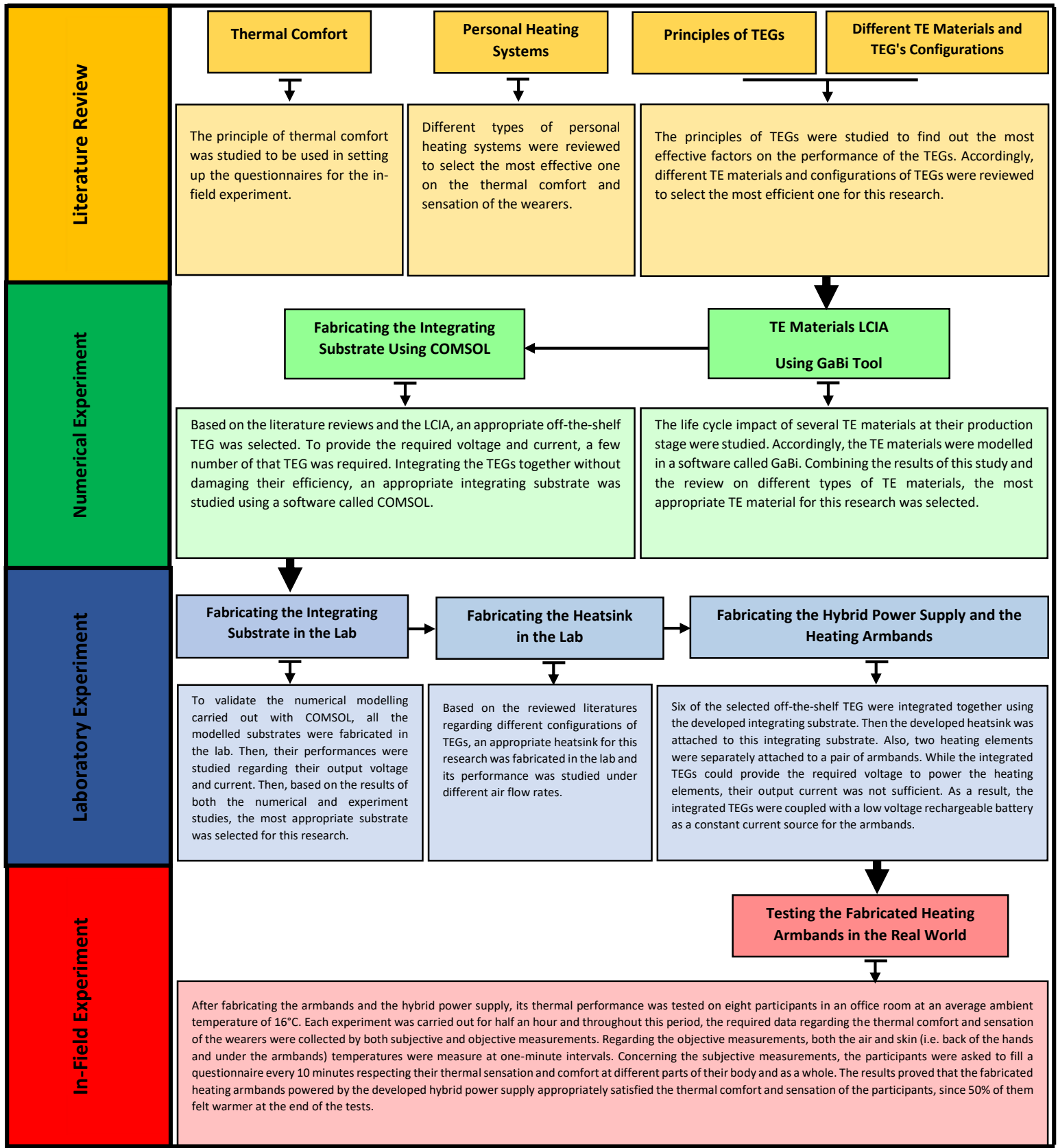


Fig. 67: The research methodology flowchart.

Chapter 7

The Life Cycle Impact Assessment

7.1 Introduction

Undoubtedly, in recent decades, enormous efforts have been devoted to replace fossil fuel based power supplies with the renewable ones. Accordingly, the aim of this research is to develop a hybrid power supply for a heating garment, while one of its power source is an energy harvester (i.e. TEG). To specify, energy harvesters are considered as a renewable power source, because they harvest waste ambient energy and convert it into electricity. TEGs are considered as a renewable power supply because they harvest ambient waste heat and convert it into electricity. However, moving toward green technologies not only requires the renewability of their power supply, but also demands their least environmental impacts over their life cycle. Accordingly, the life cycle impact assessment (LCIA) comes into use in assessing the environmental impacts of technologies and products. Regarding TEGs, as a renewable power supply, so far the conducted LCIA's have focused on evaluating their life cycle impacts with respect to their usage. However, none of them focused on the life cycle impact of their TE materials as the most vital elements of the TEGs. To clarify, so far the benchmark for comparing the TE materials with each other has been their TE specifications (i.e. the Seebeck coefficient, the electrical and thermal conductivities), but not their life cycle impact. The only concerns regarding the environmental impact of the TE materials have been the toxicity and abundance of their constitutive raw materials. Accordingly, the organic and hybrid (inorganic/organic) TE materials have taken priority over the inorganic ones over the last decade. This is mainly attributed to the fact that the inorganic TE materials mostly consist of toxic elements and suffer from resource scarcity [122,171]. However, the main issue about this prioritizing is that it is limited to the toxicity and abundance of the constitutive raw materials. Whereas, the environmental impact of a product includes several additional factors, such as its input-output mass flow, primary energy demand, global warming potential, ozone depletion potential, and human toxicity potential. Nevertheless, so far no prior studies assessed the life cycle impact of the TE materials concerning the above mentioned impact categories. To fill this gap, this chapter is dedicated to the life cycle impact assessment (LCIA) of the most recently developed TE materials to clarify and compare their environmental impacts from different perspectives. It is notable that the main objective of this chapter is to objectively select the most environmental friendly TE materials for this research. As a result, combining the result of this

chapter with that of [Chapter 4](#), the most environmental friendly and energy conversion efficient TE material will be selected for this research.

As mentioned before, the conducted LCIA in the TE field have focused on evaluating the life cycle impacts of the TEGs in specific applications. For example, Patyak [\[319\]](#) examined the life cycle impact of a TEG coupled with a combined heat and power (CHP) unit. Therefore, the hot gas exhausted from the CHP unit was used to heat the TEG. The study considered TeSi as the TE material, thus it assessed the life cycle impact of tellurium (Te) and silicon (Si) as the constructive raw materials. Although the results demonstrated the greater environmental impact of silicon than tellurium at the supply stage, the life cycle impact of TeSi as the final TE material was not entirely addressed. To put it another way, the authors assessed the life cycle impact of TeSi only based on its raw materials acquisition, regardless of its manufacturing processes. In addition, the study considered only a single TE material for the assessment. Therefore, the impact of selecting other TE materials on the environmental impact of the whole system was ruled out.

Kishita et al. [\[320\]](#) evaluated the life cycle impact of the TEGs fabricated on the exhaust pipes of the taxis in Japan. The determined TE material was Bi_2Te_3 , and the authors studied the relationship between its energy conversion efficiency and the CO_2 emission of the system. The results revealed that increasing the energy conversion efficiency of Bi_2Te_3 from 7.2% to 17.7% reduced the CO_2 emission in a range of between 0.07% and 0.30%. It should be noted that the study only considered the effect of varying the conversion efficiency of Bi_2Te_3 on the life cycle impact of the TEG at its using stage, but not at the production stage of Bi_2Te_3 . Also, despite the aim of the study, which was assessing the life cycle impact of the TEG from cradle to end of use, the authors excluded the life cycle impact of the manufacturing stage of the TEGs for simplicity.

In a later study, Kishita et al. [\[321\]](#) developed their previous study [\[320\]](#) by considering two different driving patterns for the taxis. The first driving pattern was specified based on 18km/hr average speed as the most common driving speed in Japan. The second driving pattern followed the average driving speed in the United States, which was 44km/hr. The results showed that under both driving patterns, a TEG with 7.2% energy conversion efficiency resulted in greater annual CO_2 emission compared with that of with 17.7% conversion efficiency. Notably, the authors indicated that they only applied Bi_2Te_3 in their study due to lack of data on the life cycle impact

of the other TE materials. Nevertheless, the life cycle impact of Bi_2Te_3 was limited to its raw materials acquisition, and its manufacturing stage was ruled out from the assessment.

Driven by these literatures, there is insufficient knowledge regarding the life cycle impact of the TE materials at their production stage. Therefore, this chapter aims to fill this gap by assessing and comparing the life cycle impact of several TE materials with each other. To specify, rather than assessing the life cycle impact of a TEG in different applications, this chapter assesses the life cycle impacts of different TE materials as the main element of the TEGs. This assessment includes all the production stages related to the TE materials, namely the raw materials acquisition, transporting the raw materials to the manufacturing site, and manufacturing the final TE material. As a result, the outcomes of this chapter provide an opportunity for this research to take into account the environmental performance of different TE materials along with their energy conversion efficiencies.

7.2 Life cycle impact assessment stages

In this research, the LCIA was undertaken with regard to the four stages outlined by the International Organization for Standards (ISO) 14040/ 14044. These four stages are as follow:

1. Goal and Scope Definition: which determines the scopes of the assessment, the functional units, and the boundaries of the study. Regarding the scopes of the assessment, herein, it was divided into five impact categories, including the input-output mass flow, the primary energy demand, the global warming potential, the ozone depletion potential, and the human toxicity potential.
2. Inventory Analysis: which specifies the inputs and outputs inventory, including the required resources (i.e. materials and energies), the potential emissions to the water, air, and soil, and the potential wastes of the TE materials during their lifetime.
3. Impact Assessment: which assesses the life cycle impact of the three specified inputs and outputs with regard to the five determined impact categories.
4. Interpretation of the Results: which interprets the life cycle impacts of the TE materials and providing recommendations for further improvements.

7.3 Goal and scope of the assessment

The goal of this chapter is assessing the life cycle impact of the three types of the TE materials at their production stage (i.e. the cradle to gate). To illustrate, the total life cycle impact (i.e. the cradle to grave) of the TE materials involves four stages, including the production stage, the fabrication stage, the using stage, and the end of life stage, as [Fig.68](#) shows. Obviously, each of these four stages could be divided into several sub-stages. As mentioned before, the boundary of this chapter is assessing the life cycle impact of the TE materials at their production stage, resulting in the cradle to gate LCIA. The reason of excluding the LCIA of the other three stages is the variation of the manufacturing stage of the TE legs in each study. To specify, in each research, the TEGs and the applied TE legs are shaped based on the desired output power, as reviewed in [Chapter 5](#). Therefore, any changes in the configuration of the TE legs impacts on the required manufacturing processes and ultimately the life cycle impacts of the whole system. Accordingly, herein, assessing the life cycle impacts of the TE materials sets a baseline to select the most environmental friendly TE material for the hybrid power supply. Back to the production stage, as can be seen in [Fig.68](#), it consists of three sub-stages, namely the raw materials supply, transportation of the raw materials to the manufacturing site, and manufacturing the final TE materials.

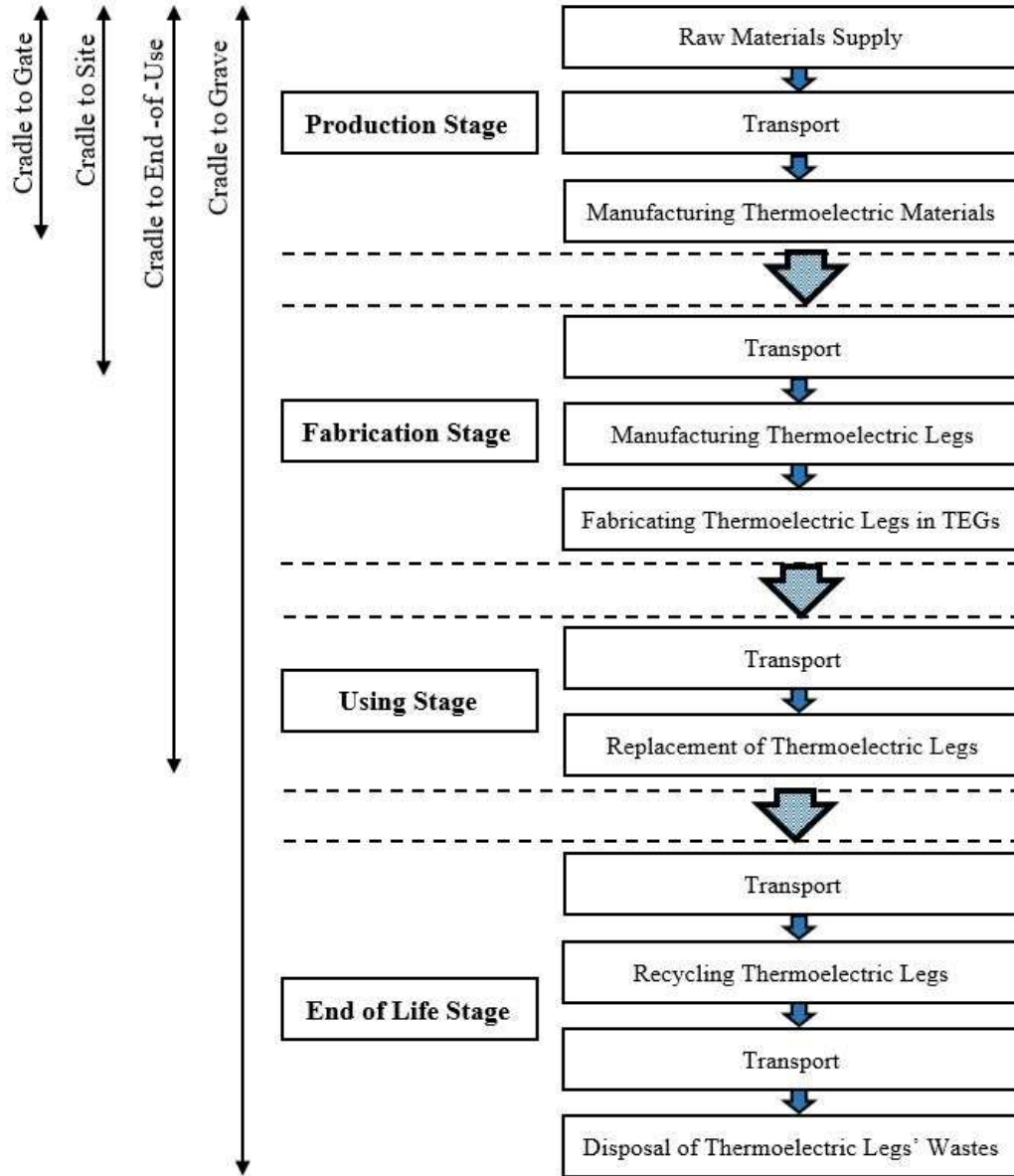


Fig. 68: The different stages and sub-stages of the life cycle of the TE materials [322].

In this study, the input inventory was prepared based on the data derived from CES EduPack™ 2018 and some relevant literatures. Precisely, CES EduPack™ 2018 was used to gather data on the primary energy demand of the raw materials. Whereas, the relevant literatures were used to collect data on the required manufacturing processes and the equipment used to produce the final TE materials. For the sake of simplicity, the transportation phase was assumed to be one-step from the extraction plant to the manufacturing site with an average distance of 100 km. Also, the

transportation vehicle was considered to be a diesel fuel based lorry with a weight in a range of between 26ton and 28ton.

After collecting the input and output inventories of the TE materials, they were modelled in GaBi v.4.4 to assess their life cycle impacts individually. It is noteworthy that the impact categories were selected with regard to the EU's 20-20-20 climate and energy targets, aiming to increase the energy efficiency by 20%, reduce the CO₂ emissions by 20%, and reach 20% renewables by 2020. As a result, seven life cycle impact categories were determined for investigation, including resource consumption, emissions, wastes, primary energy demand, global warming potential (GWP 100 year), ozone depletion potential (ODP), and human toxicity potential (HTP). The specified unit for the primary energy demand was MJ- equivalent (Eq). This was because according to CES EduPack™ 2018 and the literatures, electricity was the dominant energy source of supplying the raw materials and manufacturing the final TE materials. Notably, to simulate the life cycle performance in GaBi v.4.4, natural gas was determined as the source of electricity generation. In addition, GaBi v.4.4 applied an appropriate conversion factor to convert the diesel fuel consumed for transportation to an equivalent electricity consumption.

Regarding the GWP of the TE materials, it was evaluated with respect to the IPCC 2007 methodology in kg CO₂- Eq for a time horizon of 100 years. Like the primary energy demand, the GWP value involved the CO₂ emissions of the three determined sub-stages of the production stage. The ozone depletion potential was expressed as R11 equivalents [kg] to illustrate the relationship between the production stages of the TE materials and thinning of the ozone layer in the upper atmosphere. R-11 stands for Trichlorofluoromethane (CCl₃F) that consists of three chlorine atoms in every molecule, causing a massive potential of degrading the ozone layer. The human toxicity potential (HTP) measures the relative impact of the toxic substances on the human beings concerning their emissions to the environmental components such as air, fresh water, and etc. The selected reference unit for HTP was kg 1,4-DCB equivalent emitted, referring to the equivalent kg of 1,4 Dichlorobenzene released from the production stage of a TE material. It is notable that the quantity of each input material was determined based on producing 1kg of the final TE material.

7.4 Life cycle inventory

The input raw materials of the inorganic TE materials are limited to the inorganic elements (e.g. Bi, Te, Sb, Se) existing in their chemical formulas. However, the organic and hybrid TE materials not only consist of the existing elements in their chemical formula, but also comprise of some additives for their chemical treatments. Accordingly, there is inadequate data on the primary energy demand of all the raw materials of the organic and hybrid types. Therefore, herein, the raw materials of these two types were limited to those that their data were available. Concerning the manufacturing processes, initially the required manufacturing processes were defined for each TE material based on the relevant literatures. Then, the most appropriate machines for undertaking these processes were specified to calculate the associated power consumptions. Table 10 to Table 13 show the energy demand of the input raw materials and the required manufacturing processes of the TE materials regarding their TE type.

Table 10: Inventory data list on the raw materials of the TE materials derived from CES EduPack™ 2018 [323].

Thermoelectric Types	Product	Raw Material Acquisition	
		Input Materials	Energy Demand MJ/kg
Inorganic	$\text{Bi}_{0.4}\text{Sb}_{1.59}\text{Ge}_{0.01}\text{Te}_3$	Bi	138
		Sb	134
		Ge	8510
		Te	150
	Bi_2Te_3	Bi	138
		Te	150
	$\text{Bi}_2\text{Te}_{2.7}\text{Se}_{0.3}$	Bi	138
		Te	150
		Se	69.3
	$\text{Sb}_{1.85}\text{In}_{0.15}\text{Te}_3$	Sb	134
In		2720	
Te		150	
$(\text{BiSbTe}_{1.5}\text{Se}_{1.5})_{0.3}\text{Ag}_{0.3}$	Bi	138	
	Sb	134	
	Te	150	
	Se	69.3	
	Ag	1400	
PEDOT:PSS films treated with H_2SO_4 and NaOH	PEDOT:PSS	208.2	
	Deionized water	0.4	
	Isopropyl alcohol (IPA)	151	
	H_2SO_4	4	
	CNT/PEDOT:PSS	209	
	PEDOT:PSS	208.2	

Organic	SWNTs/ PEDOT: PSS treated with DMSO	Deionized water	0.4
		PEDOT:PSS	208.2
		SWCNT	209
		Dimethyl sulfoxide	4
	PEDOT:PSS /RTCVD graphene composite film	PVDF	98.7
		PEDOT:PSS	208.2
	DWNT-PEI/graphene-PVP nanocomposites	Graphene	209
		Polyethylene mine (PEI)	197
		Polyvinylpyrrolidone (PVP)	49.3
		Graphene	209
Double-walled carbon nanotubes(DWNT)		209	
Ultrapure water		0.4	
Deionized water		0.4	
Hybrid	Te-PEDOT:PSS	PEDOT:PSS	208.2
		Te	150
		Ethanol	151
	PEDOT:PSS/ Si-NP	PEDOT: PSS	208.2
		Si	116
		Ethanol	151
	Bi-Te based alloy nanosheet /PEDOT:PSS	PEDOT:PSS	208.2
		Ethanol	151
		Dimethyl sulfoxide	4.01
		Nylon	8.7
		PVDF	98.7
		Bi	138
		Te	150
	Bi _{0.48} Sb _{1.52} Te ₃ + graphene	Bi	138
Te		150	
Sb		134	
Graphene		209	

Table 11: Inventory data list on the manufacturing processes of the inorganic TE materials.

Product	Manufacturing Process				Ref
	Process	Equipment	Power Consumption (W)	Typical Processing Time (hr)	
Sb _{1.85} In _{0.15} Te ₃	Evacuated quartz tube melting	EQ-SP-15VIM	8000	24	[131]
	Evacuated quartz tube annealing	EQ-SP-15VIM	8000	48	
	Spark Plasma Sintering	SPS, LABOX-350, Sinter Land Inc., Japan	25000	0.08	
Bi _{0.4} Sb _{1.59} Ge _{0.01} Te ₃	Evacuated quartz tube melting	EQ-SP-15VIM	8000	10	[138]
	Hot pressing	PTH-600A (Zhengzhou Protech Technology Co.,Ltd)	500	1	

(BiSbTe _{1.5} Se _{1.5}) _{0.3} Ag _{0.3}	Evacuated quartz tube melting	EQ-SP-15VIM	8000	10	[144]
	Evacuated quartz tube annealing	EQ-SP-15VIM	8000	48	
	Spark Plasma Sintering	SPS, LABOX-350, Sinter Land Inc., Japan	25000	0.08	
Bi ₂ Te _{2.7} Se _{0.3}	Evacuated quartz tube melting	EQ-SP-15VIM	8000	12	[152]
	Evacuated quartz tube annealing	EQ-SP-15VIM	8000	48	
	Spark Plasma Sintering	SPS, LABOX-350, Sinter Land Inc., Japan	25000	0.16	
	Evacuated quartz tube annealing	EQ-SP-15VIM	8000	168	
Bi ₂ Te ₃	Melting with Electric oven	Carbolite-Gero Laboratory Oven - AX	1000	4	[157]
	Ball Milling	PM-100, Retsch	750	3	
	Spark Plasma Sintering	SPS, LABOX-350, Sinter Land Inc., Japan	25000	0.08	

Table 12: Inventory data list on the manufacturing processes of the organic TE materials.

Product	Manufacturing Process				Ref
	Process	Equipment	Power Consumption (W)	Typical Processing Time (hr)	
SWNTs/ PEDOT: PSS treated with DMSO	Sonication	VCX750 Vibra-Cell, Sonics & Materials	750	2	[130]
	Vacuum oven	DZF-5090S (Kenton)	2400	24	
PEDOT:PSS films treated with H ₂ SO ₄ and NaOH	Spin Coating	MS-B100 Spin Coater	1000	0.01	[169]
	Drying on hot plate	Stuart US150 Hot Plate	700	0.5	
CNT/PEDOT:PSS	Sonication	VCX750 Vibra-Cell, Sonics & Materials	750	1	[190]
	Annealing	Stuart US150 Hot Plate	700	0.16	
PEDOT:PSS /RTCVD graphene composite film	UV irradiation	Irradiation chamber BS-02	180	0.08	[193]
	Spin Coating	MS-B100 Spin Coater	1000	0.7	
	Annealing	Stuart US150 Hot Plate	700	0.03	
DWNT-PEI/graphene-PVP nanocomposites	Sonication	VCX750 Vibra-Cell, Sonics & Materials	750	2.45	[194]
	Centrifuge	FrontierTM Centrifuge FC5513	170	0.16	

Table 13: Inventory data list on the manufacturing processes of the hybrid TE materials.

Product	Manufacturing Process				Ref
	Process	Equipment	Power Consumption (W)	Typical Processing Time (hr)	
PEDOT:PSS/ Si-NP	Sonication	VCX750 Vibra-Cell, Sonics & Materials	750	2.25	[152]
	Annealing	Stuart US150 Hot Plate	700	0.32	
	Spin Coating	MS-B100 Spin Coater	1000	0.016	
Te-PEDOT:PSS	Sonication	VCX750 Vibra-Cell, Sonics & Materials	750	0.25	[206]
	Vacuum oven	DZF-5090S (Kenton)	2400	0.25	
Bi-Te based alloy nanosheet /PEDOT:PSS	Sonication	VCX750 Vibra-Cell, Sonics & Materials	750	3.5	[212]
	Annealing	Stuart US150 Hot Plate	700	24	
	Vacuum oven	DZF-5090S (Kenton)	2400	14	
Bi _{0.48} Sb _{1.52} Te ₃ graphene	+ Evacuated quartz tube annealing	EQ-SP-15VIM	8000	2	[324]
	Spark Plasma Sintering	SPS, LABOX-350, Sinter Land Inc., Japan	25000	0.16	

7.5 Results

After gathering the life cycle inventories of the TE materials and modelling them in GaBi v.4.4, the life cycle impacts of each TE material were assessed individually concerning the five impact categories, including the input-output mass flow, the primary energy demand, the global warming potential, the ozone depletion potential, and the human toxicity potential.

7.5.1 Input-output mass flow

Categorizing the input-output mass flow into the emissions, the resources, and the deposited goods (i.e. wastes), in general the greatest input-output mass flow was achieved by the inorganic TE materials, as Fig.69 and Table 14 depict. Then, the hybrid and the organic TE materials took second and third places, respectively. The only exceptions to this fact were Bi₂Te₃ and Bi_{0.4}Sb_{1.59}Ge_{0.01}Te₃ that in spite of being belonged to the inorganic type, their individual input-output mass flow was by far lower than that of most of their hybrid and organic counterparts. Precisely, the input-output mass flow of the inorganic materials varied between 2e⁴ and 87e⁴ kg, whilst it fluctuated between 4e⁴ and 9e⁴ kg for the organic type and between 6e⁴ and 12e⁴ kg for the hybrid type. Therefore, Bi₂Te₃ with 2 e⁴ Kg input-output mass flow was the most mass efficient TE material among the

three types. Regarding $\text{Bi}_{0.4}\text{Sb}_{1.59}\text{Ge}_{0.01}\text{Te}_3$, its $5e^4$ kg input-output mass flow was in the same range with that of most of the organic TE materials and much less than that of the hybrid type.

In addition, the mass flow associated with the emissions of the three types of the TE materials was greater than that of associated with their resources and deposited goods. To clarify, the mass emitted by these three types was 1.4 times greater than that of related to their resources, and it was nearly 515 times greater than their wastes. Importantly, the highest emission of these TE materials was to fresh water, whilst their emissions to sea water and air stood second and third, respectively. Therefore, it could be interpreted that there was a direct relationship between the resource requirement and the fresh water pollution of these TE materials.

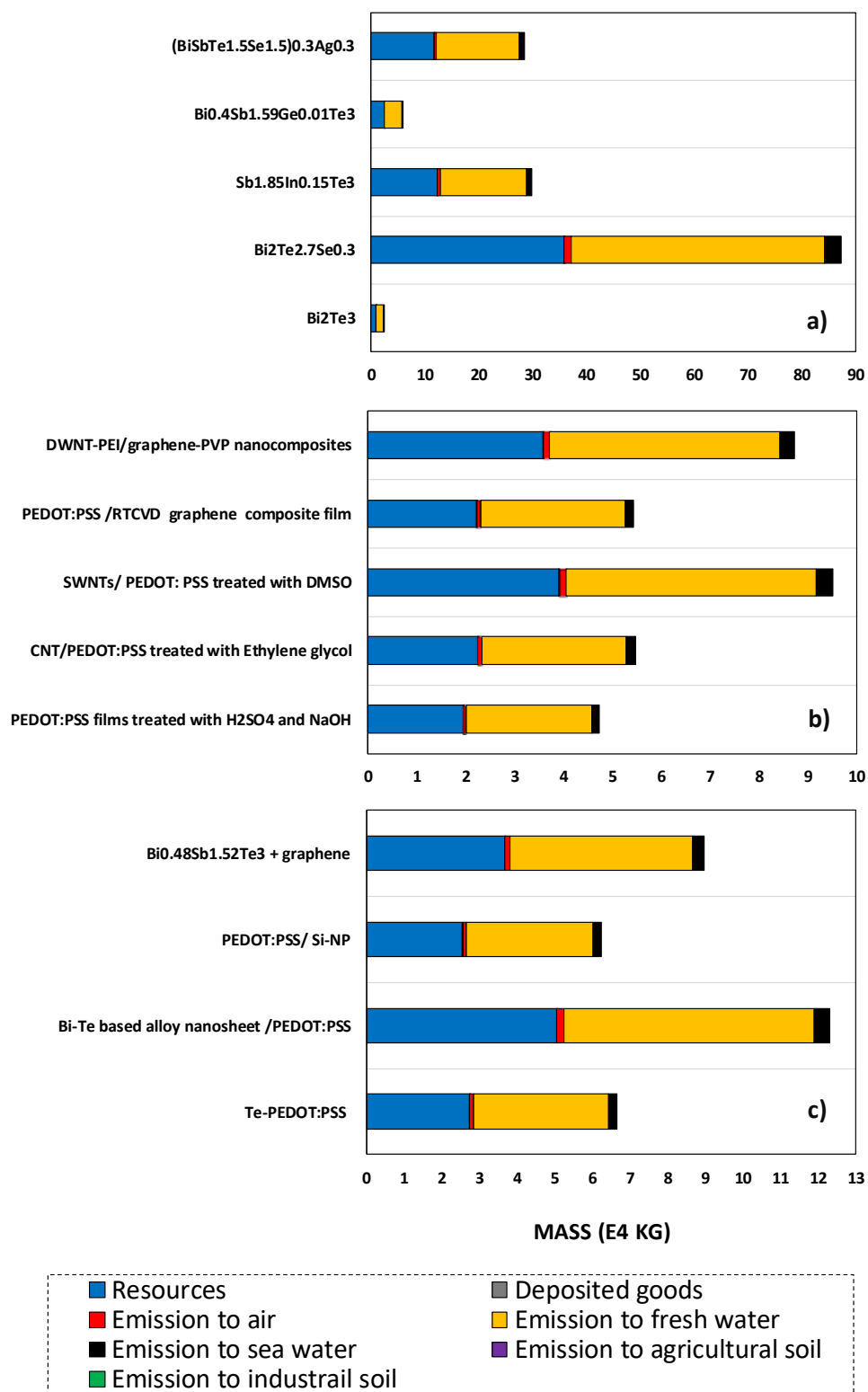


Fig. 69: Comparing the environmental input and outputs of different types of TE materials: a) inorganic; b) organic; and c) hybrid TE materials.

Table 14: Summary of the environmental input and outputs of the TE materials at the production stage.

Type	TE material	Resources	Deposited Goods	Emissions
		mass(kg)	mass(kg)	mass(kg)
Inorganic	(BiSbTe _{1.5} Se _{1.5}) _{0.3} Ag _{0.3}	117000	326	168200
	Bi _{0.4} Sb _{1.59} Ge _{0.01} Te ₃	24000	66.8	34508
	Sb _{1.85} In _{0.15} Te ₃	123000	341	175890
	Bi ₂ Te _{2.7} Se _{0.3}	358000	996	514400
	Bi ₂ Te ₃	9310	25.9	13431
Organic	DWNT-PEI/graphene-PVP nanocomposites	35800	99.6	51440
	PEDOT:PSS /RTCVD graphene composite film	22300	62.2	32117
	SWNTs/ PEDOT: PSS treated with DMSO	39000	109	56040
	CNT/PEDOT:PSS treated with Ethylene glycol	22400	62.4	32169
	PEDOT:PSS films treated with H ₂ SO ₄ and NaOH	19400	54.1	27958
Hybrid	Bi _{0.48} Sb _{1.52} Te ₃ + graphene	36800	102	52870
	PEDOT:PSS/ Si-NP	25600	71.4	36810
	Bi-Te based alloy nanosheet /PEDOT:PSS	50500	141	72630
	Te-PEDOT:PSS	27300	75.9	39210

7.5.2 Primary energy demand

Fig.70 and Table 15 exhibit the primary energy demand of the studied TE materials concerning their three phases of the production stage. As can be seen, the primary energy demand of the inorganic TE materials was in average greater than that of the other two types. For example, the most energy consuming TE materials were Bi₂Te_{2.7}Se_{0.3}, Sb_{1.85}In_{0.15}Te₃, and (BiSbTe_{1.5}Se_{1.5})_{0.3}Ag_{0.3} with 19100 MJ/Kg, 6540 MJ/Kg, and 6240 MJ/Kg primary energy demand, respectively. Conversely, Bi₂Te₃ and Bi_{0.4}Sb_{1.59}Ge_{0.01}Te₃ were not only the most primary energy saving inorganic TE materials, but also their primary energy demands were competing with those of the organic and hybrid types. In particular, the primary energy demands of the organic and hybrid types were in a range of between 1000 and 3000 MJ/Kg, whilst it was 497 MJ/Kg for Bi₂Te₃ and 1280 MJ/Kg for Bi_{0.4}Sb_{1.59}Ge_{0.01}Te₃.

Concerning each sub-stage of the production stage, the required energies for supplying the raw materials of the inorganic type were at least 20% and 40% lower than that of the organic and the hybrid types, respectively. This could be interpreted by the fewer input raw materials of the

inorganic TE materials compared with the other two types. In addition, the contribution of the transportation of the raw materials to the manufacturing site to the primary energy demand of the TE materials was remarkably negligible. Precisely, compared with the raw materials acquisition and the manufacturing processes, the primary energy demand of the transportation was near to zero for all the studied TE materials. Thus, the remarkable difference between the primary energy demand of the inorganic TE materials and that of the other two types was mainly related to their manufacturing processes. In other words, apart from Bi_2Te_3 and $\text{Bi}_{0.4}\text{Sb}_{1.59}\text{Ge}_{0.01}\text{Te}_3$, the required energy for manufacturing the inorganic TE material was at least 8 times higher than that of the organic and the hybrid ones. Furthermore, the manufacturing processes of the inorganic TE materials accounted for three quarter of the total primary energy demand of this type. Whereas, it contributed to less than one eighth of the total primary energy demand of the organic and hybrid TE materials. In fact, these results were in line with the presented manufacturing processes and the associated processing time of the TE materials in [Table 11](#) to [Table 13](#) .

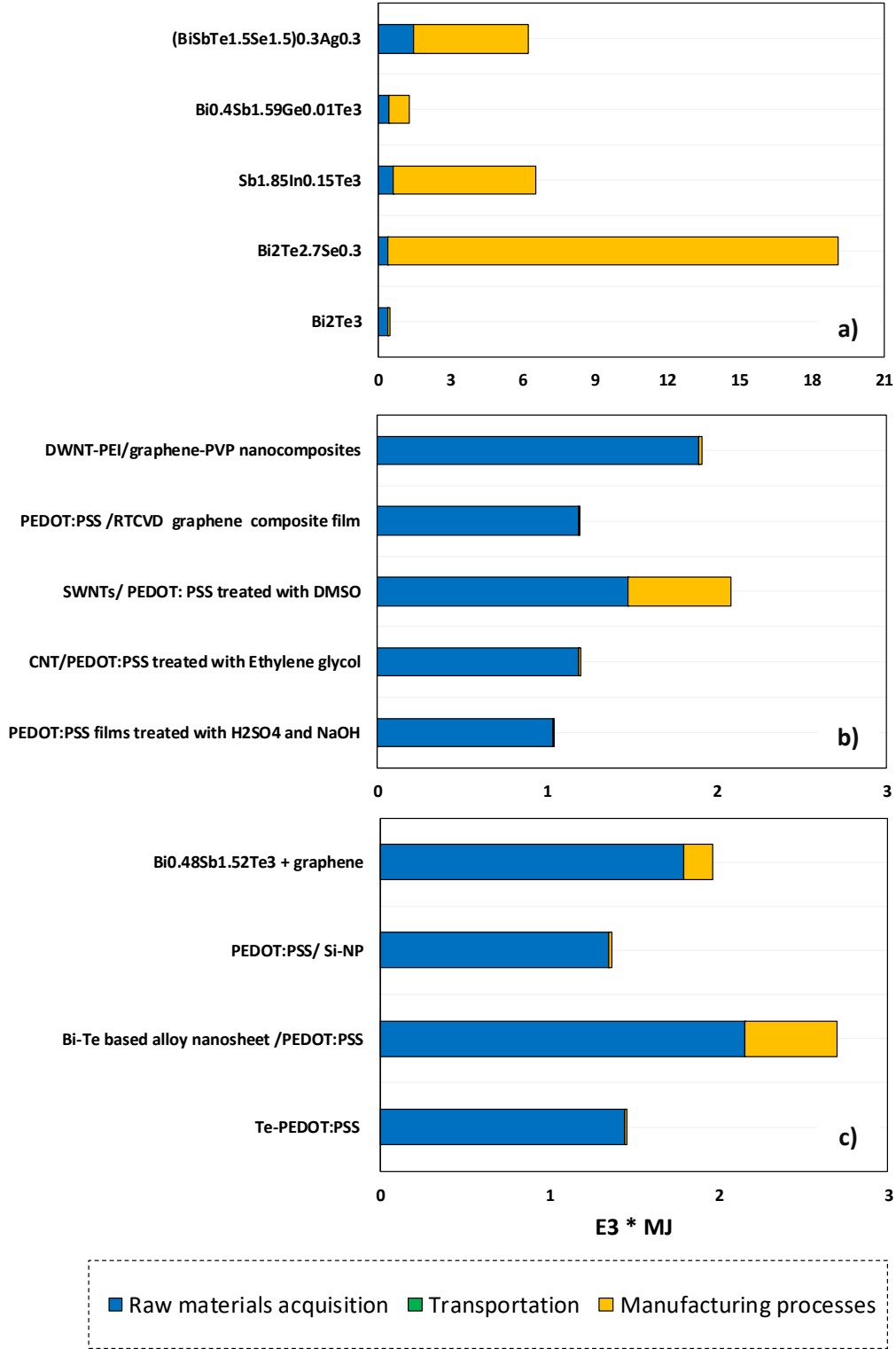


Fig. 70: The contribution of the three sub-stages of the production stage to primary energy demand: a) inorganic; b) organic; and c) hybrid TE materials.

Table 15: Summary of the total primary energy demand of the TE materials at the production stage.

Type	TE material	Total Energy Demand (MJ/kg)
Inorganic	$(\text{BiSbTe}_{1.5}\text{Se}_{1.5})_{0.3}\text{Ag}_{0.3}$	6240
	$\text{Bi}_{0.4}\text{Sb}_{1.59}\text{Ge}_{0.01}\text{Te}_3$	1280
	$\text{Sb}_{1.85}\text{In}_{0.15}\text{Te}_3$	6540
	$\text{Bi}_2\text{Te}_{2.7}\text{Se}_{0.3}$	19100
	Bi_2Te_3	497
Organic	DWNT-PEI/graphene-PVP nanocomposites	1911
	PEDOT:PSS /RTCVD graphene composite film	1193
	SWNTs/ PEDOT: PSS treated with DMSO	2083
	CNT/PEDOT:PSS treated with Ethylene glycol	1196
	PEDOT:PSS films treated with H_2SO_4 and NaOH	1037
Hybrid	$\text{Bi}_{0.48}\text{Sb}_{1.52}\text{Te}_3$ + graphene	1960
	PEDOT:PSS/ Si-NP	1370
	Bi-Te based alloy nanosheet /PEDOT:PSS	2700
	Te-PEDOT:PSS	1460

7.5.3 Global warming potential (GWP)

[Fig.71](#) displays the contribution of each phases of the production stage to the global warming potential. In addition, [Table 16](#) summarizes the total equivalent CO_2 emission of the TE materials at their production stage. In accordance with the results reported in the primary energy demand section, in general, the inorganic TE materials illustrated far greater global warming potential than the organic and the hybrid types. To illustrate, except Bi_2Te_3 and $\text{Bi}_{0.4}\text{Sb}_{1.59}\text{Ge}_{0.01}\text{Te}_3$, the GWP of the studied inorganic TE materials was between 250 and 800 $\text{kg CO}_2\text{-Eq/kg}$. However, it was in a range of between 40 to 85 $\text{kg CO}_2\text{-Eq/kg}$ and 55 to 110 $\text{kg CO}_2\text{-Eq/kg}$ for the organic and hybrid TE materials, respectively. Concerning the GWP of Bi_2Te_3 and $\text{Bi}_{0.4}\text{Sb}_{1.59}\text{Ge}_{0.01}\text{Te}_3$, it was 20 $\text{kg CO}_2\text{-Eq/kg}$ for the former and 52 $\text{kg CO}_2\text{-Eq/kg}$ for the latter. As a result, the GWPs of these two inorganic TE materials were in the same range of those of the organic and hybrid counterparts. Furthermore, although the GWPs of the organic type were approximately equal with those of the hybrid type, the former performed slightly better than the latter in this regard.

Regarding the emission of the TE materials, the manufacturing process accounts for the highest emission of the inorganic TE materials, as [Fig.71](#) shows. Precisely, at least 65% of the CO_2 equivalent emission of the inorganic TE materials was related to its manufacturing processes. The

only exception was Bi_2Te_3 as its raw materials acquisition contributed to 82% of its CO_2 equivalent emission. Likewise, supplying the raw materials was the main reason of carbon emission in the organic and hybrid types. This was mainly because, these two TE types benefit from significantly low energy manufacturing processes. To illustrate, acquiring the raw materials accounted for 90% of the CO_2 equivalent emission of majority of the organic and hybrid TE materials. Concerning the diesel based transportation, its associated CO_2 equivalent emission was by far lower than that of the gas based electricity used for the raw materials supply and the manufacturing processes.

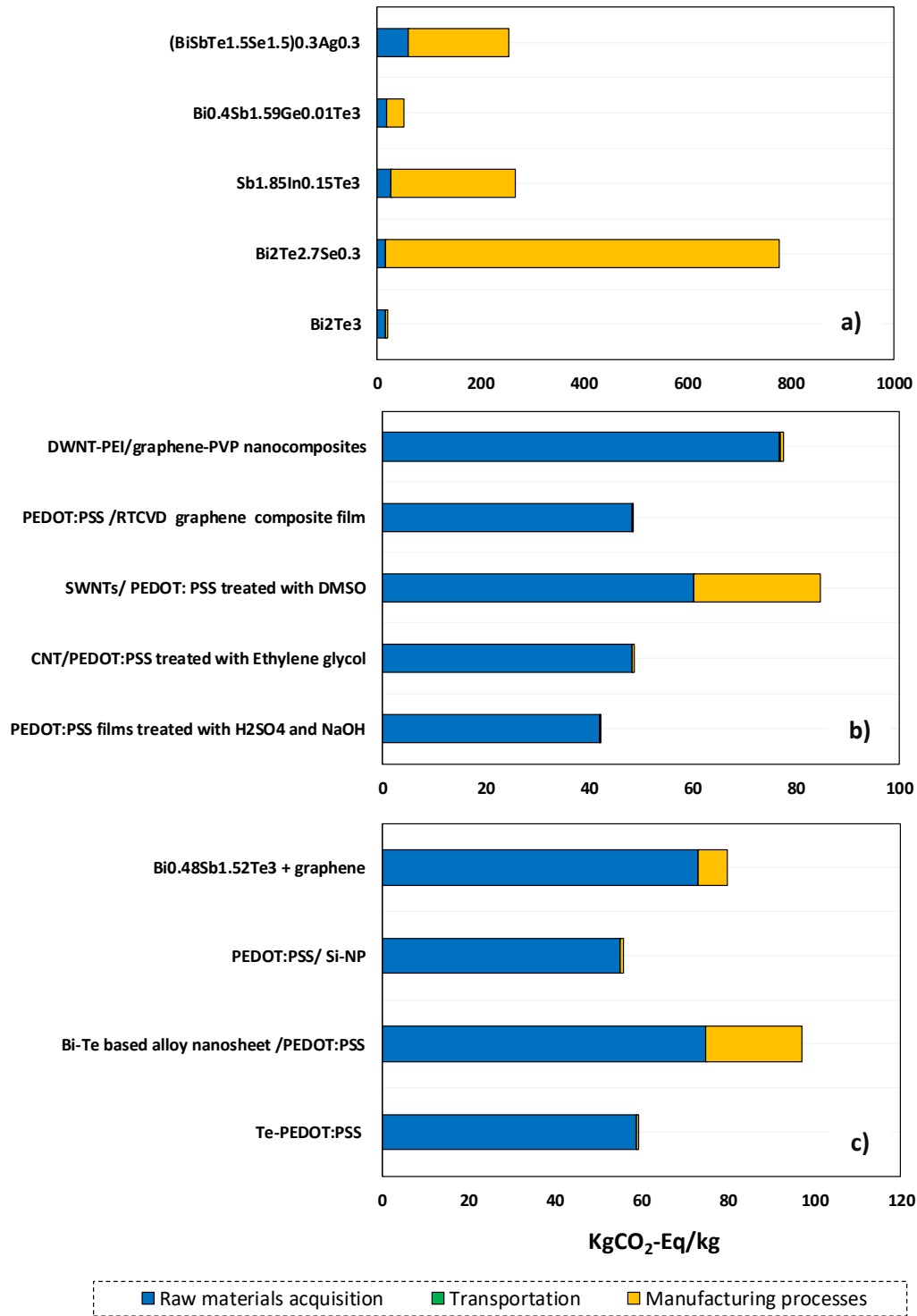


Fig. 71: The share of different phases of the TE materials production in the impact category of GWP: a) inorganic; b) organic; and c) hybrid TE materials.

Table 16: Summary of the equivalent CO₂ emission of the TE materials at the production stage.

Type	TE material	GWP (kgCO ₂ -Eq/kg)
Inorganic	(BiSbTe _{1.5} Se _{1.5}) _{0.3} Ag _{0.3}	254
	Bi _{0.4} Sb _{1.59} Ge _{0.01} Te ₃	52.1
	Sb _{1.85} In _{0.15} Te ₃	266
	Bi ₂ Te _{2.7} Se _{0.3}	777
	Bi ₂ Te ₃	20.2
Organic	DWNT-PEI/graphene-PVP nanocomposites	77.7
	PEDOT:PSS /RTCVD graphene composite film	48.5
	SWNTs/ PEDOT: PSS treated with DMSO	84.7
	CNT/PEDOT:PSS treated with Ethylene glycol	48.7
	PEDOT:PSS films treated with H ₂ SO ₄ and NaOH	42.2
Hybrid	Bi _{0.48} Sb _{1.52} Te ₃ + graphene	79.9
	PEDOT:PSS/ Si-NP	55.7
	Bi-Te based alloy nanosheet /PEDOT:PSS	110
	Te-PEDOT:PSS	59.2

7.5.4 Ozone depletion potential (ODP)

Fig.72 displays the contribution of each phases of the production stage to the ozone depletion. In addition, Table 17 summarizes the total ozone depletion potential of the TE materials at their production stage. Overall, the ozone depletion potential of all the studied TE materials was remarkably low. However, among the three types of the TE materials, in general, the inorganic type depicted higher risk of the ODP. To specify, apart from Bi₂Te₃ and Bi_{0.4}Sb_{1.59}Ge_{0.01}Te₃, the total ODP of the studied inorganic materials was in a range of between 60 and 180 E-13 × kg (R11 eq.). Whereas, this range was between 10 and 25 E-13 × kg (R11 eq.) for the organic and hybrid TE materials. Therefore, Bi₂Te₃ and Bi_{0.4}Sb_{1.59}Ge_{0.01}Te₃ were exceptions that their ODP competed with that of their organic and hybrid counterparts. To specify, Bi₂Te₃ achieved the most optimum ODP among the three types with nearly 5 E-13 × kg (R11 eq.). In addition, the ODP of Bi_{0.4}Sb_{1.59}Ge_{0.01}Te₃ was in the same range of that of the organic and hybrid types with 12 E-13 × kg (R11 eq.).

Regarding the contribution of each phases of the production stage to the ozone layer depletion, the raw material acquisition of the organic and hybrid types could cause greater ozone depletion than their manufacturing processes. Precisely, the raw materials supply and the manufacturing

processes of these two types were responsible for 98% and 2% of their total ODP, respectively. However, the contribution of the manufacturing process to ODP reached up to 30% for some organic and hybrid TE materials. Conversely, the manufacturing phase was responsible for the greatest ozone layer degradation in the inorganic type. To specify, the manufacturing processes of the inorganic TE materials accounted for at least 65% of their total ODP. However, Bi_2Te_3 was an exception as its ODP pattern followed that of the organic and hybrid TE materials. In particular, the raw material acquisition of Bi_2Te_3 was most influential on the ozone depletion than its manufacturing processes. Concerning the transportation phase, its effect on the ODP of the TE materials was negligible.

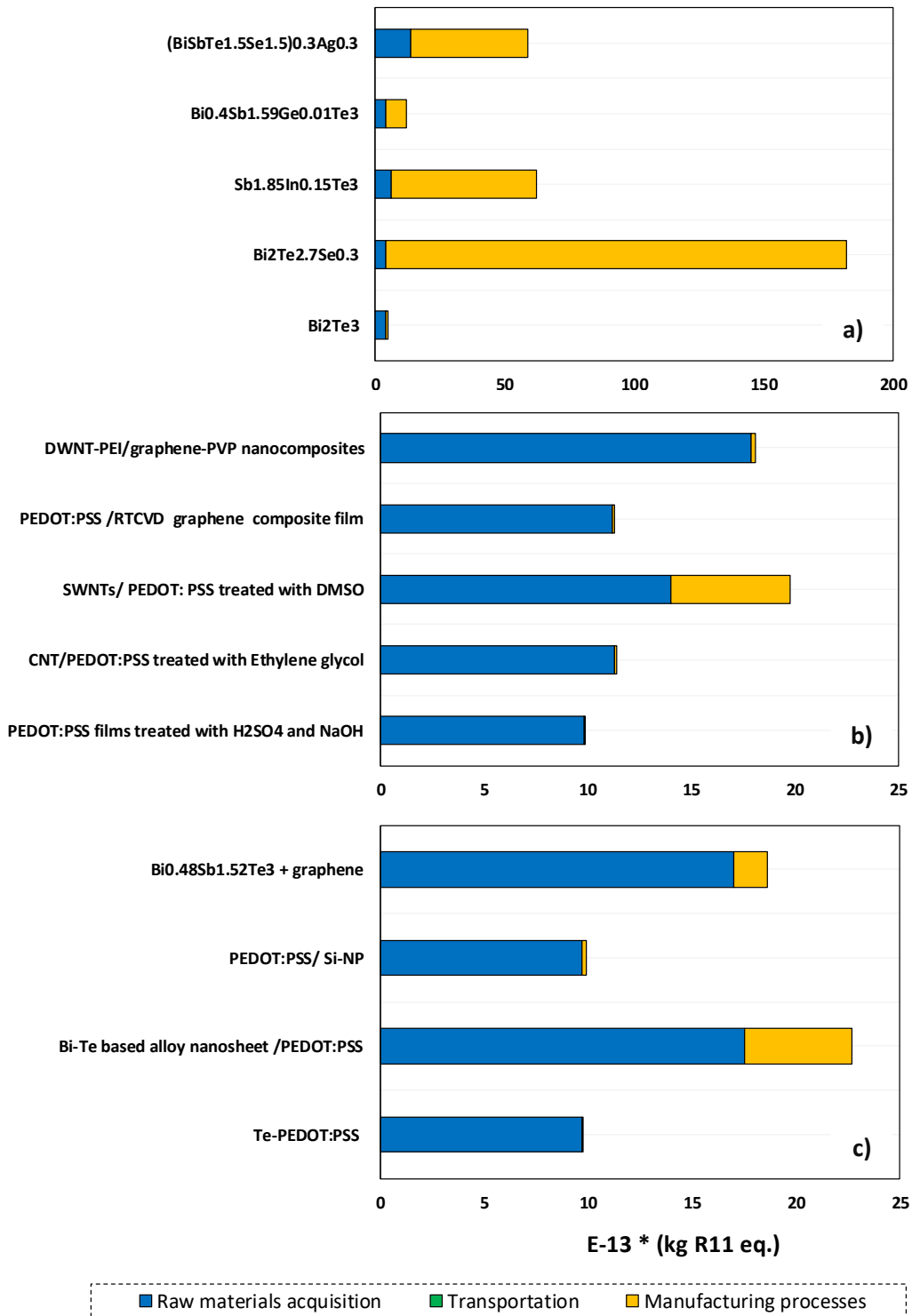


Fig. 72: The share of different phases of the TE materials production in the impact category of ODP: a) inorganic; b) organic; and c) hybrid TE materials.

Table 17: Summary of the ozone depletion potential of the TE materials at the product stage.

Type	TE material	ODP E-13× kg (R11 eq.)
Inorganic	(BiSbTe _{1.5} Se _{1.5}) _{0.3} Ag _{0.3}	58.9
	Bi _{0.4} Sb _{1.59} Ge _{0.01} Te ₃	11.89
	Sb _{1.85} In _{0.15} Te ₃	62.29
	Bi ₂ Te _{2.7} Se _{0.3}	182
	Bi ₂ Te ₃	4.7
Organic	DWNT-PEI/graphene-PVP nanocomposites	18.08
	PEDOT:PSS /RTCVD graphene composite film	11.27
	SWNTs/ PEDOT: PSS treated with DMSO	19.76
	CNT/PEDOT:PSS treated with Ethylene glycol	11.38
	PEDOT:PSS films treated with H ₂ SO ₄ and NaOH	9.86
Hybrid	Bi _{0.48} Sb _{1.52} Te ₃ + graphene	18.62
	PEDOT:PSS/ Si-NP	9.89
	Bi-Te based alloy nanosheet /PEDOT:PSS	22.66
	Te-PEDOT:PSS	9.77

7.5.5 Human toxicity potential (HTP)

[Fig.73](#) displays the contribution of each phases of the production stage to the human toxicity potential. In addition, [Table 18](#) summarizes the total human toxicity potential of the TE materials at their production stage. Overall, the human toxicity potential of the inorganic type was at least 3 times greater than that of the organic and hybrid types. In particular, the HTP of the inorganic type varied in a range of between 16 and 52 kg (DCB eq.), whilst it was between 2 to 5 kg (DCB eq.) and 3 to 6 kg (DCB eq.) for the organic and hybrid types, respectively. However, in spite of belonging to the inorganic category, Bi₂Te₃ was reported as the least toxic TE material with 1.3 kg (DCB eq.) HTP. Also, Bi_{0.4}Sb_{1.59}Ge_{0.01}Te₃ was another inorganic TE material that its 3.3 (DCB eq.) HTP was competitive with that of its organic and hybrid counterparts.

Concerning the inorganic TE materials, their manufacturing processes caused 2 times greater HTP than their raw materials supply. It should be noted that this ratio was 45 times greater for some inorganic TE materials. However, Bi₂Te₃ was an exception that its manufacturing process resulted in lower HTP compared with its raw materials supply. In contrary, supplying the raw materials of the organic and hybrid TE materials accounted for at least 70% of their total HTP. In other words,

compared with the manufacturing processes, supplying the raw materials of the organic and hybrid types impacted more on their total HTP. Furthermore, the share of transportation on the total HTP of all the studied TE materials was insignificant compared with the other two phases of the production stage.

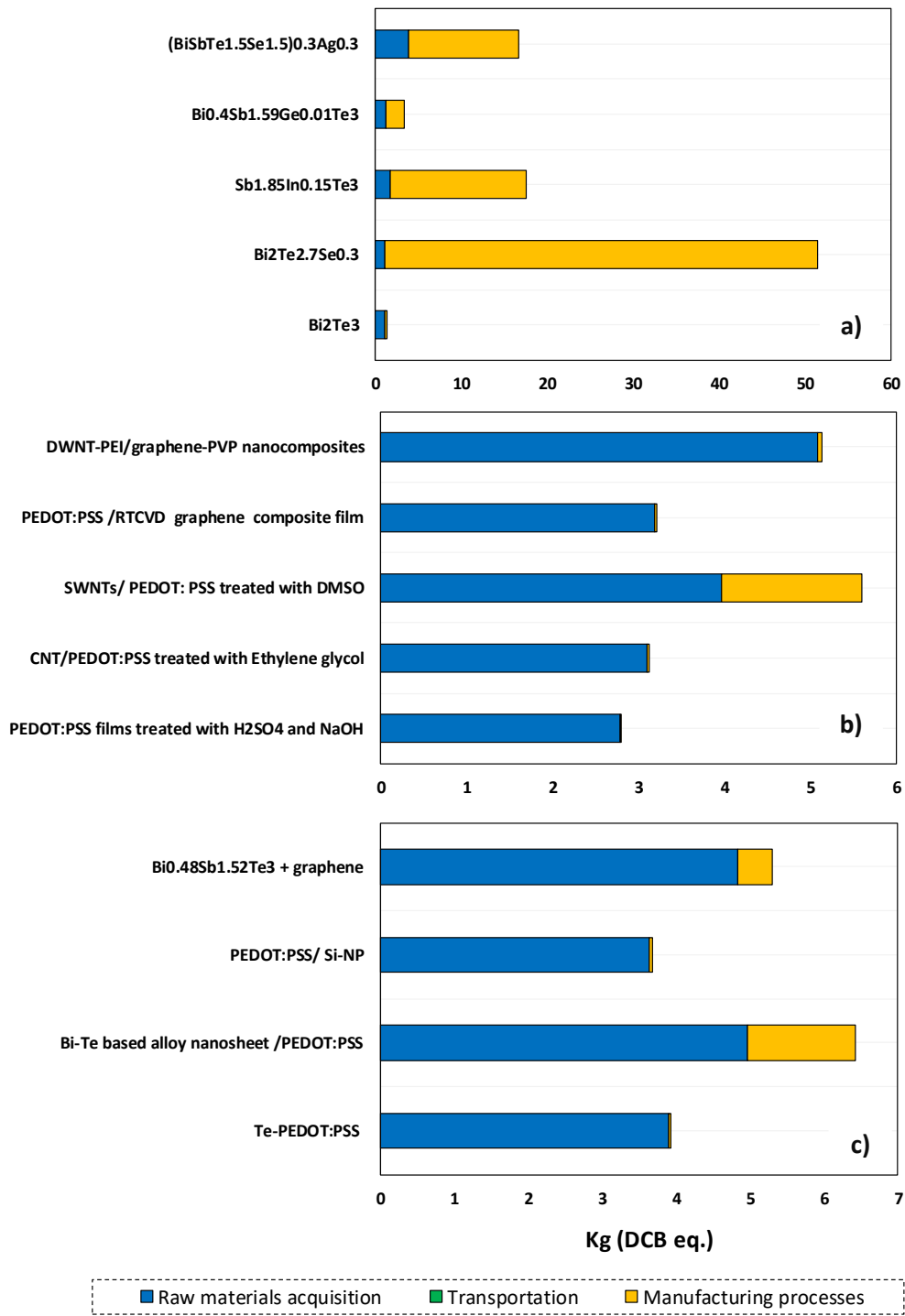


Fig. 73:The share of different phases of the TE materials production in the impact category of HTP: a) inorganic; b) organic; and c) hybrid TE materials.

Table 18: Summary of the human toxicity potential of the TE materials at the product stage.

Type	TE material	HTP kg (DCB eq.)
Inorganic	(BiSbTe _{1.5} Se _{1.5}) _{0.3} Ag _{0.3}	16.64
	Bi _{0.4} Sb _{1.59} Ge _{0.01} Te ₃	3.36
	Sb _{1.85} In _{0.15} Te ₃	17.59
	Bi ₂ Te _{2.7} Se _{0.3}	51.5
	Bi ₂ Te ₃	1.33
Organic	DWNT-PEI/graphene-PVP nanocomposites	5.14
	PEDOT:PSS /RTCVD graphene composite film	3.2
	SWNTs/ PEDOT: PSS treated with DMSO	5.6
	CNT/PEDOT:PSS treated with Ethylene glycol	3.12
	PEDOT:PSS films treated with H ₂ SO ₄ and NaOH	2.78
Hybrid	Bi _{0.48} Sb _{1.52} Te ₃ + graphene	5.29
	PEDOT:PSS/ Si-NP	3.67
	Bi-Te based alloy nanosheet /PEDOT:PSS	6.42
	Te-PEDOT:PSS	3.92

7.6 Summary

As discussed in this chapter, the inorganic TE materials accounted for considerably greater life cycle impact compared with their organic and hybrid counterparts. This was primarily because the manufacturing phase of the inorganic TE materials was extremely high energy consuming, which was the exact converse of that of the organic and hybrid types. To put it another way, in comparison with the organic and hybrid types, the inorganic TE materials required greater amount of resources to generate energy to accomplish their manufacturing processes. Thus, the manufacturing phase of the inorganic type contributed to their highest life cycle impact. Conversely, the greatest resource requirement of the organic and hybrid TE materials was attributed to their raw materials supply. Therefore, the raw materials supply was responsible for the greatest life cycle impact of the organic and hybrid TE materials. As a result, to optimize the life cycle impact of the inorganic type, the focus should be on their manufacturing processes. Whereas, the most environmentally critical stage of the organic and hybrid types was their raw materials supply.

As can be seen from the graphs, although the life cycle impacts of the organic and hybrid TE materials were nearly in the same range, there was a great difference between those of the inorganic type. This huge difference could not be related to the inventory data list of their raw materials supply. To prove it, not only the same database (CES EduPackTM 2018) was used for preparing this inventory data list, but also the list included all the raw materials required for preparing the TE materials. Therefore, not only there was no mismatch between the source of the data, but also there was no missing data on the required raw materials of the inorganic TE materials. Thus, the primary reason for this huge difference between the life cycle impacts of the inorganic materials could be attributed to the inventory list of their manufacturing processes that were collected from different literatures.

To specify, each literature applied a specific manufacturing processes to optimize the energy conversion efficiency of the inorganic TE materials. As a result, while some of the studied literatures employed high energy consuming manufacturing processes to optimize the energy conversion efficiency of the final material, the others used more energy efficient approaches to reach the same target. In fact, part of this difference in the manufacturing processes was inevitable as it was strongly dependent on the intrinsic properties of the input raw materials. Since the manufacturing processes of the inorganic TE materials were mostly machine-based, applying different manufacturing processes caused variation in the required machines, the associated energy consumptions, and the processing time. Therefore, this extensive difference in the life cycle impacts of the inorganic TE materials provides a room for future research on how a balance could be made between optimizing their energy conversion efficiencies and life cycle impacts.

Conversely, the main approach for optimizing the energy conversion efficiency of the organic TE materials was varying their input raw materials. Based on the relevant literatures, although organic TE materials required a great number of raw materials, their manufacturing processes were mostly manual and less machine-based. This was mainly attributed to the intrinsic properties of the organic TE materials. As a result, the life cycle impacts of the organic TE materials were almost in the same range. The remaining difference between their life cycle impact could be related to two reasons. First, the difference in the nature of their input raw materials, which strongly impacted on their manufacturing processes and processing time. Second, the raw materials of some organic and hybrid TE materials were eliminated from the assessment due to lack of data on them. In total,

the outcomes of this chapter is in congruence with the extensive ongoing researches on replacing the inorganic TE materials with the organic and hybrid ones. However, this chapter also proved that Bi_2Te_3 , which is the most conventional inorganic TE material, is the only exception that its low life cycle impact could compete with that of the organic and hybrid types.

Chapter 8

The Lightweight Integrating Substrate

8.1 Introduction

To meet the aim of this research, which is powering a heating armband with a set of TEGs and a rechargeable battery, the TEGs were considered to be incorporated into a whole with a lightweight substrate. To specify, integrating the TEGs as one piece was essential to prevent their individual displacement by the force of an impact to the power supply (i.e. the power box). Furthermore, in accordance with the determined design for the power box, the lightweight substrate served also as a thermal barrier between the hot plate and the fan to avoid cooling down the former by the latter. In addition, it was determined to prepare the substrate from a lightweight material to minimize the weight of the power supply that is in the shape of a benchtop power box. Notably, it was of critical importance to avoid any negative effects by the lightweight substrate on the conversion efficiency of the TEGs. To satisfy the weight requirement of the substrate, one promising approach is to fully enclose the ingot-shaped TE legs with the stretchable elastomer called PDMS [325-327], as reviewed in Chapter 5. To illustrate, PDMS features softness, stretch ability, electrical insulation, non-toxicity, and easy processing [328]. However, several researches proved the negative effect of fully covering the legs with the PDMS substrate on the output power of the TEGs.

To clarify, Shi et al. [329] carried out an investigation to find out the relationship between encapsulating the TE legs with PDMS and the output voltage of the TEGs. The results indicated that the output voltage of the air-exposed legs was superior to that of the PDMS coated legs in all the determined boundary conditions. Precisely, at 30 °C temperature difference, the measured output voltage of the encapsulated legs was 3.20 mV that was approximately 7% lower than that of the air-exposed legs. Likewise, Hyland et al. [243] enclosed the TE legs of a TEG in a PDMS layer to explore its impact on the electricity performance of the TEG, resulting in a negative effect. To specify, the output power of the PDMS coated legs was 12% lower than that of the air-exposed legs. In addition, Suarez et al. [31] compared the effect of surrounding the legs with different types of materials, including air and PDMS. The results attested that surrounding the legs with air stood first concerning the maximum output power. Therefore, the outcomes of these researches are consistent with each other regarding the negative effect of fully coating the legs with PDMS on the output power of the TEGs. This is mainly attributed to the higher thermal conductivity of PDMS (0.15-0.2 W/m.K [328]) than air (0.025 W/m.K [31]). Precisely, the air layer surrounding the legs of a conventional TEG possesses lower thermal conductivity than the PDMS substrate.

Therefore, the PDMS substrate performs as a thermal bridge, transferring the heat from the hot side to the cold side of the TEG faster than the air layer. As a result, the temperature difference along the PDMS coated legs is lower than that of the air-exposed one, resulting in an inevitable lower output power of the former than the latter [329]. In a recent study, Lv et al. [330] replaced PDMS with low thermal conductivity fillers, such as aerogel and fibre glasses. Although the authors proved that coating the air-exposed legs with an aerogel layer improved the efficiency of the TEG by 8.22%, this improvement was achieved at temperature differences higher than 150 °C. However, in this study, the maximum temperature difference between the heat source (i.e. the candle) and the cooling ambient (i.e. air) is kept below 150 °C to avoid any damages to the TEGs in long term.

Getting back to the disadvantage of fully enclosing the legs with a PDMS substrate, it is apparent that no previous study has replaced this homogeneous boundary condition by a non-homogeneous one to improve the conversion efficiency of the TEG. Precisely, instead of fully coating the legs with a plain PDMS substrate, no previous study segmented the substrate to vary the thermal boundary condition along the legs. To fill this gap, this chapter aims to provide a nonhomogeneous boundary condition along the legs with a PDMS substrate. In particular, it is suggested to vary the boundary condition along the legs concerning three variables: 1) partially covering the legs with the PDMS substrate; 2) changing the coating region of the PDMS substrate; and 3) varying the thermal conductivity of the PDMS substrate by adding different fillers to it.

8.2 Device overview

Herein, the required energy is considered to be generated with a commercial TE module (GM 250-71-14-16), consisting of 71 pairs of *p*- and *n*-type Bi₂Te₃-based legs [331]. The TE legs with the dimensions of 1.4mm (width) × 1.4 mm (length) × 1.6 mm (height) were electrically connected together in series with 0.1mm thick copper strips. Then, the TE legs and the electrodes were sandwiched between two aluminium oxide (Al₂O₃)-based substrates, resulting in a TEG with the dimensions of 30 mm (width) × 30 mm (length) × 3.8 mm (height). To measure the thermal conductivity (λ), the Seebeck coefficient (α), and the electrical conductivity (σ) of the *p*- and *n*-type TE legs, the formulas and data provided by the manufacturer [332] were employed.

Since a too small size sample reduces the power of the study and increases the margin of error, it was determined to increase the height of the legs. Accordingly, another TEG was glued on the cold substrate of the first one, resulted in a two stage cascaded TEG with 142 pairs TE legs, see Fig.74. In particular, the outcomes of this two stage cascaded TEG could be applied to a one stage TEG since the variables only focused on the boundary conditions along the legs, but not the height of the legs. In particular, whilst the boundary condition along the legs varied over the tests, the height of the legs remained constant. It should be added that selecting this TE module with its cross-plane configuration and Bi₂Te₃-based TE material is based on three main reasons. First, as demonstrated in Chapter 4, the inorganic TE materials benefit from a greater $Z\bar{T}$ value and power factor than the organic and hybrid ones. Second, the cross plane TEGs benefit from higher power generation than the in-plane ones, as illustrated in Chapter 5. Third, Bi₂Te₃ causes the lowest negative environmental impacts among all the three type of the TE materials, as presented in Chapter 7.

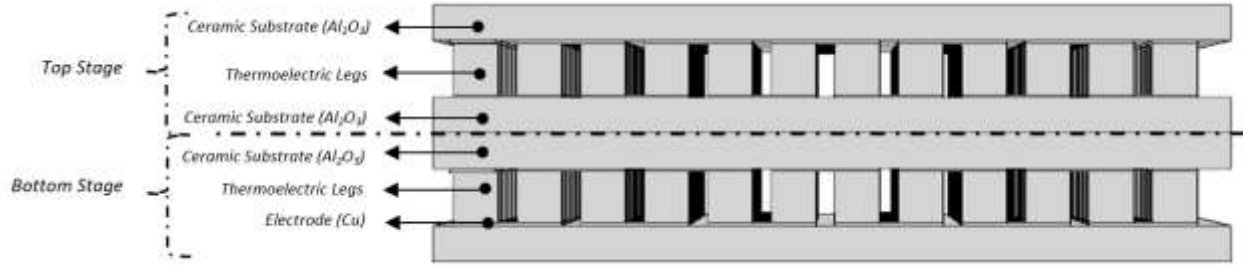


Fig. 74: The schematic of the two stage cascaded TEG fabricated for this chapter.

Along with the PDMS layer, a low density polyethylene (LDPE) sheet was also considered as the candidate to integrate the TEGs together. To provide a non-homogeneous thermal condition along the legs, the core strategy was coating the legs partially with the two considered lightweight substrates (i.e. PDMS and LDPE), separately. Accordingly, three different coating regions were specified for the substrates, including coating the top stage, the bottom stage, or both stages as Fig.75 shows. Notably, Model 1 was adopted as the reference model, and the configurations and properties of the TE legs and electrodes were stable in all the four models.

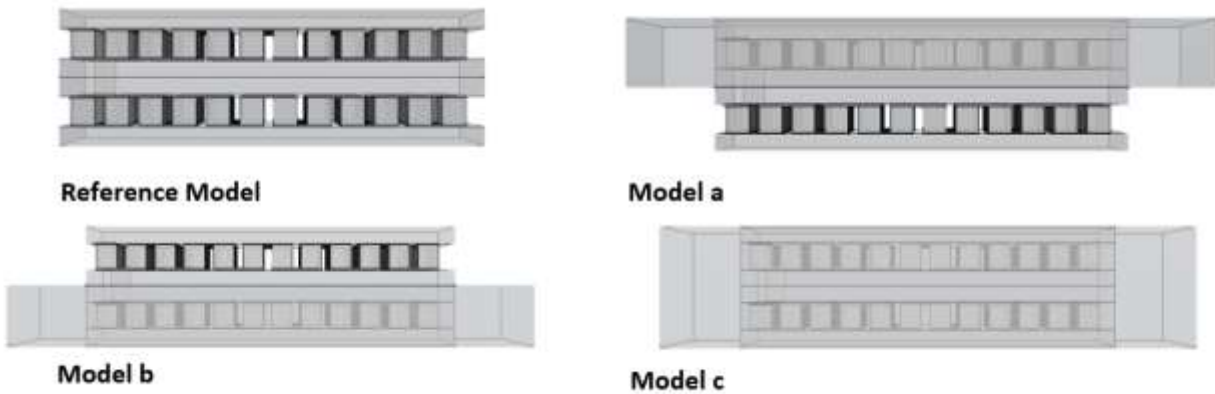


Fig. 75: The schematic diagram of the four specified models in COMSOL Multiphysics.: Model 1 (the reference model); Model a (the top stage coated); Model b (the bottom stage coated); and Model c (both stages coated).

To further manipulate the boundary condition along the legs, two fillers were separately added to the PDMS substrate with a weight percent of 50 (wt%). The fillers were gallium-based liquid alloy and air bubbles with 16.5 W/mK and 0.026 W/mK thermal conductivities, respectively. Based on the provided equations in the TEG’s manufacturer datasheet [332] and the applied hot temperature, the thermal conductivity (λ), the Seebeck coefficient (α), and the electrical conductivity (σ) of the *p*- and *n*-type Bi₂Te₃-based legs were calculated. In fact, in reality these TE properties are

temperature dependent, meaning they vary based on temperature changes. However, for the sake of simplicity, they were determined to be temperature independent in the simulations. Table 19 summarizes some properties of the materials used for fabrication of the samples. In addition, Table 20 illustrates the thirteen specified samples concerning the coating region of the integrating substrates and the added fillers. Using COMSOL Multiphysics, the mean effective thermal conductivity of the integrating substrate of models 2 to 5 were 0.15 W/mK, 0.085 W/mK, 8.32 W/mK, and 0.33 W/mK, respectively.

Table 19: Details regarding material’s parameters used in the manufacturing and analysis.

Geometry	Material	α ($\mu\text{V/K}$)	σ (S/cm)	λ (W/mK)	ρ (kg/m ³)	c (J/kg*K)
P leg	p-Bi ₂ Te ₃	189	127e ²	1.65	7700	154
N leg	n-Bi ₂ Te ₃	-210	108e ²	1.67	7700	154
Electrode	Cu	-	599800	400	8960	385
Rigid Substrate	Al ₂ O ₃	-	-	35	3965	730
Thermal glue	ArcticSilver® 5	-	-	1.7	-	-
Coating Substrate	PDMS	-	1e ⁻¹⁵	0.2	970	1460
Coating Substrate	LDPE	-	-	0.33	920	2100
Filler 1	Air	-	-	0.026	1.2	1005
Filler 2	Galinstan	-	3.3e ³	16.5	6440	296

Table 20: The codes of the prepared samples based on the coating region and the added filler.

Sample ID	Plain PDMS			Air Bubble +PDMS			Galinstan+ PDMS			LDPE		
	Top	Bottom	Both	Top	Bottom	Both	Top	Bottom	Both	Top	Bottom	Both
1(reference)	-	-	-	-	-	-	-	-	-	-	-	-
2a	✓	-	-	-	-	-	-	-	-	-	-	-
2b	-	✓	-	-	-	-	-	-	-	-	-	-
2c	-	-	✓	-	-	-	-	-	-	-	-	-
3a	-	-	-	✓	-	-	-	-	-	-	-	-
3b	-	-	-	-	✓	-	-	-	-	-	-	-
3c	-	-	-	-	-	✓	-	-	-	-	-	-
4a	-	-	-	-	-	-	✓	-	-	-	-	-
4b	-	-	-	-	-	-	-	✓	-	-	-	-
4c	-	-	-	-	-	-	-	-	✓	-	-	-
5a	-	-	-	-	-	-	-	-	-	✓	-	-
5b	-	-	-	-	-	-	-	-	-	-	✓	-
5c	-	-	-	-	-	-	-	-	-	-	-	✓

8.3 Numerical modeling

8.3.1 Governing equation

A finite element multi-physics program called COMSOL™ was used to develop the numerical modelling of this study. This was mainly because this programme benefits from the required physics (i.e. Heat transfer and Electric current) and the coupling Mulyphysics (i.e. Thermoelectric Effect). Regarding the finite element modelling, the heat transfer formulas are combined with an electrical phenomena to model the TE effect (i.e. the Seebeck effect) [333]. Therefore, simulating a TEG in COMSOL Multiphysics, it is required to integrate the thermal and the electrical phenomena of the system together with a solution containing partial differential equations [334]. Such a solution spatially distributes the temperature (T) and the electric potential (V). In this study, a steady state finite element model was assumed to compute the temperature and the electric potential values corresponding to the spatial coordinates. Accordingly, the employed physics to study the TE effect of the samples were *Heat transfer in porous/solid media* and *Electric currents*. To couple these two physics together, COMSOL benefits from an arbitrary Multiphysics called *Thermoelectric Effect*. In what follows, each of these physics and Mutliphysics are explained in more detail.

8.3.2 Physic 1: Heat transfer in solids

The employed physic to compute the heat transfer in Models 1, 2, and 5 was *Heat transfer in solid media*. Selecting the *Heat transfer in solid media* was attributed to the homogeneous materials of these Models, comprising solid materials with no fluid phase. Accordingly, the following equations were used by COMSOL to solve the heat transfer of these Models:

$$\rho c_p \frac{\partial T}{\partial t} + \nabla \cdot \mathbf{q} = Q \quad (6)$$

$$\mathbf{q} = -k\nabla T + \alpha T \mathbf{j} \quad (7)$$

where ρ , c_p , P , T , α , and Q represent the density (kg/m^3), the specific heat at a constant pressure (J/kg K), the Peltier coefficient (J/C), the temperature (K), the Seebeck effect ($\mu\text{V/K}$), and the extrinsic heat source (J), respectively. In Eq. (6), the first and the second terms describe the Fourier

heat conduction and the Peltier effect, respectively. Since the temperature distribution in a steady state solution depends on the very nature of the TE device, hence the heat balance equation changes to:

$$\nabla \cdot (-k\nabla T + \alpha T J) = Q \quad (8)$$

Notably, the energy accumulation term is equal to zero in a steady state operation, i.e.

$$-\nabla \cdot (k\nabla T) + \nabla \cdot (T\alpha J) = 0 \quad (9)$$

8.3.3 Physic 2: Heat transfer in porous media

To compute the heat transfer in Models 3 and 4, the employed physic was *Heat Transfer in porous media*. This was because these Models were composed of a nonhomogeneous substrate comprising both solid (i.e. PDMS substrate) and fluid (i.e. filler) parts. Thus, the conduction heat transfer occurred through both phases of these Models at the same time. Assuming the fast equilibration of the heat transfer between both phases, no heat was transferred from one phase to the other. Eqs. (10) and (11) present the formulas related to the heat transfer in the solid and fluid phases of the nonhomogeneous materials respectively, whilst the radiation heat transfer was ignored.

$$(1 - \varphi)(\rho c)_s \frac{\partial T_s}{\partial t} = (1 - \varphi) \nabla \cdot (k_s \nabla T_s) + (1 - \varphi) q_s^m \quad (10)$$

$$\varphi(\rho c_p)_f \frac{\partial T_f}{\partial t} + (\rho c_p)_f V \cdot \nabla T_f = \varphi \nabla \cdot (k_f \nabla T_f) + \varphi q_s^m \quad (11)$$

The subscripts s and f denote the solid and fluid phases of the materials respectively, c is the specific heat capacity of the solid phase (J/K), c_p is the specific heat at the constant pressure of the fluid phase (J/kg K), k is the thermal conductivity W/(m·K), ρ is the density (kg/m³), and q is heat generation per unit volume (J). Eqs. (10) and (11) were combined together since the heat transfer in both phases were in parallel, resulting in Eq. (12) where T_s and T_f were equal to T .

$$(\rho c_p)_m \frac{\partial T_f}{\partial t} + (\rho c_p)_f V \cdot \nabla T_f = \nabla \cdot (k_m \nabla T) + q_m^m \quad (12)$$

The second term on the left side of Eq. (12) denotes the energy transport owing to the fluid flow, and the first term on the right side of the same formula is the rate of the heat conduction in a unit volume of the fluid. Eqs. (13) to (15) define the overall heat capacity per unit volume, the overall thermal conductivity, and the overall heat production per unit volume of the porous medium, respectively. Herein, φ denotes the porosity of the medium.

$$(\rho c)_m = (1 - \varphi)(\rho c)_s + \varphi(\rho c_p)_f \quad (13)$$

$$k_m = (1 - \varphi)k_s + \varphi k_f \quad (14)$$

$$q_m^m = (1 - \varphi)q_s^m + \varphi q_f^m \quad (15)$$

8.3.4 Physic 3: Electric currents

Eq. (16) presents the current continuity principle:

$$\nabla J = 0 \quad (16)$$

where J is the electrical current density (A / m^2). For the TE devices, the current density is given by

$$J = -\sigma \nabla V - \sigma \alpha \nabla T \quad (17)$$

here σ , V , α , T are the electrical conductivity (S/cm), the electric potential (V), the Seebeck coefficient ($\mu V/K$), and the temperature (K), respectively. The first and the second terms in Eq. (17) describe the Ohm's law and the Seebeck effect, respectively. Notably, the Seebeck effect represents an "External Current Density" in COMSOL. However, since there was no external current density in the simulations, Eq. (17) changes to:

$$J = -\sigma \nabla V \quad (18)$$

Substituting Eq. (18) into Eq. (16) results in Eq. (19), which presents the electric potential distribution:

$$-\nabla \cdot (\sigma \cdot \nabla V) = 0 \quad (19)$$

8.3.5 Coupling multiphysics: thermoelectric effect

Solving the heat transfer and the electric currents equations at the same time, COMSOL offers a Multiphysics called *Thermoelectric Effect* to combine these equations together. Eqs. (20) and (21) present these coupled equations:

$$-\nabla \cdot ((\sigma S^2 T + \lambda) \nabla T) - \nabla \cdot (\sigma S T \nabla V) = \sigma ((\nabla V)^2 + S \nabla T \nabla V) \quad (20)$$

$$\nabla \cdot (\sigma S T \nabla V) + \nabla \cdot (\sigma \nabla V) = 0 \quad (21)$$

where σ , S , λ , V , and T are the electrical conductivity (S/cm), the Seebeck coefficient ($\mu\text{V}/\text{K}$), the thermal conductivity $\text{W}/(\text{m}\cdot\text{K})$, the voltage (V), and the temperature (K), respectively. These equations must first be transformed into the COMSOL's coefficient form for the arbitrary PDE-application mode, following Eq. (22):

$$C_a \frac{\partial^2 u}{\partial t^2} + d_a \frac{\partial u}{\partial t} + \nabla \cdot (-c \nabla u - \alpha u + \gamma) + \beta \cdot \nabla u + a u = f \quad (22)$$

The resulting coefficients for the TE field equations in the PDE form are:

$$c = \begin{pmatrix} \lambda + \sigma S^2 T & \sigma S T \\ \sigma S & \sigma \end{pmatrix} \quad (23)$$

$$f = \begin{pmatrix} \sigma ((\nabla V)^2 + S \nabla T \nabla V) \\ 0 \end{pmatrix} \quad (24)$$

And

$$d = \begin{pmatrix} \rho C \\ 0 \end{pmatrix} \quad (25)$$

where ρ and C are the density (kg/m^3) and the specific heat capacity (J/K), respectively. Coefficient d is equal with zero in the static conditions but for the transitional conditions incorporates the displacement current associated with the capacitive influences.

8.3.6 Boundary and initial conditions

Fig. 76 illustrates the boundary condition of the reference model, which was consistent in all the four models. To specify the temperatures of the hot and cold sides of the TEG, the hot side was considered to be heated at low temperature. This was because, in case of heating the hot side at high temperature, it was essential to cool down the cold side with a fan to avoid any damage to the TEG. To eliminate the cooling effect of the fan on the performance of the TEG, the hot side was heated at the low temperature of $33\text{ }^\circ\text{C}$ to avoid the fan requirement. Thus, the cold side was exposed to the ambient air with a constant temperature of $22\text{ }^\circ\text{C}$ (T_{cold}). Since the legs and the cold side of the TEG were cooler than the hot side, a heat flux was defined around them to simulate the heat dissipation. Simulating the TEGs' performance under the sitting and walking conditions, an external natural convection with 0 m/s speed and an external forced convection with 1.2 m/s airflow were specified for the heat flux, respectively. Since no external electric potential passed through the module, one surface of the n -type leg was grounded ($V=0$), resulting in the transformation of the potential current from the p -type legs to the n -type ones. To simplify the simulation, the properties of the TE material (Bi_2Te_3), including its thermal conductivity, electrical conductivity, and the Seebeck coefficient, were assumed to be temperature independent.

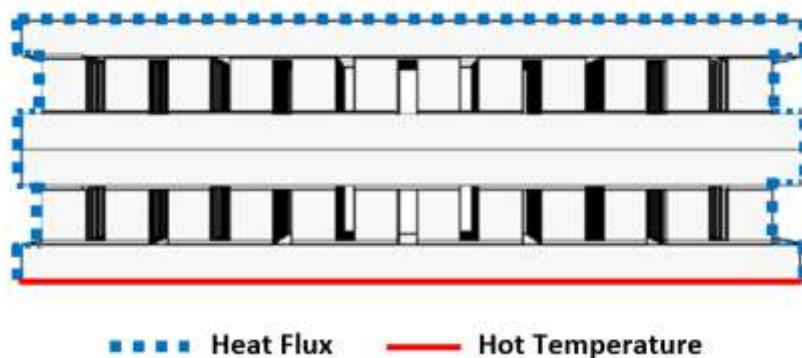


Fig. 76: The specified boundary conditions for the modelled samples in COMSOL.

8.3.7 Grid independence test and solution convergence analysis

Three grid sizes of 2.19 mm (i.e. the fine grid), 2.74 mm (i.e. the medium grid), and 4.11 mm (i.e. the course grid) with a triangular meshing structure in a 3D geometry were considered for the grid independence analysis. [Fig.77](#) **Fig. 77a** compares the mesh independence of the solution concerning the temperature in the middle of the TEG. Obviously, the results of the fine (i.e. 936275 cells) and the medium (i.e. 417100 cells) grids were almost identical, whilst the results of the coarse grid (i.e. 196638 cells) showed discrepancies with those of the finer grid. Therefore, being both accurate and time saving, the medium grid was selected for meshing the models in all simulations. [Fig.77b](#) presents the meshing of the reference model with the medium grid size.

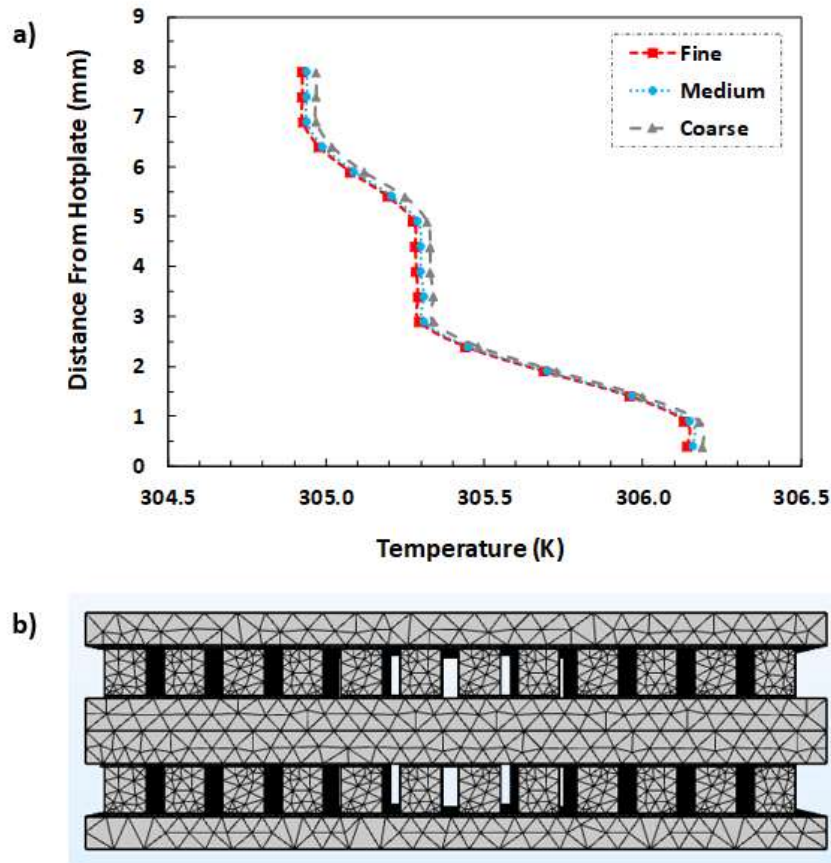


Fig. 77: a) Mesh sensitivity analysis results for the reference model; b) meshing the models with medium size grid.

The Segregated Solution approach, which is particularly appropriate for the Multiphysics systems, was determined to solve the non-linear equations of this study. Accordingly, the Segregated approach solved the two unknowns (i.e. the temperature and the electric potential) individually because each physics required specific iterative solver settings, depending on the nature of the involved governing equations. Thus, the Segregated approach solved each physics sequentially until the convergence occurred. Herein, the model was considered to be converged when the estimated errors in the iterative segregated solvers was within 10^{-4} . As Fig.78 shows, it took 13 iterations for the temperature and the electric potential solutions to converge.

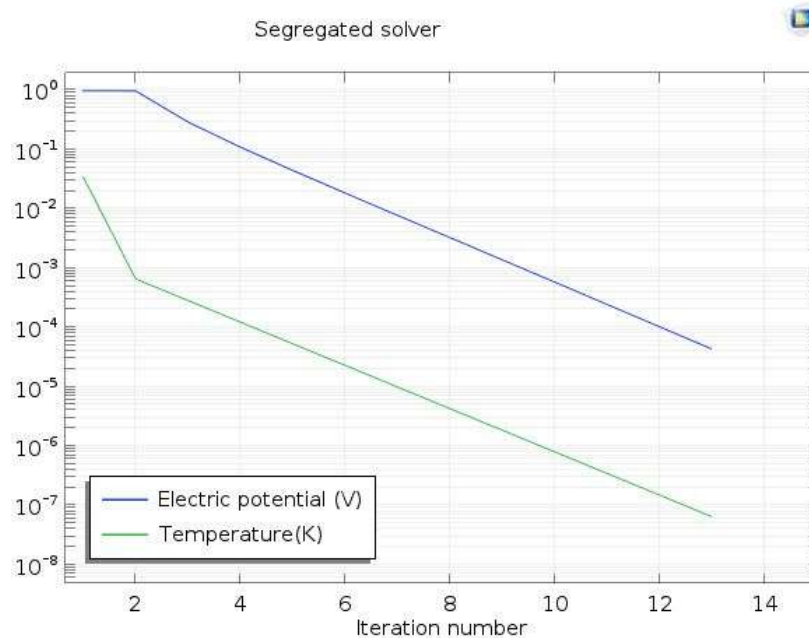


Fig. 78: The convergence monitoring of the electric potential and temperature (created automatically in COMSOL).

8.3.8 Results of the numerical simulation

8.3.8.1 Electrical current

[Fig.79](#) presents the minimum, average, and maximum electrical currents of the thirteen prepared samples under both the stagnant air and 1.2 m/s air speed. Accordingly, the samples were classified into five categories regarding the filler type (i.e. models 1 to 5), then each category was divided into three sub-categories (i.e. model a, b, or c) based on the covering region of the integrating substrate. Overall, the average currents of model 1 (i.e. the reference mode) ranked first under both the stagnant and flowing air conditions with 2mA and 6mA electrical currents, respectively. In the stagnant air, the filler type was ineffective on the output currents of the samples. Conversely, the covering region of the integrating substrate was influential on the samples' currents. To specify, in the still air, the first to third highest output currents were achieved by covering the top, bottom, and both stages of the samples, respectively.

At 1.2m/s air speed, both the covering region of the integrating substrate and the thermal conductivity of the fillers were influential on the output current of the samples. To specify, like the stagnant air condition, covering the top, bottom, and both stages of the samples resulted in the best to worst output currents, respectively. It is noteworthy that the highest difference between the

maximum and minimum currents of the samples was achieved by coating the top stage. As mentioned above, unlike the stagnant air condition, the output currents of the samples at 1.2 m/s air speed were also dependent on the thermal conductivity of the fillers. In this regard, the output current deteriorated by coating either the top or the bottom stages of the samples with a high thermal conductivity filler (i.e. Galinstan). In contrast, when both stages were covered with a high thermal conductivity filler, the electrical currents of the samples were improved.

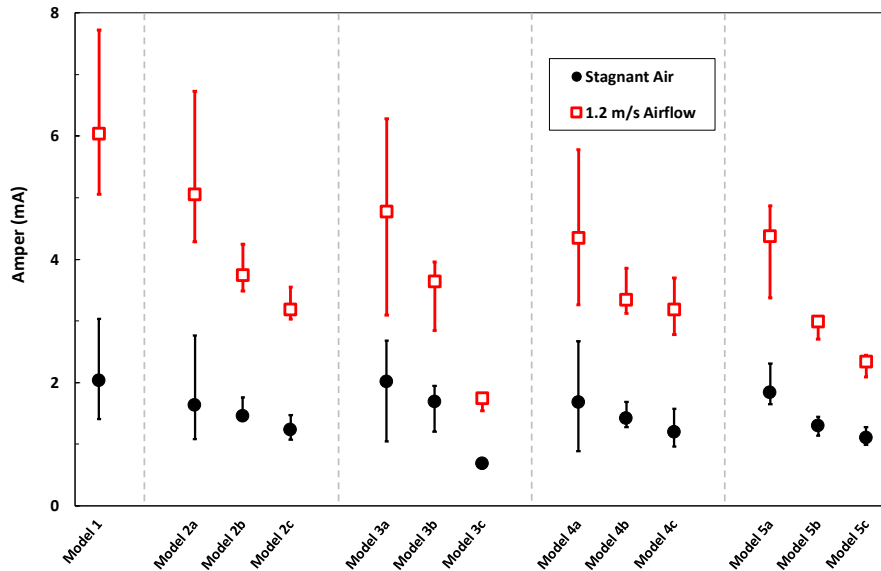


Fig. 79: Changes in the output currents of the simulated samples concerning different air flow conditions.

8.3.8.2 Electric potential

Fig.80 illustrates the output voltages of the thirteen samples at 0m/s and 1.2m/s air speeds. Overall, the highest output voltages at 0m/s and 1.2 m/s airflows were obtained by model 1 with nearly 30mV and 80mV, respectively. Furthermore, at both air speeds, covering the top stage resulted in 1.5 times greater output voltage than covering the bottom stage. Then, covering the bottom stage and both stages stood second and third specially at 1.2 m/s air speed. Notably, when both stages were covered, the effect of the filler type on the output voltage was most dominant at both air speeds. In addition, using a low thermal conductivity filler (i.e. air bubble) to cover both stages caused a negative effect on the output voltage. On the contrary, such a filler was appropriate for covering either the top or the bottom stages.

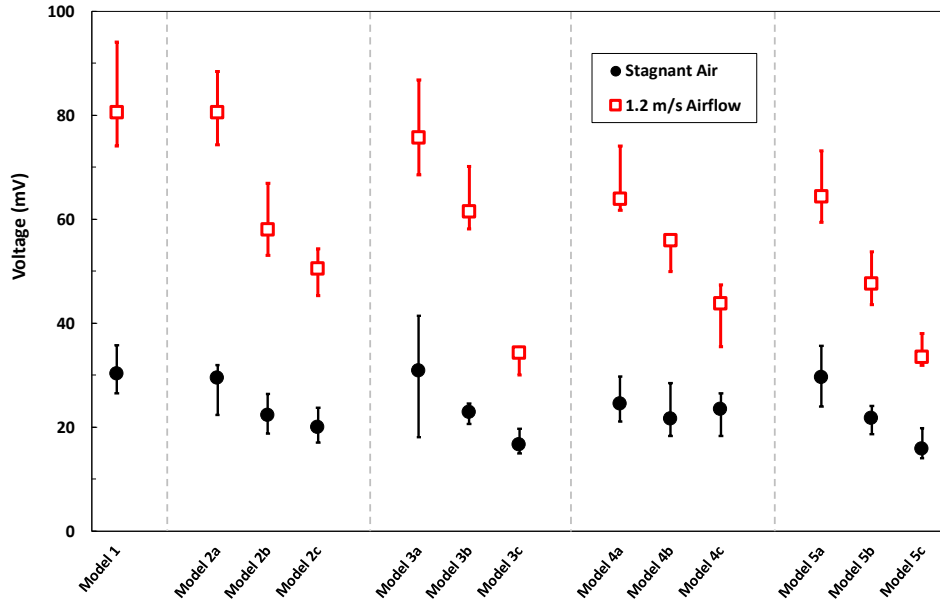


Fig. 80: Changes in the output voltage of the simulated samples concerning different air flow conditions.

8.3.8.3 Output Power

Fig.81 provides the output powers of the thirteen models at both 0m/s and 1.2m/s air velocities. Obviously, model 1 stood first by reaching the average output powers of 60mW and 500mW at 0m/s and 1.2m/s air speeds, respectively. Precisely, under both air conditions, the average output powers of model 1 were approximately 1.5 times greater than that of those stood second. After model 1, the best to worst samples were the top stage, the bottom stage, and the both stages covered samples, respectively. Under both air conditions, the impact of the covering region of the substrate on the output power was superior to the filler type. In addition, the covering region was more influential on the output power at 1.2m/s air speed. Regarding the correlation between the filler type and the covering region, filling either the top or the bottom stage with a relatively low thermal conductivity filler resulted in the highest output powers. On the contrary, it was superior to coat both stages with a relatively high thermal conductivity filler. In total, after model 1, the most optimum sample was the top stage covered sample with a low thermal conductivity filler (model 2a), obtaining the highest output powers at both air speeds.

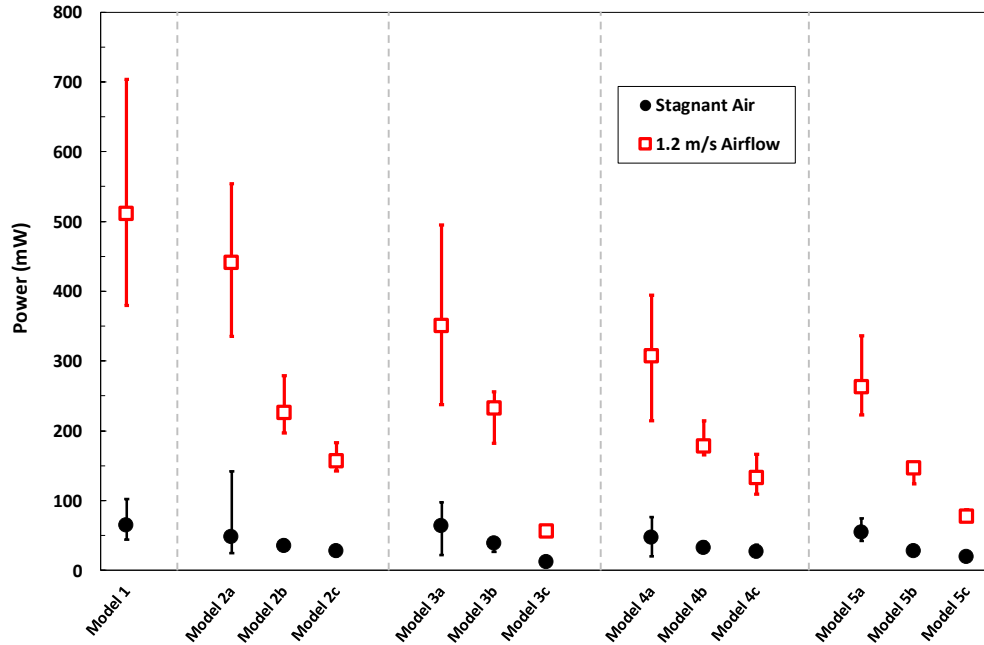


Fig. 81: Changes in the output power of the simulated samples concerning different air flow conditions.

8.4 Validation of the numerical modeling

To validate the numerical modeling, all the thirteen simulated samples were prepared in the lab and tested under the boundary and initial conditions similar to those of the computational modelling. Then, the results of the computational modelling and the lab tests were compared to each other.

8.4.1 Fabrication procedure

Fig.82 illustrates the general overview of the fabrication procedure of the thirteen samples in the lab, whilst the details of these fabrications are as follow:

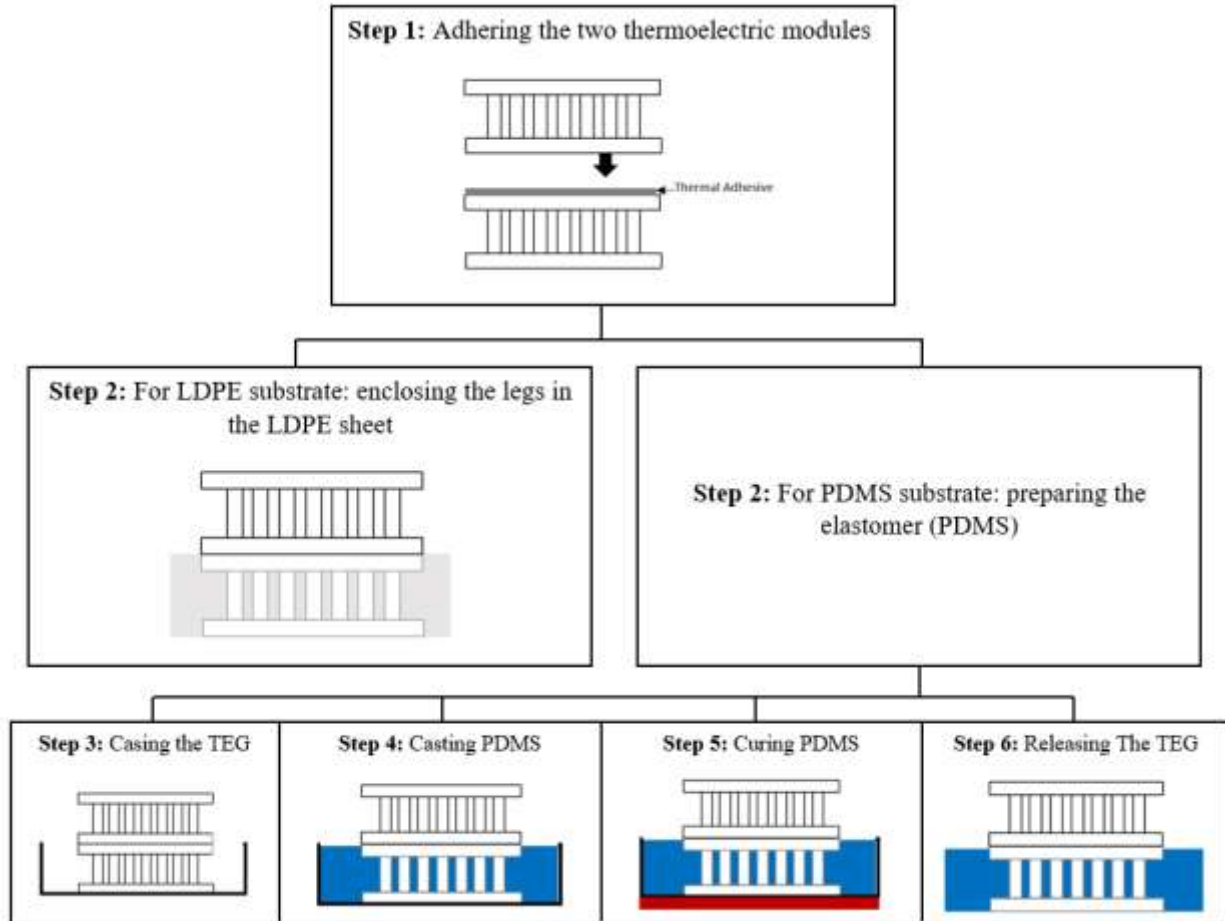


Fig. 82: Different stages and sub-stages of the fabrication procedure.

Step 1: Adhering the two TE modules together

First, a thin layer of ArcticSilver[®] 5 (as a thermal adhesive) was spread on the cold side of the TE module (GM 250-71-14-16). Then, the second TE module was placed from its hot side on the glued surface. After a while, the modules were completely stacked together at the lab's air temperature. Notably, the LDPE and PDMS substrates had two separate fabrication procedures in step 2.

Step 2 for the LDPE substrate: Enclosing the legs by the LDPE sheet

Following the surface area of the TEGs, a hole with the dimensions of 30 mm × 30 mm was punched in an LDPE sheet. Then, the punched sheet was passed through the TEGs to enclose the legs concerning the coating regions of the integrating substrates.

Step 2 for the PDMS substrate: Preparing the elastomer (PDMS)

To prepare the pristine PDMS and the air filled PDMS mixtures, the curing agent of PDMS was added to its silicone base (DOWSIL Sylgard 184) with a weight ratio of 1 to 3. Next, the materials were mixed rigorously together for 20 min by hand, forming air bubbles in the mixture. To prepare the Galinstan filled PDMS, the liquid alloy (Galinstan) and the silicone base of PDMS were initially mixed together by manual stirring, generating air bubbles in the mixture. Then, the mixture was stirred at higher speed with a magnetic stirrer for 10 min. After cooling down the mixture in the ambient room temperature for 30 min, the curing agent of PDMS was added to the mixture with a weight ratio of 18:1 and mixed with them by hand.

Step 3 for the PDMS substrate: Casing the cascaded TEG

Then, the fabricated cascaded TEG was placed inside a cubic silicon mould.

Step 4 for the PDMS substrate: Casting the PDMS mixture

Next, the as prepared PDMS mixtures were poured around the cascaded TEG separately regarding the determined coating regions.

Step 5 for the PDMS substrate: Curing the mixtures

Except the air filled PDMS samples, the ones coated with either pristine PDMS or Galinstan filled PDMS were placed in a $-20\text{ }^{\circ}\text{C}$ fridge for 6 hrs to remove the air bubbles from them. Then, all samples were cured on a $100\text{ }^{\circ}\text{C}$ hot plate for 2 hrs.

Step 6 for the PDMS substrate: Releasing the cascaded TEG

After curing the PDMS mixtures, the integrated TEG with the PDMS substrate were removed from the silicon mould. [Fig.83](#) presents the photos of the thirteen prepared samples.

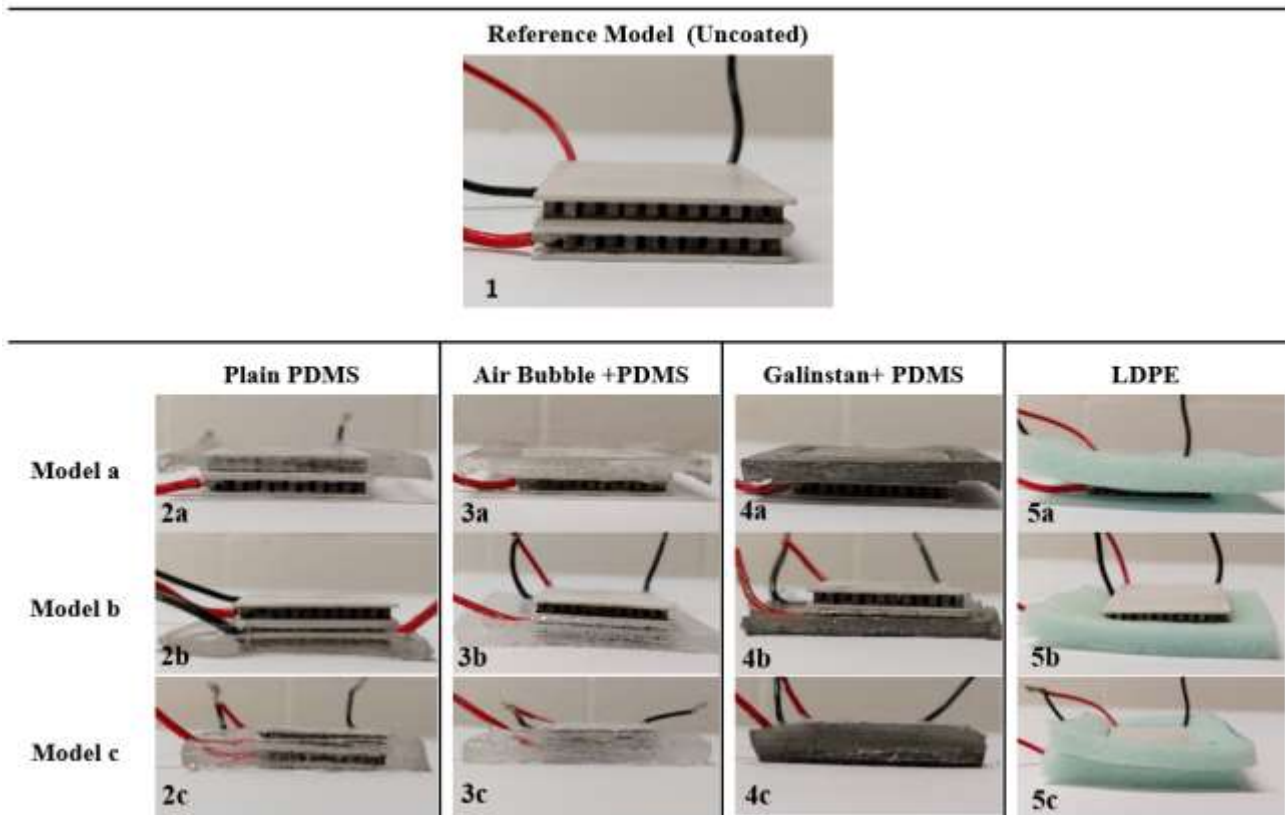


Fig. 83: Photographs of the thirteen prepared samples.

8.4.2 Equipment and testing condition

Following the boundary and thermal conditions of the numerical modelling, the samples were placed on a 33 °C hot plate to resemble the skin temperature, whilst the ambient temperature fluctuated between 21 °C and 23 °C. Notably, using a 4 channel thermometer (HH374) with $\pm 0.1\%$ of rdg +0.7 °C accuracy, the ambient and the hot plate's temperatures were being checked throughout the experiments. Resembling the sitting and walking conditions, all the prepared samples were characterized at 0 and 1.2 m/s air speeds, respectively. To maintain a uniform and linear airflow over the TEG at 1.2 m/s air speed, a mini wind tunnel was designed and fabricated

as Fig.84 illustrates. As it could be seen, the assembled mini wind tunnel is composed of five primary sections: Settling Chamber, Contraction Cone, Test Section, Diffuser, and a Micro Fan. Settling Chamber is at the very front of the wind tunnel, which straighten out the air and removes turbulence from incoming air. Contraction Section forces a large volume of air through a small opening in order to smoothly accelerates airflow in the tunnel. Test Section contains straight airflow for testing and is the place where the model is mounted on the hot plate. Diffuser is at the end of the Test Section, and keeps the air running smoothly as it goes toward the back. It also increases in volume in order to slow the air down as it exits the tunnel. A micro fan was used at the very back of the wind tunnel to pull air into the wind tunnel. Using a fan with three adjustable speeds, the required air flow (1.2 m/s) was generated in the tunnel. The design of each part depends on each other regarding various design parameters. However, herein, the contraction and the diffuser sections were made symmetric to provide a uniform air flow. The air velocity was measured above the samples by an anemometer (HHF81) having 3% accuracy. Using a multimeter/data logger (HHM-EX542) with $\pm 0.06\%$ accuracy, the obtained voltage and ampere of each experiment were recorded for 30 min at one-second interval. It is noteworthy that recording the output voltage and ampere were started after reaching a roughly stable condition (i.e. after ~30 min). Fig.85 depicts the tests' set up at 1.2 m/s air speed.

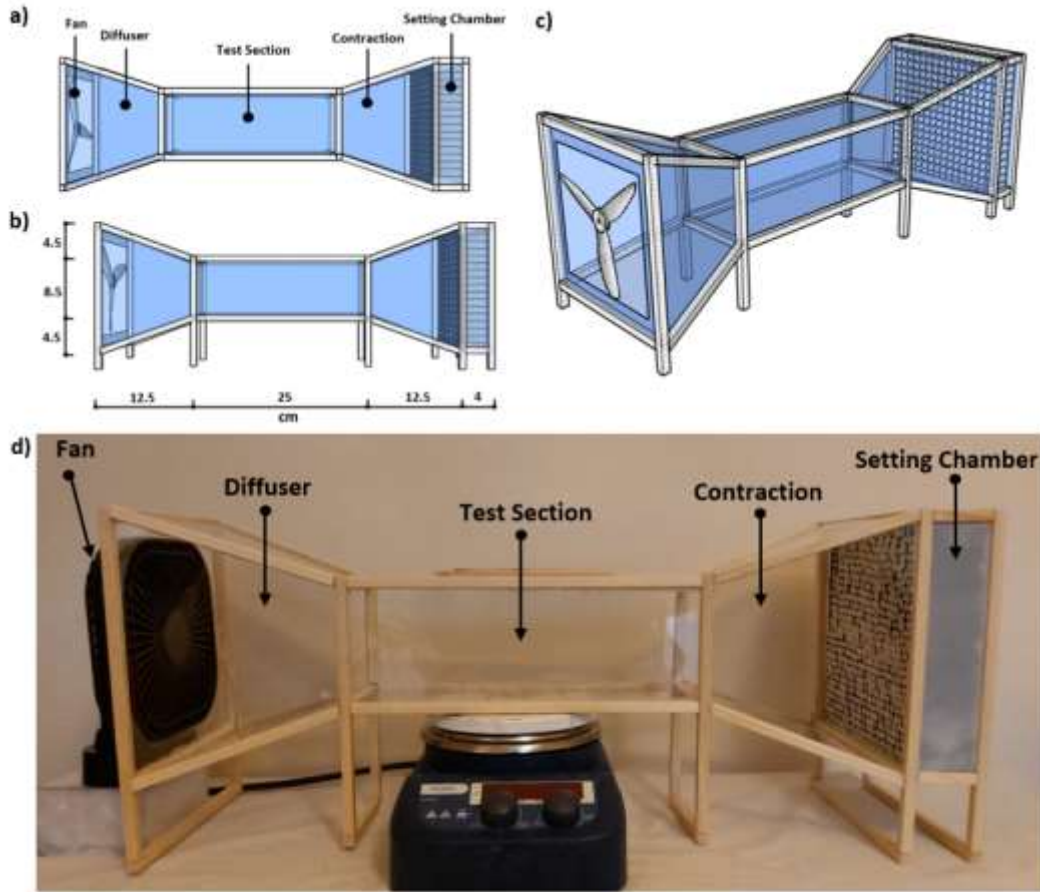


Fig. 84: Top: different views of the wind tunnel: a) the top view; b) the side view; and c) the perspective view; Bottom: d) the assembled wind tunnel.

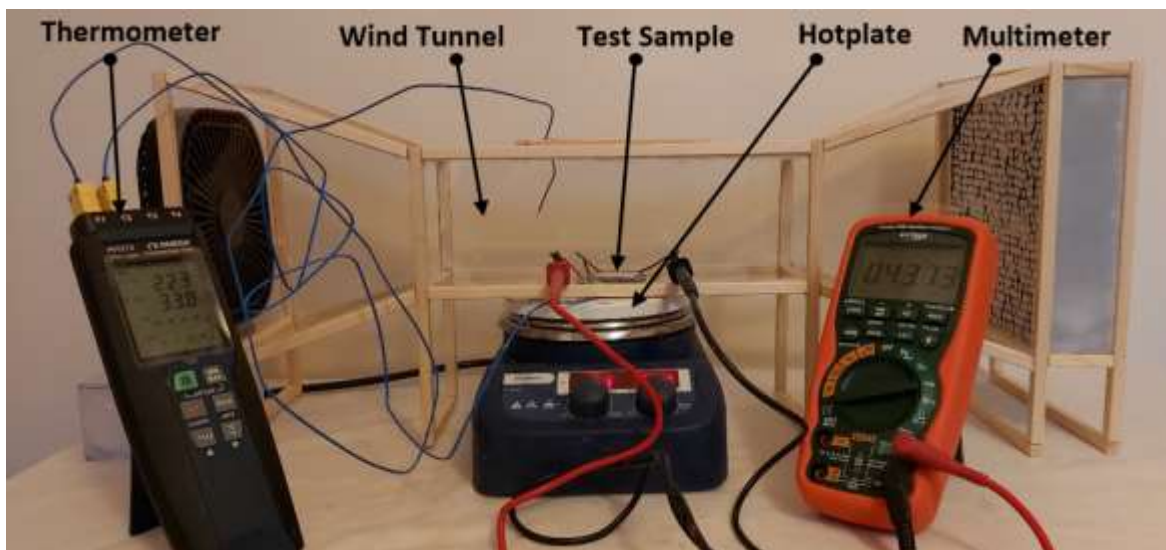


Fig. 85: Test-setup at 1.2 m/s air velocity.

8.4.3 Results of the experiments

8.4.3.1 Electrical current

[Fig.86a](#) depicts the average electrical currents generated by the top stage covered samples (i.e. models a). As mentioned before, model 1 was used as the reference model to analyse the outcomes of the other samples in comparison with its. Overall, the average output currents of all the five samples were almost in the same range of 2mA in the stagnant air. To specify, in the still air, neither covering the top stage nor varying the thermal conductivity of the integrating substrate had significant impact on the output current of the TEG. Raising the airflow speed to 1.2 m/s, the output currents of all samples considerably increased compared with those of at 0 m/s air speed. This was mainly attributed to the higher temperature difference between the hot and cold sides of the TEG, resulting in the higher output currents. In addition, at 1.2 m/s air speed, the difference between the output currents of the samples were greater than those of at the lower speed. Accordingly, the two highest output currents at 1.2 m/s air speed were $6.280\pm 0.013\text{mA}$ and $5.312\pm 0.011\text{mA}$ that were achieved by the reference model and model 2a, respectively.

Furthermore, models 4a and 5a with relatively higher thermal conductivity substrates than models 2a and 3a stood fourth and fifth concerning the highest output currents, respectively. As a result, covering the top stage of the TEG with a low thermal conductivity substrate resulted in greater output current compared with that of with a high thermal conductivity substrate. Based on these results, besides increasing the temperature gradient between the top and bottom stages of the TEG, it was also of critical importance to provide an adequate temperature difference along the legs of each stage. To clarify, as [Fig.87](#) illustrates, models 4a and 5a ranked the worst regarding the output current because in spite of having a considerable temperature difference between their two stages, there was an even thermal distribution along the legs of their upper stage. Following the same principle, the output current of model 2a was superior to that of model 3a, because not only the former provided an adequate temperature difference along the legs of each stage, but also it generated a higher temperature difference between its two stages.

[Fig.86b](#) illustrates the average electrical currents of the bottom stage covered samples (i.e. models b). Apparently, the electrical current of model 1 was superior to that of the other four samples

under both airflow conditions. Although model 1 exhibited intense fluctuations in its output current, the current generation of the other four samples was almost constant at both air speeds. Furthermore, the average currents of models 2b to 4b in the stagnant air were roughly the same (with almost 1.5mA). Whereas, the recorded output current of model 5a was 1.249 ± 0.002 mA, which was slightly lower than that of the other four models. At 1.2m/s air speed, the difference between the electrical current of model 1 and that of the other four samples remarkably increased. To specify, the electrical current of model 2b with 3.894 ± 0.004 mA gained second place after that of model 1. Next, models 3b and 4b unanimously achieved third place with 3.525 ± 0.003 mA and 3.515 ± 0.004 mA output currents, respectively. Finally, the lowest output current was recorded for model 5b with 2.868 ± 0.002 mA.

These results proved that compared with covering the top stage, covering the bottom stage remarkably deteriorated the output current of the TEG under both air flow conditions. Like covering the top stage of model 2, covering its bottom stage (i.e. model 2b) provided an adequate temperature difference both between the two stages and along the legs of the top stage, see [Fig.87](#). Comparing models 2b and 3b, the latter left behind the former because in spite of providing the greatest temperature difference between its top and bottom stages, there was an even temperature distribution along the legs of its top stage. Based on the same principles, the output current of model 4b was almost the same as that of model 3b. In particular, model 4b provided the lowest temperature difference between its two stages but an adequate temperature difference along the legs of the top stage. Finally, model 5b become the inferior sample as neither provided a reasonable temperature difference between the two stages nor along the legs of its top stage, as shown in [Fig.87](#).

[Fig.86c](#) shows the average currents of the samples that both of their stages were covered (i.e. model c). As can be seen, model 1 stood first regarding the output current at both air flow speeds. In addition, the negative effect of covering both stages on the output current was greater than covering only the top or the bottom stage. To put it another way, regardless of the thermal conductivity of the integrating substrate, covering both stages reduced the output current at both air flow conditions. Notably, the difference between the output currents of the four models and that of model 1 was lower in the stagnant air than 1.2 m/s air speed. When the air speed was 0m/s, the output currents of models 2c, 4c,5c were almost in the same range but superior to that of model

3c. Thereby, it could be understood that when both stages were covered with the integrating substrate, using a high thermal conductivity substrate was superior to a low thermal conductivity one. When the air started flowing, both models 2c and 4c unanimously took second place regarding the highest output current with an average current around 3.2mA. Then mode 5c ranked the third with 2.286 ± 0.002 mA average output current, followed by model 3c with an average current of 1.650 ± 0.001 mA. These results verify this fact that when both stages were covered with the integrating substrate, reducing the temperature difference between the top and bottom stages was superior to increasing it.

Comparing the effect of the covering region on the electrical current, covering the top stage (i.e. models a) resulted in remarkably greater output powers than covering the bottom or both stages (i.e. models b and c). To put it another way, the generated currents of the four models were closer to that of model 1 when only their top stages were covered. In addition, the impact of the thermal conductivity of the integrating substrate on the output current was offset when the top stage was covered. Concerning models b and c, covering the bottom stage (i.e. model b) was dominant over covering both stages (i.e. model c). In addition, using a low thermal conductivity substrate was preferred for covering either the top or the bottom stage as long as the substrate provided an adequate temperature difference along the legs. Conversely, covering both stages gave priority to the high thermal conductivity substrates.

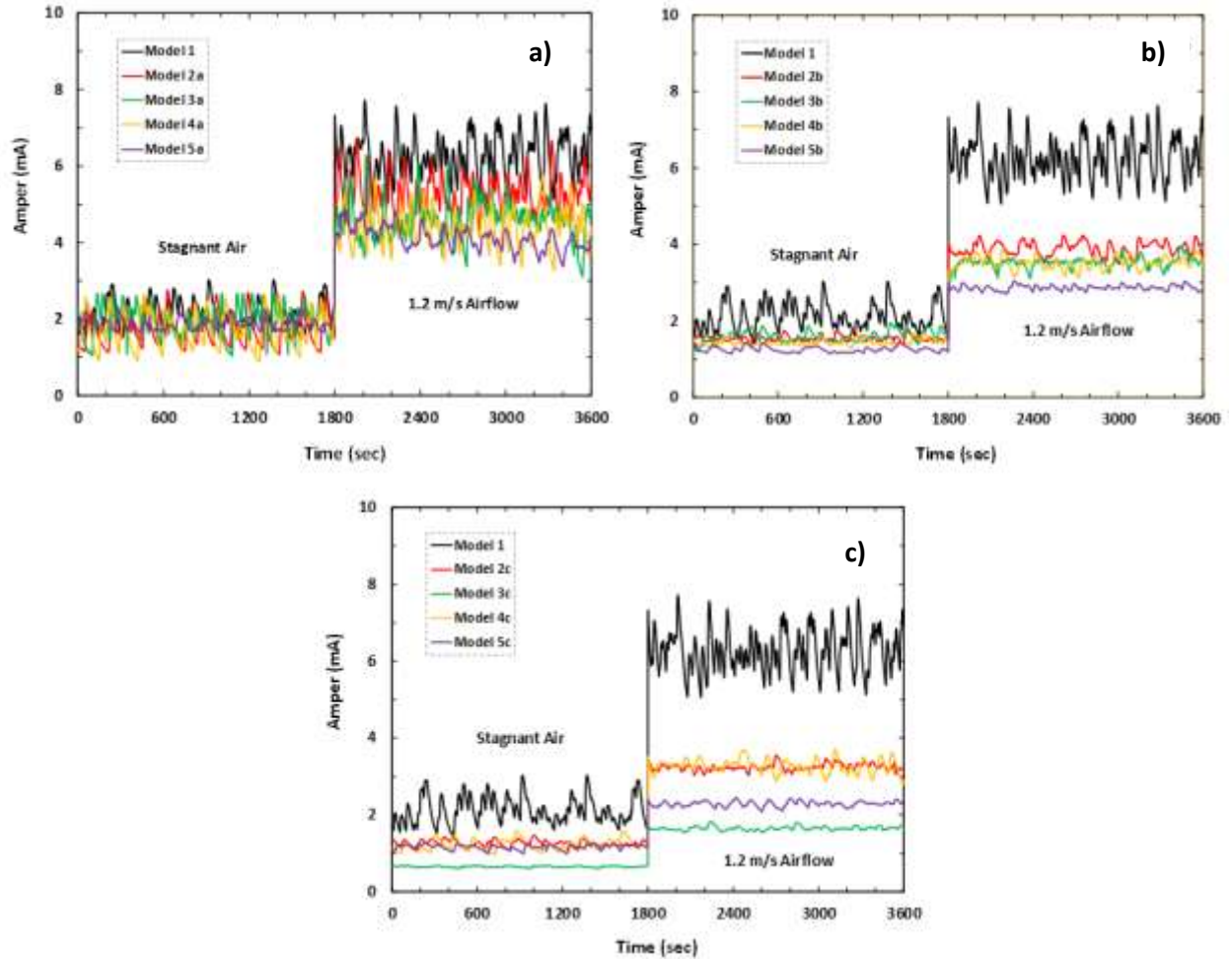


Fig. 86: Changes in the output current of the samples regarding different air flow conditions: covering a) the top; b) the bottom; and c) both stages.

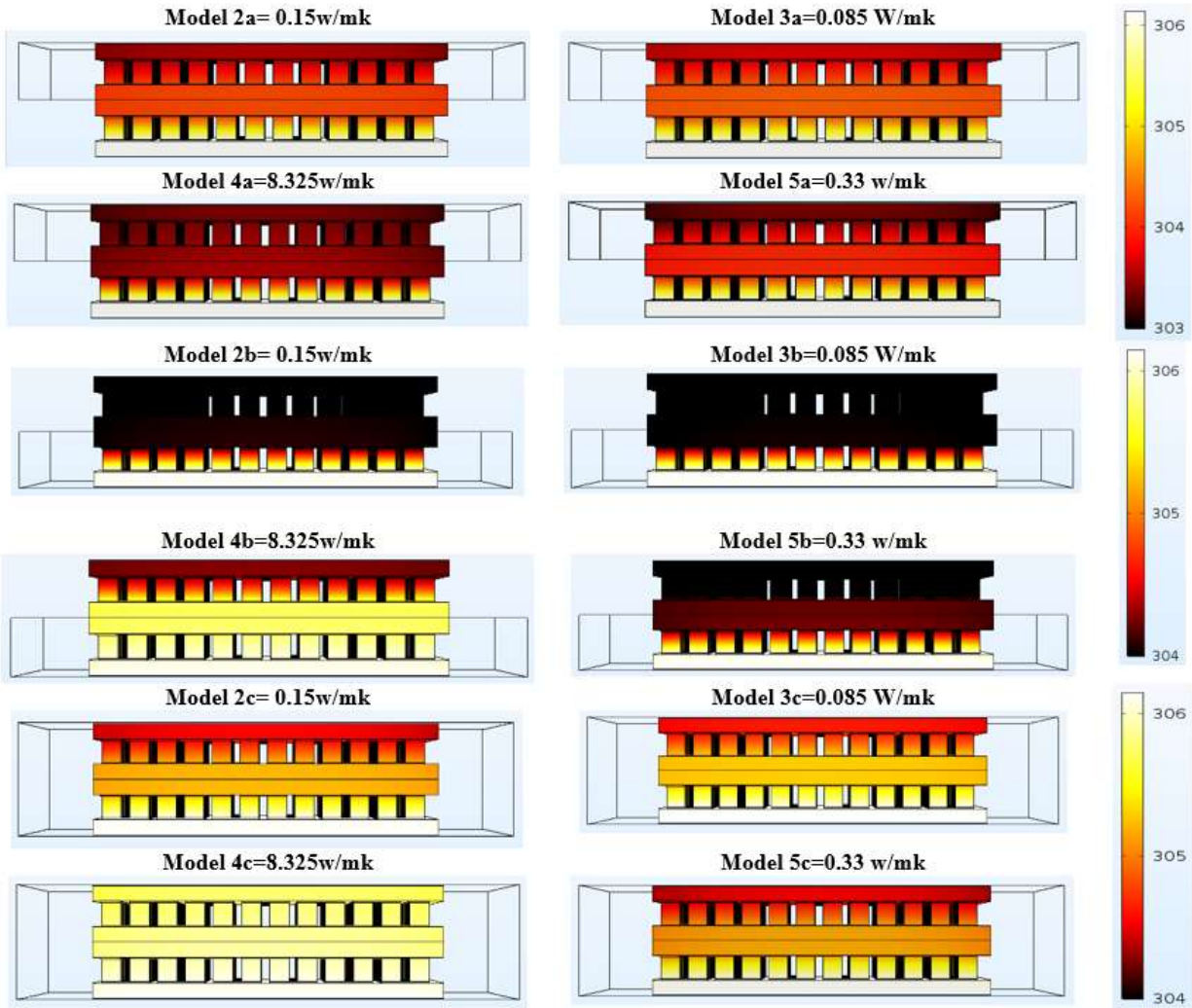


Fig. 87: Temperature profiles of the samples at 1.2 m/s air flow derived from COMSOL simulation.

8.4.3.2 Electric potential

Fig.88a shows the average output voltage of the five samples when their top stages were covered. Obviously, at 0 m/s air speed, the output voltages of all the five samples were almost the same and in a range around 30mV. However, at 1.2 m/s air speed, the reference model, models 2a, and 3a unanimously obtained the highest average output voltages of ~ 83 mV. Then, models 5a and 4a stood second and third with an average electric potentials of 67.71 ± 0.07 mV and 66.59 ± 0.05 mV, respectively. Thereby, it could be understood that regardless of the thermal conductivity of the substrate, covering the top stage caused no negative effect on the output voltage of the samples in the still air. Conversely, the thermal conductivity of the integrating substrate was influential on the output voltage of the samples at 1.2m/s air speed. To specify, although using a low thermal conductivity substrate for covering the top stage caused no negative effect on the output voltage, using a high thermal conductivity substrate remarkably deteriorated it. To illustrate these results, the generated high temperature difference between the two stages with a high thermal conductivity substrate was offset by the respective low temperature difference along the legs of the top stage, see Fig.87. However, the low thermal conductivity substrates satisfied the required temperature difference both between the two stages and along the legs of the top stage.

Fig.88b depicts the average output voltage of the bottom stage covered samples. Obviously, the output voltage of model 1 was by far greater than that of the other four samples under both air conditions. Furthermore, whilst the output voltages of the four samples were almost around 20mV at the 0 m/s airflow, they were totally different from each other at 1.2 m/s air speed. Thus, it could be understood that in the stagnant air, covering the bottom stage deteriorated the output voltage of the samples without the impact of the thermal conductivity of the substrates. However, at 1.2 m/s air speed, models 3b, 2b, 4b and 5b ranked second to fifth with 64.00 ± 0.05 mV, 59.76 ± 0.07 mV, 53.76 ± 0.03 mV, and 48.53 ± 0.04 mV output voltages, respectively. Thus, covering the bottom stage with a low thermal conductivity substrate was dominant over a high thermal conductivity substrate regarding the output voltage. This was because a relatively low thermal conductivity substrate provided the highest temperature difference between the two stages. Model 5b was an exception because neither provided a reasonable temperature difference between the two stages nor along the legs of the top stage, as shown in Fig.87.

Fig.88c illustrates the average output voltage of the five models, when both stages were covered. Overall, at both air speeds, the reference model obtained the highest output voltages, whereas models 3c and 5c unanimously obtained the lowest output voltages. In the stagnant air, after model 1 with nearly 30mV output voltage in average, models 2c and 4c stood second with average output voltages of 20mV and 22mV, respectively. At the same air speed, models 3c and 5c achieved the lowest output voltages of $17.17\pm 0.02\text{mV}$ and $16.43\pm 0.03\text{mV}$, respectively. At the 1.2 m/s air velocity, model 1 recorded the greatest output voltage of $83.88\pm 0.12\text{mV}$, but models 3c and 5c achieved the lowest average output voltages of $32.34\pm 0.02\text{mV}$ and $34.17\pm 0.02\text{mV}$, respectively. However, compared with the stagnant air, the performance of models 2c and 4c were completely different from each other at 1.2 m/s air speed. To specify, after model 1, models 2c and 4c took second and third places with an average output voltage of $49.52\pm 0.04\text{mV}$ and $42.48\pm 0.05\text{mV}$, respectively. Therefore, these results proved that covering both stages of the TEG and using a low thermal conductivity integrating substrate unanimously deteriorated the output voltage of the samples. Regarding model 2c, it was superior to model 4c because it provided higher temperature gradient along the legs of the top stage.

Concerning the impact of the coating region on the output voltage, Fig.87 shows that covering the top stage (i.e. model a) was dominant over the other two covering models (i.e. models b and c). This was mainly because the output voltages of the top stage covered models were closer to that of the reference model. Then, covering the bottom stage and both stages got second and third places, respectively. Noticeably, compared with a high thermal conductivity substrate, a low thermal conductivity one resulted in a greater output voltage when either the top or the bottom stage of the TEG was covered. Conversely, the superiority of a high thermal conductivity substrate was demonstrated when both stages were encapsulated.

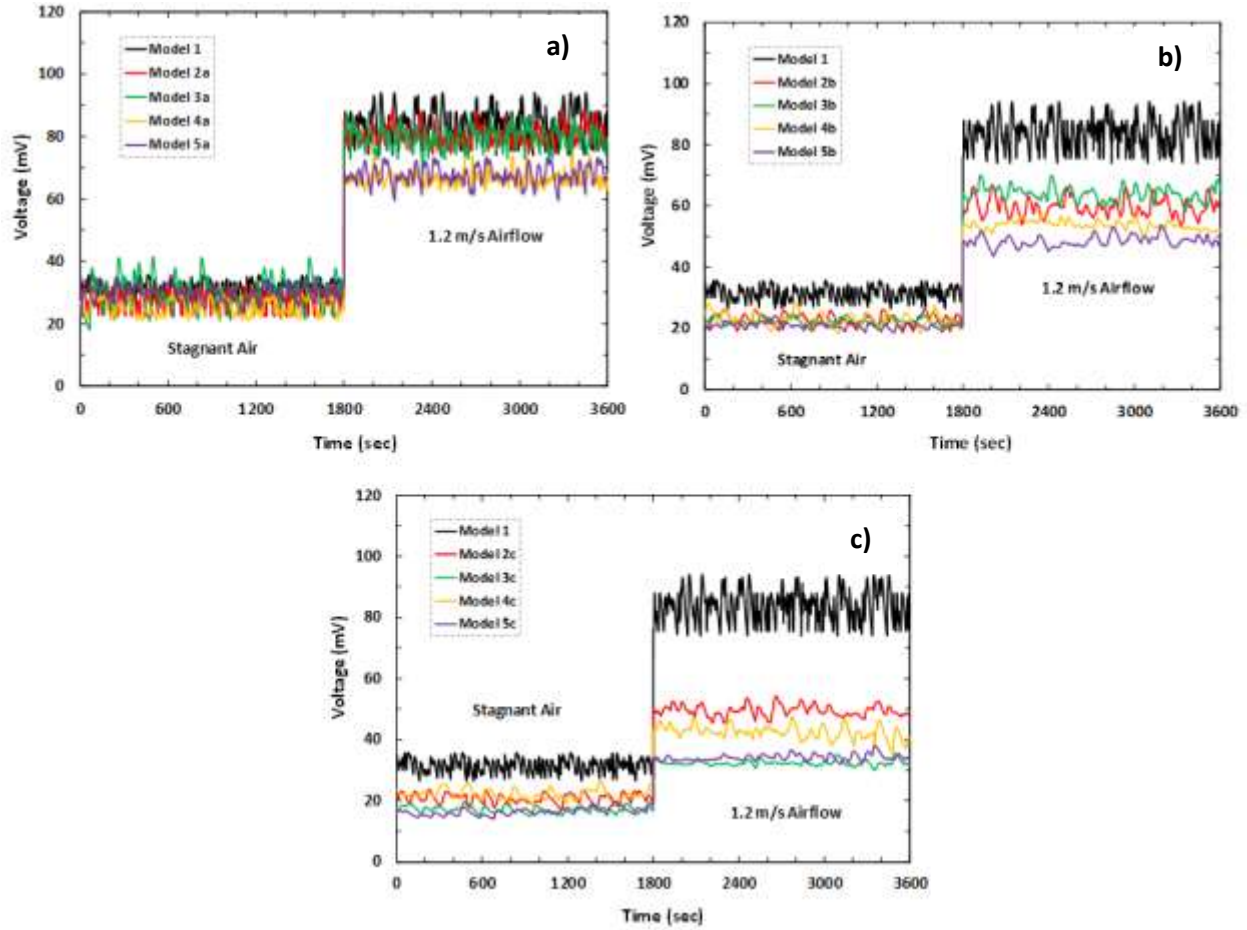


Fig. 88: Changes in the average output voltage of the samples regarding different air flow conditions: covering a) the top; b) the bottom; and c) both stages.

8.4.3.3 Output power

Fig.89a shows the output powers of the five samples when their top stages were covered. Overall, in the stagnant air, the average output powers of all the four prepared samples were around 50mW, which was equal with that of the reference model. Thus, the output power of the TEG in the stagnant air affected neither by covering its top stage nor the thermal conductivity of the integrating substrate. However, at the 1.2 m/s air velocity, the average output power of model 1 ($527\pm 1\text{mW}$) was greater than that of the other four models. Then, the average output powers of model 2a ($428.9\pm 0.9\text{mW}$), 3a ($369\pm 1\text{mW}$), and 4a ($295\pm 1\text{mW}$) ranked second, third, and fourth, respectively. Among the five models, model 5a recorded the minimum output power with $279.2\pm 0.5\text{mW}$. Thereby, at 1.2m/s air speed, it could be understood that using a low thermal conductivity substrate could diminish the negative effect of covering the top stage of the TEG.

Fig.89b illustrates the information on the output powers of the samples when their bottom stages were covered. Obviously, the output power of the reference model obtained the highest records at both air speeds. Whereas, the differences between its output power and those of the other four models were lower at 0m/s air speed than 1.2 m/s air speed. Concerning the output powers of models 2b to 5b in the still air, they unanimously delivered the same average output power of 30 mW. Thus, it could be interpreted that while covering the bottom stage of the TEG was negatively influential on the output power of the TEG, the thermal conductivity of the substrate was ineffective. When the ambient air started to flow at 1.2 m/s air speed, the average output power of the samples started to differ from each other. To specify, after model 1, models 2b and 3b stood second by reaching an average output power of $232.7\pm 0.4\text{mW}$ and $225.6\pm 0.3\text{mW}$, respectively. Furthermore, the minimum output power was obtained by model 5 with an average of $139.2\pm 0.1\text{mW}$. Consequently, at 1.2m/s air velocity, both covering the bottom stage and using a high thermal conductivity substrate deteriorated the output power of the TEG.

Fig.89c compares the output powers of the five samples when both stages were covered. In general, model 1 was dominant over the other four models at both air speeds. However, the four covered samples performed more similar to the reference model in the stagnant air. Precisely, the difference between the output power of models 2c to 5c and that of model 1 was in a range of between 40.64mW to 55.69mW in the still air. While this difference increased to the range between 366.40mW and 473.65mW at 1.2m/s air speed. In the still air, the second highest output power was recorded for models 2c and 4c with roughly 26mW. In contrast, model 3c obtained the lowest output power with an average output power of $11.21\pm 0.05\text{ mW}$. When the air started flowing, the second and third highest output powers were attained by models 2c and 4c with an average of $160.6\pm 0.2\text{mW}$ and $139.1\pm 0.3\text{mW}$, respectively. Then, model 5c recorded the fourth highest output power with nearly $78.10\pm 0.08\text{mW}$ followed by model 3c with the minimum output power of $53.35\pm 0.05\text{mW}$. Based on these results, covering both stages with a low thermal conductivity filler was the worst case scenario at both air speeds.

Concerning the effect of the covering region on the output power, encapsulating the top stage was superior to covering either the bottom stage or both stages. To put it another way, the output powers of the four samples were closer to that of the reference model when only their top stages were covered. In addition, when the top stage was covered, the effect of the thermal conductivity of the

substrate on the output power was negligible compared with that of when the bottom stage or both stages were covered. Then, covering the bottom stage and both stages delivered the second and the third highest output powers, respectively. Notably, when only the bottom stage was covered, the impact of the thermal conductivity of the substrate on the output power was less than that of when both stages were covered. In the stagnant air, the effect of the covering region was dominant over the thermal conductivity of the substrate. Whereas, at 1.2 m/s air velocity, both factors significantly influenced on the output power. In particular, using a low thermal conductivity substrate had priority over a high thermal conductivity one, when either the top or the bottom stage was covered. However, when both stages were covered, a high thermal conductivity substrate was listed as the best option.

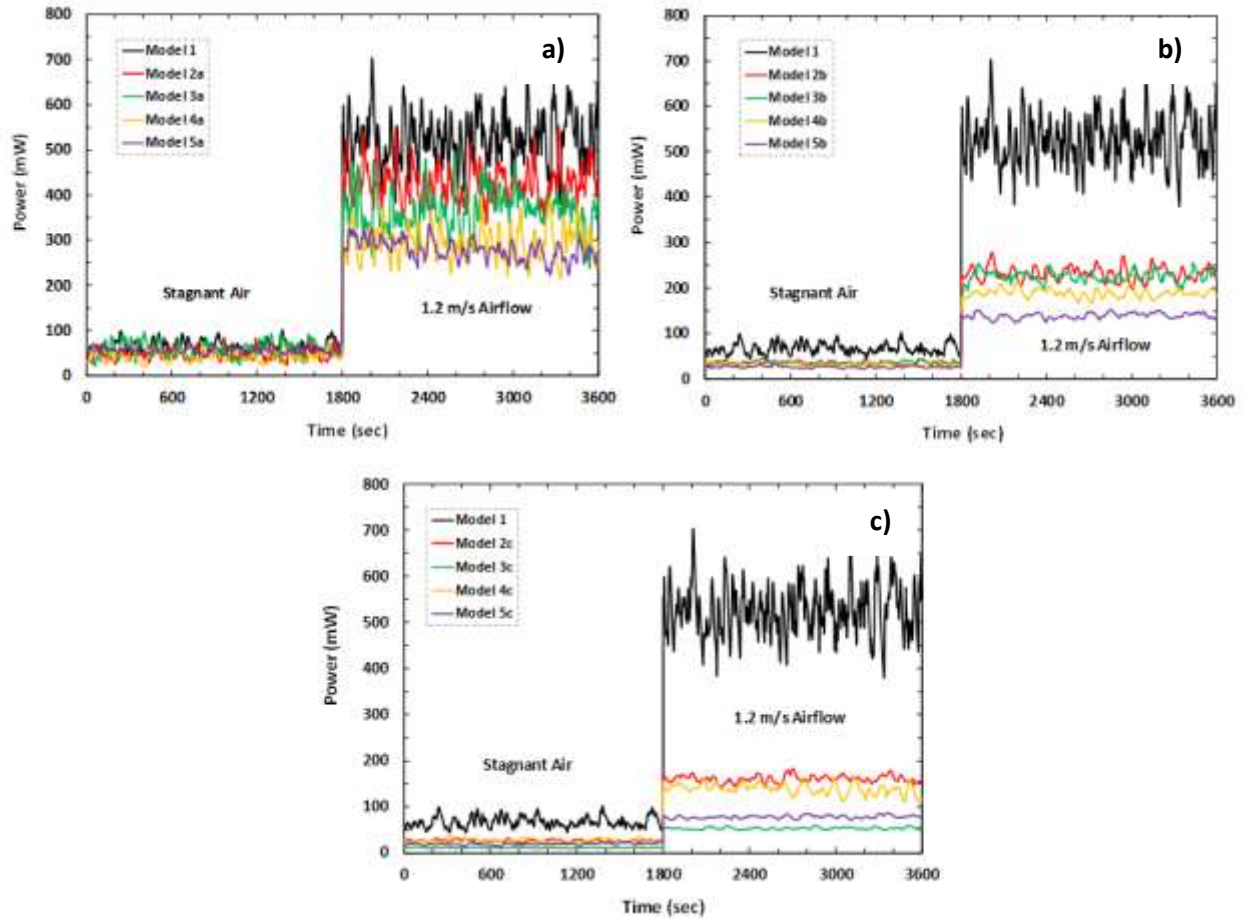


Fig. 89: Changes in the output powers of the samples regarding different air flow conditions: covering a) the top; b) the bottom; and c) both stages.

8.5 Comparison of the numerical modelling and the experiments

Validating the results of the COMSOL models against those of the experimental tests, there must be an acceptable level of the percentage error between the two sets of data and the same trend in both. Accordingly, [Fig.90](#) shows the comparison between the numerical and the experimental results regarding their average output currents, output voltages, and output powers. As can be seen, there was an acceptable difference and a good trend agreement between the numerical and the experimental studies. Obviously, the identical boundary conditions of these two studies resulted in such a tiny error between their outcomes. However, being more precise, these tiny errors were greater at 1.2m/s air speed than the still air. This was mainly because, to simplify the simulations, the TE properties of the TE materials were determined to be temperature independent. Whereas

in reality, varying the temperature directly changes the TE properties of the materials. Therefore, the difference between the outcomes of the numerical and the experimental studies were negligible at 0m/s air speed, because there was no change in the ambient thermal condition over the time. However, when air started flowing, the change in the ambient temperature affected the TE properties of the legs, but it was not considered in the simulation. Therefore, the divergence of the numerical study from that of the experimental one became greater at 1.2 m/s air flow.

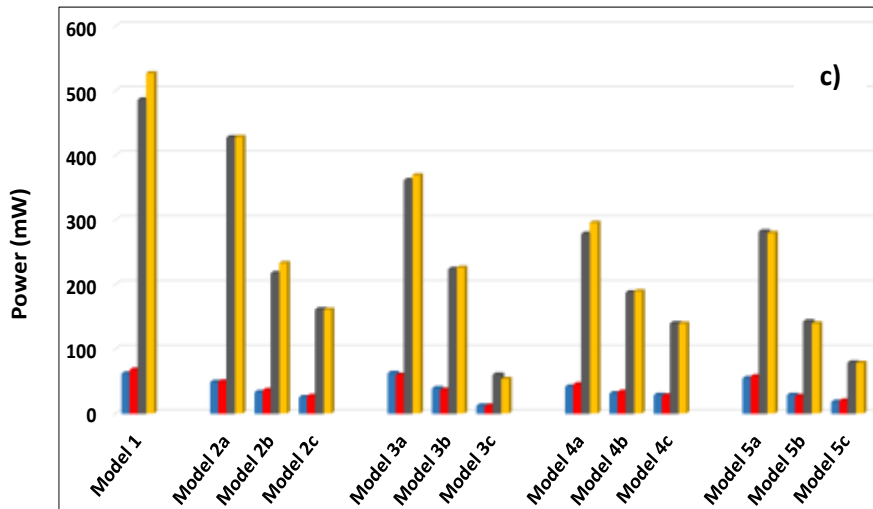
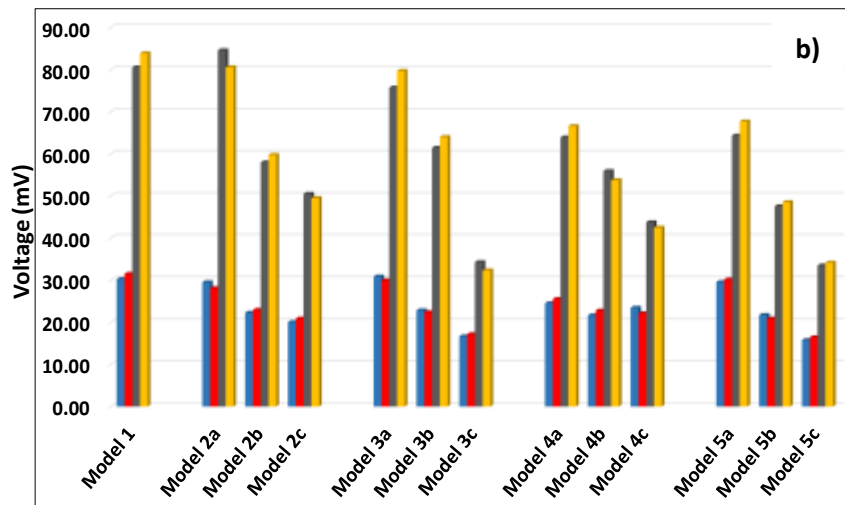
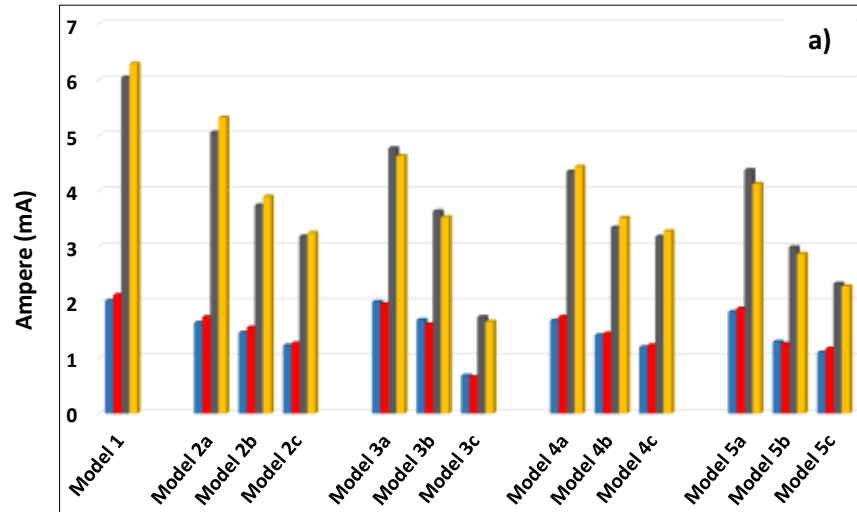


Fig. 90: Comparison between the experimental results and the simulation outcomes: a) average output amperes; b) average output voltages; and c) average output powers.

Next, the output power of the superior (i.e. 2a) and the inferior (i.e. 3c) samples of this study were compared with that of the other relevant studies, and the results were summarized in [Table 21](#). It should be noted that the comparison was conducted with the studies having the same ambient conditions. Precisely, in these studies, the TEGs were heated by either the wrist or the upper arm, which their temperatures were roughly between 33 °C to 36 °C. Also, the ambient air was stagnant and its temperature was in a range between 21 °C to 24 °C. According to the table, not only the superior sample of this study (i.e. 2a) stood first among all the studies, but also its inferior sample (i.e. 3c) was dominant over the others. In general, the superiority of models 2a and 3c is attributed to three reasons. The first one is the lower device area of some of the listed samples in [Table 21](#) compared with that of models 2a and 3c. The second reason is related to the nonhomogeneous boundary condition along the TE legs of models 2a. To illustrate, the boundary condition along all of the listed samples was homogeneous, which was either air or PDMS. Whereas, the boundary condition along the TE legs of models 2a was nonhomogeneous. To put it another way, the top half of the model was covered with plain PDMS and the bottom half was covered with air. Whereas, in both rigid and flexible samples, the TE legs were coated with a homogeneous boundary condition (either air or PDMS). The third reason is the applied heatsink in the listed samples which were either anodized aluminium or copper sheet. In fact, the negative aspect of these heatsinks is that they are required to be attached to the cold substrate by a thermal adhesive. Since, the thermal adhesive applies a thermal resistance, it reduces the efficiency of the heatsinks.

Table 21: Summary of the physical specification and output power of the TEGs consisted of ingot-shaped legs.

Type	Parameters used	Heatsink	Device area (cm ²)	Output power (mW/cm ²)	Ref
	Model 2a	No	9	5.4	Current study
	Model 3c	No	9	1.2	Current study
Rigid	Integration of seven units of one stage TEG with air-exposed legs	Anodized aluminium	18.20	0.014	[238]
	Integration of five units of one stage TEG with 6mm distance from each other , whilst the legs were embedded in the air gap between two fabric substrates	Anodized aluminium	1.25	0.024	[242]
	A one stage TEG with air-exposed legs	Anodized aluminium	5	0.011	[266]

	A one stage TEG with thermal insulated legs	Grooved copper sheet	28	0.028	[267]
	A one stage TEG with air-exposed legs	PCM	42.25	0.02	[271]
	A one stage TEG with air-exposed legs	Flexible spreader	1.5	0.044	[335]
	TE legs were coated in PDMS and sandwiched by two ceramic headers.	Copper sheet	0.87	0.006	[243]
Flexible	TE legs were coated in PDMS	No	4	0.0005	[259]
	TE legs were coated in PDMS	No	11.20	0.003	[260]
	The top and bottom electrodes were coated with a combination of PDMS and high thermal conductivity liquid metal (EGaIn), while the gap between the legs was filled with plain PDMS	Copper sheet	8	0.008	[269]

8.6 Summary

This section numerically and experimentally examined the relationship between providing a nonhomogeneous boundary condition along the TE legs and the efficiency of the TEGs at room temperature. The investigation was conducted on a standard off-the-shelf TEG, and two methods were considered for generating the nonhomogeneous boundary condition. The first method was fully (i.e. the whole legs) or partially (i.e. either the top/bottom half of the legs) encapsulating the TE legs with a lightweight substrate. The second method was varying the thermal conductivity of the coating substrate, using different fillers. Accordingly, the TE performances of the thirteen specified samples were studied under two air conditions. It should be noted that the results of both the computational modelling and the laboratory tests showed reasonable congruency. The main results could be summarized as follow.

- 1) The air-exposed legs were dominant over the fully or partially coated legs concerning the TE performance. In particular, the TE performance of the TEG deteriorated when its legs were coated with the lightweight substrate. Therefore, it was important to achieve a right balance between the coating area of the lightweight substrate and the output power of the TEG.
- 2) Due to the necessity of using a lightweight substrate to integrate the required TEGs together, coating only the top half of the TE legs was dominant over the other two coating patterns. This was because it illustrated the closest TE performance to that of the fully air-exposed TEG.

3) When coating the top half was not possible, the most optimum alternative was covering only the bottom half of the legs.

4) Further improvement of the TE performance was possible by manipulating the thermal conductivity of the substrate based on its coating region. Precisely, both the coating region and the thermal conductivity of the substrate directly impacted on the TE performance of the TEG. To illustrate, using a low thermal conductivity substrate was dominant over a high thermal conductivity one when either the top or the bottom stage were covered. In contrary, using a high thermal conductivity substrate was suggested in case the TE legs were totally coated. Accordingly, sample 2a that its top half was covered with a low thermal conductivity substrate (i.e. plain PDMS substrate) was the most optimal sample both in the stagnant air and 1.2 m/s air flow.

5) Whilst the previous studies covered the legs fully with the substrate, this study proved that the greatest conversion efficiency could be achieved when only the top half of the TE legs was enclosed. To clarify, in the stagnant air and 1.2 m/s air flow, coating only the top half of the legs with the plain PDMS substrate (i.e. sample 2a) resulted in respectively 186% and 267% greater output powers compared with fully covering them with the same substrate. Even, enclosing only the bottom half of the legs in the plain PDMS substrate was 135% and 145% more efficient than fully coating them with this substrate, respectively.

6) Last but not least, the effect of the coating region and the thermal conductivity of the substrate on the efficiency of the TEG was more influential at higher air speeds. To specify, the thermal conductivity of the substrate had no impact on the efficiency of the TEG at 0m/s air speed. On the contrary, at 1.2m/s air speed, not only the thermal conductivity of the substrate intensified the effect of the coating region, but also each coating region required a specific thermal conductivity.

Chapter 9

The Lightweight Heatsink

9.1 Introduction

As mentioned before, a heatsink accelerates the dissipation of heat from the cold conjunction of the legs, resulting in higher temperature gradients along them. This is in accordance with this fact that only a small part of the absorbed heat by the TE legs is converted into electricity, and most of it ends up heating the legs followed by reducing their energy conversion efficiency. In general, the heatsinks could be classified into air cooled and water cooled types, whilst the former is more prevalent in indoor applications, such as wearable TEGs [124]. To specify, the air cooled heatsinks are cooled by either natural or forced ventilation. For example, Nozariasbmarz et al. [266] attached an anodized aluminium heatsink having a size of $2.54 \text{ cm} \times 2.54 \text{ cm} \times 0.95 \text{ cm}$ to a commercial TEG. The TEG consisted of 6 pairs of commercial nickel coated *p*- and *n*-type TE legs each with the dimensions of $0.16 \times 0.16 \times 0.16 \text{ cm}^3$. The fill factor of the TEG was 12% regarding the base area of the TEG ($1.6 \times 1.6 \text{ cm}^2$) and the dimensions of the legs. The tests were carried out on different parts of the body including arm, forearm, wrist, and foot at $17 \text{ }^\circ\text{C}$ still air. The results demonstrated that at $2.5 \text{ }^\circ\text{C}$ temperature difference, the delivered output powers were $34 \text{ }\mu\text{W}/\text{cm}^2$, $14 \text{ }\mu\text{W}/\text{cm}^2$, $12 \text{ }\mu\text{W}/\text{cm}^2$, and $16 \text{ }\mu\text{W}/\text{cm}^2$, respectively.

Zohreh et al. [336] numerically evaluated the relationship between the heatsinks' configuration and the performance of the TEGs at different air speeds. Accordingly, the authors proposed four configurations for the heatsink and examined their performance by simulating them in the COMSOL Multiphysics software. The performances of these four proposed configurations were compared with that of a conventional straight fin-shaped heatsink, as Fig.91 depicts. Considering the same dimensions for the heatsinks, they were coupled with an off-the-shelf TEG comprising rigid metal interconnects (i.e. copper) and rigid top and bottom ceramic (i.e. Al_2O_3) substrates. The TEG consisted of 72 pairs of ingot-shaped TE legs, whilst both the *p*- and *n*-type legs were composed of Bi_2Te_3 . The performances of the heatsinks were studied at three different air speeds, including 0 m/s (resembling a seated person), 1.4 m/s (resembling a walking person), and 3 m/s (resembling a jogging person). At $19 \text{ }^\circ\text{C}$ temperature difference between the heat source and the ambient air, the heatsinks' configuration were influential at higher air speeds. Furthermore, the T-shape and the wavy shape heatsinks achieved the highest power generation at all the defined air speeds.

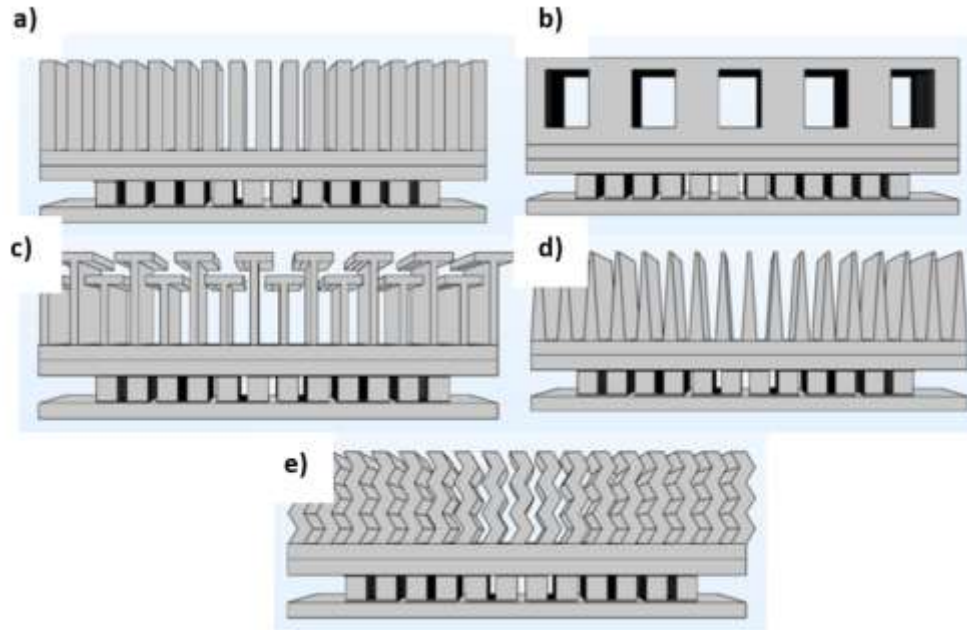


Fig. 91: The schematic of the modelled heatsinks in COMSOL: a) straight fins; b) perforated fins; c) T-shape fins; d) trapezium fins; and e) wavy fins [336].

Instead of a rigid heatsink, Hyland et al. [243] used a flexible one to cool down 25 ingot-shaped and Bi_2Te_3 -based thermocouples. To clarify, the legs were sandwiched between two rigid Aluminum Oxide ceramic substrates. To accelerate the heat absorption and dissipation, a copper sheet was attached to the hot and cold sides of the TEG, respectively. The results illustrated that increasing either the heatsink's base area or the air velocity improved the output power of the TEG. Accordingly, at 1.4m/s air speed and 17.35 °C ambient temperature, the highest to the lowest output powers were obtained by placing the TEG on the upper arm ($21\mu\text{W}/\text{cm}^2$), wrist ($13\mu\text{W}/\text{cm}^2$), chest ($10\mu\text{W}/\text{cm}^2$), and T shirt ($2\text{--}8\mu\text{W}/\text{cm}^2$). Fig.92 depicts the experimental setup of the TEG on the wrist.

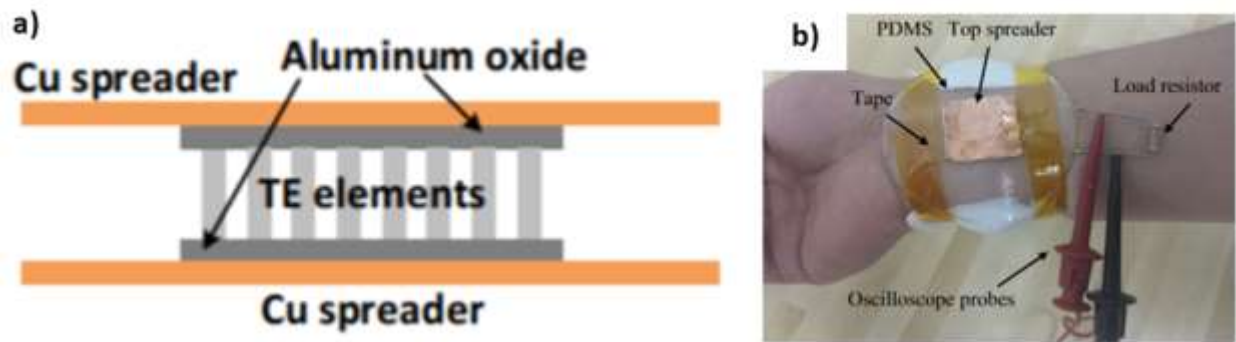


Fig. 92: a) Schematic of the developed TEG; b) the experimental setup of the TEG on the wrist [243].

Apart from using a copper sheet, Sargolzaeiaval et al. [269] intensified the temperature gradient along the legs by encapsulating the electrodes with a high thermal conductivity substrate. To illustrate, 32 pairs of ingot-shaped TE legs were arranged in an array of 4×16 , and the space between them was filled with plain PDMS, see Fig.93. Notably, the *p*- and *n*-type legs were composed of $\text{Bi}_{0.5}\text{Sb}_{1.5}\text{Te}_3$ and $\text{Bi}_2\text{Se}_{0.3}\text{Te}_{2.7}$ composites, respectively. After connecting the legs electrically together with EGaIn, two different layers were considered to coat the electrodes, including a plain PDMS layer and a PDMS: EGaIn layer. The results showed that the latter performed as a heatsink due to its higher thermal conductivity than the former. After that, a thin copper sheet was fabricated onto the PDMS: EGaIn layer to intensify its heat dissipation. In total, when the TEG was worn on the wrist at 20 °C to 22 °C ambient temperature, the highest output power under windless and 1.2m/s air velocity were 5 and 30 $\mu\text{W}/\text{cm}^2$, respectively.

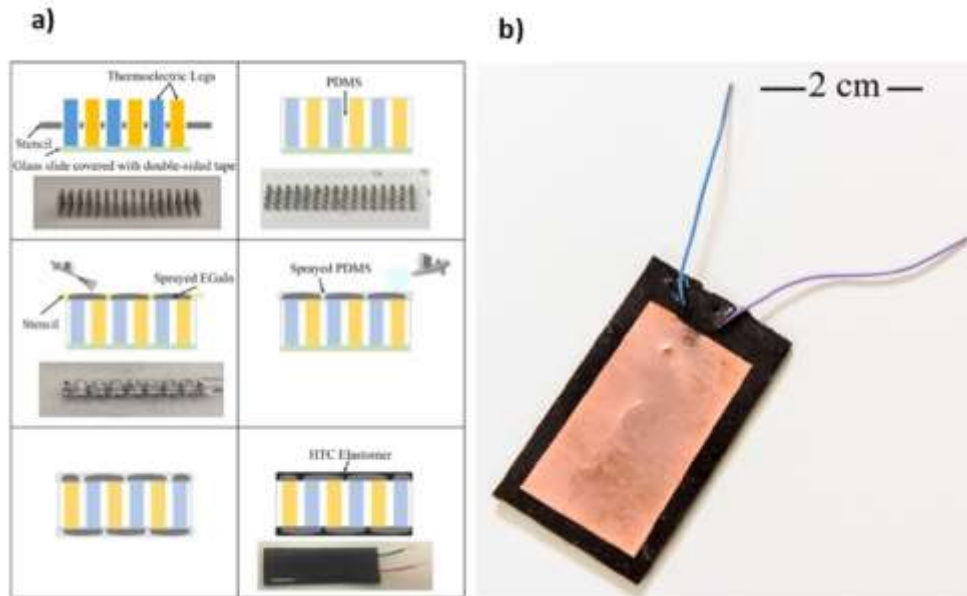


Fig. 93: a) The fabrication process of the TEG; b) photo of the TEG fabricated with copper sheet as the heatsink [269].

Lee et al. [271] used a PCM called n-octadecane ($C_{18}H_{38}$) to develop a flexible heatsink. This was because n-octadecane benefits from a low melting point ($28\text{ }^{\circ}\text{C}$), thus resulting in a large amount of heat absorption at low temperature gradients. To fabricate the heatsink, 25 copper foam blocks each with the dimensions of $1\text{ cm} \times 1\text{ cm} \times 0.5\text{ cm}$ were filled with the PCM. This was because, the copper foam blocks could spread the heat uniformly within the PCM. Then, the filled copper foam blocks were arrayed in a 5×5 matrix followed by filling the gaps between them with polyurethane elastomer. While four sides of the filled copper foam blocks were coated with the elastomer, their upper and lower sides were covered with a metal foil to accelerate the vertical heat flow, see Fig.94. Finally, the generated heatsink was attached to the top substrate of a cross-plane TEG. The results showed that at a temperature difference of $3\text{ }^{\circ}\text{C}$, the highest delivered output power was around $20\text{ }\mu\text{W}/\text{cm}^2$.

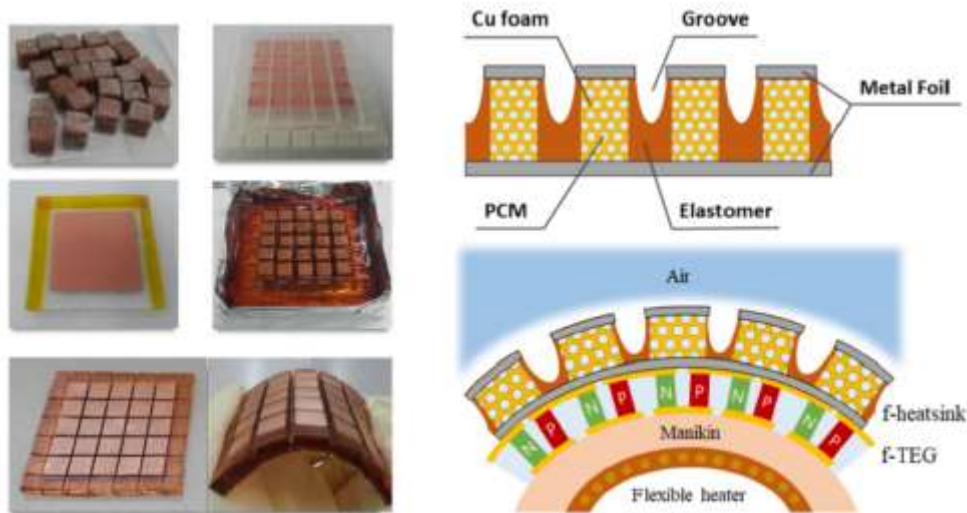


Fig. 94: Fabrication process of the flexible heatsink [271].

Likewise, Shi et al. [272] used copper foam blocks as the heatsink of their previously developed TEG [260]. To illustrate, the authors determined two different heatsinks for fabrication, including the copper foam blocks and the copper-based plate-fins, see Fig.95. While the overall dimensions of the TEG were $2.65\text{cm} \times 4.35\text{cm} \times 0.26\text{ cm}$, the height of both heatsinks were approximately 0.4 cm. The heatsinks were mounted on the top surface of the TEG separately using a 0.01 cm-thick thermal conductive layer. The results showed that both heatsinks slightly improved the output power of the TEG at temperature differences higher than $15\text{ }^\circ\text{C}$. In addition, the copper foam heatsink was slightly superior to the plate-fin one, because it achieved the highest output power of $3.5\text{ }\mu\text{W}/\text{cm}^2$ at $20\text{ }^\circ\text{C}$ temperature difference.

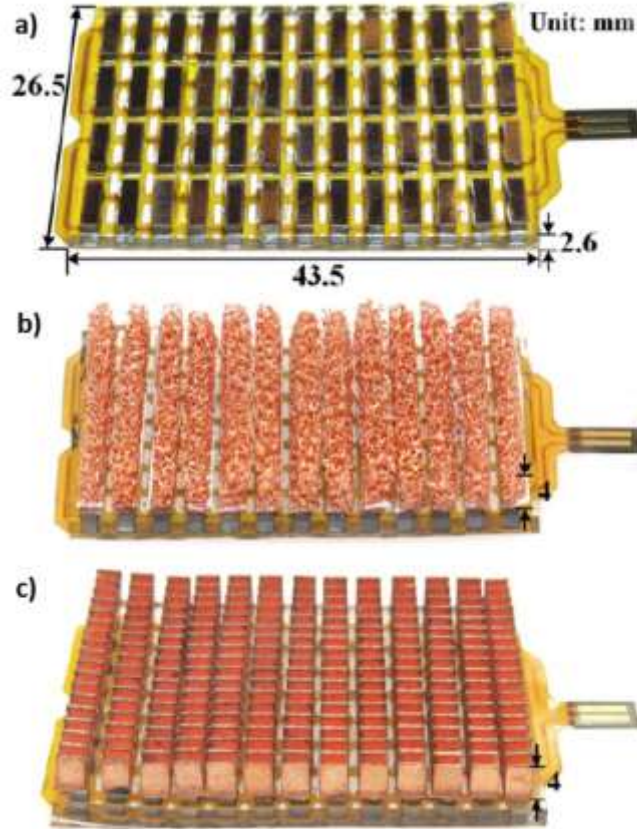


Fig. 95: Fabricated wearable TEGs: a) without heat sink; b) with copper-foam heat sink; and c) with plate-fin heat sink [272].

Park et al. [273] applied a solid-state gel due to its high thermal effusivity, heat capacity, and flexibility as the heatsink to cool down a mat-like wearable TEG. The TEG consisted of 15 pairs of ingot-shaped TE legs placed inside Bakelite holders. The holders were connected together by passing a flexible wire through the holes punched into the opposite sides of the holders. Then, the solid-state cool gel was poured onto the air exposed side of the TEG as shown in Fig.96. The results showed that placing the TEG on the lower arm resulted in the highest output power of $5.60 \mu\text{W}/\text{cm}^2$ at $9.3 \text{ }^\circ\text{C}$ temperature difference.

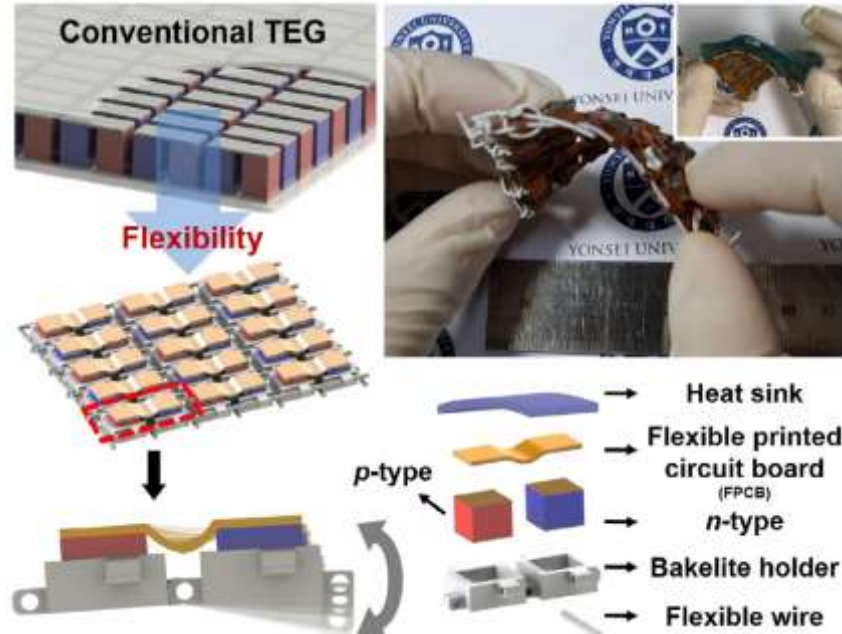


Fig. 96: Schematic of the design and structure of the fabricated TEG and its gel-based heatsink [273].

Lee et al. [274] encapsulated 15 pairs of ingot-shaped $\text{Bi}_{0.5}\text{Sb}_{1.5}\text{Te}_3$ (*p*-type) and $\text{Bi}_2\text{Te}_{2.7}\text{Se}_{0.3}$ (*n*-type) legs in a PDMS substrate. Concerning the bottom electrodes, the legs were soldered to the double-layer copper of a FPCB. To stabilize the TEG, a flexible resin holder was placed around the legs followed by filling the gaps between them with PDMS. Notably, the PDMS layer was poured up to the upper side of the legs to leave space for EGaIn as the top electrodes. To specify, EGaIn was deposited onto the upper sides of the legs to connect them electrically together followed by being encapsulated with a PDMS layer. Ultimately the TEG was coupled with a flexible hydrogel-based heatsink, as Fig.97 shows. The authors demonstrated that the developed TEG obtained $8.30 \mu\text{W}/\text{cm}^2$ by harvesting heat from 36.5°C upper arm at 28.5°C ambient temperature.



Fig. 97: The flexible hydrogel-based heatsink fabricated onto the TEG [274].

Park et al. [275] used the printed copper layer of a FPCB as the bottom electrode and soldered 20 couples of ingot-shaped legs from their bottom sides to it. Then, the thermocouples were inserted into the 40 holes of a bendable Bakelite holder arranged in a 4×10 matrix. It should be noted that the legs were composed of *p*-type $\text{Bi}_{0.5}\text{Sb}_{1.5}\text{Te}_3$ and *n*-type $\text{Bi}_2\text{Te}_{2.7}\text{Se}_{0.3}$ composites. Next, the legs were electrically connected together from their top side with a copper film. After that, a fin-shaped copper heatsink was placed on the upper electrodes and screwed down, as Fig.98 depicts. The authors demonstrated that their developed TE module with approximately $7.9\text{cm} \times 1.7\text{ cm}$ base area obtained the highest output power of $6.97\ \mu\text{W}/\text{cm}^2$ at ΔT of 12.5°C .

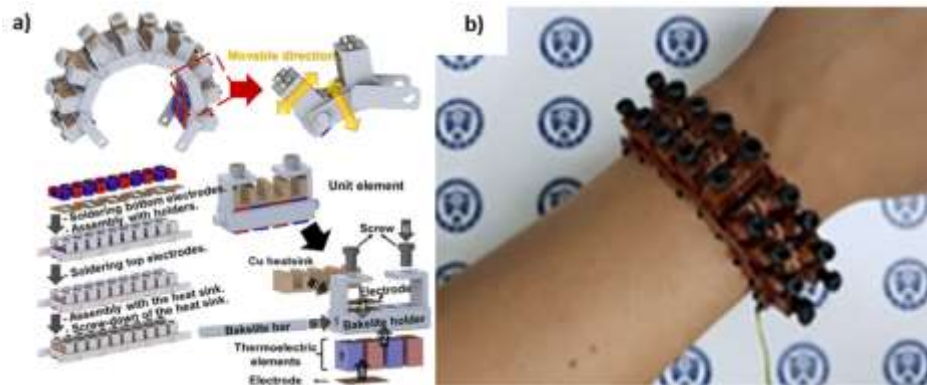


Fig. 98: a) Schematic of the fabrication process and the components of the TEG; b) the fabricated device on the human wrist [275].

Concerning these literatures, the focus of recent studies is moving toward lightweight, flexible, and highly efficient heatsinks. However, current lightweight heatsinks suffer from two main

issues. First, they are not influential in low temperature gradients, especially when there is no airflow. Second, they require some structural supports to either be coupled with a TEG or to become thick. To put it another way, not only their structural supports and thickness offset their lightness, but also they are ineffective in low temperature differences. Therefore, the aim of this section is to develop a lightweight heatsink that is beneficial both at low temperature differences and stagnant air.

9.2 Fabrication procedure

To address the aim of this chapter, two lightweight heatsinks were proposed to improve the TE performance of the optimal sample of [Chapter 8](#) (i.e. sample 2a). Accordingly, sample 2a served as the reference model of this chapter, and its performance was studied before and after being coupled with either of those proposed heatsinks. Concerning the two developed heatsinks, both of them were composed of plain PDMS to be matched with the material of the integrating substrate. To specify, matching the thermal conductivity of the heatsinks with that of the integrating substrate reduced the thermal resistivity at their interfaces. In addition, using no structural support to combine the heatsinks with the integrating substrate resulted in a lighter and more flexible heatsink. Regarding the configuration of the heatsinks, as [Fig.99](#) shows, the first one consisted of 44 semi-spherical PDMS blocks attached to the PDMS layer of the reference model. The second heatsink was composed of 44 pin-shaped PDMS blocks following the configuration of the conventional rigid heatsinks. To prepare the semi-spherical and the pin-shaped PDMS blocks, the prepared PDMS mixture in the second step of [Section 8.4.1](#) was poured into some pre-developed moulds, as [Fig.100](#) shows. Then, the moulds containing the plain PDMS mixture were placed in a $-20\text{ }^{\circ}\text{C}$ freezer for 6 hrs to remove air bubbles from them. After that, the moulds were heated by a $100\text{ }^{\circ}\text{C}$ hot plate for 2 hrs to cure their containing PDMS mixture. Finally, the PDMS blocks were removed from the moulds and adhered to the PDMS substrate of the reference model using a thin layer of plain PDMS.

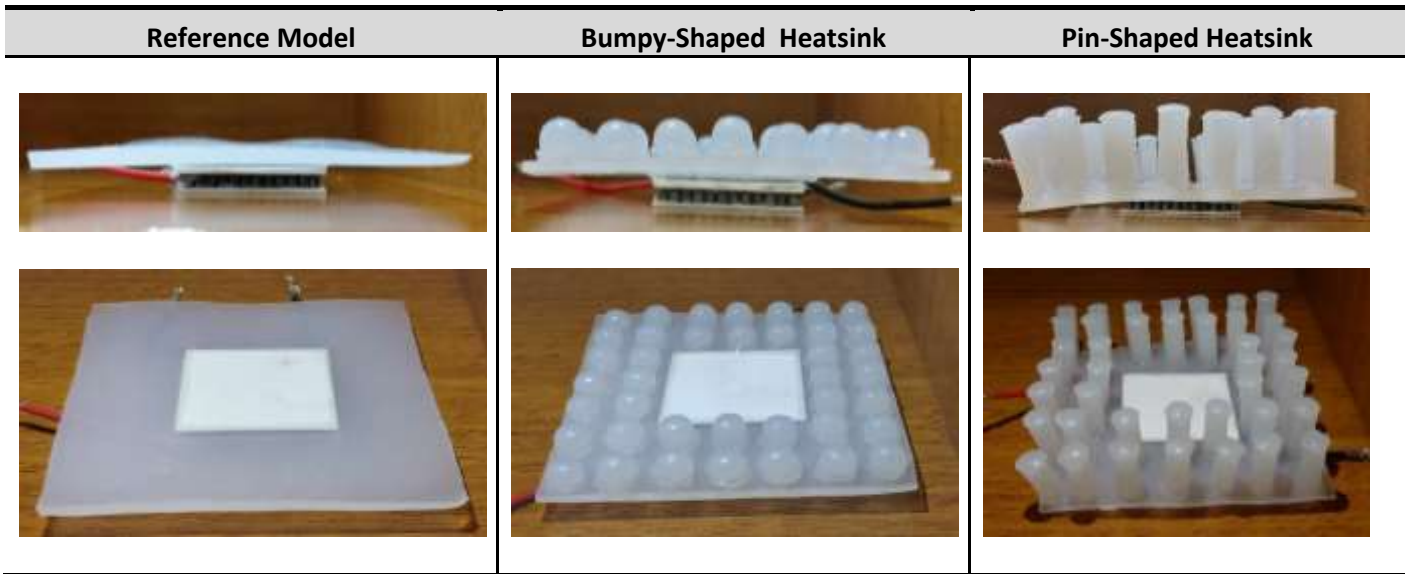


Fig. 99: Photographs of the three prepared sample concerning the determined configurations for the heatsink.

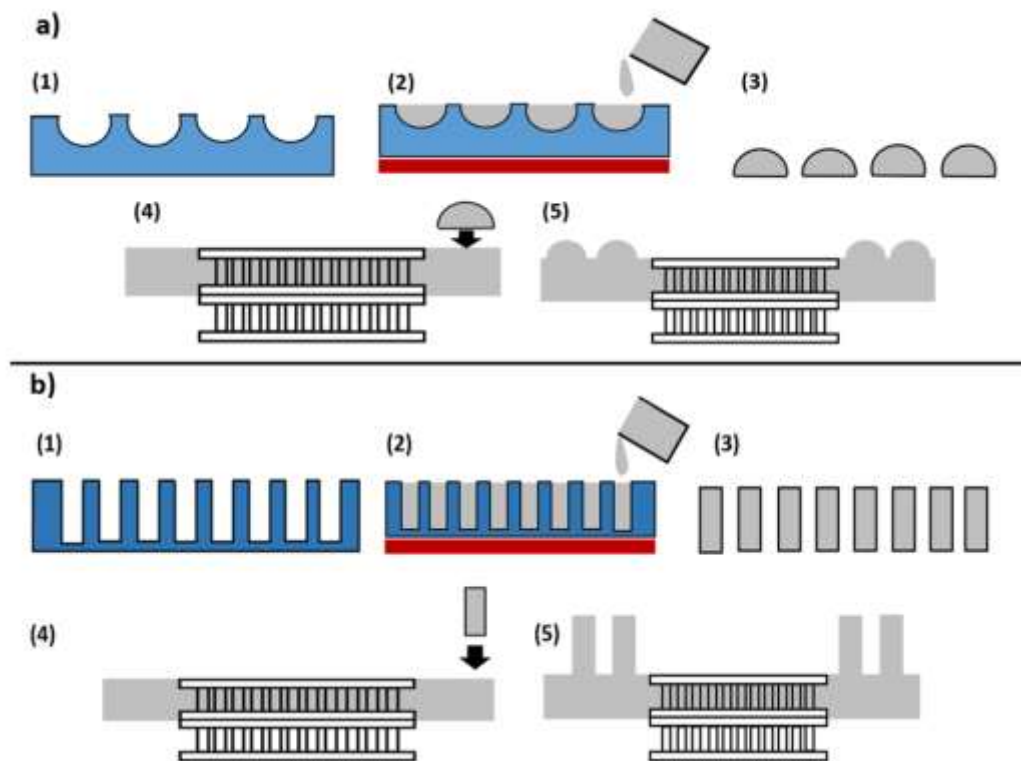


Fig. 100: Schematic of the fabrication procedure of the a) bumpy-shaped heatsink and b) the fin-shaped heatsink.

9.3 Equipment and testing conditions

A series of laboratory experiments were conducted to study the TE impact of the prepared heatsinks. Accordingly, a hot plate with 33 °C temperature was used as the heat source and the ambient temperature varied in a range of between 20 °C and 22 °C. Notably, the ambient and the hot plate's temperatures were kept checking throughout the experiments using a 4 channel thermometer (HH374) having $\pm (0.1\% \text{ of rdg} + 0.7 \text{ }^\circ\text{C})$ accuracy. All the prepared samples were characterized under three air flow conditions, including 0 m/s, 1.2 m/s, and 2.4 m/s, equalling with the air speed at sitting, walking, and running conditions, respectively. The developed wind tunnel in [Chapter 8](#) was used to provide a linear airflow over the TEG at 1.2 m/s and 2.4 m/s airflows. The airflow speed of the applied fan was adjustable to create the specified airflows inside the tunnel. The air velocity above the samples was measured with an anemometer (HHF81) having 3% accuracy. In each experiment, the generated voltage and ampere were recorded for 30 min at one-second interval using a multimeter/data logger (HHM-EX542) with $\pm 0.06\%$ accuracy. It is noteworthy that recording the output voltage and ampere of the samples were started after reaching a steady state (i.e. after ~30min). [Fig.101](#) illustrates the complete set-up of each experiment.

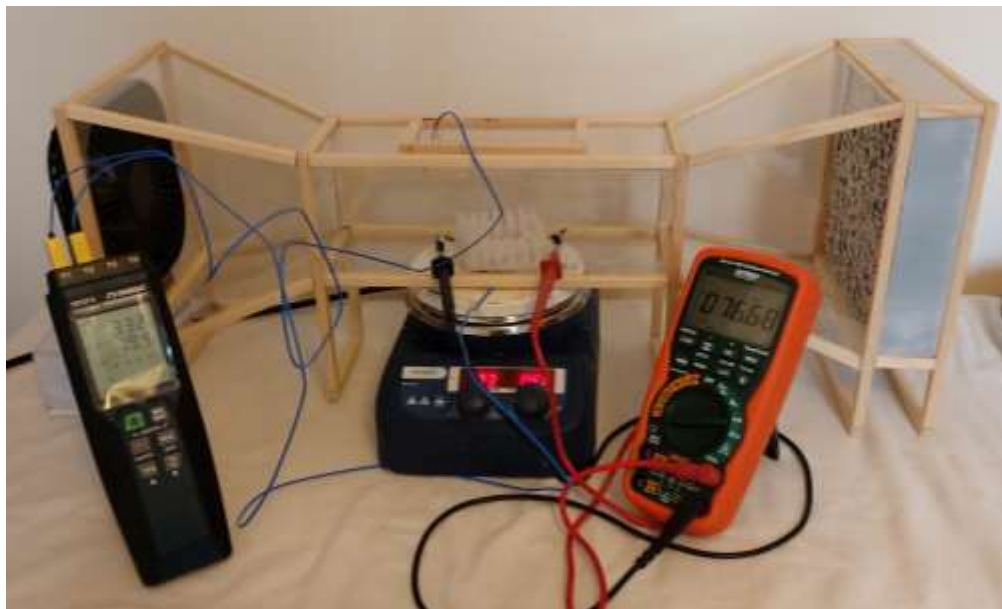


Fig. 101: The complete test set-up for pin-shaped heatsink.

9.4 Results of the experiments

9.4.1 Electrical current

Fig.102 compares the average electrical currents generated by the three samples at the three specified air speeds. As it could be seen, the reference model obtained the lowest output currents under all the three airflow conditions. Conversely, the highest output currents were achieved by the pin-shaped and the bumpy-shaped heatsinks, respectively. Precisely, using the heatsinks increased the electrical current of the reference model specially at higher air speeds. Regarding the still air condition, the average output current of the reference model was almost 1.6 mA, and it slightly increased to 1.8 mA after fabricating the bumpy-shaped heatsink. However, the maximum output current of 2mA was achieved by the pin-shaped heatsink. As it could be seen, in spite of the difference between the output currents of the three samples in the stagnant air, the performance of the reference model was almost the same as that of the bumpy-shaped heatsink. However, at the same air speed, the output current of the pin-shaped heatsink was 125% superior to that of the reference sample.

Concerning the output currents of the three samples at 1.2 m/s air velocity, obviously they were improved superior to those of the stagnant air. Furthermore, whilst the reference model achieved the minimum output current of 3.4 mA, applying the bumpy-shaped and the pin-shaped heatsinks improved its output current by 110% and 118%, respectively. Notably, not only both heatsinks remarkably raised the output current of the reference model, but also their TE effects were almost the same. The same principles applied to the output currents of the three samples at 2.4 m/s airflow. But it should be noted that by increasing the air speed, the effect of the heatsinks on the output current of the reference model became more significant. To illustrate, the difference between the output current of the reference model and that of the bumpy-shaped and the pin-shaped heatsinks was 122% and 127%, respectively.

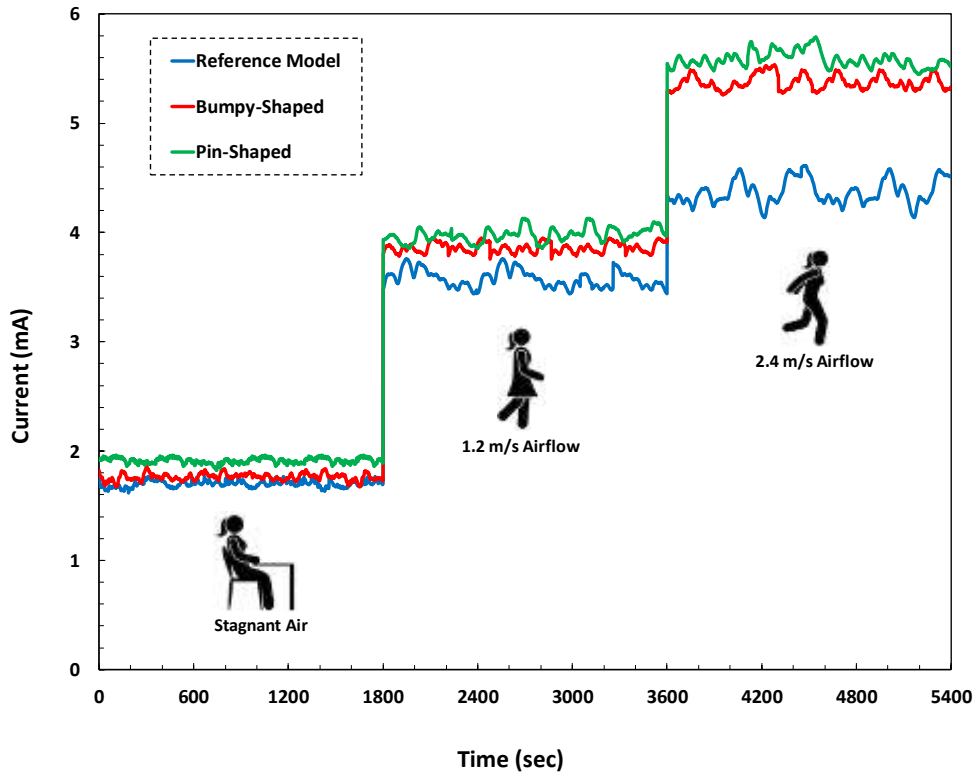


Fig. 102: Changes in the output current of the samples regarding different air flow conditions.

9.4.2 Electric potential

[Fig.103](#) depicts the electric potential of the developed samples under the three specified airflow conditions. Obviously, the reference sample and the pin-shaped heatsink recorded the lowest and the highest output voltages under all the three air flow conditions, respectively. Concerning the bumpy-shaped heat sink, it was ineffective on the output voltage of the TEG in the stagnant air. However, it was superior to the reference model and inferior to the pin-shaped heatsink at 1.2 m/s air speed. When the air velocity raised to 2.4 m/s, the performance of the bumpy-shaped heatsink became similar with that of the pin-shaped heatsink. Precisely, in the stagnant air, the minimum output voltage was 24mV that was achieved simultaneously by the reference model and the bumpy-shaped heatsinks. However, using the pin-shaped heatsink improved the output voltage to 28mV, which was 116% greater than that of the reference model and the bumpy-shaped heatsink.

At 1.2m/s airflow, the three prepared samples illustrated dissimilar performances, and the best to worst output voltages were obtained by the pin-shaped heatsink, bumpy-shaped heatsink, and the reference model, respectively. In fact, the pin-shaped heatsink recorded an average output voltage of 64mV that was 106% and 118% greater than that of the two latter, respectively. When the air speed raised from 1.2 m/s to 2.4 m/s, the bumpy-shaped and the pin-shaped heatsinks achieved the same output voltage of 78 mV, which was 111% greater than that of the reference model (70mV). Based on these outcomes, not only the pin-shaped heatsink was definitely superior to the other two samples, but also its greatest impacts were recorded at 1.2 m/s, 0 m/s, and 2.4 m/s air speeds, respectively.

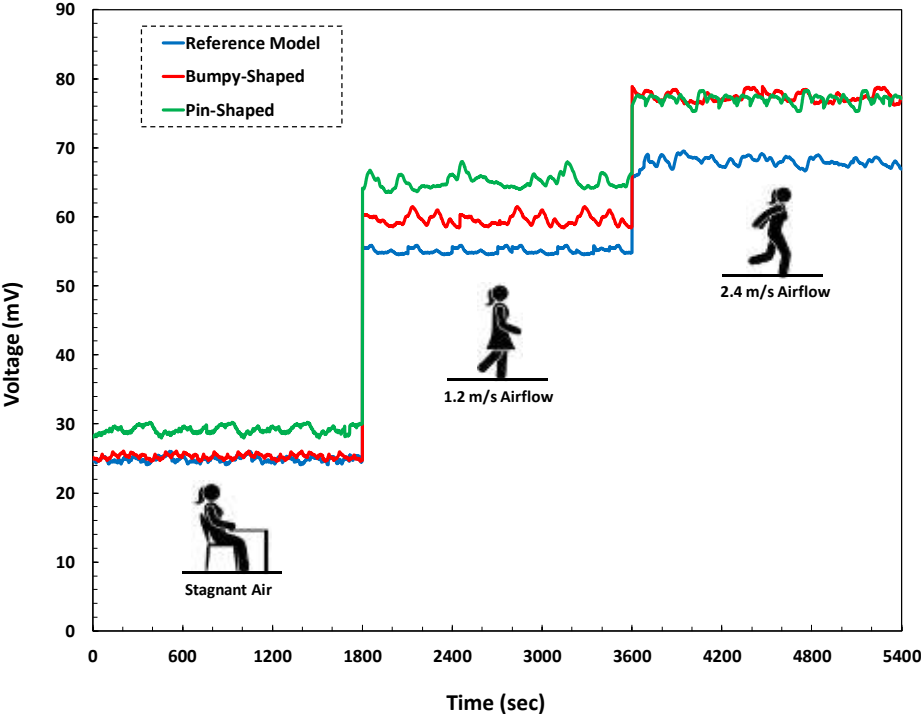


Fig. 103: Changes in the output voltage of the samples regarding different air flow conditions.

9.4.3 Output power

Fig.104 depicts the output power of the developed samples under the three specified air speeds. Obviously, the pin-shaped heatsink and the reference model recorded the superior and the inferior

output powers at the three specified air conditions, respectively. In particular, in the stagnant air, the reference model and the bumpy-shaped heatsink unanimously obtained the lowest output power of 40 mW, signifying that using the bumpy-shaped heatsink was ineffective on the output power in the still air. However, the pin-shaped heatsink achieved nearly 55mW that was 137% higher than that of the other two samples. When the air started blowing with 1.2 m/s speed, the three samples illustrated remarkably distinct results. Precisely, the pin-shaped model, the bumpy-shaped model, and the reference model stood first to third in order regarding the highest output power. To put it another way, the pin-shaped model achieved 255mW output power that was 110% and 135% greater than those of the bumpy-shaped and the reference models, respectively. When the air speed raised from 1.4 m/s to 2.4 m/s, the performance of the pin-shaped and the bumpy-shaped heatsinks became remarkably closer to each other, although still the former was superior to the latter. To illustrate, the highest output power of 430 mW was obtained by the pin-shaped heatsink followed by 420mW that was achieved by the bumpy-shaped model. These values were 150% and 145% greater than that of the reference model with 290mW output power.

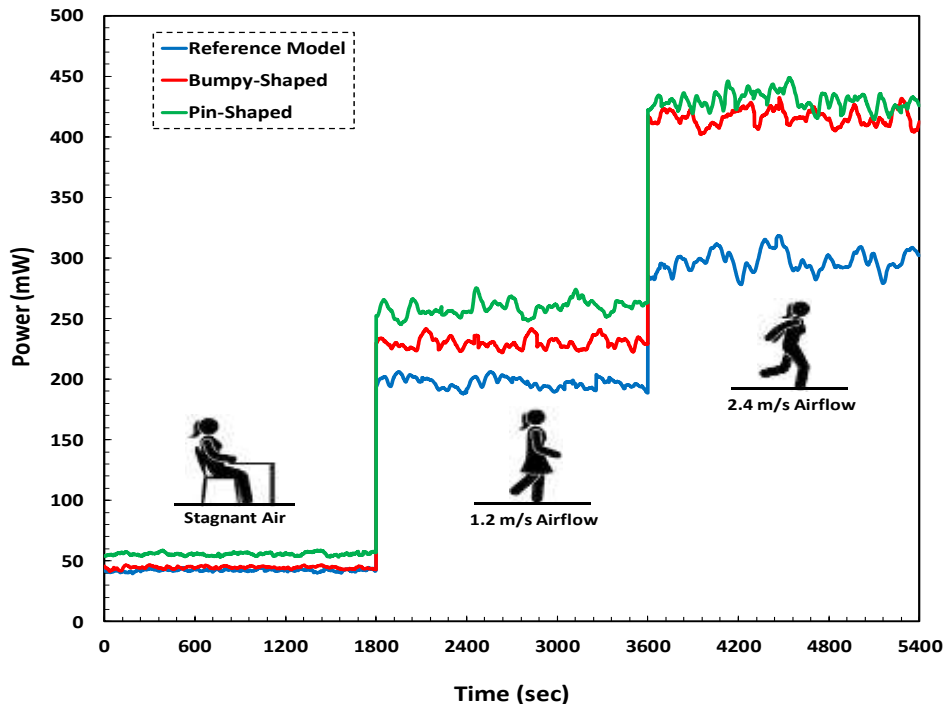


Fig. 104: Changes in the output power of the samples regarding different air flow conditions.

9.5 Summary

In this chapter, two types of flexible heatsinks were developed and attached to the PDMS substrate of the optimal sample of [Chapter 8](#) (i.e. sample 2a). The heatsinks were namely the bumpy-shaped and the pin-shaped heatsinks. To reduce the thermal resistivity at the intersection of the heatsinks and the PDMS substrate, the heatsinks were also prepared with PDMS. The results demonstrated that in the still air, the bumpy-shaped heatsink had no or a slight effect on the TE performance of the reference model. However, when the air started flowing, its effect became dominant specially at the highest air speed (2.4 m/s). Regarding the pin-shaped heatsink, it was in general superior to the bumpy-shaped heatsink at all the three air flow conditions. To clarify, not only it recorded the highest output powers at all the three air flow conditions, but also it improved the output power of the reference model by 137% in the still air. Thus, due to the superiority of the pin-shaped heatsink, it was selected for optimizing the TE performance of the integrated TEGs in [Chapter 10](#).

Chapter 10

Fabricating the Heating Armbands

10.1 Introduction

As explained in [Chapter 1](#), the goal of this research is to provide a hybrid power supply to power a pair of heating armbands. Concerning the literatures reviewed in [Chapters 4](#) and [5](#) and the results obtained in [Chapters 7](#), [8](#) and [9](#), this Chapter intends to fabricate the hybrid power supply comprising a set of TEGs and a rechargeable battery to power the heating armbands. To study the performance of the developed heating prototype in the real life, it was ultimately tested on some individuals in an office room during the heating month of March in the UK.

10.2 Fabrication procedure

10.2.1 Coupling the TEGs

To fabricate the TEG part of the hybrid power supply, the outcomes of [Chapters 8](#) and [9](#) were combined together. However, the TEGs used in [Chapters 8](#) and [9](#) (i.e. GM 250-71-14-16) were replaced by another commercial TE power generator (i.e. SP1848-27145) with the dimensions of 40 mm (width) \times 40 mm (length) \times 3.4 mm (height). This was mainly because replacing the 9cm² area GM 250-71-14-16 module with the 16cm² area SP1848-27145 module reduced the required number of TEGs from 8 to 6. In addition, as mentioned before, the purpose of cascading the TEGs in [Chapters 8](#) and [9](#) was to provide enough height to examine the effect of varying the thermal boundary condition along the legs. Therefore, the outcomes of those chapters were used as the baseline of this chapter to integrate six single stage TEGs together. Whilst the TEGs were connected together electrically in series and thermally in parallel, their top halves were covered with a plain PDMS substrate based on the optimal sample of [Chapter 8](#) (i.e. model 2a).

[Fig.105](#) presents the integrating procedure of the TEGs. As could be seen, the six TEGs were arranged in a 3 by 3 array inside a pre-developed mould ([Fig.105a](#)). To cover only the top half of the TEGs, they were placed from their cold side in the mould with 0.5 cm intervals from each other. Then the as-prepared plain PDMS mixture in [Section 8.4.1](#) was poured into the mould to cover only half of the TEGs' height ([Fig.105b](#)). After that, the mould was placed in a freezer at -20 °C for 6 hrs to degas the PDMS mixture ([Fig.105c](#)) followed by curing the mixture on the hot

plate at 100 °C for 2 hrs (Fig.105d). Next, the cured mixture was peeled off the mould, incorporating the six individual TEGs as a whole (Fig.105e). Finally, the as-prepared pin-shaped heatsinks in Section 9.2 were adhered to the PDMS substrate of the TEGs, using the plain PDMS mixture as a paste (Fig.105f). Fig.106 illustrates the photos of the integrated TEGs comprising the PDMS substrate and the pin-shaped heatsinks.

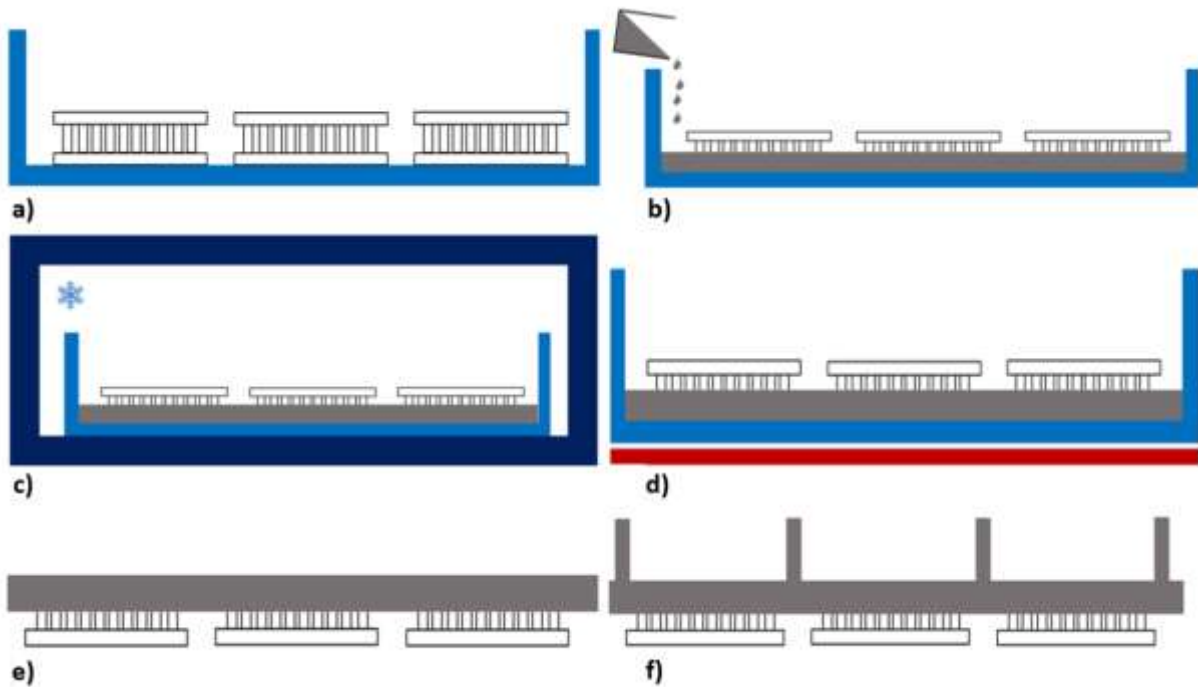


Fig. 105: The schematic procedure of integrating the TEGs.

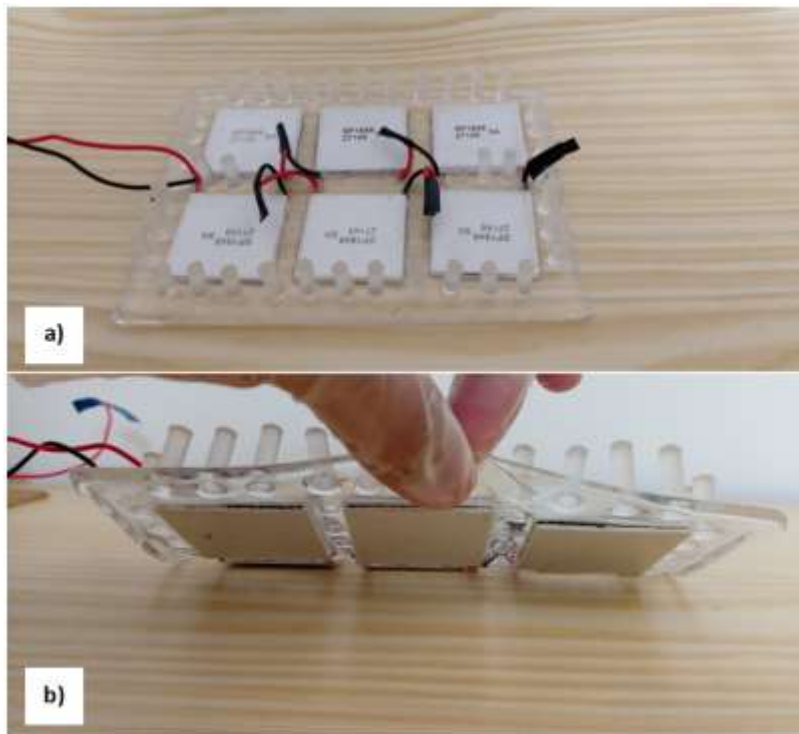


Fig. 106: a) The integrated TEGs with the PDMS substrate and the pin-shaped heatsinks; b) covering only the top half of the TEGs with the PDMS substrate.

10.2.2 Fabricating the hybrid power supply

As explained in [Chapter 1](#), the hybrid power supply consisted of a series of TEGs and a rechargeable battery. Accordingly, the integrated TEGs in [Section 10.2.1](#) were installed in a box to be heated by a candle as the heat source. Using the candle as the heat source of the TEG was attributed to two main reasons, including its accessibility even in remote areas and providing point-based and controllable heat source inside the buildings. Regarding its controllability, it was also impossible to replace the candle with any other internal heat sources (i.e. a radiator or a hot pipework) to provide the required temperature difference along the legs. This was mainly because the temperature of any internal heat source should stay within a certain temperature limit to avoid burning or injuring the occupants. To put it another way, the temperature of none of the internal heat sources should exceed 43 °C in public spaces to prevent burns. As a result, providing the required temperature difference via any other internal heat sources was almost impossible.

Accordingly, a semi-closed box with the dimensions of 18cm (width) \times 22cm (length) \times 10cm (height) was initially prepared as the supporting structure of the hybrid power supply to allow oxygen to reach the candle, see [Fig.107a](#). Notably, the size of the box was determined with respect to providing an adequate space for placing the 6 integrated TEGs inside it. The final size of the integrated TEGs was 12cm (width) \times 17cm (length). Then a stool-shaped structure with the dimensions of 10cm (width) \times 16cm (length) \times 5cm (height) and an aluminum top surface was placed inside the box to put the 6 integrated TEGs on it, see [Fig.107b](#). To heat the TEGs from their hot side, the candle was placed under the stool-shaped structure. Notably, as [Fig.107c-d](#) depict, the candle was placed on a separate plate to be slid effortlessly in and out of the stool-shaped structure. To satisfy the fire safety, it was considered that the applied plate be heat-resistant and nothing could be felt on the burning candle. Then, the integrated TEGs were placed from their hot side on the aluminium surface of the stool-shaped structure, as [Fig.107e](#) shows. Finally, a fan was coupled with the structure of the box to cool down the cold side of the TEGs. To clarify, the fan was inserted into the female joints that were cut out of the box's frame, see [Fig.107f](#). Therefore, not only the PDMS substrate incorporated the 6 individual TEGs together as a whole and hold them in place, but also it served as a thermal barrier between the fan and the aluminium plate. To specify, the PDMS substrate protected the aluminium plate to be cooled down by the fan.

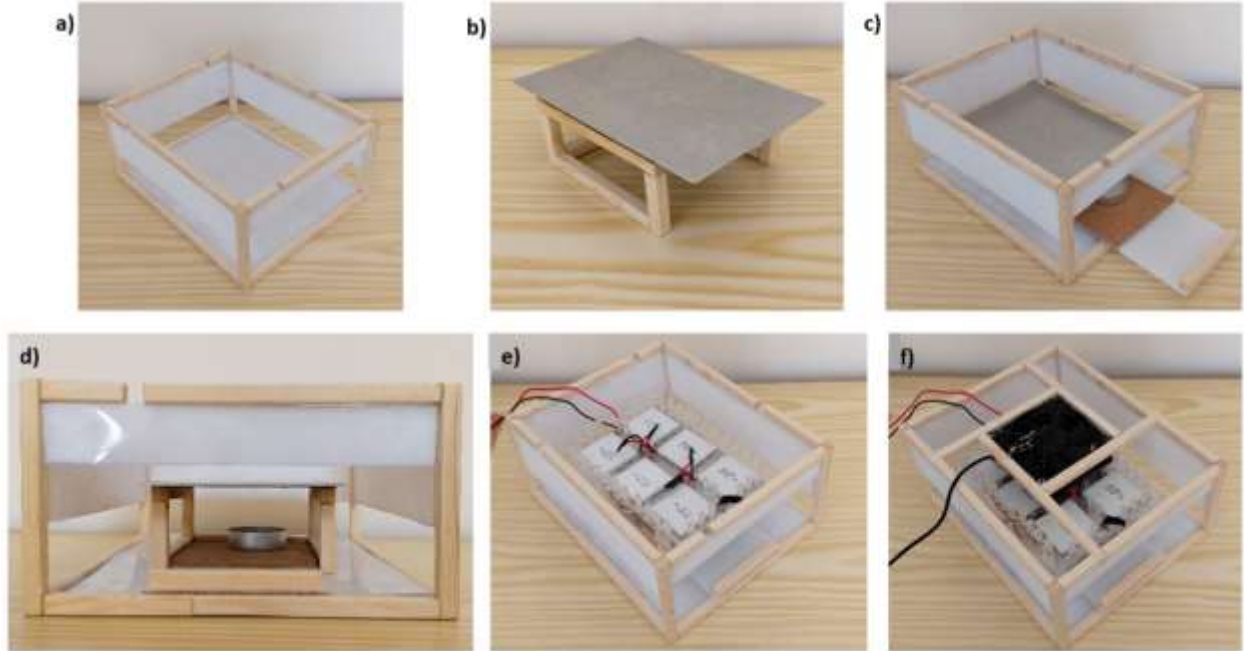


Fig. 107: Fabrication process of the benchtop power supply.

After one minute of lighting the candle and running the fan at 1.2 m/s air speed, the temperature difference between the hot and cold sides of the TEGs reached to 30 °C. Details on the temperature differences along the TEGs are provided in [Section 10.2.3](#). Due to this temperature difference, in total, the integrated TEGs generated a constant DC voltage of 1.5V and an output current of 200mA that was not enough for powering the 5V heating pads embedded in the armbands. Therefore, a commercial voltage booster circuit (i.e. PFM control DC/DC booster) was used to boost the voltage from 1.5V to 5V. [Fig.108](#) shows the photo of this booster circuit, operating by an input voltage in a range of between 0.9V and 5V DC and giving a stable 5V DC output through its USB female socket.

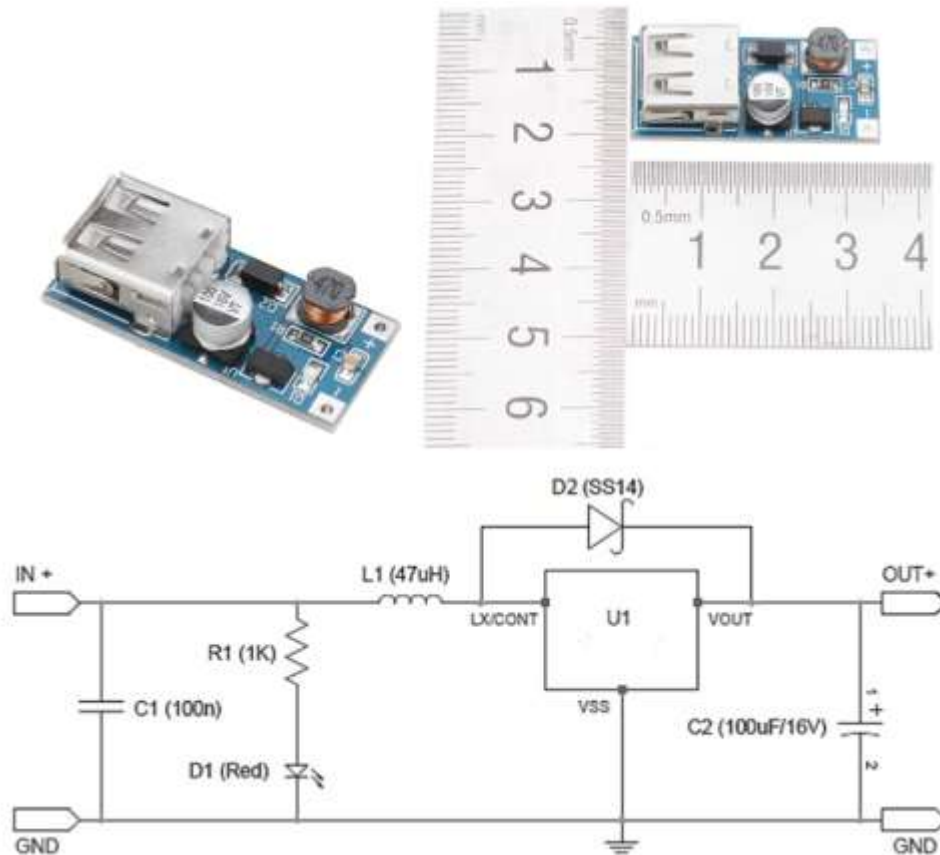


Fig. 108: Photo of the PFM control DC/DC booster and blueprint of its internal circuitry [337].

As Fig.108 illustrates, the module comprised of two capacitors (C1-C2), one resistor (R1), one inductor (L1), one rectifier diode (D2), one LED (D1), and an IC (U1). All of these components are in Surface-mount technology (SMD) form, except the USB ‘A’ female socket [337]. Observed values of the components are:

- C1: 100nF (Input Filter)
- C2: 100uF/16V (Output Filter)
- L1: 470 (47uH Inductor)
- D2: SS14 (Schottky Diode)
- D1: Red LED (Input Power Indicator)
- R1: 102 (1K Resistor- LED Current Limitor)
- U1: E5 0P (smd marking code)

Accordingly, the negative and positive terminals of the integrated TEGs were soldered to the negative and positive holes of the booster circuit. With up to 96% conversion efficiency, the DC/DC booster increased the input voltage of 1.5V to 5V. However, based on the energy conservation principle, it reduced the 200mA input current of the integrated TEGs to 60 mA. Thus, although the booster satisfied the required voltage, its output current was inadequate to heat the two heating elements embedded in the armbands. To specify, the required electric potential and electrical current for each heating element were 5V and 1A, respectively, resulting in 2A current requirement in total for powering the two heating elements at the same time. So, there were four alternatives to boost the current of the power supply, such as increasing the number of the TEGs, storing the generated electricity in an ultra-capacitor/battery, or coupling the integrated TEGs with another power supply. Concerning the number of the TEGs, it should be raised from 6 to 54 to provide the required 2A. This number of TEGs was too space consuming to be fabricated in a benchtop box. Regarding the electricity storage, the low output current of the booster circuit resulted in extremely slow or no charging. Replacing the battery with an ultra-capacitor, its great downside was that its lasting power was far less than that of the battery. Precisely, charging and discharging a battery took nearly 1-5 hrs and 0.3-3 hrs, respectively. However, it took 0.3-3 seconds for an ultra-capacitor to either be charged or discharged [338]. For example, the capacitance of one of the largest available capacitor is 400 Farads. Converting Farads to Ah (i.e. the unit of batteries' capacity), the following formulas can be used:

$$E_b = Ah \times V_b \times 3600 \quad (26)$$

$$E_c = \frac{1}{2} F \times V_c^2 \quad (27)$$

where E_b , Ah, V_b are the energy stored in the battery (Wh), capacity of the battery (mAh), and voltage of the battery (V), respectively. E_c , F, V_c are the energy stored in the capacitor (J), capacitance of the capacitor (F), and the voltage of the capacitor (V), respectively. Thus, a 400 Farad equals with 109 mAh that was not enough for powering two heating elements. Therefore, it was considered to connect the PFM control DC/DC booster in parallel with a low voltage rechargeable battery (i.e. 26650 Li-ion Rechargeable) to provide the required current for the heating elements, as Fig.109 illustrates. Regarding the rechargeable battery, it provided 4A and 3.7V constant output current and voltage, respectively.

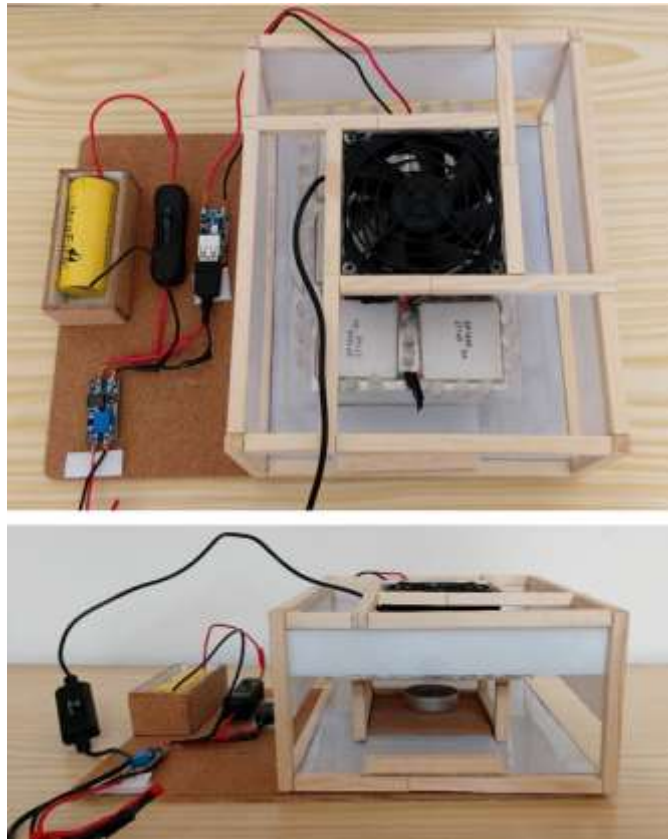


Fig. 109: Integrating the benchtop power supply with a current source (a rechargeable battery).

It should be noted that, the battery and the integrated TEGs served as a time-varying voltage source and a constant voltage source, respectively. Thus, coupling them together decreased the discharging speed of the former. To illustrate, combining the battery with the integrated TEGs, the latter with higher voltage discharged into the former until they ended up with equal voltages. Since the battery was rechargeable, it was charged by the TEGs until the two had the same voltage. In this research, since all tests lasted for half an hour, the battery was charged by the TEGs throughout the tests. Regarding the discharging time, the same battery discharged within 25 minutes for powering the two heating elements and the fan, but discharged within 45 minutes after being connected to the TEGs. Thus, splitting the provision of the required voltage between the two energy supplies reduced the number of the required batteries and increased the battery's run time. Consequently, the TEGs and the battery performed as the constant voltage and current sources, respectively. Finally, since the PFM control DC/DC booster and the rechargeable battery were electrically connected in parallel, their resultant output voltage had to be adjusted based on the

required voltage of the heating elements (i.e. 5V). Accordingly, their ultimate positive and negative terminals were connected to a DC to DC adjustable step up boost converter (i.e. MT3608 Adjustable Power Supply Module) to set the output voltage on 5V.

10.2.3 Checking the thermal performance of the PDMS substrate

Based on the study carried out in [Chapter 8](#), the role of the PDMS substrate was not only integrating the TEGs together and holding them in place, but also isolating the hot and cold surfaces of the TEGs. Accordingly, the temperatures over the aluminum plate (T1), between the aluminum plate and the PDMS substrate (T2), and over the PDMS substrate (T3) were recorded by the 4 channel thermometer (HH374) for 30 min (i.e.1800 seconds). [Fig.110](#) illustrates the different levels of measuring the temperatures, and the results are presented in [Fig.111](#). As the graph shows, the average temperatures of T1, T2, and T3 were 47.71 °C, 31.60 °C, and 21.65 °C, respectively. Thus, it was proved that coupling the PDMS substrate with the flexible pin-shaped heatsinks generated a significant temperature difference (i.e. 26 °C) between the hot and cold sides of the TEGs. Furthermore, covering the top-half of the legs with the PDMS substrate provided nearly an even temperature difference along them. To specify, not only the temperature gradient between the middle of the legs and the hot side of the TEGs was ~16 °C, but also it was ~10 °C between that of and the cold side of the TEGs. In addition, the rate of the temperature gradient was almost constant over the 30 min of the test, demonstrating the long-term thermal impact of the integrating PDMS substrate and the pin-shaped heatsinks on the performance of the TEGs.

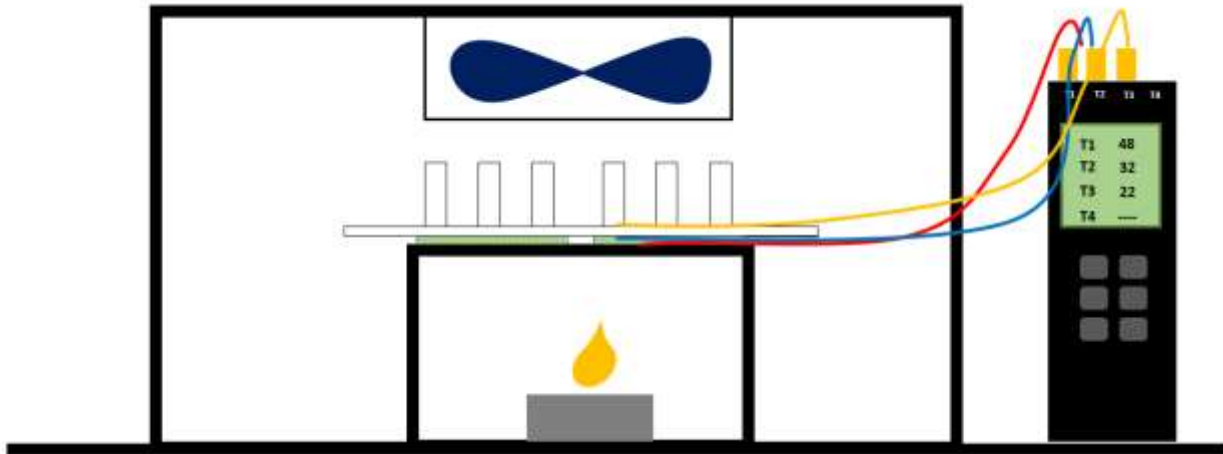


Fig. 110: Schematic of measuring temperature at different levels of the PDMS substrate.

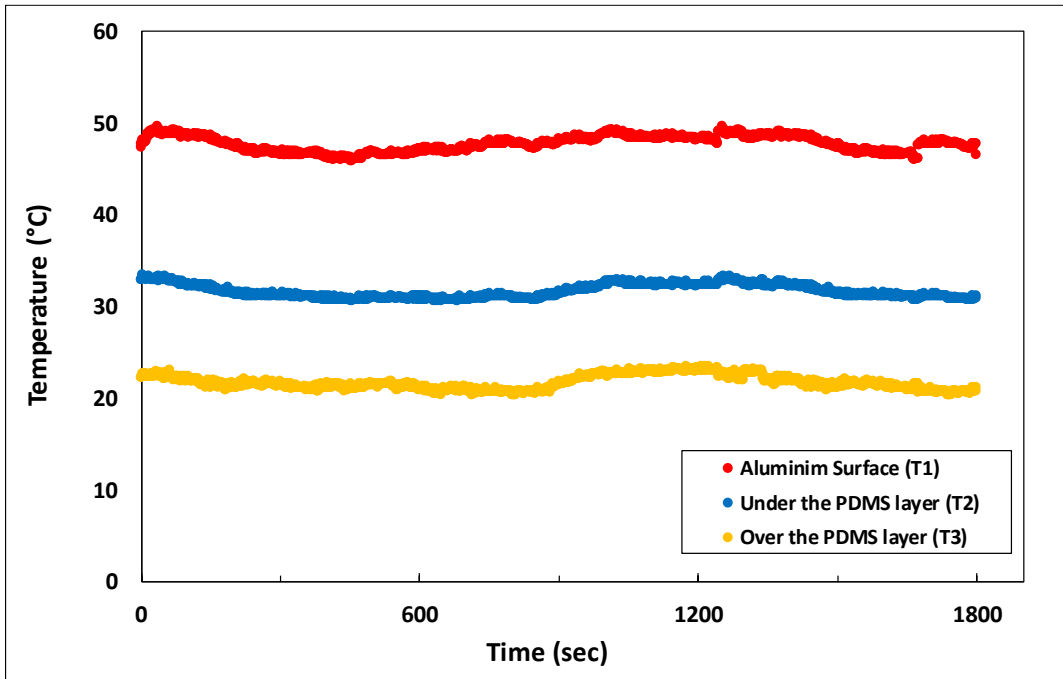


Fig. 111: Variation of temperature at different levels of the integrated TEGs.

10.2.4 Fabricating the armbands

Two off-the-shelf electrical heating pads (Adafruit) with the dimensions of 100mm× 50mm were selected as the heating elements of the armbands. The pads consisted of a polyester filament and micro stainless steel fibres laminated between two polyimide films. In fact, the films served as a

thermal insulation due to their relatively low thermal conductivity (0.12 W/mK), see [Fig.112a](#). Thus, the polyimide films were peeled off and replaced by a copper foil with extremely greater thermal conductivity (401 W/mK). Accordingly, after peeling off the polyimide films, the fabric part of the heating element was sewn onto a polycotton fabric as the supporting surface, see [Fig.112b](#). Next, the polycotton fabric was sewn onto an off-the-shelf armband, whilst the heating fabric was facing outward, as [Fig.112c](#) illustrates. After that, the Kohree copper foil tape with dual conductive adhesive was stuck onto the heating element to distribute the heat evenly on the skin, see [Fig.112d](#). Finally, the armbands were connected to a simple On/Off switch individually to provide control over their heating condition. The whole setup of the heating armbands after being integrated with the hybrid power supply is presented in [Fig.113](#).

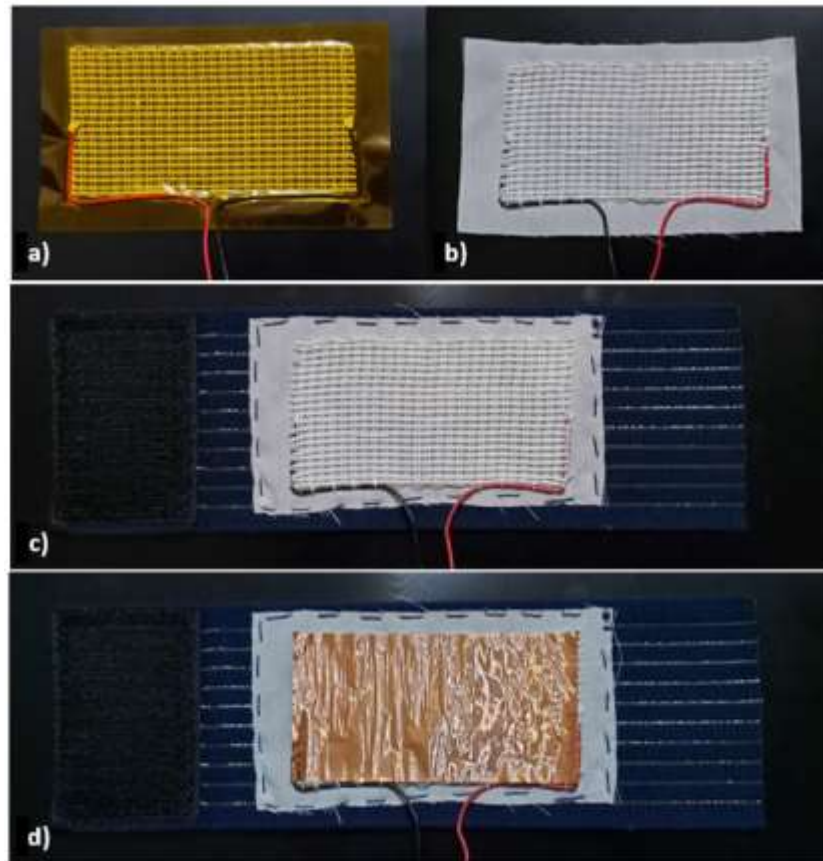


Fig. 112: Fabricating procedure of the heating armband: a) Adafruit electrical heating pad; b) sewing the heating fabric onto a polycotton fabric; c) sewing the polycotton fabric onto a commercial armband; and d) sticking a copper foil tape onto the heating fabric.

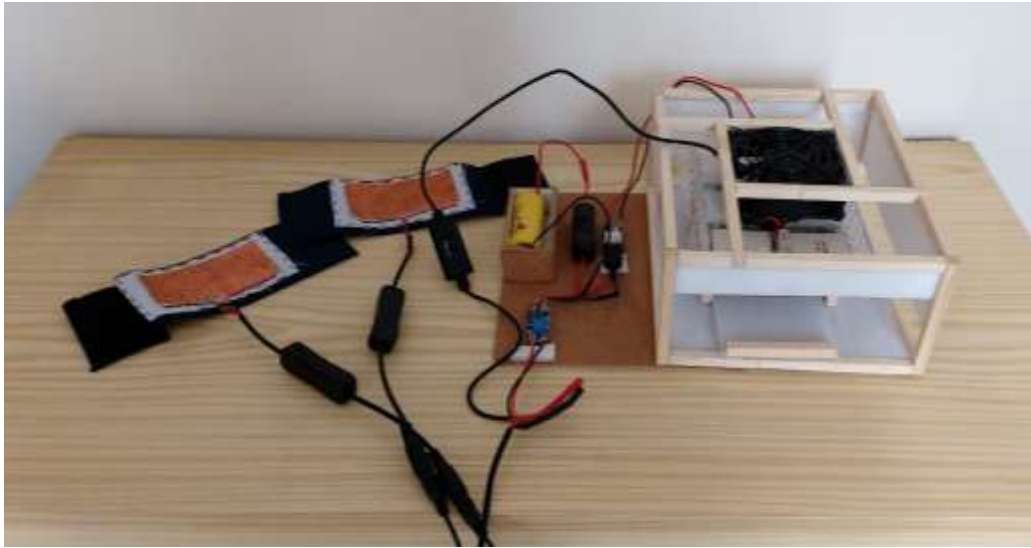


Fig. 113: The fabricated heating armband connected to the benchtop power supply.

10.3 Testing conditions

10.3.1 The experimental room

The experiments were conducted in March 2021 at the University of Derby, UK. It was impossible to conduct the tests earlier in the year due to the national lockdown applied from 4th Jan to 8th Mar 2021 attributed to the Covid-19 pandemic. To identify the performance of the heating armband in the real-life, the tests were carried out in one of the office room of the University of Derby. The dimensions of the office room were 6.37 m (length) \times 4.90 m (width) \times 3.4 m (height), comprising roughly two and half external walls and one and half internal partitions. The position of the room in the building is illustrated in [Fig.114](#), and its plan and inside view are presented in [Fig.115](#). As could be seen, the external walls were facing south-east, south-west, and west, whilst there were two small windows (0.56 m \times 1.68m), a French patio door (1.68 \times 1.82), and a medium size window (0.91m \times 1.96m) in them, respectively. The room was naturally ventilated and heated by three radiators. During the tests all radiators were kept off and windows were shut down. It should be noted that one hr before carrying out the tests, the windows were left open to reduce the room temperature to 16°C. Then, they were kept close throughout the tests. Each experiment was conducted by two subjects, one served as the control group and the other as the experimental group.

Thus, as Fig.115 shows, the two desks in the middle of the room with almost the same distance from the openings were selected for the tests to provide almost the same thermal condition for both groups. Accordingly, the two participants were sitting side by side with 2.0m distance from each other during the tests.



Fig. 114: Location and building of the experimental room.

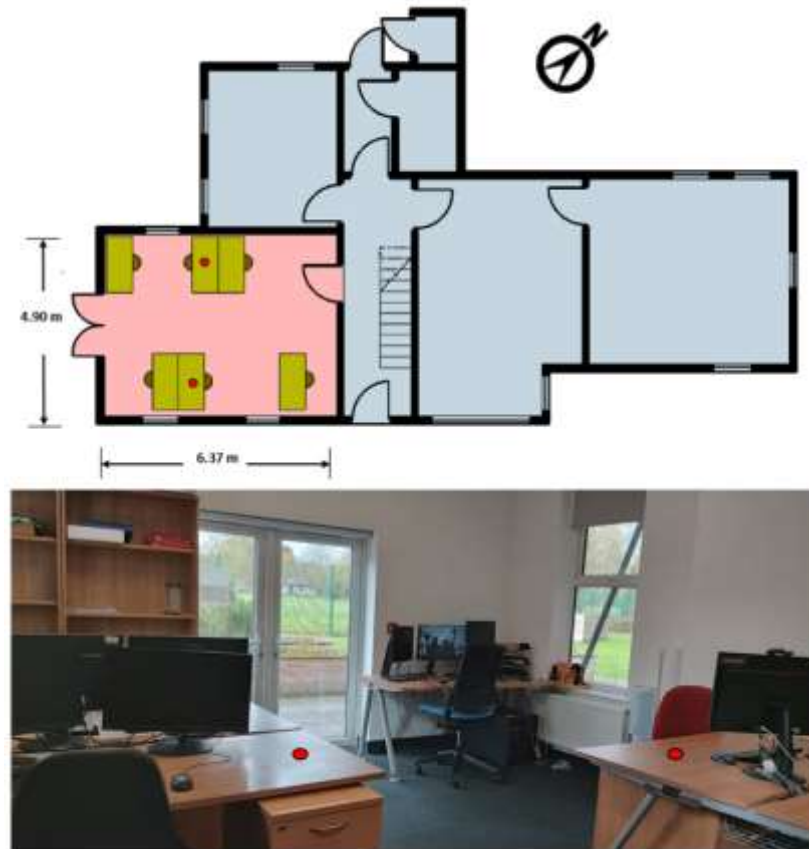


Fig. 115: Photo and layout of the experimental room.

10.3.2 Description of the subjects

Eight subjects including three females and five males in the age range of 25 to 35 were recruited for this study. It should be noted that it was challenging to find more participants due to the COVID-19 pandemic and its attributed restrictions. Each experiment was conducted with two subjects, such that one subject participated as the experimental group and the other took part as the control group. Precisely, the experimental group was wearing the armbands to evaluate their thermal performance, whereas the control group was without the armbands and served as the reference for evaluating the responses of the experimental group. [Fig.116](#) illustrates the experimental and the control subjects of one of the experiments. Swapping the participants of the experimental and the control groups in each test, 16 experiments were conducted in total to assess the thermal sensation and comfort of all the eight participants both with and without wearing the armbands. By collecting and comparing the obtained data from these two groups, it was expected to reasonably

evaluate the impact of wearing the armbands on the thermal sensation and comfort of the individuals. Notably, the participants took part in the experiments voluntarily and without being paid. Before starting the experiments, the eight participants were provided with an information sheet, explaining the purposes of the study. Then, their consents were obtained using the universities' standard consent form. The subjects were asked to wear a light, long sleeve shirt (0.22 clo)/blouse (0.20 clo), light trousers (0.26 clo), ankle socks (0.04 clo) and shoes (0.04 clo), resulting in the total clothing insulation of 0.56 clo and 0.54 clo for the male and female subjects, respectively [339]. Also, they were asked not to take strong exercise, medicine, drink alcohol or coffee for at least 2 hrs before the experiments.



Fig. 116: Photos of the experimental (left) and the control (right) groups in one of the experiments.

10.3.3 The experimental procedure

As Fig.117 shows, each experiment lasted for 1 hr, including the preparation, the adaptation, and the experimental periods. The duration of the tests was considered based on the literatures reviewed in Chapter 2 and the coronavirus restrictions at the time. To clarify, the room was naturally ventilated, and all the windows were kept close throughout the tests. As a result, the participants were wearing mask during the 1 hr tests, which was uncomfortable for them for a longer period. Regarding the preparation period, the subjects were asked to stay in a preparation room for about 15 min where the air temperature was around 26 °C. During this period, the tests' procedure and the questionnaires' content were explained to the subjects. Then, the adaptation period started, when the subjects entered the experimental room and were asked to sit at the specified workstations. During this period, the hybrid power supply was turned on to pre-heat the armbands for the experimental period. In the last 5 min of the adaptation period, the subjects were asked to fill the first questionnaire, which was mainly attributed to their demographic information (gender, age, and ethnicity), thermal sensation, and thermal comfort at the time. Next, the experimental section was started and the heating armbands were worn by the experimental group. During this period, both groups filled the second questionnaire three times at 10 min intervals. The details of both questionnaires will be illustrated in details in Section 10.4.2. The survey's questions automatically appeared on the subjects' computer screen based on pre-set schedules. During the tests, the subjects could freely choose to read books, listen to music, surf the internet or watch movies on the computer, but drinking, eating, smoking and walking were prohibited.

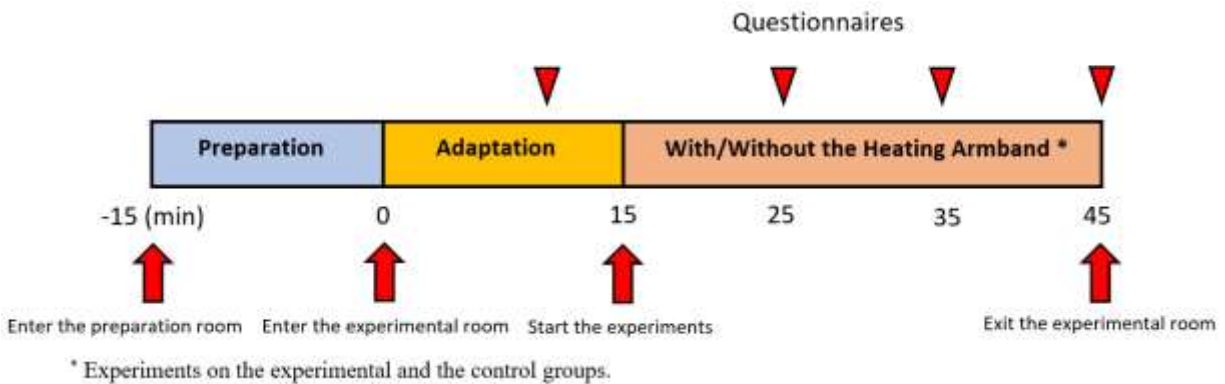


Fig. 117: The experimental procedure of this study.

10.4 Measurements

10.4.1 Objective measurements

In each experiment, two types of physical measurements were carried out simultaneously, including the environmental and the skin measurements.

- The environmental measurement:

Whilst the relative humidity (i.e. 45%) and the air speed (i.e. 0 m/s) of the experimental room were constant over the tests, the air temperature was measured at one-minute interval throughout the experimental sessions (i.e. for 30 min). Notably, the humidity and air speed were measured by the HHF81 anemometer and the temperature with the 4 channel thermometer (HH374), which were used in [Chapter 8](#). In fact, this measurement was conducted in between the two workstations three different height levels, including 10 cm, 70 cm, and 110 cm from the floor level. In fact, these heights were respectively at the feet, hands, and head levels of the subjects, whilst they sat at their workstations. This ensures that the room was in a thermally stable environment throughout the experiments. The data were used to compare the occupants' subjective responses with the environmental measurements to characterize the influence of the prototype on the thermal sensation and comfort of the participants.

- The skin measurement:

The skin temperatures of the eight participants were recorded at one-minute interval during the experiments. Precisely, it was measured at the back of their hands and under the armband. Obviously, the former was measured for both the control and the experimental groups and the latter was measured only for the experimental group.

10.4.2 Subjective questionnaire survey

As explained in [Section 10.3.3](#), two questionnaires were filled by the subjects over the experiments, and the responses were scaled according to [Table 22](#). To specify, both questionnaires surveyed the temperature satisfaction, thermal sensation, preferred thermal sensation, and thermal comfort of the subjects during the experiments. Respecting the difference in the thermal sensation and comfort of different body parts, they were surveyed for seven body parts, including forehead,

torso front and back, hands, thighs front and back, and feet. [Appendices A](#) and [B](#) presents the details of the two questionnaires.

Table 22: Scales of the subjective responses.

Scale	Thermal sensation	Thermal comfort	Thermal preference	Scale	Thermal acceptability	Scale	Other Discomforts
3	Hot	Very comfortable	Much warmer	6	Totally acceptable	4	No feeling
2	Warm	Comfortable	Warmer	5	Acceptable	3	Slightly uncomfortable
1	Slightly warm	Slightly comfortable	Slightly warmer	4	Slightly acceptable	2	Uncomfortable
0	Neutral	No feeling	No change	3	Slightly unacceptable	1	Very uncomfortable
-1	Slightly cool	Slightly uncomfortable	Slightly cooler	2	Unacceptable		
-2	Cool	Uncomfortable	Cooler	1	Totally unacceptable		
-3	Cold	Very uncomfortable	Much cooler				

10.5 Results of the objective measurements

[Fig.118](#) illustrates the average variation in the room’s temperature at the three specified height levels (i.e. 10 cm, 70 cm, and 110 cm) during the experiments. The results showed that not only the three heights were experiencing three different temperatures, but also the temperature of each level was almost consistent over the experiments. In particular, the feet level was experiencing the coldest temperature in the room with 13 °C on average, whilst the hands and the head levels obtained the second and the third coldest temperatures, respectively. To illustrate, the hands and the head of the subjects were surrounded with 15 °C to 16 °C and 18 °C to 19 °C air temperatures, respectively. [Fig.119](#) depicts the temperature of back of the hand for both the experimental and the control groups and under the armband for the experimental groups over 30 min of the tests. Regarding the temperature under the armbands, it was initially high at the beginning of wearing them but reduced to a roughly constant value after 10 min. To illustrate, the temperature under the armbands was around 41 °C when the tests commenced, but reduced to 39 °C after 10 min of wearing them. Notably, from 10 min to 30 min of wearing the armbands, the temperature under the armbands was mostly constant and reduced with a smooth slope to 38 °C.

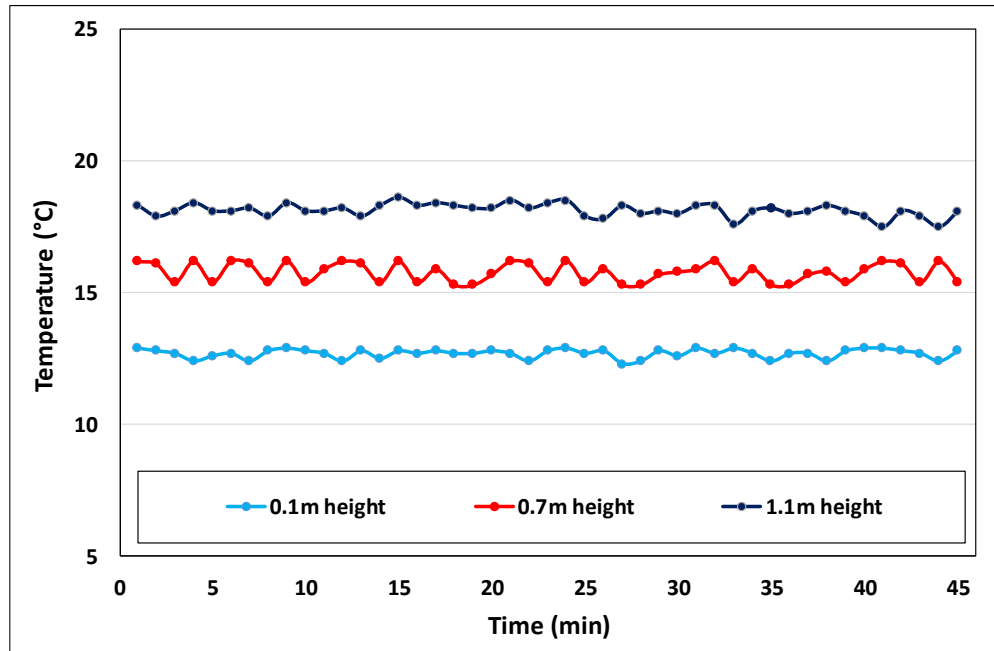


Fig. 118: Variation in the room’s temperature at different heights.

Concerning the temperature of back of the hand, obviously it constantly decreased for both the experimental and the control groups. However, this reduction was smoother for the former and sharper for the latter. To clarify, at the beginning of the tests, both groups experienced the same temperature of 30 °C at the back of their hands, reducing to 27 °C and 27.5 °C for the control and the experimental groups at the end of the tests, respectively. This reduction in the skin temperature was attributed to the low ambient temperature (15 °C -16 °C), resulting in a constant dissipation of heat from the hands to the ambient. Notably, in spite of the reduction in the skin temperature of both groups in the first 18 min of the tests, the skin temperature of the control group was slightly higher than that of the experimental group. The main reason for the colder skin temperature of the experimental group was fastening the armbands around the wrist, resulting in a slightly slower blood flow to the hands’ vessels. However, from 18 min to 30 min of the tests, the heating effect of the armbands overcame the blood flow issue, thus the skin temperature of the experimental participants slightly increased compared with that of the control participants. [Fig.120](#) shows the thermal image of the hands of an experimental participant. As could be seen, the ambient air temperature during the test was 16°C, which validates the result achieved by the thermometer at hand level (0.7m height from floor level). Also, the temperature on the outer surface of the heating

armbands was 30.5°C. Definitely, this temperature could reach up to 41°C under the armbands, which again validates the results of the thermometer under the armband.

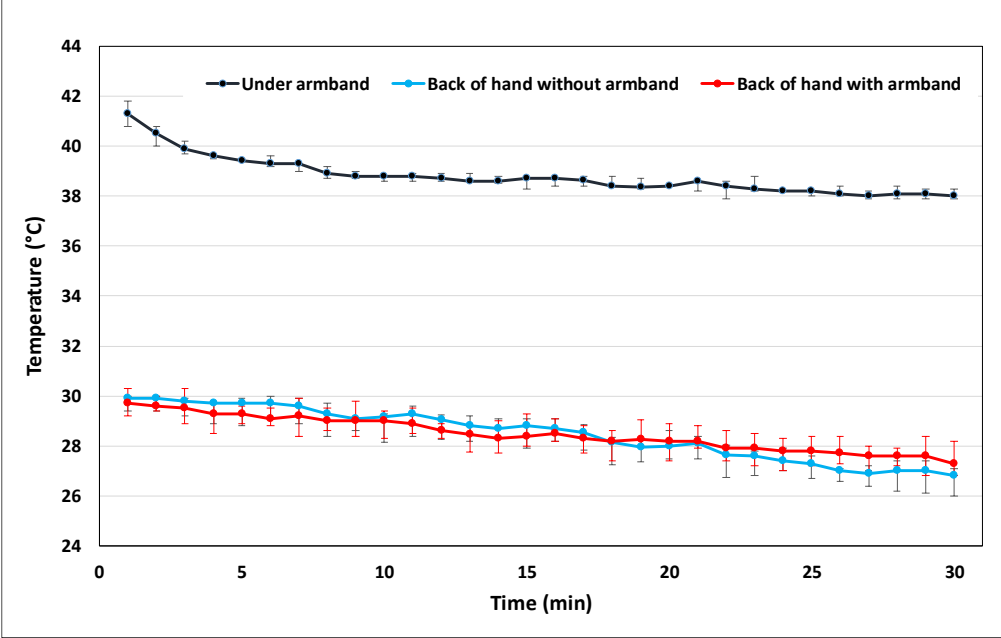


Fig. 119: Variation in the skin's temperature of the subjects at the back of their hands and arms.

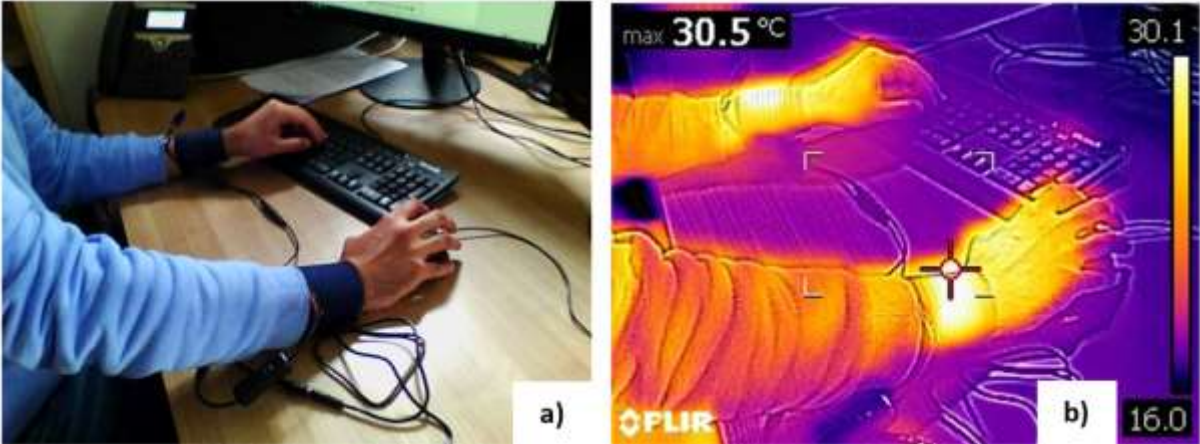


Fig. 120: a) The armbands worn by an experimental participant; b) the thermal image of the hands and armbands (FLIR T660).

10.6 Results of the subjective questionnaire survey

10.6.1 Thermal sensation and comfort of body parts

10.6.1.1 Forehead

Based on [Fig.121a](#), the participants on average felt neutral on their forehead over the tests. In general, their thermal sensation before and after wearing the armbands spread from slightly cool to slightly warm and neutral to slightly warm, respectively. The only exception was the experimental group at the 25 min of the test, demonstrating the broadest range of thermal sensation from slightly cool to warm. To clarify, before wearing the armbands, one half of the participants felt between slightly cool to neutral and the other half sensed in a range of between neutral to slightly warm. Ten minutes after wearing the armbands, whilst 50% of the participants still felt between slightly cool to neutral, the other half felt between neutral to warm. In particular, 25% of the participants who felt slightly warm before wearing the armbands sensed in a range of between slightly warm to warm in the first 10 min of wearing them. Also, 25% of the participants who felt in a range of between slightly cool and neutral before wearing the armbands felt neutral after wearing them. Changing the thermal sensation of these 50%, it could be interpreted that wearing the armbands affected on the forehead's thermal sensation. This effect became intense after 20 and 30 min of wearing them, because the lowest thermal sensation of the participants was changed from slightly cool to neutral. However, due to the adaptation of the body to the applied heat, the thermal sensation of 25% of the participants dropped to roughly neutral at the 35 min of the test, but raised again to slightly warm at the 45 min of the test.

Based on [Fig.121b](#), neutral was the average comfort level of the participants in all the experiments except at the 25 min of the test. To illustrate, 10 min after wearing the armbands, the average comfort level of the participants was improved from neutral to the range of between neutral and slightly comfortable. The worst comfort level of the participants before and after wearing the armbands was respectively uncomfortable and slightly uncomfortable, showing the positive effect of wearing the armbands on the forehead's thermal comfort. Regarding the best recorded comfort level, it was constantly comfortable over the experiments. Concerning the control groups, the comfort level of 50% of them was in a range of between uncomfortable and neutral, and the other

half felt in a range of between neutral and comfortable. As mentioned above, after 10 min of wearing the armbands, their comfort level improved to the range of between neutral and comfortable, but this improvement slightly decreased over the time. Precisely, 100% of the participants felt neutral and hotter at the 25 min of the test, reducing to 75% at the 35 and 45 min of the tests. In addition, the comfort level of the participants at the 45 min of the tests was lower than that of at the 35 min of the tests. Precisely, the comfort level of 25% of the participants at the 35 min of the tests was in a range of between neutral to slightly comfortable but reduced to around neutral at the 45 min of the tests. In spite of these, in general, the comfort level of the experimental group was superior to that of the control group.

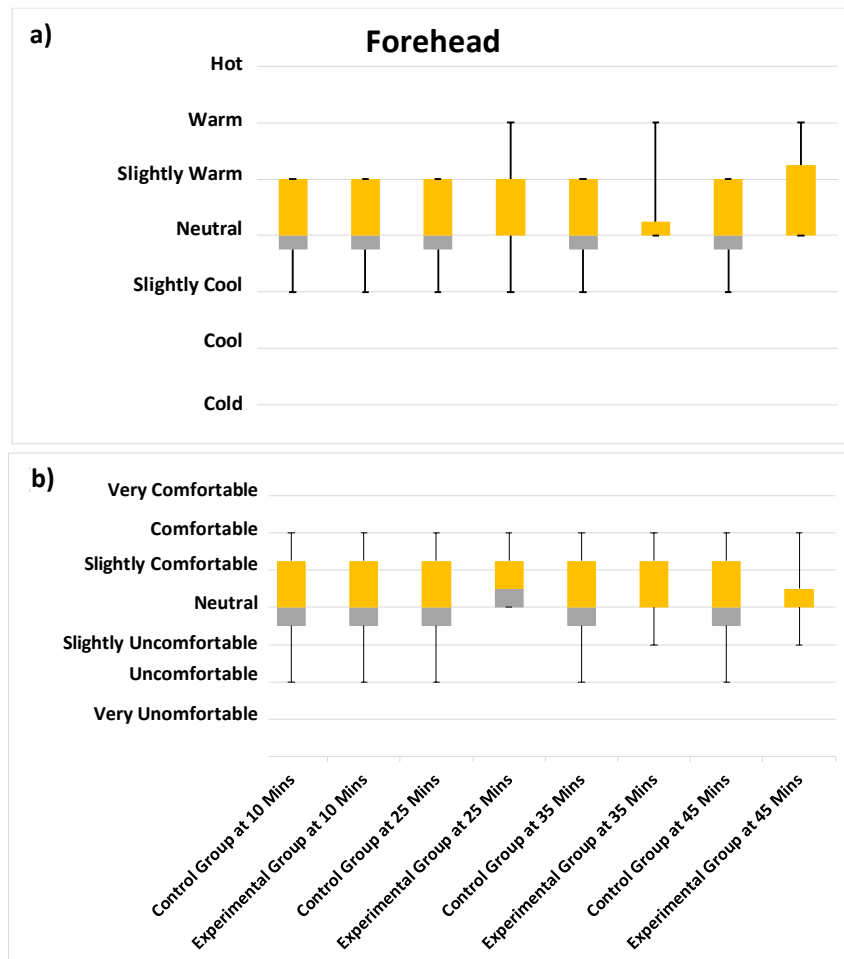


Fig. 121: Forehead's thermal sensation (a) and comfort (b).

10.6.1.2 Torso front and back

As Fig.122a shows, before wearing the armbands, the thermal sensation of the participants on their front torso was in a range of between slightly cool to warm, but changed to neutral and warm after wearing them. This illustrates the thermal effect of the armbands on the thermal sensation of the front torso. The only exception was the first 10 min of wearing them that the thermal sensation of the participants over this period showed the narrowest spread (i.e. between neutral and slightly warm). In spite of this, compared with before wearing the armbands, the thermal sensation of at least 25% of the participants improved from slightly cool to neutral and all participants felt either neutral or above. Notably, the thermal effect of the armbands on the thermal sensation of the front torso was gradually increased over the tests. Precisely, after 20 and 30 min of wearing the armbands, whilst 50% and 25% of the participants felt the same as before wearing them, the rest 50% and 75% felt warmer, respectively.

Based on Fig.122b, before and after wearing the armbands, there was not a significant difference between the comfort level of the subjects on their front torso. To illustrate, under both conditions, the comfort level of the front torso was in a range of between slightly uncomfortable and comfortable, and it was neutral on average. However, after 10 min of wearing the armbands, the comfort level of approximately 75% of the participants was slightly improved due to the concentration of their thermal sensation in a range of between neutral and slightly warm. However, after 20 min of wearing the armbands, their comfort level slightly deteriorated due to feeling warmer (i.e. overheating) than the previous 10 min. Nevertheless, since the participants were adapted to feeling warm at the 45 min of the tests, the comfort level of 50% of them was slightly improved again. In general, by the end of the tests, 25% of the experimental group felt more comfortable than before wearing the armbands.

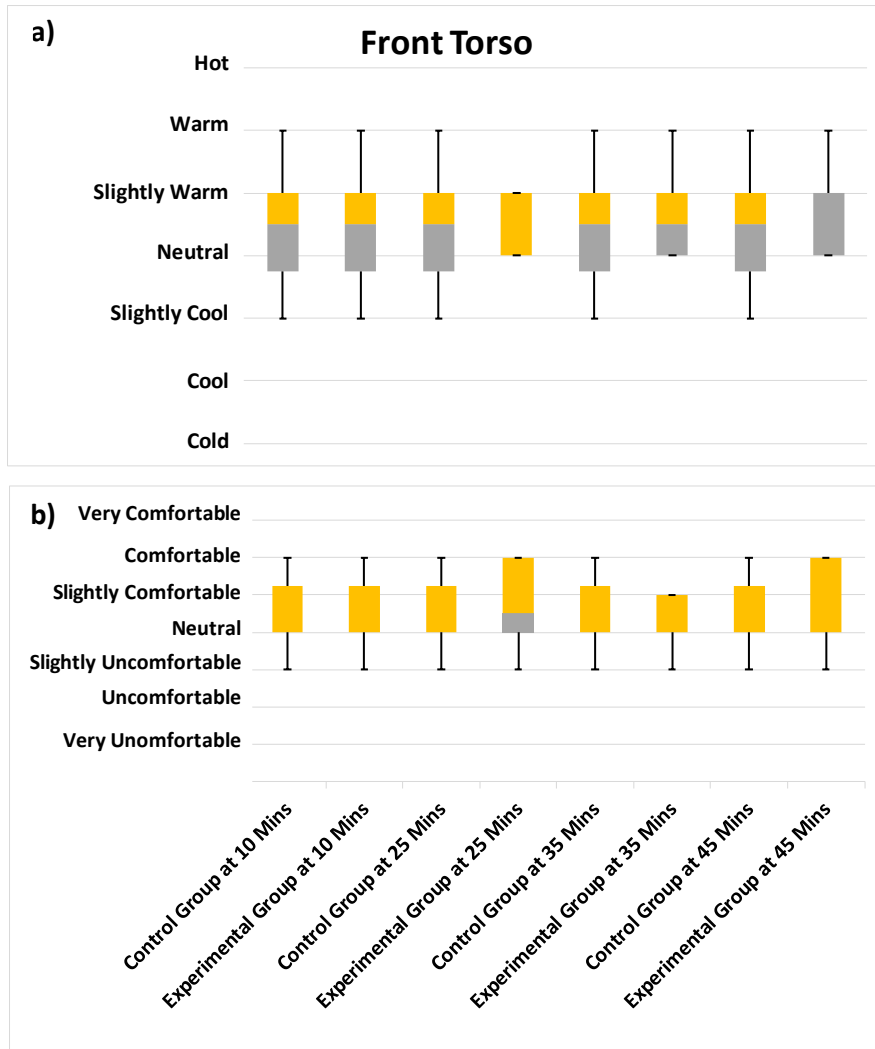


Fig. 122: Front torso's thermal sensation (a) and comfort (b).

As Fig.123a illustrates, before wearing the armbands, the thermal sensation of back torso ranged from neutral to warm, and it was between neutral and slightly warm on average. However, in the first 20 min of wearing the armbands, the range of thermal sensation became broader and spread from slightly cool to warm, whilst it was neutral on average. To specify, in the first and second 10 min of wearing the armbands, 75% and 100% of the participants respectively felt cooler at their back torso in comparison with before wearing them. In fact, this cooler thermal sensation could be attributed to the sitting position of the participants and altering it over the tests. For example, some participants took rest at 25 and 35 min of the tests by leaning forward, resulting in greater exposure of their back to the cold ambient air, see Fig.124. However, at the 45 min of the experiments, the average thermal sensation of the participants improved to slightly warm. This could be attributed

to the heating effect of the armbands coupled with the sitting position of the participants (e.g. leaning back in the chair). To specify, after 30 min of wearing the armbands, 50% and 75% of the participant felt warmer than the 10 and 20 min of wearing them, respectively. In addition, 50% of the participants felt warmer than before wearing the armbands, and the other half felt the same.

As [Fig.123b](#) depicts, both before and after wearing the armbands, the comfort level of the participants was neutral on average and varied in a range of between slightly uncomfortable and comfortable. Precisely, before wearing the armbands, one fourth of the participants felt between slightly uncomfortable to neutral, half of them felt around neutral, and the other one fourth sensed between neutral and comfortable. However, after 20 min of wearing the armbands, the comfort level of 50% of the participants improved remarkably and raised toward the comfortable level. Notably, this improvement was not stable because after 20 min of wearing the armbands the comfort level changed back to that of before wearing them. This was mainly because, the participants felt cooler at the 35 min of the experiments than the previous 10 min. However, in the last 10 min of the tests, the comfort level of 50% of the participants surpassed that of the previous 45 min owing to the warmer feelings of the participants.

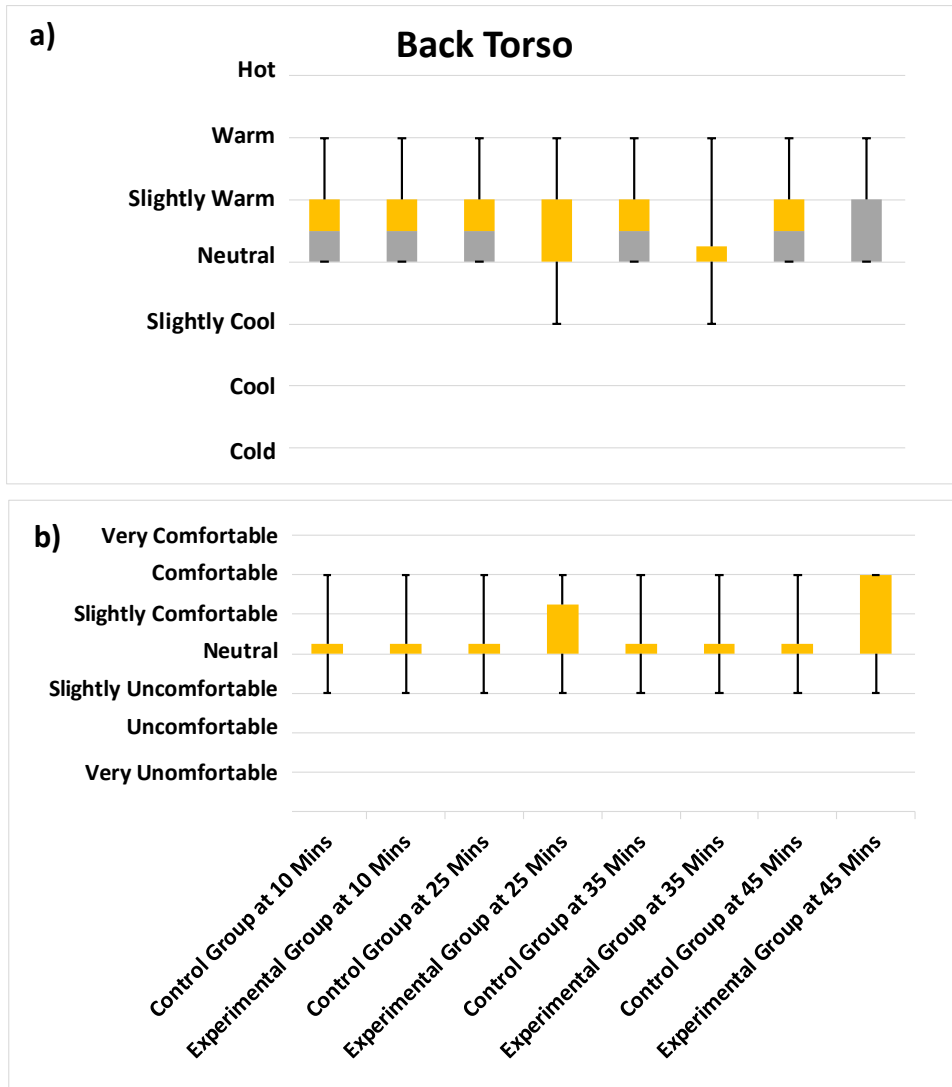


Fig. 123: Back torso's thermal sensation (a) and comfort (b).



Fig. 124: Sitting behavior of the participants at the 25 and 35 min of the experiments.

10.6.1.3 Hands

As [Fig.125a](#) illustrates, wearing the armbands remarkably affected on the thermal sensation of the subjects at their hands. To specify, the thermal sensation of the participants was in a range of between cool to neutral before wearing the armbands, and it was slightly cool on average. However, the average thermal sensation boosted to slightly warm after wearing them. To clarify, in the first 10 min of wearing the armbands, 50% felt between slightly cool to slightly warm, and the other half felt between slightly warm to warm. Thus, at least 60% of the participants felt warmer than before wearing the armbands. Heating the arm for 20 min, roughly 40% of the participants felt warmer than the first 10 min of wearing the armbands. Likewise, at the 45 min of the tests, the participants felt warmer than the previous 20 min, and their thermal sensation narrowed to the range between neutral to warm. To illustrate, after 30 min of wearing the armbands, each 25% of the participants felt either neutral, between neutral to slightly warm, between slightly warm to warm, or warm at their hands. Therefore, after 30 min of wearing the armbands, 40% and 25% of the participants felt warmer than the first 10 and 20 min of wearing them, respectively. Furthermore, at the end of the experiments, 100% of the participants felt warmer than before wearing the armbands.

As Fig.125b shows, the range of comfort level was between uncomfortable to comfortable before wearing the armbands. In particular, the average comfort level was between slightly uncomfortable to neutral, and 75% of the participants were suffering from cold before wearing the armbands. However, after wearing them, the comfort level extremely improved and its range changed to slightly uncomfortable to comfortable. Precisely, the average comfort level of the participants changed to slightly comfortable after 10 min of wearing the armbands. Thus, 50% of the participants felt from slightly uncomfortable to slightly comfortable, and the other half felt from slightly comfortable to comfortable. However, 20 min after wearing the armbands, the comfort level slightly deteriorated compared with the previous 10 min, because 25% of the participants felt in a range of between uncomfortable to slightly uncomfortable. It might be because, the participants felt warmer on their hands at the 35 min of the tests than the 25 min of the tests, which was uncomfortable for 25% of them. Being adapted to the emitted heat from the armbands, the participants felt comfortable on average at the 45 min of the tests in spite of reporting their hottest sensations. To specify, 25% felt slightly uncomfortable to slightly comfortable, 25% sensed slightly comfortable to comfortable, and 50% felt comfortable after 30 min of wearing the armbands. Thus, wearing the armbands boosted the comfort level of at least 50% of the participants.

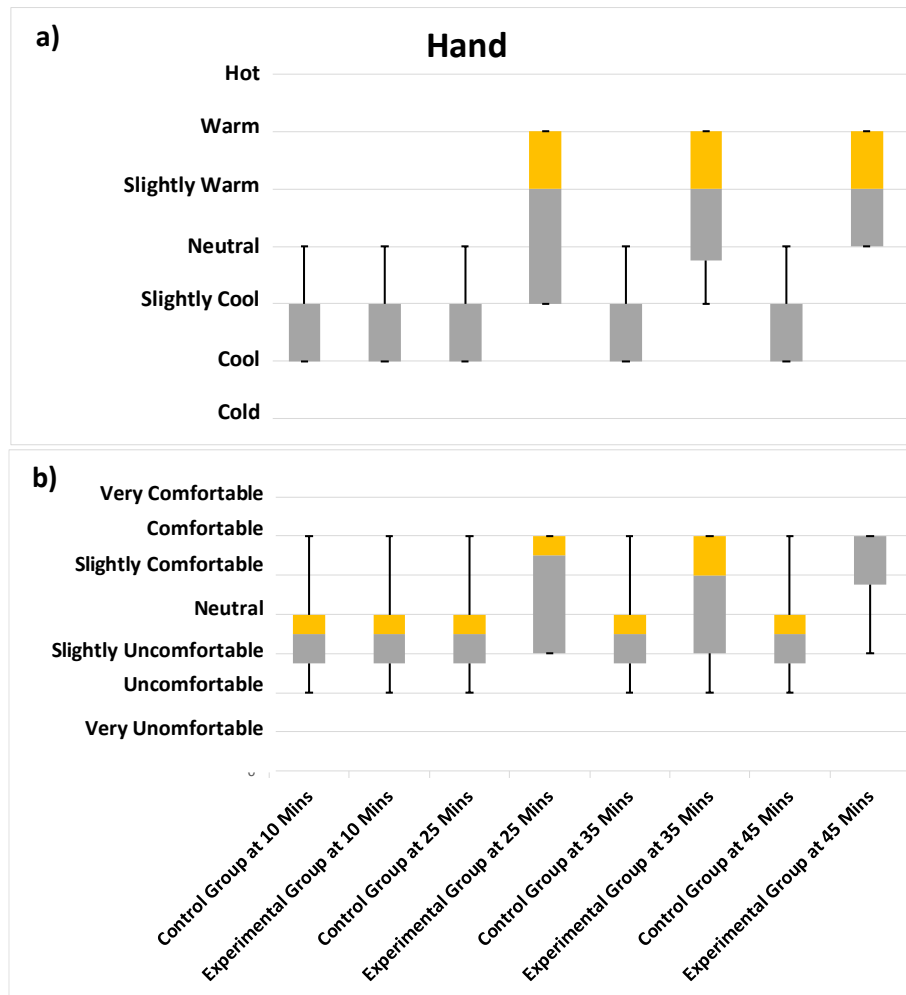


Fig. 125: Hand's thermal sensation (a) and comfort (b).

10.6.1.4 Thigh front and back

As Fig.126a depicts, the thermal sensation of the subjects at their front thigh before wearing the armbands was on average neutral and in a range of between slightly cool to slightly warm. After 10 min of wearing the armbands, the participants felt warmer at their front thigh as all of them felt at least neutral. After 20 min of wearing the armbands, the participants felt even warmer and their thermal sensation was slightly warm on average. To specify, at least 50% of the participants felt warmer than the first 10 min of wearing the armbands. It should be noted that although the range of thermal sensation became wider after 20 min of wearing the armbands and spanned from slightly cool to warm, less than 25% of the participants felt cooler than before. However, at the 45 min of the tests, the range of thermal sensation was changed back to that of before wearing the armbands,

but still 50% of the participant felt warmer than before. Thus, it could be interpreted that the thermal sensation of the participants at their front thigh may also be related to their sitting position, such as crossing the legs.

Based on [Fig.126b](#), the comfort level was neutral on average with a range of between slightly uncomfortable to comfortable in the first 10 min of the tests. Therefore, before wearing the armbands, 50 % of the participants felt slightly uncomfortable at their front thigh, and the other half felt between neutral to comfortable. However, after 10 min of wearing the armbands, the comfort level of the participants remarkably improved and all of them felt either neutral or above. In spite of feeling warmer after 20 min of wearing the armbands, the comfort level of at least 25% of the participants deteriorated and they felt slightly uncomfortable. Weirdly, in the third 10 min of wearing the armbands when the participants felt cooler than the previous 10 min, their comfort level slightly improved. From these set of data, it could be understood that there was a non-linear and indirect relationship between wearing the armbands and the thermal sensation and comfort of the front thigh.

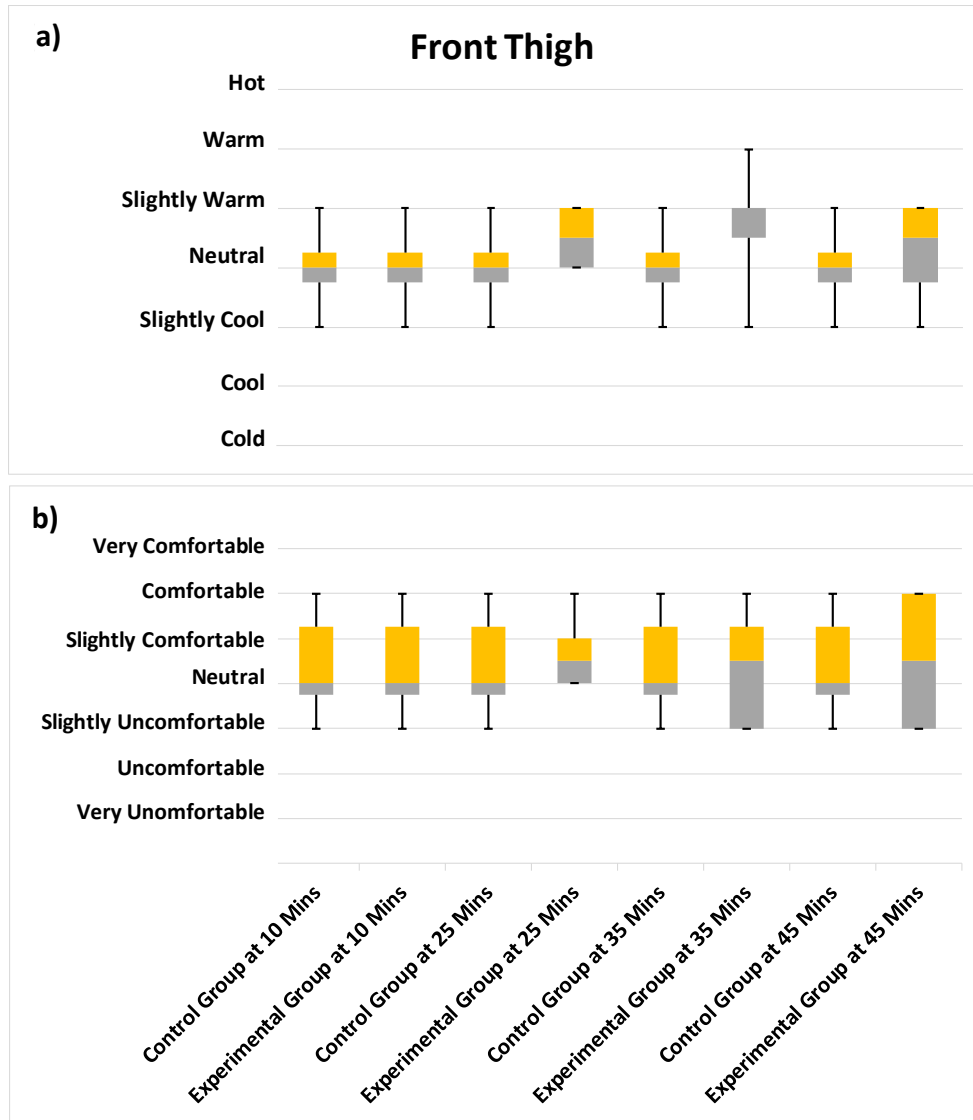


Fig. 126: Front thigh's thermal sensation (a) and comfort (b).

Regarding Fig.127a, the average thermal sensation of the participants at their back thigh was neutral before wearing the armbands, whilst 50% of them felt neutral and the other half felt between neutral and slightly warm. However, the average thermal sensation increased to slightly warm after wearing the armbands. Precisely, 75% of the participants felt warmer after 10 min of wearing the armbands, and the other 25% felt the same as before. After 20 min of wearing the armbands, 60% and 40% of the participants felt warmer and cooler than before wearing the armbands, respectively. Concerning the 45 min of the tests, 50% felt either warmer or cooler than before. According to these data, the relationship between the thermal sensation of the back thigh and wearing the armbands was not linear. This could be because the participants continuously changed their sitting position during the tests. To specify, apart from switching between leaning backward and forward, crossing the legs was another factor affecting their thermal sensation.

Based on Fig.127b, the average comfort level before wearing the armbands was neutral, whilst 50% of the participants felt neutral and the other half sensed between neutral and comfortable. After 10 min of wearing the armbands, although the average comfort level was still neutral, 50% of the participants felt less comfortable than before. To specify, instead of feeling between neutral and comfortable, 50% of the participants felt between neutral and slightly comfortable. This thermal discomfort became more severe after 20 min of wearing the armbands. In particular, whilst the average thermal sensation was still neutral, 50% of the participants felt between slightly uncomfortable and neutral, and the other half felt between neutral and comfortable. However, this approach changed after 30 min of wearing the armbands, because at least 50% of the participants felt more comfortable than the previous 10 min. Thus, in general, due to non-linear relationship between the thermal sensation of the back thigh and wearing the armbands, its comfort level was unpredictable.

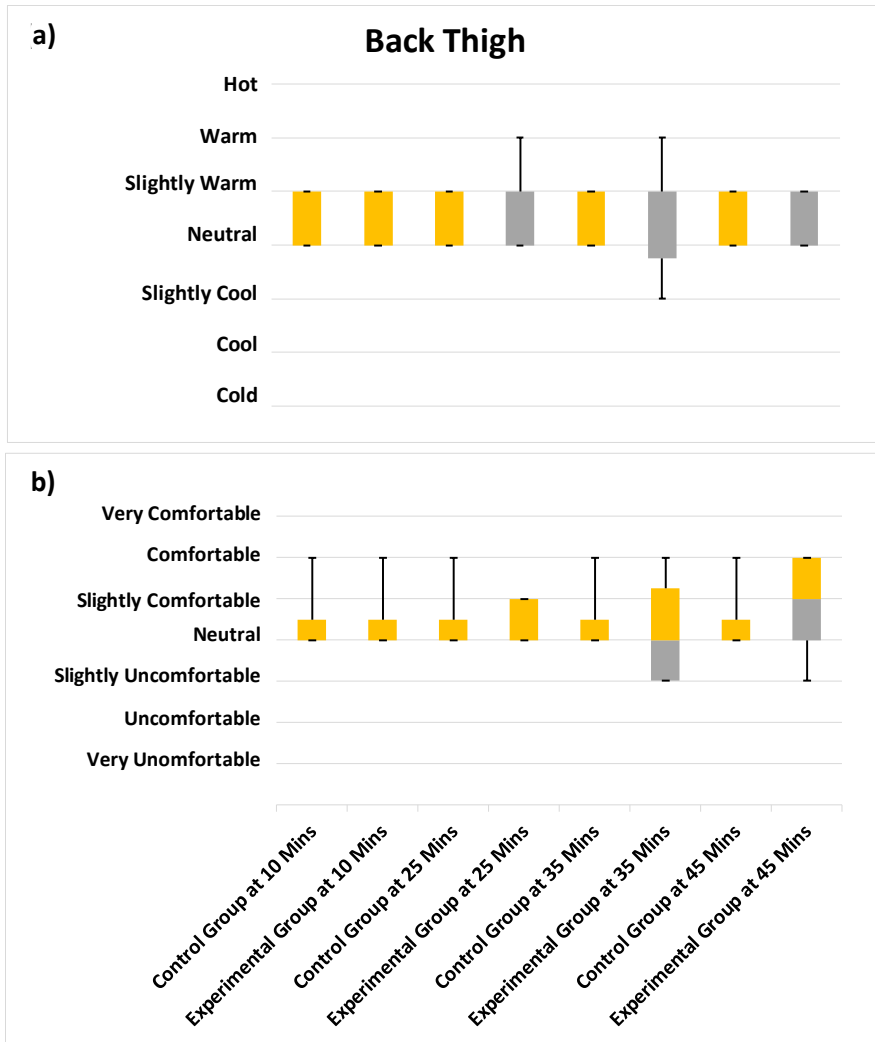


Fig. 127: Back thigh's thermal sensation (a) and comfort (b).

10.6.1.5 Feet

As Fig.128a illustrates, wearing the armbands considerably affected on the thermal sensation of the feet. To specify, the participants felt in a range of between cool to slightly warm in their feet before wearing the armband, whilst their thermal sensation was slightly cool on average. Wearing the armbands, they felt warmer at their feet because their least, average, and most thermal sensations were changed to slightly cool, neutral, and warm, respectively. Regarding the first 10 min of wearing the armbands, at least 50% of the participants felt warmer at their feet than before wearing them. Compared with the first 10 min of wearing the armbands, the participants felt warmer after 20 min of wearing them, because all of them felt at least neutral. To clarify, 75% and 25% of the participants felt between neutral to slightly warm and slightly warm to warm, respectively. However, at the third 10 min of wearing the armbands, the thermal sensation of the participants changed back to that of the first 10 min of wearing them. In spite of this, still at least 50% of the participants felt warmer than before wearing the armbands.

Based on Fig.128b, the comfort level of the participants was on average neutral and in a range of between slightly uncomfortable to comfortable before wearing the armbands. After 10 min of wearing them and feeling warmer at their feet, the comfort level of at least 25% of them improved. However, despite the fact that the participants felt even warmer after 20 min of wearing the armbands, the rate of thermal discomfort increased compared with that of the previous 35 min. To illustrate, the range of comfort level spanned from uncomfortable to slightly comfortable after 20 min of wearing the armbands. It should be noted that although 75% of the participants felt between neutral to slightly comfortable, the thermal comfort of at least 25% of them deteriorated compared with the previous 35 min. This deterioration extended to the 30 min of wearing the armbands. To clarify, whilst a few participants felt better than the previous 10 min, at least 50% of them felt more thermal discomfort. Based on these set of data, it could be understood that even though wearing the armbands can improve the comfort level of feet in short term, it was not adequate to offset the negative effect of the low ambient temperature (15 °C -16 °C) in long term.

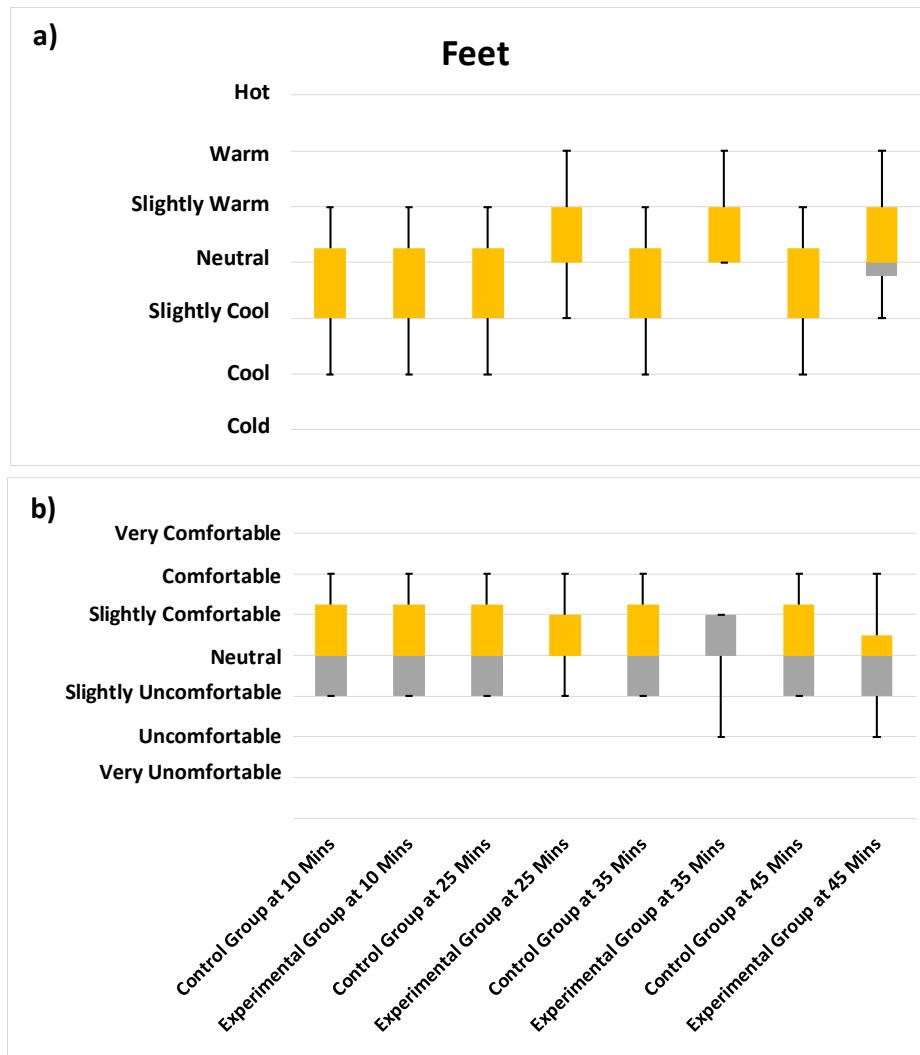


Fig. 128: Feet's thermal sensation (a) and comfort (b).

10.6.2 Whole-body thermal sensation and comfort

Based on Fig.129a, the whole thermal sensation of the participants before wearing the armbands was in a range of between cool and slightly warm, whilst they felt between slightly cool and neutral on average. However, after 10 min of wearing the armbands, the participants on average felt warmer than before wearing them, because the range of their thermal sensation changed to slightly cool to warm. After 20 min of wearing the armbands, the participants felt even warmer than the first 10 min of wearing them. To specify, the whole thermal sensation range became narrower and spanned from neutral to warm. Furthermore, 75% of the subjects felt between neutral to slightly warm, and the remaining 25% felt between slightly warm and warm. Nevertheless, the armbands

reached their maximum heating effects after 30 min of wearing them. Precisely, 50% of the participants felt between neutral and slightly warm and the other half felt between slightly warm and warm at the 45 min of the tests. Therefore, not only wearing the armbands made the participants feel remarkably warmer than before wearing them, but also their heating effect on the whole thermal sensation was raising over time.

In accordance with [Fig.129b](#), although the maximum comfort level of the whole body deteriorated by wearing the armbands, the average comfort level improved after wearing them. Precisely, the average comfort level was in a range of between slightly uncomfortable and neutral before wearing the armbands, improving to slightly comfortable after wearing them. Notably, the range of the comfort level was broader before wearing the armbands compared with that of after wearing them. Precisely, before wearing the armbands, at least 50% of the participants felt between slightly uncomfortable to neutral, and the other roughly 50% felt between neutral to very comfortable. However, after 10 min of wearing the armbands, at least 75% of the participants felt in a range of between neutral to comfortable, and the remaining 25% felt uncomfortable (i.e. in a range of between slightly uncomfortable and neutral). Thus, the percentage of the participants who felt uncomfortable reduced from 50% to 25% after 10 min of wearing the armbands.

After 20 min of wearing the armbands, the thermal comfort of 25% of the participants decreased from comfortable to slightly comfortable, whilst the other 75% felt the same as the previous 10 min. This reduction in the thermal comfort could be attributed to feeling warmer than the previous 10 min, which was uncomfortable for 25% of the participants. However, the highest comfort level was achieved after 30 min of wearing the armbands. To clarify, at the 45 min of the tests, 25% of the participants felt from slightly uncomfortable to slightly comfortable, 25% sensed slightly comfortable, and 50% felt between slightly comfortable and comfortable. Therefore, wearing the armbands improved the average comfort level of the participants from less than neutral (i.e. between slightly uncomfortable and neutral) to slightly comfortable.

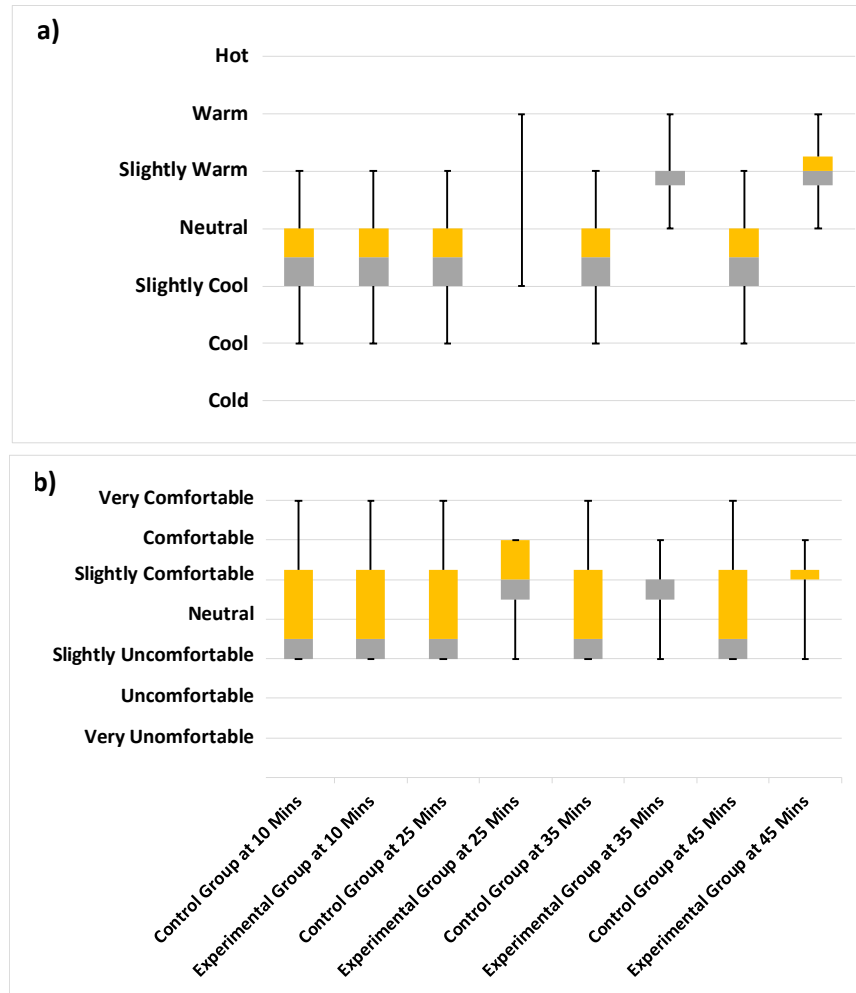


Fig. 129: Whole-body thermal sensation (a) and comfort (b).

10.6.3 Whole-body thermal acceptability

According to Fig.130, the thermal acceptability of the participants improved after wearing the armbands because the range of acceptability became narrower and closer to the acceptable conditions. Precisely, the range of acceptability was from unacceptable to acceptable before wearing the armbands, and the average acceptability was between slightly acceptable and acceptable. However, the thermal acceptability of the experimental group improved to the range of between slightly acceptable and acceptable after 10 min of wearing the armbands. To illustrate, 50% of the participants felt slightly acceptable, 25% felt between slightly acceptable and acceptable, and 25% felt completely acceptable. Therefore, the thermal acceptability of at least 40% of the participants improved after wearing the armbands. After 20 min of wearing the

armbands, although some participants less accepted the thermal condition compared with the previous 10 min, still their acceptability was higher than that of before wearing them. To specify, slightly unacceptable was the least acceptability level after 20 min of wearing the armbands, which was superior to that of (i.e. unacceptable) before wearing them. However, the greatest thermal acceptability was reached after 30 min of wearing the armbands, because 50% of the participants fully accepted the thermal condition. Precisely, the thermal acceptability of 25% of the experimental group was between slightly unacceptable and slightly acceptable, 25% voted between slightly acceptable and acceptable, and 50% fully accepted the thermal condition. Therefore, compared with the previous 45 min, fully accepting the thermal condition raised from 25% to 50%, whilst the least acceptability level changed from unacceptable to slightly unacceptable. Thus, it could be interpreted that definitely wearing the armbands improved the thermal acceptability of the participants.

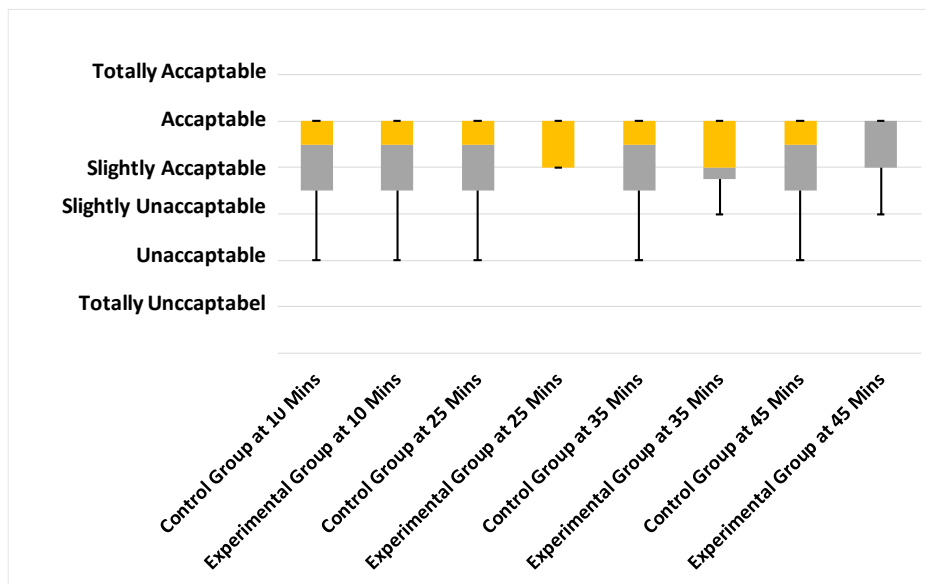


Fig. 130: Whole-body thermal acceptability.

10.6.4 Whole-body preferred thermal sensation

As Fig.131 depicts, 75% and 25% of the participants preferred respectively feeling slightly warmer and warmer before wearing the armbands. However, wearing the armbands remarkably improved their thermal sensation and made the participants feel warmer. To specify, after 10 min of wearing

the armbands, no participants wanted a warmer environmental condition anymore. In addition, the percentages of those who asked for a slightly warmer condition decreased from 75% to 60%. Instead, 40% of the participants asked for no change in the thermal condition of the environment. As a result, after 10 min of wearing the armbands, 40% of the participants felt warmer than before wearing them, and 60% of them felt the same as before. After 20 min of wearing the armbands, the participants felt cooler than the previous 10 min since 12% of them asked for a warmer environment. Accordingly, the vote for a slightly warmer environment and no change in the thermal condition reduced to 50% and 38%, respectively. However, still 38% of the participants felt warmer than before wearing the armbands, whilst the other 62% felt the same as before. The maximum thermal effect of the armbands was revealed after 30 min of wearing them. To clarify, the highest vote (i.e. 50%) was for no change in the thermal condition of the environment, whilst 38% and 12% asked for a slightly warmer and warmer environment, respectively. Therefore, at the 45 min of the experiments, 50% of the participants felt warmer than before wearing the armbands, and the other half felt the same as before.

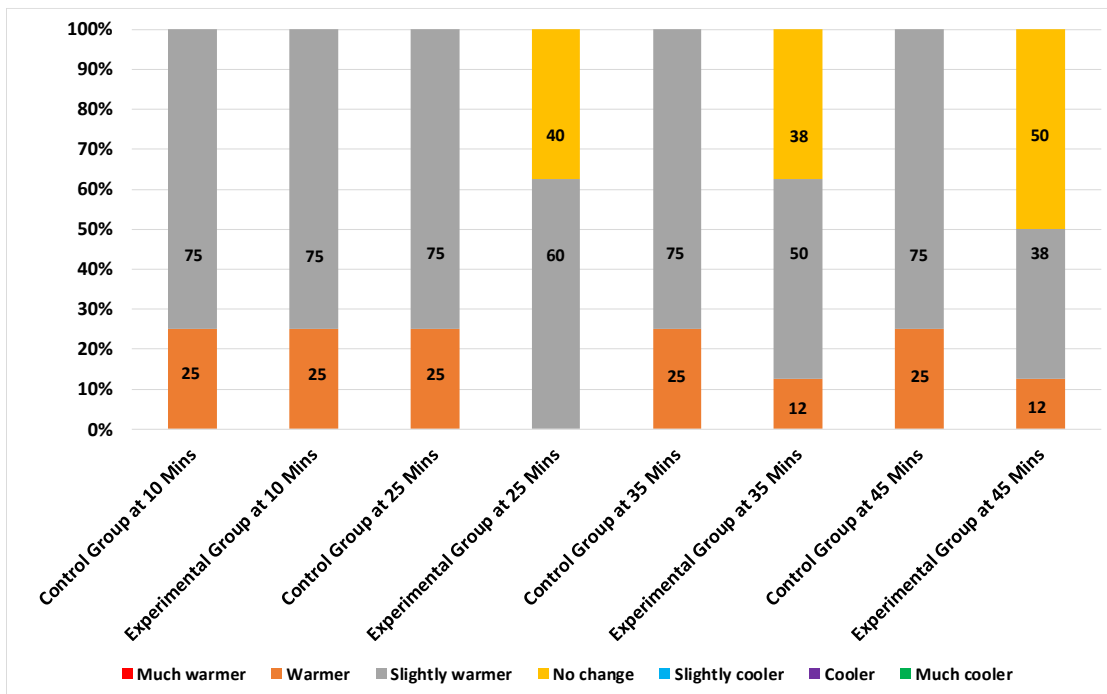


Fig. 131: Whole-body preferred thermal sensation.

10.7 Discussion

Based on the collected data from the objective measurements and the subjective questionnaires, at 18 °C ambient temperature (i.e. 1.1m height from the floor level), 50% of the participants felt uncomfortable to neutral, and the other half felt neutral to comfortable at their forehead. This was because half of them felt between slightly cool and neutral and the other half felt between neutral to slightly warm. Ten min after wearing the armbands, 50% of the subjects felt warmer at their forehead, resulting in 50% improvement in their comfort level. The thermal effect of the armbands became more intense after 20 and 30 min of wearing them, since more than 50% of the participants felt warmer than the first 10 min of wearing them. However, feeling warmer deteriorated the comfort level of 25% of the subjects after 20 and 30 min of wearing them. To illustrate, being close to the warm-blood-pumping heart, the head is considered as one of the warmest body part along with the front torso and armpit. Therefore, it could be understood that although in general wearing the armbands improved the comfort level of the participants at their forehead, some considerations should be taken to regulate the temperature concerning the thermal preference of each individual.

Regarding the front torso, the participants felt warmer over the time by wearing the armbands. However, the greatest thermal satisfaction was achieved when they felt in a range of between neutral and slightly warm. To specify, feeling either warm or slightly cool caused negative effect on the thermal satisfaction of the participants at their front torso. Comparing the forehead and the front torso, although the forehead was surrounded by the warmest ambient temperature (i.e. 18 °C), the participants felt cooler at their forehead than their front torso. This could be attributed to the covering area of the cloth that to some extent protected their front torso region from the cooler ambient temperature (i.e. 15 °C). As a result, wearing the armbands affected more on the forehead's thermal sensation and comfort than those of the front torso. Regarding the back torso, its thermal sensation was influenced by two factors, including the sitting position of the participants and the heating armbands. In the first 20 min of wearing the armbands, the effect of the sitting position on the thermal sensation was dominant compared with that of the armbands. However, after 30 min of wearing them, the effect of both resulted in the warmest thermal sensation and the greatest comfort level of the participants over the tests. Notably, compared with

the forehead and the front torso before wearing the armbands, the participants felt warmer at their back torso owing to leaning back to the chair.

Based on the objective measurements, the temperatures of back of the hand and under the armband continuously decreased over the tests. In spite of this, the experimental participants felt warmer at their hands over the time, whilst the thermal sensation of the control group was stable at the same time. To clarify, in the first 10 min of wearing the armbands, at least 60% of the participants felt warmer at their hands than before wearing them, whilst the average temperature of back of their hands reduced from 30 °C to 29 °C. Likewise, after 20 and 30 min of wearing the armbands, the participants felt warmer than the previous ten min, whereas the temperature of back of their hands reduced to 28 °C and 27.5 °C, respectively. In accordance with the thermal sensations of the hands, the comfort level of at least 50% of the experimental subjects boosted after wearing the armbands. Regarding the control group, the skin temperature of back of their hands reduced from 30 °C to 27 °C over the 30 min of the tests. Although their hands were constantly dissipating heat into the cold ambient (i.e. 15 °C), the thermal sensation of their hands was constant over the tests.

This contradiction between the recorded temperatures and the thermal sensation/comfort of the participants could be attributed to the generalization of the thermal sensation by the experimental group and adaptation to the ambient environment by the control group. To clarify, undoubtedly the experimental participants felt warm at their arm regions due to the armbands, thus this thermal sensation was generalized to the hands regions and influenced on the thermal perception of the participants at their hands. To put it another way, the participants experienced a generalized thermal perception at the back of their hands, which overcame the dropping temperature of their hands. Concerning the control participants, they felt cold at their hands (i.e. 30 °C temperature) at the beginning of the tests owing to be exposed to the extreme low ambient temperature (i.e. 15 °C) for 15 min. However, being adapted to this low skin temperature, the control group was insensible of the gradual and slight (i.e. up to 3 °C) decrease in their skin temperature over the 30 min.

Regarding the front and back thigh, although wearing the armbands changed the thermal sensation of the participants at these parts to some extent, but it was not considerably influential. This was because, apart from the heating armbands, the thermal sensation of the participants at these parts was also dependent on their sitting position and leg posture. For example, crossing the legs, putting

the hands on the thighs and leaning forward were some factors that affected on the thigh's thermal sensation. In spite of this principle, there was no change in the thermal sensation of the control group over the tests. This could be attributed to the lower temperature difference between different parts of their body during the tests. To specify, heating only the arm region unconsciously derived the experimental participants to compare the thermal sensation of different parts of their body against that of the arm region, resulting in their higher thermal expectation. However, for the control group, there was not such a thermal baseline, thus they exhibited a higher adaptation to the thermal condition.

Concerning the feet's thermal sensation before wearing the armbands, it was the second coldest body part after the hands. Based on the results, although the thermal sensation of the feet was affected by wearing the armbands, this effect was temporary and some participants felt the same as before wearing them after a while. To put it another way, although the participants felt warmer at their feet by wearing the armbands, the low ambient temperature (i.e. 13 °C) overcame this effect after a short period of time. In general, regardless of the ambient temperature, it could be understood that the most sensitive body parts to cold over the tests were the hands, feet, forehead, front thigh, back thigh, front torso, and back torso, respectively. Whereas, wearing the armbands permanently influenced on the thermal sensation of the hands and forehead, and temporary impacted on that of the feet, front and back torso/thigh.

In accordance with the thermal sensation and comfort level of different parts of the body, the overall average comfort level of the participants improved after wearing the armbands. However, the overall maximum and minimum comfort levels deteriorated and remained stable, respectively. To specify, in total, at least 75% of the experimental group felt warmer than the control group at the end of the tests, leading to an increase in their average comfort level. Precisely, by wearing the armbands, the average comfort level changed from a rate between slightly uncomfortable and neutral to slightly comfortable. However, since the maximum thermal sensation changed from slightly warm to warm after wearing the armbands, the maximum comfort level of the experimental participants dropped from very comfortable to comfortable. Thus, it could be understood that although feeling cold was the main reason of the thermal discomfort among the participants before wearing the armbands, some of them suffered from overheating at their arm region after wearing them. Conversely, since the minimum comfort level remained slightly

uncomfortable over the tests, in total a few participants preferred a warmer condition in spite of feeling neutral.

Notably, all participants kept the armbands on over the tests despite feeling warm, showing that they preferred feeling warmth rather than cold. As a result, it was of critical importance to consider different temperatures for the armbands to let the participants tune them based on their thermal preferences. Following the overall thermal sensation and comfort of the participants, in general, their thermal acceptability improved after wearing the armbands due to feeling warm. However, since the participants preferred feeling slightly warm rather than warm, some fluctuations occurred in the rate of their thermal acceptability over the tests. This was in accordance with their preferred thermal sensation presented in [Fig.131](#). According to this graph, before wearing the armbands, 75% of the participants preferred a slightly warmer condition and the rest 25% voted for a warmer condition. Being heated by the armbands for 10 min, no one preferred a warmer condition anymore, but 60% and 40% voted for a slightly warmer condition and no change in the thermal condition, respectively. Being adapted to the generated heat by the armbands, 12% of the participants who felt neutral preferred a warmer thermal condition at the end of the tests. As a result, the vote for a slightly warmer and no change in the thermal condition changed to 38% and 50%, respectively.

10.8 Summary

In this chapter a heating armband was developed by integrating a series of TEGs with a rechargeable battery as the energy supplies. The TEGs were integrated together following the optimal flexible integrating substrate (i.e. sample 2a) developed in [Chapter 8](#), then the fabricated pin-shaped heatsinks in [Chapter 9](#) were attached to the flexible substrate to cool it down. To reach the required voltage and current, two DC-DC voltage booster and a rechargeable battery were added to the circuit. Next, two heating elements were sewn individually onto a pair of armbands and heated by the developed hybrid power supply to provide the required thermal condition for the office workers in the cold month of March. Accordingly, a series of tests were conducted on 8 participants to evaluate their thermal sensation, comfort level, thermal acceptability, and preferred thermal condition before and after wearing the armbands. The results showed that wearing the

heating armbands improved the overall comfort level and the thermal acceptability of the participants due to feeling warmer. Notably, although some participants complained about overheating specifically at their arms region, some participants asked for a warmer thermal condition specially at their fingertips and feet. Thus, rather than a single heating target, it was suggested to distribute the heating points over the body. For example, it was superior to couple the heating armbands with fingerless heating gloves to target the fingertips' thermal satisfaction along with back of the hands. In addition, coupling the heating armbands and gloves with a feet warmer or a leg warmer could further improve the thermal satisfaction of the individuals. Notably, it was desirable to consider a temperature controller for the armbands to provide this option for the individuals to regulate the temperature based on their thermal preferences.

Chapter 11

Conclusions and Future Works

11.1 Conclusions

In this thesis, we adapted the concept of harvesting energy from available environmental energy sources to propose a hybrid power supply for a personal heating garment. This was because, recently the concept of using PCSs has received extensive attention owing to two reasons. First, they remarkably address the issues related to the huge energy consumption of the HVAC systems in the buildings. Second, they can satisfy the thermal comfort of the individuals in the shared spaces concerning their different thermal preferences. Thus, replacing the HVAC systems with the PCSs is considered as one of the eco-friendly solutions to reduce the carbon footprints of the buildings. However, as a green technology, the PCSs still suffer from being powered with a fossil fuel based power supply, namely grid electricity. Thus, along with all concerns on the heating performance of the PCSs, it is also of critical importance to consider a renewable power supply for them to entirely fulfill their eco-friendly mission.

11.2 “State of the art”

This thesis proposed developing a hybrid power supply comprising a set of TEGs and a rechargeable battery to power a pair of heating armbands. The TEGs were considered to generate electricity based on scavenging the temperature gradient between a lit candle and the ambient air. In accordance with this proposal, initially the life cycle impacts of several TE materials were numerically assessed using a software called GaBi. As mentioned before, it was because the ultimate target of this thesis was to consider the environmental aspects of the power supply of the PCSs along with their performances. Thus, initially the life cycle impacts of different TE materials were numerically assessed to select a TEG comprised of the most eco-friendly TE materials. This numerical assessment was carried out with GaBi software and included the life cycle impact of different types of TE materials from cradle to gate (i.e. from raw materials acquisition to manufacturing the final TE materials). Accordingly, the TE materials were classified into inorganic, organic, and hybrid (i.e. inorganic-organic) types, and their life cycle impacts were assessed regarding five different categories, including input-output mass flow, primary energy demand, GWP, ODP, and HTP. The results demonstrated that the inorganic TE materials caused extremely greater negative environmental impacts than the organic and hybrid types. However,

the only exception among the studied inorganic TE materials was Bi_2Te_3 that its life cycle impacts were competing with those of the organic and hybrid counterparts.

Based on these results and the outcomes of the literature reviews (i.e. [Chapters 4 and 5](#)), an off-the-shelf TEG comprising ingot-shaped and Bi_2Te_3 -based TE legs was selected to serve the rest of this research. To provide the required output power by the TEG part of the hybrid power supply, it was essential to integrate a number of TEGs together. Thus, there was a demand to provide an appropriate integrating substrate to connect the TEGs together without damaging their output powers and adding to the weight of the benchtop power supply. Thus, the TEGs were determined to be connected together with a lightweight substrate, such as a PDMS layer or an LDPE sheet. However, as mentioned before, the negative effect of fully coating the legs with the substrate on the output power of the TEGs was considered to be alleviated via providing a non-homogeneous boundary condition along the legs. Hence, these non-homogeneous boundary conditions were provided with two techniques, including partially coating the legs with the specified substrates and manipulating the thermal conductivity of the PDMS substrate by adding different fillers to it. Accordingly, 13 samples were proposed and their performances were studied both by computational modelling (i.e. COMSOL Multiphysics) and laboratory tests. The results of both studies proved that coating only the top half of the legs with a plain PDMS substrate led to the highest output currents, voltages, and powers under both 0 m/s and 1.2 m/s air speeds.

Since increasing the temperature difference along the TE legs improves the TE performance of the TEGs, in the next step, it was proposed to develop a lightweight heatsink using the PDMS mixture. This was mainly because, matching the materials of the heatsink and the substrate results in the lowest thermal resistivity at their junctions. Accordingly, two types of configuration were specified for the PDMS-based heatsink, including pin and bumpy shapes. Then each of these heatsinks were separately adhered to the plain PDMS substrate, covering only the top half of the legs. Then, their results were compared with that of the plain PDMS substrate without a heatsink. The results proved that adding the pin-shaped heatsinks to the PDMS-based integrating substrate resulted in the superior TE performance of the TEG at the three specified airflow conditions (i.e. 0 m/s, 1.2 m/s, and 2.4 m/s). To put it another word, it was proved that the pin-shaped heatsink caused the greatest temperature differences along the legs even in the stagnant air.

Based on these results, the hybrid benchtop power supply was fabricated via connecting 6 TEGs and a rechargeable battery together. The 6 TEGs were brought together into a whole via coating only the top half of their legs with the plain PDMS substrate. Then, the pin-shaped heatsinks were adhered to the PDMS substrate to increase the temperature gradient along the legs. After that, the integrated TEGs were placed on a stool-shaped object to be heated by a candle from the bottom and cooled by a fan from the top. After that, the integrated TEGs were electrically connected to a rechargeable battery in parallel, whilst the former and the latter served as the constant voltage and current supplies, respectively. In total, the fabricated hybrid benchtop power supply generated an output voltage and current of 5V and 4A, respectively.

Finally, the fabricated hybrid power supply were connected to two heating elements sewn individually onto two armbands. Then, the performances of the developed heating armbands were evaluated in a real life study by recruiting eight subjects (i.e. three females and five males). The tests were conducted in the cold month of March in an office room of university of Derby. During the tests, the participants were divided into the the experimental and control groups, and the temperatures of their hands and the ambient air were measured at one-minute interval throughout the tests. The results showed that wearing the armbands improved the overall thermal comfort of the participants compared with before wearing them. This was mainly because in spite of the consistent decrease in their hands' temperature over the time, 50% of the participants felt warmer than before wearing the armbands at the end of the tests, and the other half felt the same as before.

11.3 Contributions

The outcomes of this thesis contributed to the relative studies in the following manners:

- i. We proposed a personal heating garment powered by a hybrid power supply, comprising a set of integrated TEGs and a rechargeable battery. Accordingly, not only the PCSs could be used in off-the-grid regions, but also they could be powered by the least battery requirement, resulting in the least associated negative environmental impacts. In addition, this research paves the ways for other researchers to use different types of energy harvesters such as thermoelectric, triboelectric, piezoelectric, and pyroelectric generators in a practical scale. To put it another way, the required power for any types of PCSs could be

provided by either of the above mentioned energy harvesters or a combination of them. Thus, via determining an appropriate design and energy source for each of the above mentioned energy harvesters, it is possible to provide a renewable power supply for the PCSs.

- ii. This research highlighted the importance of studying the life cycle impact of the TE materials at the time of preparing and selecting them. This is critically important because the ultimate merit of a TEG is producing green energy out of waste heats. Thus, as a green technology, the life cycle impact of the components of the TEGs should also be taken into account at the time of selection and fabrication. Accordingly, the life cycle impact of a vast range of TE materials was assessed in [Chapter 7](#) from cradle to gate, paving the way for researchers to build on it for a cradle to grave assessment. To put it another way, the researchers can use the outcomes of [Chapter 7](#) to study the cradle to gate life cycle impact of the employed TE materials in their research. Then, regarding the fabrication procedure, the size of the TE legs, and other components of TEGs, the researchers can define the cradle to grave life cycle impact of their own developed TEGs.
- iii. This research scientifically proved the impact of the boundary conditions of the TE legs on the output powers of the TEGs. Accordingly, it casts light on researchers to consider an appropriate coating region and thermal conductivity for the integrating substrates. Thus, other researchers could develop further integrating substrates comprising separate coating regions with different thicknesses. In addition, they can manipulate the thermal conductivity of these separate coating regions by differentiating their additives. Also, they can tune the weight ratio of the additives or the ratio of the low to high thermal conductivity coating regions to reach the superior output powers.
- iv. Last but not least, this research developed two types of efficient and lightweight heatsinks and attached them to the TEGs without using any additional supporting unit. Precisely, the heatsinks were made of the same material as the integrating substrate. In addition, the heatsinks were simply adhered to the substrate using the same material (i.e. plain PDMS). Consequently, the thermal resistivity at the junctions of the heatsinks and the substrate was reduced due to the sameness of the materials of the substrate, the heatsinks, and the

adhesive. In addition, in spite of the flexibility of these heatsinks, they were firm enough to stand alone. Therefore, they provided a great contact area with the surrounding air, which accelerated the dissipation of heat from their height. Accordingly, this research shed some light on researchers to further reduce the weight of the lightweight heatsinks by omitting the required supporting units. In addition, in future, the researchers can manipulate the thermal conductivity of such lightweight heatsinks by adding different additives to them with different weight ratios. Furthermore, not only the researchers can tune the dimensions of these heatsinks, but also they can propose several other configurations concerning their research.

11.4 Limitations

Our research had some limitations that needs to be considered:

i. Life cycle inventory of the organic and hybrid TE materials:

In [Chapter 7](#), we assessed the cradle to gate life cycle impact of different TE materials, belonging to the inorganic, organic, and hybrid types. As mentioned in [Section 7.4](#), the organic and hybrid TE materials were composed of a larger number of input raw materials than the inorganic ones. However, there was limited data on the primary energy demands of all the constituent materials of the two former. Thus, only some of their constituent materials with available primary energy demand data were included in their life cycle inventory. Thus, in case of availability of the primary energy demand of all the constituent materials of the organic and hybrid types, enormous changes may occur in their life cycle impacts' results. To put it another way, considering the primary energy demand of all the input raw materials of the organic and hybrid types would either equal or make closer their life cycle impacts with that of the inorganic type.

ii. Temperature independent TE materials:

In [Chapter 8](#), the impacts of different non-homogeneous boundary conditions along the TE legs on the outputs of a TEG were studied, via conducting both numerical and laboratory experiments. For the numerical experiment, as it was explained in [Section 8.2](#), instead of defining the TE properties of the employed TE material (i.e. Bi_2Te_3) temperature

dependent, they were specified temperature independent. This was mainly because, specifying such a non-linear feature (i.e. temperature dependency of the TE properties) in COMSOL would have led to an extreme time-consuming simulation. Thus, in case of specifying the TE properties of Bi_2Te_3 temperature dependent, it is possible to reduce the divergence between the outputs of the numerical simulation and those of the lab experiments. Precisely, this reduction in the divergence would be more sensible at higher airflows when the temperature difference along the TE legs increases.

iii. Usage of DC/DC voltage boosters and a rechargeable battery:

In [Chapter 10](#), it was explained that two separate DC/DC voltage boosters were required to boost the generated output voltages up to 5V. Also, a rechargeable battery was demanded to address the required electric current (i.e. 2A). However, generating the required voltage and current by the integrated TEGs could eliminate the usage of the boosters and the rechargeable battery. Theoretically, it could be possible by either increasing the number of the TEGs, increasing the dimensions of the TEGs, or providing higher temperature differences along the TE legs. Regarding the first solution, to provide the required voltages and current at the same time, the number of the TEGs should be increased from 6 to 54, resulting in a too space-consuming benchtop power supply. In addition, a bigger or more fans were required to cool down this number of TEGs, increasing the electricity demand of the system.

Concerning the second solution, it should be considered that scaling up the TEGs to provide the required output voltage could again lead to a too space-consuming and heavy benchtop power supply. Thus, again the energy requirement of the system would be increased due to requiring a bigger or more fans. Regarding the provision of a higher temperature difference along the TE legs, although using more candles could increase the surface temperature of the hot plate, this temperature should be kept less than 150 °C to avoid any damage to the TEGs. Accordingly, the fan should run significantly faster to confront with this extreme higher temperature, which is not only impractical but also is extremely energy consuming. In this regard, it was also impossible to replace the candle with any other internal heat sources (i.e. a radiator or a hot pipework) to provide higher temperature

differences. This was mainly because the temperature of any internal heat source should stay within a certain temperature limit to avoid burning or injuring the occupants. To put it another way, the temperature of none of the internal heat sources should exceed 43 °C in public spaces to prevent burns. As a result, providing a higher temperature difference via replacing the candle with an internal heat source was almost impossible.

112.5 Future works

Both the PCSs and the TE generation are known as growing concepts owing to their eco-friendly features. Precisely, the former moves toward reducing the energy consumption of the HVAC systems (i.e. the background conditioning systems), and the latter is based on renewable electricity generation. To clarify, the renewability of the TE generation is related to scavenging the waste heat available in the ambient and converting it into electricity. Thus, combining these two concepts together to power a PCS with a TEG benefits from both a lower energy consumption and a renewable power supply. However, in case of powering the TEGs with an internal heat source, it is barely possible to provide the required temperature difference for them to power a PCS in long term. For example, regarding this thesis, the candle had a limited life time and required to be replaced with a new one at least every 5hrs. It should be noted that the intensity of the flame was reducing over time, resulting in a reduction in the output voltage of the TEGs after 2hrs. Thus, there are two possible solutions available for this problem, such as replacing the internal heat source (i.e. the candle) with an external one or applying hybrid energy harvesters.

11.5.1 Applying external heat sources

As mentioned before, the internal heat sources (i.e. radiators and hot pipework) provide low surface temperatures to protect the occupants from getting burned. Thus, it is possible to replace them with external heat sources, such as Trombe walls and solar chimneys. To specify, the temperature of the air layer in the Trombe walls and solar chimneys could exceed 60 °C without ventilation and shading devices, depending on the climatic conditions [340]. In addition, the surface area of the Trombe walls and solar chimneys are remarkably greater than the developed benchtop semi-closed box in this thesis. Thus, a greater number of TEGs could be installed in them, resulting in a greater output voltage and current. For example, a bespoke TEG could be

fabricated in the internal divider of a wind tower that its exhaust duct is designed like a solar chimney. Accordingly, the TEG generates electricity based on the temperature difference between the supply and exhaust ducts, see [Fig.132](#). To specify, the outside air enters the supply duct and flows over the cold substrate of the TEG, whilst the stale and hot inside air moves into the exhaust duct and flows over the hot surface of the TEG. As a result, the TEG generates electricity based on the temperature difference between the two ducts. Then, the generated electricity could be used to power not only the PCSs, but also the artificial lighting of the buildings or their electric devices. Obviously, the amount of the resultant output power remarkably depends on the climatic condition, configuration of the TEGs, the employed TE materials, the fabricated heatsink, and the temperature difference between the hot and cold side of the TEGs. However, in general, using such a method leads to a greater output power in harsh (i.e. extremely hot or cold) climatic conditions.

It should be noted that some previous researches proposed fabricating the TEGs in the buildings' fabrics (i.e. walls, ceilings, and windows) to harvest the temperature difference between inside and outside to generate electricity [\[341,342\]](#). However, the main challenge of such fabrications is the resultant thermal bridging that should be delicately addressed to avoid offsetting the positive aspect of the TE generation. Also, there is potential to power the TEGs by installing them on hot pipework, boilers, back of solar panels, or the condensers of the heat pumps. However, due to the high temperature of these heat sources, it is of critical importance to cool down the cold side of the TEGs by designing appropriate heatsinks.

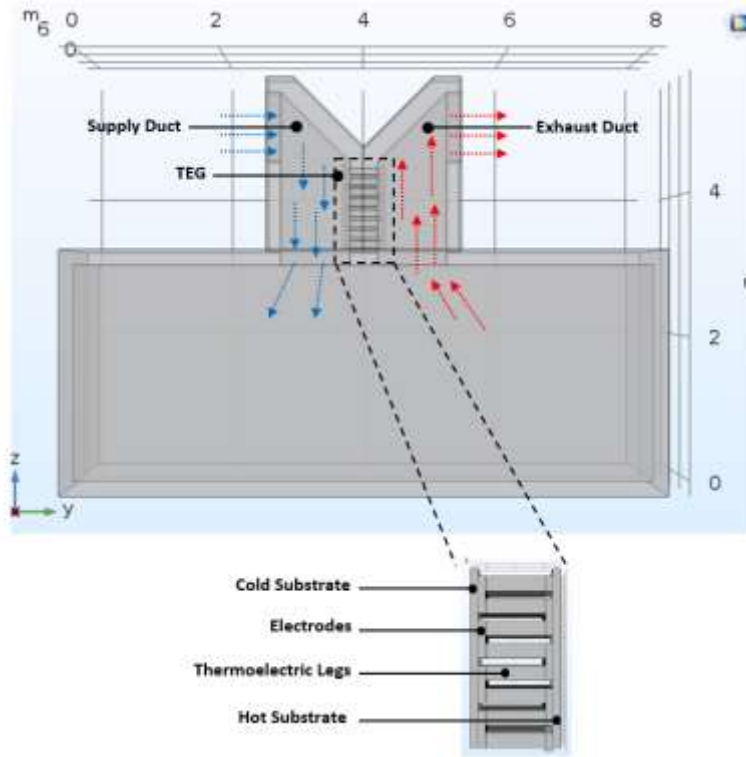


Fig. 132: The modelled concept in COMSOL Multiphysics.

11.5.2 Applying hybrid energy harvesters

The second solution to power a PCS with a TEG is to apply a hybrid energy harvester. Precisely, hybrid harvesting benefits from both scavenging energy from multiple sources and converting energy into electricity by multiple types of transduction mechanisms [343]. Regarding multiple sources, in the case of this research, half of the employed TEGs could be heated by a boiler, whilst the other half could be heated by the condenser of a heat pump. Concerning the multiple types of transduction mechanisms, the integrated TEGs could be coupled with other types of energy harvesters, such as a triboelectric generator [344], a piezoelectric generator [345], or a light-to-thermal conversion layer [346], to fulfil the power requirement at different levels. Thus, in future, rather than solely using the TEGs to power the PCSs, it is more possible to couple it with other types of energy harvesters to harvest different types of available energies at the same time.

References

- [1] Key Aspects of the Paris Agreement, United Nations, Climate change. Available at: <https://unfccc.int/process-and-meetings/the-paris-agreement/the-paris-agreement/key-aspects-of-the-paris-agreement>. (Accessed June 02, 2021).
- [2] The Ten Point Plan for a Green Industrial Revolution (HTML version). Available at: <https://www.gov.uk/government/publications/the-ten-point-plan-for-a-green-industrial-revolution/title>. (Accessed November 18, 2021).
- [3] Energy Demand by Sector, Energy Economics. Available at: <https://www.bp.com/en/global/corporate/energy-economics/energy-outlook/demand-by-sector.html>. (Accessed June 12, 2020).
- [4] Energy Efficiency, IEA. Available at: <https://www.iea.org/topics/energy-efficiency>. (Accessed December, 2020).
- [5] Tracking Buildings 2020, IEA, Paris. Available at: <https://www.iea.org/reports/tracking-buildings-2020>. (Accessed June 12, 2020).
- [6] D. Teli, (2013) Thermal Performance and Occupant Comfort in Naturally Ventilated UK Junior Schools Outside the Heating Season. PhD Thesis. University of Southampton, United Kingdom.
- [7] P. O. Fanger, "Human requirements in future air-conditioned environments," *Int. J. Refrig.*, vol. 24, no. 2, pp. 148–153, 2001.
- [8] J. Dong, C. Winstead, J. Nutaro, and T. Kuruganti, "Occupancy-based HVAC control with short-term occupancy prediction algorithms for energy-efficient buildings," *Energies*, vol. 11, no. 9, pp. 2427, 2018.
- [9] W. Wang, J. Zhang, M. R. Brambley, and B. Futrell, "Performance simulation and analysis of occupancy-based control for office buildings with variable-air-volume sSystems," *Energies*, vol. 13, no. 15, pp. 3756, 2020.
- [10] M. Veselý, P. Molenaar, M. Vos, R. Li, and W. Zeiler, "Personalized heating – comparison of heaters and control modes," *Build. Environ.*, vol. 112, pp. 223–232, 2017.
- [11] A. K. Melikov, "Advanced air distribution: Improving health and comfort while reducing energy use," *Indoor Air*, vol. 26, no. 1, pp. 112–124, 2016.
- [12] J. Jalaludin, "Thermal comfort assessment-A study toward workers, satisfaction in a low energy office building." *Am. J. Appl. Sci.*, vol. 9, no. 7, pp. 1037-1045, 2012.
- [13] S. Shahzad, J. K. Calautit, K. Calautit, B. Hughes, and A. I. Aquino, "Advanced personal comfort system (APCS) for the workplace: A review and case study," *Energy Build.*, vol. 173, pp. 689–709, 2018.
- [14] M. Luo, M. Luo, Z. Wang, H. Zhang, E. Arens, D. Filingeri, L. Jin, A. Ghahramani, W. Chen, Y. He, and B. Si, "High-density thermal sensitivity maps of the human body," *Build. Environ.*, vol. 167, pp. 106435, 2020.
- [15] E. Arens, H. Zhang, and C. Huizenga, "Partial- and whole-body thermal sensation and comfort - Part I: Uniform environmental conditions," *J. Therm. Biol.*, vol. 31, no. 1-2, pp. 53–59, 2006.
- [16] A. K. Mishra, M. G. L. C. Loomans, and J. L. M. Hensen, "Thermal comfort of heterogeneous and dynamic indoor conditions — An overview," *Build. Environ.*, vol. 109, pp. 82–100, 2016.

- [17] H. Zhang, (2003) Human Thermal Sensation and Comfort in Transient and Non-Uniform Thermal Environments. PhD Thesis. University of California, USA.
- [18] L. Schellen, W. D. van Marken Lichtenbelt, M. G. L. C. Loomans, J. Toftum, and M. H. de Wit, "Differences between young adults and elderly in thermal comfort, productivity, and thermal physiology in response to a moderate temperature drift and a steady-state condition," *Indoor Air*, vol. 20, no. 4, pp. 273–283, 2010.
- [19] L. J. Lo and A. Novoselac, "Localized air-conditioning with occupancy control in an open office," *Energy Build.*, vol. 42, no. 7, pp. 1120–1128, 2010.
- [20] M. Veselý and W. Zeiler, "Personalized conditioning and its impact on thermal comfort and energy performance - A review," *Renewable Sustainable Energy Rev.*, vol. 34, pp. 401–408, 2014.
- [21] J. Verhaart, M. Veselý, and W. Zeiler, "Personal heating: Effectiveness and energy use," *Build. Res. Inf.*, vol. 43, no. 3, pp. 346–354, 2015.
- [22] Udayraj, Z. Li, Y. Ke, F. Wang, and B. Yang, "A study of thermal comfort enhancement using three energy-efficient personalized heating strategies at two low indoor temperatures," *Build. Environ.*, vol. 143, pp. 1–14, 2018.
- [23] F. Wang, C. Gao, K. Kuklane, and I. Holmér, "A review of technology of personal heating garments," *Int. J. Occup. Saf. Ergon.*, vol. 16, no. 3, pp. 387–404, 2010.
- [24] SDG 7 Report Warns 650 Million People Could Lack Electricity Access in 2030 Without Sustained Effort. Available at: <https://sdg.iisd.org/news/sdg-7-report-warns-650-million-people-could-lack-electricity-access-in-2030-without-sustained-effort/>. (Accessed May 28, 2019).
- [25] Renewables-Fuels & Technologies, IEA. Available at: <https://www.iea.org/fuels-and-technologies/renewables>. (Accessed November 24, 2020).
- [26] Emissions from Public Electricity and Heat Production - Explanatory Indicators (ENER 009). Available at: <https://www.eea.europa.eu/data-and-maps/indicators/emissions-co2-so2-nox-from-1/assessment-1>. (Accessed May 11, 2021).
- [27] M. Armand and J. M. Tarascon, "Building better batteries," *Nature*, vol. 451, pp. 652–657, pp. 652–657, 2008.
- [28] T. E. Starner, "Powerful change part 1: Batteries and possible alternatives for the mobile market," *IEEE Pervasive Comput.*, vol. 2, no. 4, pp. 86–88, 2003.
- [29] C. Liu, Z. G. Neale, and G. Cao, "Understanding electrochemical potentials of cathode materials in rechargeable batteries," *Mater. Today*, vol. 19, no. 2, pp. 109–123, 2016.
- [30] B. Yang, X. Ding, F. Wang, and A. Li, "A review of intensified conditioning of personal micro-environments: Moving closer to the human body," *Energy Built Environ.*, vol. 2, no. 3, pp. 260–270, 2021.
- [31] F. Suarez, A. Nozariasbmarz, D. Vashaee, and M. C. Öztürk, "Designing thermoelectric generators for self-powered wearable electronics," *Energy Environ. Sci.*, vol. 9, no. 6, pp. 2099–2113, 2016.
- [32] P. Roelofsen, "A computer model for the assessment of employee performance loss as a function of thermal discomfort or degree of heat stress," *Intell. Build. Int.*, vol. 8, no. 4, pp. 195–214, 2016.

- [33] W. J. Fisk, "Health and productivity gains from better indoor environments and their relationship with building energy efficiency," *Annu. Rev. Energy Environ.*, vol. 25, pp. 537–566, 2000.
- [34] L. Lan, P. Wargocki, and Z. Lian, "Quantitative measurement of productivity loss due to thermal discomfort," *Energy Build.*, vol. 43, no. 5, pp. 1057–1062, 2011.
- [35] N. Nasrollahi, I. Knight, and P. Jones, "Workplace satisfaction and thermal comfort in air conditioned office buildings: Findings from a summer survey and field experiments in Iran," *Indoor Built Environ.*, vol. 17, no. 1, pp. 69–79, 2008.
- [36] P. Šujanová, M. Rychtáriková, T. S. Mayor, and A. Hyder, "A healthy, energy-efficient and comfortable indoor environment, a review," *Energies*, vol. 12, no. 8, pp. 1414, 2019.
- [37] M. Frontczak and P. Wargocki, "Literature survey on how different factors influence human comfort in indoor environments," *Build. Environ.*, vol. 46, no. 4, pp. 922–937, 2011.
- [38] J. van Hoof and J. L. M. Hensen, "Quantifying the relevance of adaptive thermal comfort models in moderate thermal climate zones," *Build. Environ.*, vol. 42, no. 1, pp. 156–170, 2007.
- [39] A. Leaman and B. Bordass, "Productivity in buildings: The 'killer' variables," *Build. Res. Inf.*, vol. 27, no. 1, pp. 4–19, 1999.
- [40] A. Wagner, E. Gossauer, C. Moosmann, T. Gropp, and R. Leonhart, "Thermal comfort and workplace occupant satisfaction-Results of field studies in German low energy office buildings," *Energy Build.*, vol. 39, no. 7, pp. 758–769, 2007.
- [41] J. F. Nicol and M. A. Humphreys, "Adaptive thermal comfort and sustainable thermal standards for buildings," *Energy Build.*, vol. 34, no. 6, pp. 563–572, 2002.
- [42] ASHRAE, "ASHRAE Standard 55-2020 – Thermal Environmental Conditions for Human Occupancy," 2020.
- [43] ISO, "ISO 7730:2005, Ergonomics of the Thermal Environment – Analytical Determination and Interpretation of Thermal Comfort Using Calculation of the PMV and PPD Indices and Local Thermal Comfort Criteria." 2005.
- [44] L. Pérez-Lombard, J. Ortiz, and C. Pout, "A review on buildings energy consumption information," *Energy Build.*, vol. 40, no. 3, pp. 394–398, 2008.
- [45] J. Van Hoof, "Forty years of Fanger's model of thermal comfort: Comfort for all?," *Indoor Air*, vol. 18, no. 3, pp. 182–201, 2008.
- [46] M. Balbis-Morejón, J. M. Rey-Hernández, C. Amaris-Castilla, E. Velasco-Gómez, J. F. S. José-Alonso, and F. J. Rey-Martínez, "Experimental study and analysis of thermal comfort in a university campus building in tropical climate," *Sustain.*, vol. 12, no. 21, pp. 8886, 2020.
- [47] A. C. L. Broega, (2008) Contribuição para a Definição de Padrões de Conforto de Tecidos Finos de Lã. PhD Thesis. Universidade do Minho, Portugal.
- [48] Role of CFD in Evaluating Occupant Thermal Comfort. Available at: <https://www.linkedin.com/pulse/role-cfd-evaluating-occupant-thermal-comfort-sandip-jadhav/>. (Accessed November 3, 2018).
- [49] What is ASHRAE 55? Basics of Thermal Comfort. Available at:

<https://www.simscale.com/blog/2019/08/what-is-ashrae-55-thermal-comfort/>. (Accessed December 20, 2020).

- [50] ASHRAE, "ANSI/ASHRAE Standard 55-2010 – Thermal Environmental Conditions for Human Occupancy," American Society of Heating, Refrigerating and Air-Conditioning Engineers, Inc., 2010.
- [51] R. Yao, B. Li, and J. Liu, "A theoretical adaptive model of thermal comfort - Adaptive Predicted Mean Vote (aPMV)," *Build. Environ.*, vol. 44, no. 10, pp. 2089–2096, 2009.
- [52] R. J. De Dear and G. S. Brager, "Thermal comfort in naturally ventilated buildings: Revisions to ASHRAE Standard 55," *Energy Build.*, vol. 34, no. 6, pp. 549–561, 2002.
- [53] P. Ricciardi and C. Buratti, "Thermal comfort in open plan offices in northern Italy: An adaptive approach," *Build. Environ.*, vol. 56, pp. 314–320, 2012.
- [54] M. K. Nematchoua, R. Tchinda, P. Ricciardi, and N. Djongyang, "A field study on thermal comfort in naturally-ventilated buildings located in the equatorial climatic region of Cameroon," *Renewable Sustainable Energy Rev.*, vol. 39, pp. 381–393, 2014.
- [55] S. Dhaka, J. Mathur, G. Brager, and A. Honnekeri, "Assessment of thermal environmental conditions and quantification of thermal adaptation in naturally ventilated buildings in composite climate of India," *Build. Environ.*, vol. 86, pp. 17–28, 2015.
- [56] M. P. Deuble and R. J. de Dear, "Mixed-mode buildings: A double standard in occupants' comfort expectations," *Build. Environ.*, vol. 54, pp. 53–60, 2012.
- [57] F. Nicol, "Adaptive thermal comfort standards in the hot-humid tropics," *Energy Build.*, vol. 36, no. 7, pp. 628–637, 2004.
- [58] S. I. U. H. Gilani, M. H. Khan, and W. Pao, "Thermal comfort analysis of PMV model prediction in air conditioned and naturally ventilated buildings," *Energy Procedia*, vol. 75, pp. 1373–1379, 2015.
- [59] F. Nicol and M. Humphreys, "Maximum temperatures in European office buildings to avoid heat discomfort," *Sol. Energy*, vol. 81, no. 3, pp. 295–304, 2007.
- [60] R. J. de Dear, and G. S. Brager, "Developing an adaptive model of thermal comfort and preference," *ASHRAE Trans.*, vol 104, no. 1, pp. 145–167, 1998.
- [61] F. Nicol and M. Humphreys, "Derivation of the adaptive equations for thermal comfort in free-running buildings in European standard EN15251," *Build. Environ.*, vol. 45, no. 1, pp. 11–17, 2010.
- [62] P. Ole Fanger and J. Toftum, "Extension of the PMV model to non-air-conditioned buildings in warm climates," *Energy Build.*, vol. 34, no. 6, pp. 533–536, 2002.
- [63] M. A. Humphreys and J. F. Nicol, "Understanding the adaptive approach to thermal comfort," *ASHRAE Trans.*, vol. 104, no. Pt 1B, pp. 991–1004, 1998.
- [64] Y. Yau and B. Chew, "A review on predicted mean vote and adaptive thermal comfort models," *Build. Serv. Eng. Res. Technol.*, vol. 35, no. 1, pp. 23–35, 2014.
- [65] Y. Lin, L. Yang, and M. Luo, "Physiological and subjective thermal responses to heat exposure in northern and southern Chinese people," *Build. Simul.*, vol. 14, pp. 1619–1631, 2021.
- [66] C. L. Lim, "Fundamental concepts of human thermoregulation and adaptation to heat: A review in the context of global warming," *Int. J. Environ. Res. Public Health*, vol. 17, no. 21, pp. 1–33, 2020.

- [67] K. Katić, R. Li, and W. Zeiler, "Thermophysiological models and their applications: A review," *Build. Environ.*, vol. 106, pp. 286–300, 2016.
- [68] Z. Li, D. Loveday, and P. Demian, "Feedback messaging, thermal comfort and usage of office-based personal comfort systems," *Energy Build.*, vol. 205, pp. 109514, 2019.
- [69] J. Han, G. Zhang, Q. Zhang, J. Zhang, J. Liu, L. Tian, C. Zheng, J. Hao, J. Lin, Y. Liu, and D. J. Moschandreas, "Field study on occupants' thermal comfort and residential thermal environment in a hot-humid climate of China," *Build. Environ.*, vol. 42, no. 12, pp. 4043–4050, 2007.
- [70] R. L. Hwang, T. P. Lin, and N. J. Kuo, "Field experiments on thermal comfort in campus classrooms in Taiwan," *Energy Build.*, vol. 38, no. 1, pp. 53–62, 2006.
- [71] C. Huizenga, S. Abbaszadeh, L. Zagreus, and E. Arens, "Air quality and thermal comfort in office buildings: Results of a large indoor environmental quality survey," in *Proceedings on Healthy Buildings 2006, Portugal*, vol. 3, pp. 393–397, 2006.
- [72] G. Brager and L. Baker, "Occupant satisfaction in mixed-mode buildings," *Build. Res. Inf.*, vol. 37, no. 4, pp. 369–380, 2009.
- [73] Y. Al Horr, M. Arif, A. Kaushik, A. Mazroei, M. Katafygiotou, and E. Elsarrag, "Occupant productivity and office indoor environment quality: A review of the literature," *Build. Environ.*, vol. 105, pp. 369–389, 2016.
- [74] M. Schweiker and A. Wagner, "The effect of occupancy on perceived control, neutral temperature, and behavioral patterns," *Energy Build.*, vol. 117, pp. 246–259, 2016.
- [75] G. S. Brager and R. J. De Dear, "Thermal adaptation in the built environment: A literature review," *Energy Build.*, vol. 27, no. 1, pp. 83–96, 1998.
- [76] Indoor Environmental Input Parameters for Design and Assessment of Energy Performance of Buildings-Addressing Indoor Air Quality, Thermal Environment, Lighting and Acoustics," Available at: http://www.cres.gr/greenbuilding/PDF/prend/set4/WI_31_Pre-FV_version_prEN_15251_Indoor_Environment.pdf. (Accessed July 31, 2006).
- [77] M. Kwon, H. Remøy, A. van den Dobbelen, and U. Knaack, "Personal control and environmental user satisfaction in office buildings: Results of case studies in the Netherlands," *Build. Environ.*, vol. 149, pp. 428–435, 2019.
- [78] J. F. Nicol and S. Roaf, "Rethinking thermal comfort," *Build. Res. Inf.*, vol. 45, no. 7, pp. 711–716, 2017.
- [79] D. Fiala, A. Psikuta, G. Jendritzky, S. Paulke, D. A. Nelson, W. D. V. M. Lichtenbelt, and A. J. H. Frijns, "Physiological modeling for technical, clinical and research applications," *Front. Biosci. - Sch.*, vol. 2 S, no. 3, pp. 939–968, 2010.
- [80] H. Zhang, E. Arens, C. Huizenga, and T. Han, "Thermal sensation and comfort models for non-uniform and transient environments, part II: Local comfort of individual body parts," *Build. Environ.*, vol. 45, no. 2, pp. 389–398, 2010.
- [81] R. Maiti, "Physiological and subjective thermal response from Indians," *Build. Environ.*, vol. 70, pp. 306–317, 2013,
- [82] H. Liu, J. Liao, D. Yang, X. Du, P. Hu, Y. Yang, and B. Li "The response of human thermal perception

- and skin temperature to step-change transient thermal environments," *Build. Environ.*, vol. 73, pp. 232–238, 2014.
- [83] Z. Wang, H. Ning, Y. Ji, J. Hou, and Y. He, "Human thermal physiological and psychological responses under different heating environments," *J. Therm. Biol.*, vol. 52, pp. 177–186, 2015.
- [84] E. A. Arens and H. Zhang, *The Skin's Role in Human Thermoregulation and Comfort*. Thermal and Moisture Transport in Fibrous Materials, Woodhead Publishing Ltd, 2006.
- [85] C. Huizenga, H. Zhang, E. Arens, and D. Wang, "Skin and core temperature response to partial- and whole-body heating and cooling," *J. Therm. Biol.*, vol. 29, pp. 549–558, 2004.
- [86] M. Veselý, W. Zeiler, G. Boxem, and D. R. Vissers, "The human body as its own sensor for thermal comfort," in *Proceedings of the International Conference on Cleantech for Smart Cities and Buildings (CISBAT 2013)*, Switzerland, pp. 379–384, 2013.
- [87] D. Wang, H. Zhang, E. Arens, and C. Huizenga, "Observations of upper-extremity skin temperature and corresponding overall-body thermal sensations and comfort," *Build. Environ.*, vol. 42, no. 12, pp. 3933–3943, 2007.
- [88] W. Zeiler, M. Vesely, D. Vissers, and R. Li, "Thermal response of different body parts: The fingertip as control sensor for personalized heating," *Energy Procedia*, 2015, vol. 78, pp. 2766–2771.
- [89] H. Zhang, E. Arens, and Y. Zhai, "A review of the corrective power of personal comfort systems in non-neutral ambient environments," *Build. Environ.*, vol. 91, pp. 15–41, 2015.
- [90] H. Amai, S. ichi Tanabe, T. Akimoto, and T. Genma, "Thermal sensation and comfort with different task conditioning systems," *Build. Environ.*, vol. 42, no. 12, pp. 3955–3964, 2007.
- [91] R. Rawal, M. Schweiker, O. B. Kazanci, V. Vardhan, Q. Jin, and L. Duanmu, "Personal comfort systems: A review on comfort, energy, and economics," *Energy Build.*, vol. 214, pp. 109858, 2020.
- [92] Y. F. Zhang, D. P. Wyon, L. Fang, and A. K. Melikov, "The influence of heated or cooled seats on the acceptable ambient temperature range," *Ergon.*, vol. 50, no. 4, pp. 586–600, 2007.
- [93] W. Pasut, H. Zhang, E. Arens, S. Kaam, and Y. Zhai, "Effect of a heated and cooled office chair on thermal comfort," *HVAC&R Res.*, vol. 19, no. 5, pp. 574–583, 2013.
- [94] W. Pasut, H. Zhang, E. Arens, and Y. Zhai, "Energy-efficient comfort with a heated/cooled chair: Results from human subject tests," *Build. Environ.*, vol. 84, pp. 10–21, 2015.
- [95] S. Shahzad, J. K. Calautit, A. I. Aquino, D. S. N. M. Nasir, and B. R. Hughes, "A user-controlled thermal chair for an open plan workplace: CFD and field studies of thermal comfort performance," *Appl. Energy*, vol. 207, pp. 283–293, 2017.
- [96] Q. Deng, R. Wang, Y. Li, Y. Miao, and J. Zhao, "Human thermal sensation and comfort in a non-uniform environment with personalized heating," *Sci. total Environ.*, vol. 578, pp. 242–248, 2017.
- [97] H. Zhang, E. Arens, M. Taub, D. Dickerhoff, F. Bauman, M. Fountaint, W. Pasut, D. Fannon, Y. Zhai, M. Pigman, "Using footwarmers in offices for thermal comfort and energy savings," *Energy Build.*, vol. 104, pp. 233–243, 2015.
- [98] H. Zhang, E. Arens, D. E. Kim, E. Buchberger, F. Bauman, and C. Huizenga, "Comfort, perceived air quality, and work performance in a low-power task-ambient conditioning system," *Build. Environ.*,

vol. 45, no. 1, pp. 29–39, 2010.

- [99] S. Watanabe, A. K. Melikov, and G. L. Knudsen, “Design of an individually controlled system for an optimal thermal microenvironment,” *Build. Environ.*, vol. 45, no. 3, pp. 549–558, 2010.
- [100] A. K. Melikov and G. L. Knudsen, “Human response to an individually controlled microenvironment,” *HVAC&R Res.*, vol. 13, no. 4, pp. 645–660, 2007.
- [101] Y. Bai, H. Li, S. Gan, Y. Li, H. Liu, and L. Chen, “Flexible heating fabrics with temperature perception based on fine copper wire and fusible interlining fabrics,” *Meas.*, vol. 122, pp. 192–200, 2018.
- [102] O. Sahin, O. Kayacan, E. Y. Bulgun, “Smart Textiles for Soldier of the Future,” *Def Sci. J.*, vol. 55, no. 2, pp. 195–205, 2005.
- [103] F. Wang and H. Lee, “Evaluation of an electrically heated vest (EHV) using a thermal manikin in cold environments,” *Ann. Occup. Hyg.*, vol. 54, no. 1, pp. 117–124, 2010.
- [104] Y. He, X. Wang, N. Li, M. He, and D. He, “Heating chair assisted by leg-warmer: A potential way to achieve better thermal comfort and greater energy conservation in winter,” *Energy Build.*, vol. 158, pp. 1106–1116, 2018.
- [105] A. Taguchi, J. Ratnaraj, B. Kabon, N. Sharma, R. Lenhardt, D. I. Sessler, and A. Kurz, “Effects of a circulating-water garment and forced-air warming on body heat content and core temperature,” *Anesthesiology*, vol. 100, no. 5, pp. 1058, 2004.
- [106] C. Gao, K. Kuklane, and I. Holmér, “The heating effect of phase change material (PCM) vests on a thermal manikin in a subzero environment.” in 7th International Thermal Manikin and Modelling Meeting, Portugal, 2008.
- [107] M. H. Elsheikh, D. A. Shnawaha, M. F. M. Sabria, S. B. M. Said, M. H. Hassana, M. B. ALi Bashira, and M. Mohamad, “A review on thermoelectric renewable energy: Principle parameters that affect their performance,” *Renewable Sustainable Energy Rev.*, vol. 30, pp. 337–355, 2014.
- [108] H. B. Gao, G. H. Huang, H. J. Li, Z. G. Qu, and Y. J. Zhang, “Development of stove-powered thermoelectric generators: A review,” *Appl. Therm. Eng.*, vol. 96, pp. 297–310, 2016.
- [109] S. Twaha, J. Zhu, Y. Yan, and B. Li, “A comprehensive review of thermoelectric technology: Materials, applications, modelling and performance improvement,” *Renewable Sustainable Energy Rev.*, vol. 65, pp. 698–726, 2016.
- [110] D. Champier, “Thermoelectric generators: A review of applications,” *Energy Convers. Manage.*, vol. 140, pp. 167–181, 2017.
- [111] R. Kroon, D. A. Mengistie, D. Kiefer, J. Hynnen, J. D. Ryan, L. Yu and C. Müller, “Thermoelectric plastics: From design to synthesis, processing and structure-property relationships,” *Chem. Soc. Rev.*, vol. 45, no. 22, pp. 6147–6164, 2016.
- [112] A. Nour Eddine, D. Chalet, X. Faure, L. Aixala, and P. Chessé, “Optimization and characterization of a thermoelectric generator prototype for marine engine application,” *Energy*, vol. 143, pp. 682–695, 2018.
- [113] K. A. Borup, J. de Boor, H. Wang, F. Drymiotis, F. Gascoin, X. Shi, L. Chen, M. I. Fedorov, E. Müller, B. B. Iversena and G. J. Snyder, “Measuring thermoelectric transport properties of materials,” *Energy Environ. Sci.*, vol. 8, no. 2, pp. 423–435, 2015.

- [114] M. J. Newton, S. White, C. Estherby, and A. Gomez, "Meta-study: Analysis of thermoelectric figure of merit parameters for silicides with various doping agents," *PAM Rev. Energy Sci. Technol.*, vol. 3, 2016.
- [115] C. Han, Z. Li, and S. Dou, "Recent progress in thermoelectric materials," *Chin. Sci. Bull.*, vol. 59, no. 18, pp. 2073–2091, 2014.
- [116] G. T. Meaden, "The theory of the electrical resistance of metals," *Electr. Resist. Met.*, pp. 59–94, 1965.
- [117] C. Gayner and K. K. Kar, "Recent advances in thermoelectric materials," *Prog. Mater Sci.*, vol. 83, pp. 330–382, 2016.
- [118] T. Shibuya, J. M. Skelton, A. J. Jackson, K. Yasuoka, A. Togo, I. Tanaka, and A. Walsh "Suppression of lattice thermal conductivity by mass-conserving cation mutation in multi-component semiconductors," *APL Mater.*, vol. 4, no. 10, pp. 104809, 2016.
- [119] R. He, G. Schierning, and K. Nielsch, "Thermoelectric devices: A review of devices, architectures, and contact optimization," *Adv. Mater. Technol.*, vol. 3, no. 4, pp. 1700256, 2018.
- [120] I. Petsagkourakis, K. Tybrandt, X. Crispin, I. Ohkubo, N. Satoh, and T. Mori, "Thermoelectric materials and applications for energy harvesting power generation," *Sci. Technol. Adv. Mater.*, vol. 19, no. 1, pp. 836–862, 2018.
- [121] X. Shi, L. Chen, and C. Uher, "Recent advances in high-performance bulk thermoelectric materials," *Int. Mater. Rev.*, vol. 61, no. 6, pp. 379–415, 2016.
- [122] Z. Soleimani, S. Zoras, B. Ceranic, S. Shahzad, and Y. Cui, "A review on recent developments of thermoelectric materials for room-temperature applications," *Sustain. Energy Technol. Assessments*, vol. 37, pp. 100604, 2020.
- [123] H. Jin, J. Li, J. Iocozzia, X. Zeng, P. C. Wei, C. Yang, N. Li, Z. Liu, J. H. He, T. Zhu, J. Wang, Z. Lin, and S. Wang, "Hybrid organic–inorganic thermoelectric materials and devices," *Angew. Chemie Int. Ed.*, vol. 58, no. 43, pp. 15206–15226, 2019.
- [124] M. Sajid, I. Hassan, and A. Rahman, "An overview of cooling of thermoelectric devices," *Renewable Sustainable Energy Rev.*, vol. 78, pp. 15–22, 2017.
- [125] Y. Du, J. Xu, B. Paul, and P. Eklund, "Flexible thermoelectric materials and devices," *Appl. Mater. Today*, vol. 12, pp. 366–388, 2018.
- [126] P. Ren, Y. Liu, J. He, T. Lv, J. Gao, and G. Xu, "Recent advances in inorganic material thermoelectrics," *Inorg. Chem. Front.*, vol. 5, no. 10, pp. 2380–2398, 2018.
- [127] X. Chen, W. Dai, T. Wu, W. Luo, J. Yang, W. Jiang, L. Wang, "Thin film thermoelectric materials: classification, characterization, and potential for wearable applications," *Coat.*, vol. 8, no. 7, p. 244, 2018.
- [128] C.J. Yao, H.L. Zhang, and Q. Zhang, "Recent progress in thermoelectric materials based on conjugated polymers," *Polym.*, vol. 11, no. 1, pp. 107, 2019.
- [129] C. Wan, R. Tian, M. Kondou, R. Yang, P. Zong, and K. Koumoto, "Ultra-high thermoelectric power factor in flexible hybrid inorganic-organic superlattice," *Nat. Commun.*, vol. 8, no. 1, pp. 1–9, 2017.

- [130] Q. Jiang, J. Yang, Y. Liu, and H. He, "Microstructure tailoring in nanostructured thermoelectric materials," *J. Adv. Dielectr.*, vol. 6, no. 1, 2016.
- [131] W. T. Chiu, C. L. Chen, and Y. Y. Chen, "A strategy to optimize the thermoelectric performance in a spark plasma sintering process," *Sci. Rep.*, vol. 6, no. 1, pp. 1–9, 2016.
- [132] H. Mamur, M. R. A. Bhuiyan, F. Korkmaz, and M. Nil, "A review on bismuth telluride (Bi₂Te₃) nanostructure for thermoelectric applications," *Renewable Sustainable Energy Rev.*, vol. 82, pp. 4159–4169, 2018.
- [133] Z. Liu, Y. Wang, J. Mao, H. Geng, J. Shuai, Y. Wang, R. He, W. Cai, J. Sui, and Z. Ren "Lithium doping to enhance thermoelectric performance of MgAgSb with weak electron-phonon coupling," *Adv. Energy Mater.*, vol. 6, no. 7, pp. 1502269, 2016.
- [134] Y. Zheng, C. Liu, L. Miao, H. Lin, J. Gao, X. Wang, J. Chen, S. Wu, X. Li and H. Cai "Cost effective synthesis of p-type Zn-doped MgAgSb by planetary ball-milling with enhanced thermoelectric properties," *RSC Adv.*, vol. 8, no. 62, pp. 35353–35359, 2018.
- [135] W. Gao, X. Yi, B. Cui, Z. Wang, J. Huang, J. Sui, and Z. Liu, "The critical role of boron doping in the thermoelectric and mechanical properties of nanostructured α -MgAgSb," *J. Mater. Chem. C*, vol. 6, no. 36, pp. 9821–9827, 2018.
- [136] S. Duan, N. Man, J. Xu, Q. Wu, G. q. Liu, X. Tan, H. Shao, Kai Guo, X. Yang and J. Jiang, "Thermoelectric (Bi,Sb)₂Te₃-Ge_{0.5}Mn_{0.5}Te composites with excellent mechanical properties," *J. Mater. Chem. A*, vol. 7, no. 15, pp. 9241–9246, 2019.
- [137] Y. S. Wang, L. L. Huang, D. Li, J. Zhang, and X. Y. Qin, "Enhanced thermoelectric performance of Bi_{0.4}Sb_{1.6}Te₃ based composites with CuInTe₂ inclusions," *J. Alloys Compd.*, vol. 758, pp. 72–77, 2018.
- [138] Y. S. Wang, L. L. Huang, C. Zhu, J. Zhang, D. Li, H. X. Xin, M. H. Danish, X. Y. Qin, "Simultaneously enhanced power factor and phonon scattering in Bi_{0.4}Sb_{1.6}Te₃ alloy doped with germanium," *Scr. Mater.*, vol. 154, pp. 118–122, 2018.
- [139] F. Hao, P. Qiu, Q. Song, H. Chen, P. Lu, D. Ren, X. Shi, and L. Chen, "Roles of Cu in the enhanced thermoelectric properties in Bi_{0.5}Sb_{1.5}Te₃," *Mater.*, vol. 10, no. 3, 2017.
- [140] X. Guo, J. Qin, X. Jia, H. Ma, and H. Jia, "Quaternary thermoelectric materials: Synthesis, microstructure and thermoelectric properties of the (Bi,Sb)₂(Te,Se)₃alloys," *J. Alloys Compd.*, vol. 705, pp. 363–368, 2017.
- [141] F. Serrano-Sánchez, M. Gharsallah, N. M. Nemes, N. Biskup, M. Varela, J. L. Martínez, M. T. Fernández-Díaz and J. A. Alonso "Enhanced figure of merit in nanostructured (Bi,Sb)₂Te₃ with optimized composition, prepared by a straightforward arc-melting procedure," *Sci. Rep.*, vol. 7, no. 1, pp. 6277, 2017.
- [142] S. Liang, J. Xu, H. Wang, X. Tan, G. Q. Liu, H. Shao, B. Yu, S. Yue and J. Jiang, "Investigation on structure and thermoelectric properties in p-type Bi_{0.48}Sb_{1.52}Te₃ via PbTe incorporating," *J. Mater. Sci. Mater. Electron.*, vol. 29, no. 9, pp. 7701–7706, 2018.
- [143] N. Gao, B. Zhu, X. yu Wang, Y. Yu, and F. qiu Zu, "Simultaneous optimization of Seebeck, electrical and thermal conductivity in free-solidified Bi_{0.4}Sb_{1.6}Te₃ alloy via liquid-state manipulation," *J. Mater. Sci.*, vol. 53, no. 12, pp. 9107–9116, 2018.

- [144] Z. Fan, H. Wang, Y. Wu, X. J. Liu, and Z. P. Lu, "Thermoelectric high-entropy alloys with low lattice thermal conductivity," *RSC Adv.*, vol. 6, no. 57, pp. 52164–52170, 2016.
- [145] B. Bochentyn, T. Miruszewski, J. Karczewski, and B. Kusz, "Thermoelectric properties of bismuth-antimony-telluride alloys obtained by reduction of oxide reagents," *Mater. Chem. Phys.*, vol. 177, pp. 353–359, 2016.
- [146] Z. Liu, Y. Zhang, J. Mao, W. Gao, Y. Wang, J. Shuai, W. Cai, J. Sui, and Z. Ren, "The microscopic origin of low thermal conductivity for enhanced thermoelectric performance of Yb doped MgAgSb," *Acta Mater.*, vol. 128, pp. 227–234, Apr. 2017.
- [147] J. Lei, D. Zhang, W. Guan, Z. Cheng, C. Wang, and Y. Wang, "Engineering electrical transport in α -MgAgSb to realize high performances near room temperature," *Phys. Chem. Chem. Phys.*, vol. 20, no. 24, pp. 16729–16735, 2018.
- [148] Z. Liu, J. Shuai, J. Mao, Y. Wang, Z. Wang, W. Cai, J. Sui, and Z. Ren, "Effects of antimony content in MgAg_{0.97}Sb_x on output power and energy conversion efficiency," *Acta Mater.*, vol. 102, pp. 17–23, 2016.
- [149] Z. Liu, Y. Wang, W. Gao, J. Mao, H. Geng, J. Shuai, W. Cai, J. Sui, and Z. Ren, "The influence of doping sites on achieving higher thermoelectric performance for nanostructured α -MgAgSb," *Nano Energy*, vol. 31, pp. 194–200, 2017.
- [150] Y. Zheng, C. Liu, L. Miao, C. Li, R. Huang, J. Gao, X. Wang, J. Chen, Y. Zhou, and E. Nishibori, "Extraordinary thermoelectric performance in MgAgSb alloy with ultralow thermal conductivity," *Nano Energy*, vol. 59, pp. 311–320, 2019.
- [151] R. Deng, X. Su, Z. Zheng, W. Liu, Y. Yan, Q. Zhang, V. P. Dravid, C. Uher, M. G. Kanatzidis, and X. Tang, "Thermal conductivity in Bi_{0.5}Sb_{1.5}Te_{3+x} and the role of dense dislocation arrays at grain boundaries," *Sci. Adv.*, vol. 4, no. 6, pp. eaar5606, 2018.
- [152] F. Hao, T. Xing, P. Qiu, P. Hu, T. Wei, D. Ren, X. Shi, and L. Chen, "Enhanced thermoelectric performance in n-type Bi₂Te₃-based alloys via suppressing intrinsic excitation," *ACS Appl. Mater. Interfaces*, vol. 10, no. 25, pp. 21372–21380, 2018.
- [153] Y. Kang, Q. Zhang, C. Fan, W. Hu, C. Chen, L. Zhang, F. Yu, Y. Tian, and B. Xu, "High pressure synthesis and thermoelectric properties of polycrystalline Bi₂Se₃," *J. Alloys Compd.*, vol. 700, pp. 223–227, Apr. 2017.
- [154] A. Nozariasbmarz, J. S. Krasinski, and D. Vashaee, "N-Type Bismuth Telluride Nanocomposite Materials Optimization for Thermoelectric Generators in Wearable Applications," *Mater.*, vol. 12, no. 9, pp. 1529, 2019.
- [155] B. Zhu, Z. Y. Huang, X. Y. Wang, Y. Yu, N. Gao, and F. Q. Zu, "Enhanced thermoelectric properties of n-type direction solidified Bi₂Te_{2.7}Se_{0.3} alloys by manipulating its liquid state," *Scr. Mater.*, vol. 146, pp. 192–195, 2018.
- [156] B. Zhu, Y. Yu, X. yu Wang, F. qiu Zu, and Z. yue Huang, "Enhanced thermoelectric properties of n-type Bi₂Te_{2.7}Se_{0.3} semiconductor by manipulating its parent liquid state," *J. Mater. Sci.*, vol. 52, no. 14, pp. 8526–8537, 2017.
- [157] X. Y. Wang, H. J. Wang, B. Xiang, H. J. Shang, B. Zhu, Y. Yu, H. Jin, R. F. Zhao, Z. Y. Huang, L.J. Liu, F. Q. Zu and Z. G. Chen, "Attaining reduced lattice thermal conductivity and enhanced electrical

- conductivity in as-sintered pure n-type Bi₂Te₃ alloy," *J. Mater. Sci.*, vol. 54, no. 6, pp. 4788–4797, 2019.
- [158] M. Hong, T. C. Chasapis, Z. G. Chen, Lei Yang, M. G. Kanatzidis, G. J. Snyder, and J. Zou, "N-type Bi₂Te₃-xSex nanoplates with enhanced thermoelectric efficiency driven by wide-frequency phonon scatterings and synergistic carrier scatterings," *ACS Nano*, vol. 10, no. 4, pp. 4719–4727, 2016.
- [159] L. Yang, Z. G. Chen, M. S. Dargusch, and J. Zou, "High performance thermoelectric materials: progress and their applications," *Adv. Energy Mater.*, vol. 8, no. 6, 2018.
- [160] F. Hao, P. Qiu, Yunshan Tang, S. Bai, T. Xing, H. S. Chu, Q. Zhang, P. Lu, T. Zhang, D. Ren, J. Chen, X. Shi, and L. Chen, "High efficiency Bi₂Te₃-based materials and devices for thermoelectric power generation between 100 and 300 °c," *Energy Environ. Sci.*, vol. 9, no. 10, pp. 3120–3127, 2016.
- [161] B. Madavali, H. S. Kim, K. H. Lee, and S. J. Hong, "Enhanced Seebeck coefficient by energy filtering in Bi-Sb-Te based composites with dispersed Y₂O₃ nanoparticles," *Intermetallics*, vol. 82, pp. 68–75, 2017.
- [162] B. Cao, J. Jikang, L. Jiao, G. Binghui, L. Shanming, W. Hao, Z. Huaizhou, "Improved thermoelectric performance in p-type Bi_{0.48}Sb_{1.52}Te₃ bulk material by adding MnSb₂Se₄," *Chinese Phys. B*, vol. 26, no. 1, pp. 1–7, 2017.
- [163] M. Wang, P. Baek, A. Akbarinejad, D. Barker, and J. Travas-Sejdic, "Conjugated polymers and composites for stretchable organic electronics," *J. Mater. Chem. C*, vol. 7, no. 19, pp. 5534–5552, 2019.
- [164] M. E. Bhosale, S. Chae, J. M. Kim, and J. Y. Choi, "Organic small molecules and polymers as an electrode material for rechargeable lithium ion batteries," *J. Mater. Chem. A*, vol. 6, no. 41, pp. 19885–19911, 2018.
- [165] E. Kolasińska and P. Kolasiński, "A review on electroactive polymers for waste heat recovery," *Mater.*, vol. 9, no. 6, 2016.
- [166] D. Ni, Y. Chen, H. Song, C. Liu, X. Yang, and K. Cai, "Free-standing and highly conductive PEDOT nanowire films for high-performance all-solid-state supercapacitors," *J. Mater. Chem. A*, vol. 7, no. 3, pp. 1323–1333, 2019.
- [167] Y. Lu, K. Cai, Y. Ding, M. Wang, C. Jiang, Q. Yao, C. Huang, L. Chen, and J. He, "Ultrahigh power factor and flexible silver selenide-based composite film for thermoelectric devices," *Energy Environ. Sci.*, vol. 13, no. 4, pp. 1240–1249, 2020.
- [168] Y. Du, K. F. Cai, S. Z. Shen, R. Donelsonand, J. Y. Xu, H. X. Wang, and T. Lin, "Multifold enhancement of the output power of flexible thermoelectric generators made from cotton fabrics coated with conducting polymer," *RSC Adv.*, vol. 7, no. 69, pp. 43737–43742, 2017.
- [169] Z. Fan, P. Li, D. Du, and J. Ouyang, "Significantly enhanced thermoelectric properties of PEDOT:PSS films through sequential post-treatments with common acids and bases," *Adv. Energy Mater.*, vol. 7, no. 8, 2017.
- [170] H. Yao, Z. Fan, H. Cheng, X. Guan, C. Wang, K. Sun, J. Ouyang, "Recent Development of Thermoelectric Polymers and Composites," *Macromol. Rapid Commun.*, vol. 39, no. 6, pp. 1700727, 2018.

- [171] Y. Zhang, Y.-J. Heo, M. Park, and S.-J. Park, "Recent advances in organic thermoelectric materials: principle mechanisms and emerging carbon-based green energy materials," *Polym.*, vol. 11, no. 1, p. 167, 2019.
- [172] I. H. Jung, C. T. Hong, U. H. Lee, Y. H. Kang, K. S. Jang, and S. Y. Cho, "High thermoelectric power factor of a diketopyrrolopyrrole-based low bandgap polymer via finely tuned doping engineering," *Sci. Rep.*, vol. 7, no. 1, pp. 1–8, 2017.
- [173] L. Zhang, T. Goto, I. Imae, Y. Sakurai, and Y. Harima, "Thermoelectric properties of PEDOT films prepared by electrochemical polymerization," *J. Polym. Sci. Part B Polym. Phys.*, vol. 55, no. 6, pp. 524–531, 2017.
- [174] S. N. Patel, A. M. Glaudell, D. Kiefer, and M. L. Chabiny, "Increasing the thermoelectric power factor of a semiconducting polymer by doping from the vapor phase," *ACS Macro Lett.*, vol. 5, no. 3, pp. 268–272, 2016.
- [175] E. Lim, K. A. Peterson, G. M. Su, and M. L. Chabiny, "Thermoelectric properties of poly(3-hexylthiophene) (P3HT) doped with 2,3,5,6-Tetrafluoro-7,7,8,8-tetracyanoquinodimethane (F4TCNQ) by vapor-phase infiltration," *Chem. Mater.*, vol. 30, no. 3, pp. 998–1010, 2018.
- [176] H. Li, M. E. Decoster, R. M. Ireland, J. Song, P. E. Hopkins, and H. E. Katz, "Modification of the Poly(bisdodecylquaterthiophene) structure for high and predominantly nonionic conductivity with matched dopants," *J. Am. Chem. Soc.*, vol. 139, no. 32, pp. 11149–11157, 2017.
- [177] C. Pan, L. Wang, T. Liu, X. Zhou, T. Wan, S. Wang, Z. Chen, C. Gao, and L. Wang, "Polar side chain effects on the thermoelectric properties of benzo[1,2-b:4,5-b']Dithiophene-based conjugated polymers," *Macromol. Rapid Commun.*, vol. 40, no. 12, p. 1900082, 2019.
- [178] L. Wang, C. Pan, A. Liang, X. Zhou, W. Zhou, T. Wana and L. Wang, "The effect of the backbone structure on the thermoelectric properties of donor-acceptor conjugated polymers," *Polym. Chem.*, vol. 8, no. 32, pp. 4644–4650, 2017.
- [179] X. Wang, A. K. K. Kyaw, C. Yin, F. Wang, Q. Zhu, T. Tang, P. I. Yee, and J. Xu, "Enhancement of thermoelectric performance of PEDOT:PSS films by post-treatment with a superacid," *RSC Adv.*, vol. 8, no. 33, pp. 18334–18340, 2018.
- [180] H. Un, S. A. Gregory, S. K. Mohapatra, M. Xiong, E. Longhi, Y. Lu, S. Rigin, S. Jhulki, C. Y. Yang, T. V. Timofeeva, J. Y. Wang, S. K. Yee, S. Barlow, S. R. Marder, and J. Pei, "Understanding the Effects of Molecular Dopant on n-Type Organic Thermoelectric Properties," *Adv. Energy Mater.*, vol. 9, no. 24, pp. 1900817, 2019.
- [181] F. Gao, Y. Liu, Y. Xiong, P. Wu, B. Hu, and L. Xu, "Fabricate organic thermoelectric modules use modified PCBM and PEDOT:PSS materials," *Front. Optoelectron.*, vol. 10, no. 2, pp. 117–123, 2017.
- [182] S. Hwang, W. J. Potscavage, Y. S. Yang, I. S. Park, T. Matsushima, and C. Adachi, "Solution-processed organic thermoelectric materials exhibiting doping-concentration-dependent polarity," *Phys. Chem. Chem. Phys.*, vol. 18, no. 42, pp. 29199–29207, 2016.
- [183] D. Huang, H. Yao, Y. Cui, Ye Zou, F. Zhang, C. Wang, H. Shen, W. Jin, J. Zhu, Y. Diao, W. Xu, C. A. Di, and D. Zhu, "Conjugated-Backbone Effect of Organic Small Molecules for n-Type Thermoelectric Materials with ZT over 0.2," *J. Am. Chem. Soc.*, vol. 139, no. 37, pp. 13013–13023, 2017.
- [184] C. Y. Yang, W. L. Jin, J. Wang, Y. F. Ding, S. Nong, K. Shi, Y. Lu, Y. Z. Dai, F. D. Zhuang, T. Lei, C. A. Di,

- D. Zhu, J. Y. Wang, J. Pei, "Enhancing the n-type conductivity and thermoelectric performance of donor-acceptor copolymers through donor engineering," *Adv. Mater.*, vol. 30, no. 43, pp. 1802850, 2018.
- [185] D. Madan, X. Zhao, R. M. Ireland, D. Xiao, and H. E. Katz, "Conductivity and power factor enhancement of n-type semiconducting polymers using sodium silica gel dopant," *APL Mater.*, vol. 5, no. 8, pp. 086106, 2017.
- [186] V. D. Punetha, S. Rana, H. J. Yoo, A. Chaurasia, J. T. McLeskey, M. S. Ramasamy, N. G. Sahoo, and J. W. Cho, "Functionalization of carbon nanomaterials for advanced polymer nanocomposites: A comparison study between CNT and graphene," *Prog. Polym. Sci.*, vol. 67, pp. 1–47, 2017.
- [187] L. Wang, Q. Yao, J. Xiao, K. Zeng, S. Qu, W. Shi, Q. Wang, L. Chen, "Engineered molecular chain ordering in single-walled carbon nanotubes/polyaniline composite films for high-performance organic thermoelectric materials," *Chem. Asian J.*, vol. 11, no. 12, pp. 1804–1810, 2016.
- [188] Y. Wang, J. Yang, L. Wang, K. Du, Q. Yin, and Q. Yin, "Polypyrrole/graphene/polyaniline ternary nanocomposite with high thermoelectric power factor," *ACS Appl. Mater. Interfaces*, vol. 9, no. 23, pp. 20124–20131, 2017.
- [189] S. Wang, F. Liu, C. Gao, T. Wan, L. Wang, L. Wang, and L. Wang, "Enhancement of the thermoelectric property of nanostructured polyaniline/carbon nanotube composites by introducing pyrrole unit onto polyaniline backbone via a sustainable method," *Chem. Eng. J.*, vol. 370, pp. 322–329, 2019.
- [190] W. Lee, Y. H. Kang, J. Y. Lee, K. S. Jang, and S. Y. Cho, "Improving the thermoelectric power factor of CNT/PEDOT:PSS nanocomposite films by ethylene glycol treatment," *RSC Adv.*, vol. 6, no. 58, pp. 53339–53344, 2016.
- [191] Q. Jiang, X. Lan, C. Liu, H. Shi, Z. Zhu, F. Zhao, J. Xu, and F. Jiang, "High-performance hybrid organic thermoelectric SWNTs/PEDOT:PSS thin-films for energy harvesting," *Mater. Chem. Front.*, vol. 2, no. 4, pp. 679–685, 2018.
- [192] C. Cho, K. L. Wallace, P. Tzeng, J. H. Hsu, C. Yu, and J. C. Grunlan, "Outstanding low temperature thermoelectric power factor from completely organic thin films enabled by multidimensional conjugated nanomaterials," *Adv. Energy Mater.*, vol. 6, no. 7, 2016.
- [193] C. Park, D. Yoo, J. J. Lee, H. H. Choi, and J. H. Kim, "Enhanced power factor of poly (3,4-ethyldioxythiophene):poly (styrene sulfonate) (PEDOT:PSS)/RTCVD graphene hybrid films," *Org. Electron.*, vol. 36, pp. 166–170, 2016.
- [194] C. Cho, M. Culebras, K. L. Wallace, Y. Song, K. Holder, J. H. Hsu, C. Yu, and J. C. Grunlan, "Stable n-type thermoelectric multilayer thin films with high power factor from carbonaceous nanofillers," *Nano Energy*, vol. 28, pp. 426–432, 2016.
- [195] W. Zhou, Q. Fan, Q. Zhang, L. Cai, K. Li, X. Gu, F. Yang, N. Zhang, Y. Wang, H. Liu, W. Zhou, and S. Xie, "High-performance and compact-designed flexible thermoelectric modules enabled by a reticulate carbon nanotube architecture," *Nat. Commun.*, vol. 8, no. 1, pp. 1–9, 2017.
- [196] S. Horike, T. Fukushima, T. Saito, T. Kuchimura, Y. Koshiba, M. Morimoto, and K. Ishida, "Highly stable n-type thermoelectric materials fabricated: Via electron doping into inkjet-printed carbon nanotubes using oxygen-abundant simple polymers," *Mol. Syst. Des. Eng.*, vol. 2, no. 5, pp. 616–623, 2017.

- [197] C. J. An, Y. H. Kang, H. Song, Y. Jeong, and S. Y. Cho, "High-performance flexible thermoelectric generator by control of electronic structure of directly spun carbon nanotube webs with various molecular dopants," *J. Mater. Chem. A*, vol. 5, no. 30, pp. 15631–15639, 2017.
- [198] J. Chen, B. Liu, X. Gao, and D. Xu, "A review of the interfacial characteristics of polymer nanocomposites containing carbon nanotubes," *RSC Adv.*, vol. 8, no. 49, pp. 28048–28085, 2018.
- [199] M. El Rhazi, S. Majid, M. Elbasri, F. E. Salih, L. Oularbi, and K. Lafdi, "Recent progress in nanocomposites based on conducting polymer: application as electrochemical sensors," *Int. Nano Lett.*, vol. 8, no. 2, pp. 79–99, 2018.
- [200] C. Vasile, "Polymeric Nanocomposites and Nanocoatings for Food Packaging: A Review," *Mater.*, vol. 11, no. 10, pp. 1834, 2018.
- [201] K. Müller, E. Bugnicourt, M. Latorre, M. Jorda, Y. E. Sanz, J. M. Lagaron, O. Miesbauer, A. Bianchin, S. Hankin, U. Bölz, G. Pérez, M. Jesdinszki, M. Lindner, Z. Scheuerer, S. Castelló and M. Schmid, "Review on the processing and properties of polymer nanocomposites and nanocoatings and their applications in the packaging, automotive and solar energy fields," *Nanomater.*, vol. 7, no. 4. MDPI AG, 2017.
- [202] C. Blattmann and S. Pratsinis, "Single-step fabrication of polymer nanocomposite films," *Mater.*, vol. 11, no. 7, pp. 1177, 2018.
- [203] D. S. Montgomery, C. A. Hewitt, R. Barbalace, T. Jones, and D. L. Carroll, "Spray doping method to create a low-profile high-density carbon nanotube thermoelectric generator," *Carbon*, vol. 96, pp. 778–781, 2016.
- [204] X. Ye, P. Zhao, S. Zhang, Y. Zhang, Q. Wang, C. Shan, L. Wojtas, H. Guo, H. Chen, and X. Shi "Facilitating gold redox catalysis with electrochemistry: An efficient chemical-oxidant-free approach," *Angew. Chem. Int. Ed.*, vol. 58, no. 48, pp. 17226–17230, 2019.
- [205] C. J. An, Y. H. Kang, A. Y. Lee, K. S. Jang, Y. Jeong, and S. Y. Cho, "Foldable thermoelectric materials: Improvement of the thermoelectric performance of directly spun CNT webs by individual control of electrical and thermal conductivity," *ACS Appl. Mater. Interfaces*, vol. 8, no. 34, pp. 22142–22150, 2016.
- [206] C. Li, F. Jiang, C. Liu, W. Wang, X. Li, T. Wang, and J. Xu, "A simple thermoelectric device based on inorganic/organic composite thin film for energy harvesting," *Chem. Eng. J.*, vol. 320, pp. 201–210, 2017.
- [207] Q. Meng, Q. Jiang, K. Cai, and L. Chen, "Preparation and thermoelectric properties of PEDOT:PSS coated Te nanorod/PEDOT:PSS composite films," *Org. Electron.*, vol. 64, pp. 79–85, 2019.
- [208] Q. Meng, K. Cai, Y. Du, and L. Chen, "Preparation and thermoelectric properties of SWCNT/PEDOT:PSS coated tellurium nanorod composite films," *J. Alloys Compd.*, vol. 778, pp. 163–169, 2019.
- [209] E. J. Bae, Y. H. Kang, K. S. Jang, C. Lee, and S. Y. Cho, "Solution synthesis of telluride-based nanobarbell structures coated with PEDOT:PSS for spray-printed thermoelectric generators," *Nanoscale*, vol. 8, no. 21, pp. 10885–10890, 2016.
- [210] X. Hu, K. Zhang, J. Zhang, S. Wang, and Y. Qiu, "Thermoelectric properties of conducting polymer nanowire-tellurium nanowire composites," *ACS Appl. Energy Mater.*, vol. 1, no. 9, pp. 4883–4890,

2018.

- [211] Y. Wang, C. Yu, M. Sheng, S. Song, and Y. Deng, "Individual adjustment of electrical conductivity and thermopower enabled by multiple interfaces in polyaniline-based ternary hybrid nanomaterials for high thermoelectric performances," *Adv. Mater. Interfaces*, vol. 5, no. 10, pp. 1701168, 2018.
- [212] Y. Du, X. Liu, J. Xu, and S. Z. Shen, "Flexible Bi-Te-based alloy nanosheet/PEDOT:PSS thermoelectric power generators," *Mater. Chem. Front.*, vol. 3, no. 7, pp. 1328–1334, 2019.
- [213] H. Ju and J. Kim, "Fabrication of conductive polymer/inorganic nanoparticles composite films: PEDOT:PSS with exfoliated tin selenide nanosheets for polymer-based thermoelectric devices," *Chem. Eng. J.*, vol. 297, pp. 66–73, 2016.
- [214] L. Xia, L. Congcong, W. Tongzhou, W. Wenfang, W. Xiaodong, J. Qinglin, J. Fengxing, X. Jingkun, "Preparation of 2D MoSe₂/PEDOT:PSS composite and its thermoelectric properties," *Mater. Res. Express*, vol. 4, no. 11, pp. 116410, 2017.
- [215] X. Wang, F. Meng, Q. Jiang, W. Zhou, F. Jiang, T. Wang, X. Li, S. Li, Y. Lin, and J. Xu, "Simple layer-by-layer assembly method for simultaneously enhanced electrical conductivity and thermopower of PEDOT:PSS/ce-MoS₂ heterostructure films," *ACS Appl. Energy Mater.*, vol. 1, no. 7, pp. 3123–3133, 2018.
- [216] N. Saxena, M. Čorić, A. Greppmair, J. Wernecke, M. Pflüger, M. Krumrey, M. S. Brandt, E. M. Herzig, and P. Müller-Buschbaum "Morphology-function relationship of thermoelectric nanocomposite films from PEDOT:PSS with silicon nanoparticles," *Adv. Electron. Mater.*, vol. 3, no. 8, pp. 1700181, 2017.
- [217] Z. hao Zheng, J. ting Luo, F. Li, G. xing Liang, and P. Fan, "Enhanced thermoelectric performance of P-type Sb₂Te₃ thin films through organic-inorganic hybridization on flexible substrate," *Curr. Appl. Phys.*, vol. 19, no. 4, pp. 470–474, 2019.
- [218] C. Li, X. Qin, Y. Li, D. Li, J. Zhang, H. Guo, H. Xin, and C. Song, "Simultaneous increase in conductivity and phonon scattering in a graphene nanosheets/(Bi₂Te₃)_{0.2}(Sb₂Te₃)_{0.8} thermoelectric nanocomposite," *J. Alloys Compd.*, vol. 661, pp. 389–395, 2016.
- [219] Y. Zhang, X. Jia, H. Sun, B. Sun, B. Liu, H. Liu, L. Kong, and H. Ma, "Enhanced thermoelectric performance of nanostructured CNTs/BiSbTe bulk composite from rapid pressure-quenching induced multi-scale microstructure," *J. Materiomics*, vol. 2, no. 4, pp. 316–323, 2016.
- [220] G. Goo, G. Anoop, S. Unithrattil, W. S. Kim, H. J. Lee, H. B. Kim, M. H. Jung, J. Park, H. C. Ko, and J. Y. Jo, "Proton-irradiation effects on the thermoelectric properties of flexible Bi₂Te₃ /PEDOT:PSS composite films," *Adv. Electron. Mater.*, vol. 5, no. 4, pp. 1800786, 2019.
- [221] J. Lei, D. Zhang, W. Guan, Z. Ma, Z. Cheng, C. Wang, and Y. Wang, "Enhancement of thermoelectric figure of merit by the insertion of multi-walled carbon nanotubes in α -MgAgSb," *Appl. Phys. Lett.*, vol. 113, no. 8, pp. 083901, 2018.
- [222] Y. Nonoguchi, M. Nakano, T. Murayama, H. Hagino, S. Hama, K. Miyazaki, R. Matsubara, M. Nakamura, T. Kawai, "Simple salt-coordinated n-type nanocarbon materials stable in air," *Adv. Funct. Mater.*, vol. 26, no. 18, pp. 3021–3028, 2016.
- [223] E. W. Zaia, M. P. Gordon, V. Niemann, J. Choi, R. Chatterjee, C. H. Hsu, J. Yano, B. Russ, A. Sahu, J.

- J. Urban, "Molecular level insight into enhanced n-type transport in solution-printed hybrid thermoelectrics," *Adv. Energy Mater.*, vol. 9, no. 13, pp. 1803469, 2019.
- [224] Y. Chen, M. He, B. Liu, G. C. Bazan, J. Zhou, and Z. Liang, "Bendable n-type metallic nanocomposites with large thermoelectric power factor," *Adv. Mater.*, vol. 29, no. 4, pp. 1604752, 2017.
- [225] J. Luo, G. Cerretti, B. Krause, L. Zhang, Thomas. Otto, W. Jenschke, Mathias. Ullrich, W. Tremel, B. Voit, and P. Pötschke, "Polypropylene-based melt mixed composites with singlewalled carbon nanotubes for thermoelectric applications: Switching from p-type to n-type by the addition of polyethylene glycol," *Polym.*, vol. 108, pp. 513–520, 2017.
- [226] G. Wu, Z. G. Zhang, Y. Li, C. Gao, X. Wang, and G. Chen, "Exploring high-performance n-type thermoelectric composites using amino-substituted rylene dimides and Ccarbon nanotubes," *ACS Nano*, vol. 11, no. 6, pp. 5746–5752, 2017.
- [227] C. Gao, Y. Liu, Y. Gao, Y. Zhou, X. Zhou, X. Yin, C. Pan, C. Yang, H. Wang, G. Chen, and L. Wang, "High-performance n-type thermoelectric composites of acridones with tethered tertiary amines and carbon nanotubes," *J. Mater. Chem. A*, vol. 6, no. 41, pp. 20161–20169, 2018.
- [228] N. Jaziri, A. Boughamoura, J. Müller, B. Mezghani, F. Tounsi, and M. Ismail, "A comprehensive review of thermoelectric generators: Technologies and common applications," *Energy Rep.*, vol. 6, pp. 264–287, 2020.
- [229] K. Li, Q. He, J. Wang, Z. Zhou, and X. Li, "Wearable energy harvesters generating electricity from low-frequency human limb movement," *Microsyst. Nanoeng.*, vol. 4, no. 1, 2018.
- [230] N. Sezer, and M. Koç, "A comprehensive review on the state-of-the-art of piezoelectric energy harvesting," *Nano Energy*, vol. 80, pp. 105567, 2021.
- [231] P. Maharjan, T. Bhatta, M. Salauddin Rasel, M. Salauddin, M. Toyabur Rahman, and J. Y. Park, "High-performance cycloid inspired wearable electromagnetic energy harvester for scavenging human motion energy," *Appl. Energy*, vol. 256, pp. 113987, 2019.
- [232] A. Nozariasbmarz, H. Collins, K. Dsouza, M. H. Polash, M. Hosseini, M. Hyland. J. Liu, A. Malhotra, F. M. Ortiz, F. Mohaddes, V. P. Ramesh, Y. Sargolzaeiaval, N. Snouwaert, M. C. Özturk, and Daryoosh. Vashae, "Review of wearable thermoelectric energy harvesting: From body temperature to electronic systems," *Appl. Energy*, vol. 258, pp. 114069, 2020.
- [233] A. Sultana, M. M. Alam, T. R. Middy, and D. Mandal, "A pyroelectric generator as a self-powered temperature sensor for sustainable thermal energy harvesting from waste heat and human body heat," *Appl. Energy*, vol. 221, pp. 299–307, 2018.
- [234] A. Zebda, J. P. Alcaraz, P. Vadgama, S. Shleev, S. D. Minteer, F. Boucher, P. Cinquin, D. K. Martin, "Challenges for successful implantation of biofuel cells," *Bioelectrochem.*, vol. 124, pp. 57–72, 2018.
- [235] S. Wang, H. Tai, B. Liu, Z. Duan, Z. Yuan, H. Pan, Y. Su, G. Xie, X. Du, Y. Jiang, "A facile respiration-driven triboelectric nanogenerator for multifunctional respiratory monitoring," *Nano Energy*, vol. 58, pp. 312–321, 2019.
- [236] J. Li, Y. Long, F. Yang, and X. Wang, "Respiration-driven triboelectric nanogenerators for biomedical applications," *EcoMat*, vol. 2, no. 3, 2020.

- [237] A. R. M. Siddique, S. Mahmud, and B. Van Heyst, "A review of the state of the science on wearable thermoelectric power generators (TEGs) and their existing challenges," *Renewable Sustainable Energy Rev.*, vol. 73, pp. 730–744, 2017.
- [238] M. Thielen, L. Sigrist, M. Magno, C. Hierold, and L. Benini, "Human body heat for powering wearable devices: From thermal energy to application," *Energy Convers. Manage.*, vol. 131, pp. 44–54, 2017.
- [239] K. Pietrzyk, J. Soares, B. Ohara, and H. Lee, "Power generation modeling for a wearable thermoelectric energy harvester with practical limitations," *Appl. Energy*, vol. 183, pp. 218–228, 2016.
- [240] A. Fabián-Mijangos, G. Min, and J. Alvarez-Quintana, "Enhanced performance thermoelectric module having asymmetrical legs," *Energy Convers. Manage.*, vol. 148, pp. 1372–1381, 2017.
- [241] A. Montecucco, J. Siviter, and A. R. Knox, "Constant heat characterisation and geometrical optimisation of thermoelectric generators," *Appl. Energy*, vol. 149, pp. 248–258, 2015.
- [242] A. Myers, R. Hodges, and J. S. Jur, "Human and environmental analysis of wearable thermal energy harvesting," *Energy Convers. Manage.*, vol. 143, pp. 218–226, 2017.
- [243] M. Hyland, H. Hunter, J. Liu, E. Veety, and D. Vashaee, "Wearable thermoelectric generators for human body heat harvesting," *Appl. Energy*, vol. 182, pp. 518–524, 2016.
- [244] S. Qing, A. Rezanian, L. A. Rosendahl, A. A. Enkeshafi, and X. Gou, "Characteristics and parametric analysis of a novel flexible ink-based thermoelectric generator for human body sensor," *Energy Convers. Manage.*, vol. 156, pp. 655–665, 2018.
- [245] S. E. Jo, M. S. Kim, M. S. Kim, H. L. Kim, and Y. B. Kim, "Human body heat energy harvesting using flexible thermoelectric generator for autonomous microsystems." in *16th International Conference on Miniaturized Systems for Chemistry and Life Sciences, Japan*, pp. 839–841, 2012.
- [246] C. Navone, M. Soulier, M. Plissonnier, and A. L. Seiler, "Development of (Bi,Sb) 2(Te,Se) 3-based thermoelectric modules by a screen-printing process," *J. Electron. Mater.*, vol. 39, no. 9, pp. 1755–1759, 2010.
- [247] J. Yuan and R. Zhu, "A fully self-powered wearable monitoring system with systematically optimized flexible thermoelectric generator," *Appl. Energy*, vol. 271, 2020.
- [248] Y. Eom, D. Wijethunge, H. Park, S. H. Park, and W. Kim, "Flexible thermoelectric power generation system based on rigid inorganic bulk materials," *Appl. Energy*, vol. 206, pp. 649–656, 2017.
- [249] Z. Lu, H. Zhang, C. Mao, and C. M. Li, "Silk fabric-based wearable thermoelectric generator for energy harvesting from the human body," *Appl. Energy*, vol. 164, pp. 57–63, 2016.
- [250] L. Francioso, C. De Pascali, V. Sglavo, A. Grazioli, M. Masieri, and P. Siciliano, "Modelling, fabrication and experimental testing of an heat sink free wearable thermoelectric generator," *Energy Convers. Manage.*, vol. 145, pp. 204–213, 2017.
- [251] K. K. Jung, Y. Jung, C. J. Choi, J. M. Lee, and J. S. Ko, "Flexible thermoelectric generator with polydimethyl siloxane in thermoelectric material and substrate," *Curr. Appl. Phys.*, vol. 16, no. 10, pp. 1442–1448, 2016.
- [252] Y. Shi, Y. Wang, D. Mei, B. Feng, and Z. Chen, "Design and fabrication of wearable thermoelectric

- generator device for heat harvesting," *IEEE Rob. Autom. Lett.*, vol. 3, no. 1, pp. 373–378, 2018.
- [253] Q. H. Zhang, X. Y. Huang, S. Q. Bai, X. Shi, C. Uher, and L. D. Chen, "Thermoelectric devices for power generation: Recent progress and future challenges," *Adv. Eng. Mater.*, vol. 18, no. 2, pp. 194–213, 2016.
- [254] Y. Zheng, Q. Zhang, W. Jin, Yuanyuan Jing, X. Chen, Xue Han, Q. Bao, Y. Liu, X. Wang, S. Wang, Y. Qiu, C. A. Di, and K. Zhang, "Carbon nanotube yarn based thermoelectric textiles for harvesting thermal energy and powering electronics," *J. Mater. Chem. A*, vol. 8, no. 6, pp. 2984–2994, 2020.
- [255] Z. Soleimani, S. Zoras, B. Ceranic, Y. Cui, and S. Shahzad, "A comprehensive review on the output voltage/power of wearable thermoelectric generators concerning their geometry and thermoelectric materials," *Nano Energy*, vol. 89 (Part A), pp. 106325, 2021.
- [256] M. Orrill and S. LeBlanc, "Printed thermoelectric materials and devices: Fabrication techniques, advantages, and challenges," *J. Appl. Polym. Sci.*, vol. 134, no. 3, 2017.
- [257] Y. Liu, Y. Du, Q. Meng, J. Xu, and S. Z. Shen, "Effects of preparation methods on the thermoelectric performance of SWCNT/Bi₂Te₃ bulk composites," *Mater.*, vol. 13, no. 11, 2020.
- [258] C. S. Kim, G. S. Lee, H. Choi, Y. J. Kim, H. M. Yang, S. H. Lim, S. G. Lee, and B. J. Cho, "Structural design of a flexible thermoelectric power generator for wearable applications," *Appl. Energy*, vol. 214, pp. 131–138, 2018.
- [259] F. Suarez, D. P. Parekh, C. Ladd, D. Vashae, M. D. Dickey, and M. C. Öztürk, "Flexible thermoelectric generator using bulk legs and liquid metal interconnects for wearable electronics," *Appl. Energy*, vol. 202, pp. 736–745, 2017.
- [260] Y. Wang, Y. Shi, D. Mei, and Z. Chen, "Wearable thermoelectric generator to harvest body heat for powering a miniaturized accelerometer," *Appl. Energy*, vol. 215, pp. 690–698, 2018.
- [261] T. Park, H. Lim, J. U. Hwang, J. Na, H. Lee, and E. Kim, "Roll type conducting polymer legs for rigid-flexible thermoelectric generator," *APL Mater.*, vol. 5, no. 7, pp. 074106, 2017.
- [262] S. J. Jung, J. Shin, S. S. Lim, B. Kwon, S. H. Baek, S. K. Kim, H. H. Park, and J. S. Kim, "Porous organic filler for high efficiency of flexible thermoelectric generator," *Nano Energy*, vol. 81, pp. 105604, 2021.
- [263] S. Hong, Y. Gu, J. K. Seo, J. Wang, P. Liu, Y. S. Meng, S. Xu, and R. Chen, "Wearable thermoelectrics for personalized thermoregulation," *Sci. Adv.*, vol. 5, no. 5, 2019.
- [264] H. Liu, Y. Wang, D. Mei, Y. Shi, and Z. Chen, "Design of a wearable thermoelectric generator for harvesting human body energy," *Wearable Sens. Rob.*, vol. 399, pp. 55–66, 2017.
- [265] A. R. M. Siddique, R. Rabari, S. Mahmud, and B. Van Heyst, "Thermal energy harvesting from the human body using flexible thermoelectric generator (FTEG) fabricated by a dispenser printing technique," *Energy*, vol. 115, pp. 1081–1091, 2016.
- [266] A. Nozariasbmarz, R. A. Kishore, B. Poudel, U. Saparamadu, W. Li, R. Cruz, and S. Priya "High power density body heat energy harvesting," *ACS Appl. Mater. Interfaces*, vol. 11, no. 43, pp. 40107–40113, 2019.
- [267] K. T. Settaluri, H. Lo, and R. J. Ram, "Thin thermoelectric generator system for body energy harvesting," *J. Electron. Mater.*, vol. 41, no. 6, pp. 984–988, 2012.

- [268] S. H. Jeong, F. J. Cruz, S. Chen, L. Gravier, J. Liu, Z. Wu, K. Hjort, S. L. Zhang, and Z. B. Zhang, “stretchable thermoelectric generators metallized with liquid alloy,” *ACS Appl. Mater. Interfaces*, vol. 9, no. 18, pp. 15791–15797, 2017.
- [269] Y. Sargolzaeiaval, V. P. Ramesh, T. V. Neumann, V. Misra, D. Vashaee, M. D. Dickey, M. C. Öztürk, “Flexible thermoelectric generators for body heat harvesting – enhanced device performance using high thermal conductivity elastomer encapsulation on liquid metal interconnects,” *Appl. Energy*, vol. 262, pp. 114370, 2020.
- [270] B. Lee, H. Cho, K. T. Park, J. S. Kim, M. Park, H. Kim, Y. Hong and S. Chung “High-performance compliant thermoelectric generators with magnetically self-assembled soft heat conductors for self-powered wearable electronics,” *Nat. Commun.*, vol. 11, no. 1, 2020.
- [271] G. Lee, C. S. Kim, S. Kim, Y. J. Kim, H. Choi, and B. J. Cho, “Flexible heatsink based on a phase-change material for a wearable thermoelectric generator,” *Energy*, vol. 179, pp. 12–18, 2019.
- [272] Y. Shi, Y. Wang, D. Mei, and Z. Chen, “Wearable thermoelectric generator with copper foam as the heat sink for body heat harvesting,” *IEEE Access*, vol. 6, pp. 43602–43611, 2018.
- [273] H. Park, D. Lee, D. Kim, H. Cho, Y. Eom, J. Hwang, H. Kim, J. Kim, S. Han and W. Kim, “High power output from body heat harvesting based on flexible thermoelectric system with low thermal contact resistance,” *J. Phys. D: Appl. Phys.*, vol. 51, no. 36, pp. 365501, 2018.
- [274] D. Lee, H. Park, G. Park, J. Kim, H. Kim, H. Cho, S. Han, and W. Kim, “Liquid-metal-electrode-based compact, flexible, and high-power thermoelectric device,” *Energy*, vol. 188, pp. 116019, 2019.
- [275] H. Park, Y. Eom, D. Lee, J. Kim, H. Kim, G. Park, and W. Kim, “High power output based on watch-strap-shaped body heat harvester using bulk thermoelectric materials,” *Energy*, vol. 187, pp. 115935, 2019.
- [276] C. S. Kim, H. M. Yang, J. Lee, G. S. Lee, H. Choi, Y. J. Kim, S. H. Lim, S. H. Cho, and B. J. Cho, “Self-powered wearable electrocardiography using a wearable thermoelectric power generator,” *ACS Energy Lett.*, vol. 3, no. 3, pp. 501–507, 2018.
- [277] M. S. Hossain, T. Li, Y. Yu, J. Yong, J. H. Bahk, and E. Skafidas, “Recent advances in printable thermoelectric devices: Materials, printing techniques, and applications,” *RSC Adv.*, vol. 10, no. 14, pp. 8421–8434, 2020.
- [278] T. Varghese, C. Hollar, J. Richardson, N. Kempf, C. Han, P. Gamarachchi, D. Estrada, R. J. Mehta, and Y. Zhang, “High-performance and flexible thermoelectric films by screen printing solution-processed nanoplate crystals,” *Sci. Rep.*, vol. 6, no. 1, pp. 1–6, 2016.
- [279] D. L. Wen, H. T. Deng, X. Liu, G. K. Li, X. R. Zhang, X. S. Zhang, “Wearable multi-sensing double-chain thermoelectric generator,” *Microsys. Nanoeng.*, vol. 6, no. 68, 2020.
- [280] V. Karthikeyan, J. U. Surjadi, J. C.K. Wong, V. Kannan, K. H. Lam, X. Chen, Y. Lu, V. A. L. Roy, “Wearable and flexible thin film thermoelectric module for multi-scale energy harvesting,” *J. Power Sources*, vol. 455, 2020.
- [281] W. Ren, Y. Sun, D. Zhao, A. Aili, S. Zhang, C. Shi, J. Zhang, H. Geng, J. Zhang, L. Zhang, J. Xiao and R. Yang, “High-performance wearable thermoelectric generator with self-healing, recycling, and Lego-like reconfiguring capabilities,” *Sci. Adv.*, vol. 7, no. 7, pp. eabe0586, 2021.

- [282] C. Lamuta, A. Cupolillo, A. Politano, Z. S. Aliev, M. B. Babanly, E. V. Chulkov, L. Pagnotta, "Indentation fracture toughness of single-crystal Bi₂Te₃ topological insulators," *Nano Res.*, vol. 9, no. 4, pp. 1032–1042, 2016.
- [283] Z. Zhang, J. Qiu, and S. Wang, "Roll-to-roll printing of flexible thin-film organic thermoelectric devices," *Manuf. Lett.*, vol. 8, pp. 6–10, 2016.
- [284] Z. Zhang, B. Wang, J. Qiu, and S. Wang, "Roll-to-roll printing of spatial wearable thermoelectrics," *Manuf. Lett.*, vol. 21, pp. 28–34, 2019.
- [285] K. T. Park, J. Choi, B. Lee, Y. Ko, K. Jo, Y. M. Lee, J. A. Lim, C. R. Park, and He. Kim, "High-performance thermoelectric bracelet based on carbon nanotube ink printed directly onto a flexible cable," *J. Mater. Chem. A*, vol. 6, no. 40, pp. 19727–19734, 2018.
- [286] W. Zeng, X. M. Tao, S. Lin, C. Lee, D. Shi, K. H. Lam, B. Huang, Q. Wang, and Y. Zhao, "Defect-engineered reduced graphene oxide sheets with high electric conductivity and controlled thermal conductivity for soft and flexible wearable thermoelectric generators," *Nano Energy*, vol. 54, pp. 163–174, 2018.
- [287] E. Jin Bae, Y. Hun Kang, K. S. Jang, and S. Yun Cho, "Enhancement of thermoelectric properties of PEDOT:PSS and tellurium-PEDOT:PSS hybrid composites by simple chemical treatment," *Sci. Rep.*, vol. 6, no. 1, pp. 1–10, 2016.
- [288] E. J. Bae, Y. H. Kang, C. Lee, and S. Y. Cho, "Engineered nanocarbon mixing for enhancing the thermoelectric properties of a telluride-PEDOT:PSS nanocomposite," *J. Mater. Chem. A*, vol. 5, no. 34, pp. 17867–17873, 2017.
- [289] Y. Lu, Y. Ding, Y. Qiu, K. Cai, Q. Yao, H. Song, L. Tong, J. He, and L. Chen, "Good Performance and Flexible PEDOT:PSS/Cu₂Se Nanowire Thermoelectric Composite Films," *ACS Appl. Mater. Interfaces*, vol. 11, no. 13, pp. 12819–12829, 2019.
- [290] Y. Lu, Y. Qiu, K. Cai, X. Li, M. Gao, C. Jiang, J. He, "Ultrahigh performance PEDOT/Ag₂Se/CuAgSe composite film for wearable thermoelectric power generators," *Mater. Today Phys.*, vol. 14, pp. 100223, 2020.
- [291] X. Zhao, C. Zhao, Y. Jiang, X. Ji, F. Kong, T. Lin, H. Shao, W. Han, "Flexible cellulose nanofiber/Bi₂Te₃ composite film for wearable thermoelectric devices," *J. Power Sources*, vol. 479, pp. 229044, 2020.
- [292] B. Chen, M. Kruse, B. Xu, R. Tutika, W. Zheng, M. D. Bartlett, Y. Wu, and J. C. Claussen, "Flexible thermoelectric generators with inkjet-printed bismuth telluride nanowires and liquid metal contacts," *Nanoscale*, vol. 11, no. 12, pp. 5222–5230, 2019.
- [293] Y. Guo, C. Dun, J. Xu, P. Li, W. Huang, J. Mu, C. Hou, C. A. Hewitt, Q. Zhang, Y. Li, D. L. Carroll, and H. Wang, "Wearable Thermoelectric Devices Based on Au-Decorated Two-Dimensional MoS₂," *ACS Appl. Mater. Interfaces*, vol. 10, no. 39, pp. 33316–33321, 2018.
- [294] Z. Cao, E. Koukharenko, M. J. Tudor, R. N. Torah, and S. P. Beeby, "Flexible screen printed thermoelectric generator with enhanced processes and materials," *Sens. Actuators, A*, vol. 238, pp. 196–206, 2016.
- [295] H. M. Elmoughni, A. K. Menon, R. M. W. Wolfe, and S. K. Yee, "A Textile-integrated polymer thermoelectric generator for body heat harvesting," *Adv. Mater. Technol.*, vol. 4, no. 7, pp. 1800708, 2019.

- [296] L. Liu, Y. Sun, W. Li, J. Zhang, X. Huang, Z. Chen, Y. Sun, C. Di, W. Xu and D. Zhu, "Flexible unipolar thermoelectric devices based on patterned poly[K: X(Ni-ethylenetetra-thiolate)] thin films," *Mater. Chem. Front.*, vol. 1, no. 10, pp. 2111–2116, 2017.
- [297] L. Stepien, A. Roch, S. Schlaier, I. Dani, A. Kiriy, F. Simon, M. V. Lukowicz and C. Leyens, "Investigation of the thermoelectric power factor of KOH-treated PEDOT:PSS dispersions for printing applications," *Energy Harvest. Syst.*, vol. 3, no. 1, 2015.
- [298] J. Choi, Y. Jung, C. Dun, K. T. Park, M. P. Gordon, K. Haas, P. Yuan, H. Kim, C. R. Park, and J. J. Urban, "High-performance, wearable thermoelectric generator based on a highly aligned carbon nanotube sheet," *ACS Appl. Energy Mater.*, vol. 3, no. 1, pp. 1199–1206, 2020.
- [299] J. Na, Y. Kim, T. Park, C. Park, and E. Kim, "Preparation of bismuth telluride films with high thermoelectric power factor," *ACS Appl. Mater. Interfaces*, vol. 8, no. 47, pp. 32392–32400, 2016.
- [300] B. Wu, Y. Guo, C. Hou, Q. Zhang, Y. Li, and H. Wang, "High-performance flexible thermoelectric devices based on all-inorganic hybrid films for harvesting low-grade heat," *Adv. Funct. Mater.*, vol. 29, no. 25, 2019.
- [301] X. Xu, Y. Zuo, S. Cai, X. Tao, Z. Zhang, X. Zhou, S. He, X. Fang, and H. Peng, "Three-dimensional helical inorganic thermoelectric generators and photodetectors for stretchable and wearable electronic devices," *J. Mater. Chem. C*, vol. 6, no. 18, pp. 4866–4872, 2018.
- [302] Y. Lu, X. Li, K. Cai, M. Gao, W. Zhao, J. He, and P. Wei, "Enhanced-performance PEDOT:PSS/Cu₂Se-based composite films for wearable thermoelectric power generators," *ACS Appl. Mater. Interfaces*, vol. 13, no. 1, pp. 631–638, 2021.
- [303] J. A. Lee, A. E. Aliev, J. S. Bykova, M. J. de Andrade, D. Kim, H. J. Sim, X. Lepró, A. A. Zakhidov, J. B. Lee, G. M. Spinks, S. Roth, S. J. Kim, and R. H. Baughman, "Woven-yarn thermoelectric textiles," *Adv. Mater.*, vol. 28, no. 25, pp. 5038–5044, 2016.
- [304] J. Zhang, T. Zhang, H. Zhang, Z. Wang, C. Li, Z. Wang, K. Li, X. Huang, M. Chen, Z. Chen, Z. Tian, H. Chen, L. D. Zhao, L. Wei, "Single-crystal SnSe thermoelectric fibers via laser-induced directional crystallization: From 1D fibers to multidimensional fabrics," *Adv. Mater.*, vol. 32, no. 36, p. 2002702, 2020.
- [305] Q. Wu and J. Hu, "A novel design for a wearable thermoelectric generator based on 3D fabric structure," *Smart Mater. Struct.*, vol. 26, no. 4, pp. 045037, 2017.
- [306] X. Lan, T. Wang, C. Liu, P. Liu, J. Xu, X. Liu, Y. Du, F. Jiang, "A high performance all-organic thermoelectric fiber generator towards promising wearable electron," *Compos. Sci. Technol.*, vol. 182, pp. 107767, 2019.
- [307] A. Lund, Y. Tian, S. Darabi, and C. Müller, "A polymer-based textile thermoelectric generator for wearable energy harvesting," *J. Power Sources*, vol. 480, p. 228836, 2020.
- [308] J. D. Ryan, A. Lund, A. I. Hofmann, R. Kroon, R. Sarabia-Riquelme, M. C. Weisenberger, and C. Müller "All-Organic Textile Thermoelectrics with Carbon-Nanotube-Coated n-Type Yarns," *ACS Appl. Energy Mater.*, vol. 1, no. 6, pp. 2934–2941, 2018.
- [309] T. Sun, B. Zhou, Q. Zheng, L. Wang, W. Jiang, and G. J. Snyder, "Stretchable fabric generates electric power from woven thermoelectric fibers," *Nat. Commun.*, vol. 11, no. 1, 2020.

- [310] H. Xu, Y. Guo, B. Wu, C. Hou, Q. Zhang, Y. Li, and H. Wang, "Highly integrable thermoelectric fiber," *ACS Appl. Mater. Interfaces*, vol. 12, no. 29, pp. 33297–33304, 2020.
- [311] J. Choi, Y. Jung, S. J. Yang, J. Y. Oh, J. Oh, K. Jo, J. G. Son, S. E. Moon, C. R. Park, and H. Kim, "Flexible and robust thermoelectric generators based on all-carbon nanotube yarn without metal electrodes," *ACS Nano*, vol. 11, no. 8, pp. 7608–7614, 2017.
- [312] J. Y. Kim, W. Lee, Y. H. Kang, S. Y. Cho, and K. S. Jang, "Wet-spinning and post-treatment of CNT/PEDOT:PSS composites for use in organic fiber-based thermoelectric generators," *Carbon N. Y.*, vol. 133, pp. 293–299, 2018.
- [313] Y. Lin J. Liu, X. Wang, J. Xu, P. Liu, G. Nie, C. Liu, F. Jiang, "An integral p-n connected all-graphene fiber boosting wearable thermoelectric energy harvesting," *Compos. Commun.*, vol. 16, pp. 79–83, 2019.
- [314] S. Qu, Y. Chen, W. Shi, M. Wang, Q. Yao, and L. Chen, "Cotton-based wearable poly(3-hexylthiophene) electronic device for thermoelectric application with cross-plane temperature gradient," *Thin Solid Films*, vol. 667, pp. 59–63, 2018.
- [315] M. Ito, T. Koizumi, H. Kojima, T. Saito, and M. Nakamura, "From materials to device design of a thermoelectric fabric for wearable energy harvesters," *J. Mater. Chem. A*, vol. 5, no. 24, pp. 12068–12072, 2017.
- [316] L. K. Allison and T. L. Andrew, "A wearable all-fabric thermoelectric generator," *Adv. Mater. Technol.*, vol. 4, no. 5, pp. 1800615, 2019.
- [317] N. Wen, Z. Fan, S. Yang, Y. Zhao, T. Cong, S. Xu, H. Zhang, J. Wang, H. Huang, C. Li, L. Pan, "Highly conductive, ultra-flexible and continuously processable PEDOT:PSS fibers with high thermoelectric properties for wearable energy harvesting," *Nano Energy*, vol. 78, p. 105361, 2020.
- [318] H. Hardianto, G. De Mey, B. Malengier, and L. Van Langenhove, "Textile-based thermoelectric generator fabricated from carbon fibers," *J. Ind. Text.*, p. 152808372091068, 2020.
- [319] A. Patyk, "Thermoelectric generators for efficiency improvement of power generation by motor generators - Environmental and economic perspectives," *Appl. Energy*, vol. 102, pp. 1448–1457, 2013.
- [320] Y. Kishita, M. Uwasu, H. Takeda, K. Hara, Y. Ohishi, and M. Kuroda, "Assessing the greenhouse gas emissions and cost of thermoelectric generators for passenger automobiles: A life cycle perspective," in *Proceedings of the ASME 2014 International Design Engineering Technical Conferences and Computers and Information in Engineering Conference, USA*, vol. 4, 2014.
- [321] Y. Kishita, Y. Ohishi, M. Uwasu, M. Kuroda, H. Takeda, and K. Hara, "Evaluating the life cycle CO2 emissions and costs of thermoelectric generators for passenger automobiles: A scenario analysis," *J. Clean. Prod.*, vol. 126, pp. 607–619, 2016.
- [322] Z. Soleimani, S. Zoras, B. Ceranic, S. Shahzad, and Y. Cui, "The cradle to gate life-cycle assessment of thermoelectric materials: A comparison of inorganic, organic and hybrid types," *Sustain. Energy Technol. Assessments*, vol. 44, p. 101073, 2021.
- [323] Getting Started with Granta EduPack – Granta Design. Available at: <https://www.grantadesign.com/teachingresources/getting-started-with-granta-edupack>. (Accessed August 5, 2021).

- [324] D. Xie, J. Xu, G. Liu, Z. Liu, Shao, X. Tan, J. Jiang, H. Jiang, "Synergistic optimization of thermoelectric performance in p-type Bi_{0.48}Sb_{1.52}Te₃/graphene composite," *Energies*, vol. 9, no. 4, p. 236, 2016.
- [325] N. H. Trung, N. Van Toan, and T. Ono, "Fabrication of π -type flexible thermoelectric generators using an electrochemical deposition method for thermal energy harvesting applications at room temperature," *J. Micromech. Microeng.*, vol. 27, no. 12, pp. 125006, 2017.
- [326] Y. Wang, Y. Shi, D. Mei, and Z. Chen, "Wearable thermoelectric generator for harvesting heat on the curved human wrist," *Appl. Energy*, vol. 205, pp. 710–719, 2017.
- [327] S. J. Kim, H. E. Lee, H. Choi, Y. Kim, J. H. We, J. S. Shin, K. J. Lee, and B. J. Cho, "High-performance flexible thermoelectric power generator using laser multiscanning lift-off process," *ACS Nano*, vol. 10, no. 12, pp. 10851–10857, 2016.
- [328] S. H. Jeong S. Chen, J. Huo, E. K. Gamstedt, J. Liu, S. L. Zhang, Z. B. Zhang, K. Hjort and Z. Wu, "Mechanically stretchable and electrically insulating thermal elastomer composite by liquid alloy droplet embedment," *Sci. Rep.*, vol. 5, no. 1, pp. 1–10, 2015.
- [329] Y. Shi, Y. Wang, D. Mei, and Z. Chen, "Numerical modeling of the performance of thermoelectric module with polydimethylsiloxane encapsulation," *Int. J. Energy Res.*, vol. 42, no. 3, pp. 1287–1297, 2018.
- [330] S. Lv, M. Liu, W. He, X. Li, W. Gong, and S. Shen, "Study of thermal insulation materials influence on the performance of thermoelectric generators by creating a significant effective temperature difference," *Energy Convers. Manage.*, vol. 207, pp. 112516, 2020.
- [331] Z. Soleimani, S. Zoras, B. Ceranic, S. Shahzad, and Y. Cui, "Optimization of a wearable thermoelectric generator encapsulated in polydimethylsiloxane (PDMS): A numerical modelling," in *2019 IEEE 2nd International Conference on Renewable Energy and Power Engineering (REPE)*, pp. 212–215, 2019.
- [332] GM250-71-14-16, European Thermodynamics Seebeck Effect Module, 2.9W, 1.1A, 5.3V, 30 x 30mm. Available at: <https://uk.rs-online.com/web/p/peltier-modules/6937078/>. (Accessed August 13, 2021).
- [333] K. Tappura, "A numerical study on the design trade-offs of a thin-film thermoelectric generator for large-area applications," *Renew. Energy*, vol. 120, pp. 78–87, 2018.
- [334] R. Gałek, "Two-dimensional numerical simulation of a thermoelectric cooler module," *Tech. Trans.*, vol. 115, no. 7, pp. 167–178, 2018.
- [335] A. Nozariasbmarz, F. Suarez, J. H. Dycus, M. J. Cabral, J. M. LeBeau, M. C. Öztürk, D. Vashaee, "Thermoelectric generators for wearable body heat harvesting: Material and device concurrent optimization," *Nano Energy*, vol. 67, pp. 104265, 2020.
- [336] Z. Soleimani, S. Zoras, Y. Cui, B. Ceranic, and S. Shahzad, "Design of heat sinks for wearable thermoelectric generators to power personal heating garments: A numerical study," in *IOP Conference Series: Earth and Environmental Science*, vol. 410, no. 1, pp. 012096, 2020.
- [337] PFM Module - Circuit Surgery. Available at: <https://www.electroschematics.com/pfm-module-circuit-surgery/>. (Accessed August 5, 2021).
- [338] Tecate Group - Ultracapacitor. Available at:

<https://www.tecategroup.com/products/ultracapacitors/ultracapacitor-FAQ.php> (Accessed July 17, 2021).

- [339] Z. Wang, B. Cao, W. Ji, and Y. Zhu, "Study on clothing insulation distribution between half-bodies and its effects on thermal comfort in cold environments," *Energy Build.*, vol. 211, pp. 109796, 2020.
- [340] A. Briga Sá, J. Boaventura-Cunha, J. C. Lanzinha, and A. Paiva, "An experimental analysis of the Trombe wall temperature fluctuations for high range climate conditions: Influence of ventilation openings and shading devices," *Energy Build.*, vol. 138, pp. 546–558, 2017.
- [341] A. Zuazua-Ros, C. Martín-Gómez, E. Ibañez-Puy, M. Vidaurre-Arbizu, and Y. Gelbstein, "Investigation of the thermoelectric potential for heating, cooling and ventilation in buildings: Characterization options and applications," *Renew. Energy*, vol. 131, pp. 229–239, 2019.
- [342] A. T. Baheta, K. K. Looi, A. N. Oumer, and K. Habib, "Thermoelectric air-conditioning system: building applications and enhancement techniques," *Int. J. Air-Conditioning Refrig.*, vol. 27, no. 2, 2019.
- [343] H. Liu, H. Fu, L. Sun, C. Lee, and E. M. Yeatman, "Hybrid energy harvesting technology: From materials, structural design, system integration to applications," *Renewable Sustainable Energy Rev.*, vol. 137, pp. 110473, 2021.
- [344] Y. Wu, S. Kuang, H. Li, H. Wang, R. Yang, Y. Zhai, G. Zhu, and Z. L. Wang "Triboelectric–thermoelectric hybrid nanogenerator for harvesting energy from ambient environments," *Adv. Mater. Technol.*, vol. 3, no. 11, 2018.
- [345] X. Q. Wang, C. F. Tan, K. H. Chan, X. Lu, L. Zhu, S. W. Kim and G. W. Ho, "In-built thermo-mechanical cooperative feedback mechanism for self-propelled multimodal locomotion and electricity generation," *Nat. Commun.*, vol. 9, no. 1, 2018.
- [346] D. L. Wen, X. Liu, J. F. Bao, G. K. Li, T. Feng, F. Zhang, D. Liu, and X. S. Zhang, "Flexible hybrid photo-thermoelectric generator based on single thermoelectric effect for simultaneously harvesting thermal and radiation energies," *ACS Appl. Mater. Interfaces*, vol. 13, no. 18, pp. 21401–21410, 2021.

Appendices

Appendix A: First Questionnaire (Background Questions)

Date:

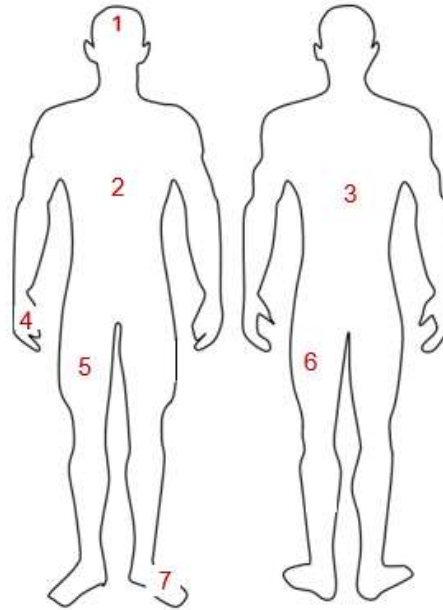
Name:

Age:

Gender:

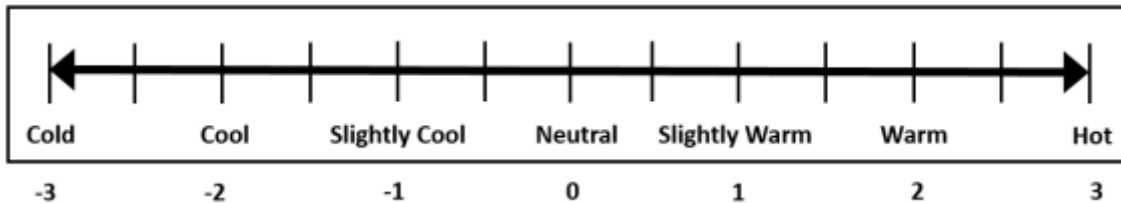
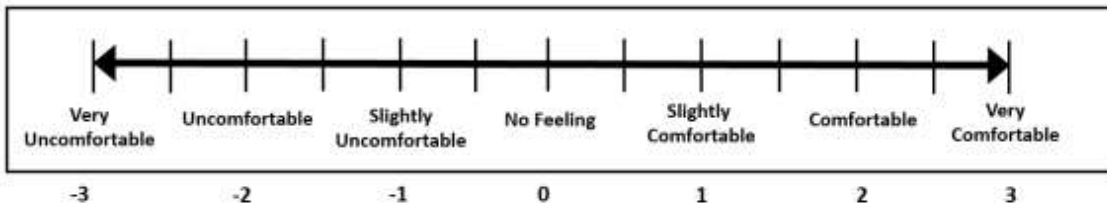
Ethnicity:

- 1) Forehead
- 2) Torso Front
- 3) Torso Back
- 4) Hands
- 5) Thighs Front
- 6) Thighs Back
- 7) Feet

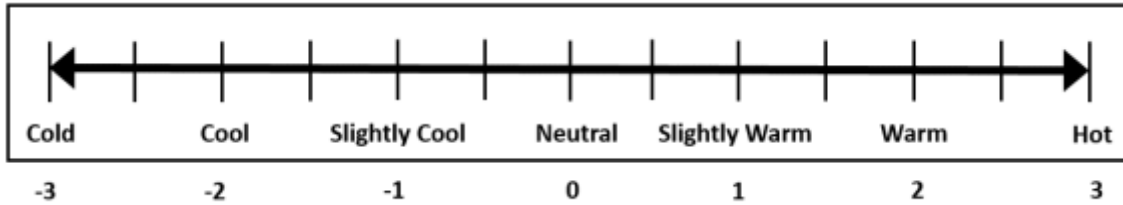
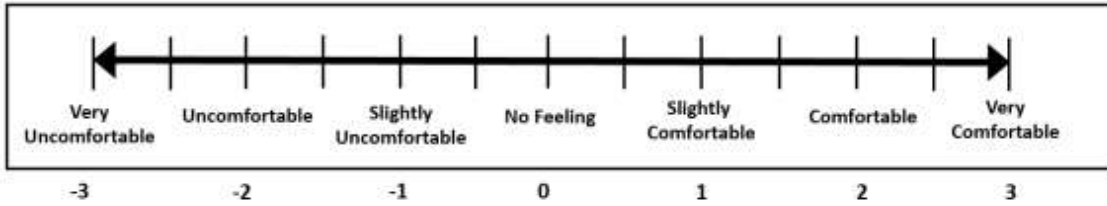


1) Rate your thermal sensation and thermal comfort at each parts:

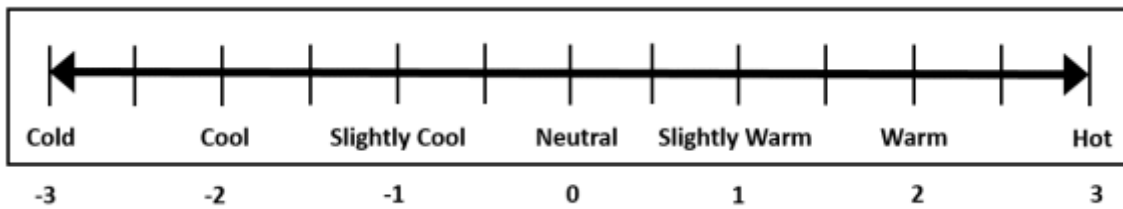
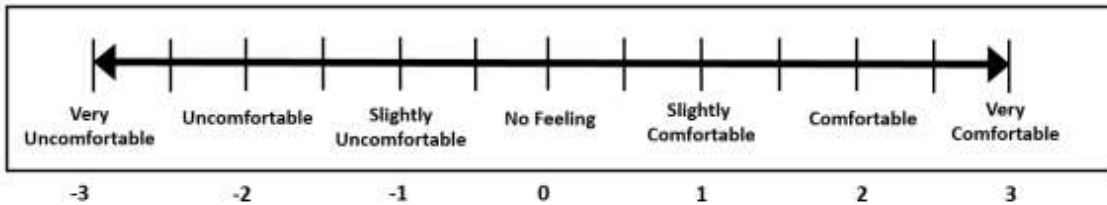
a) **Forehead**



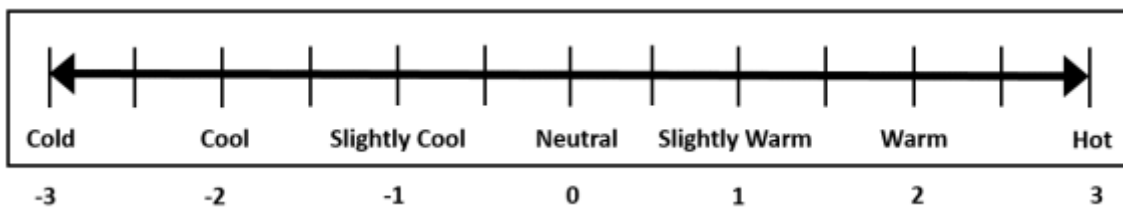
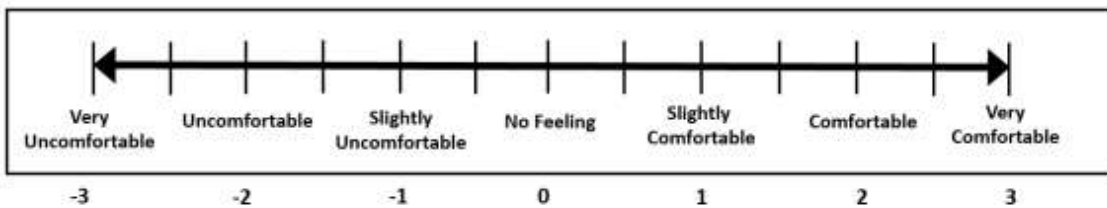
b) **Torso Front**



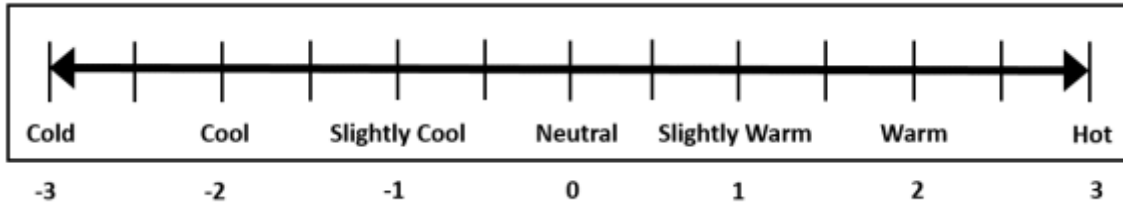
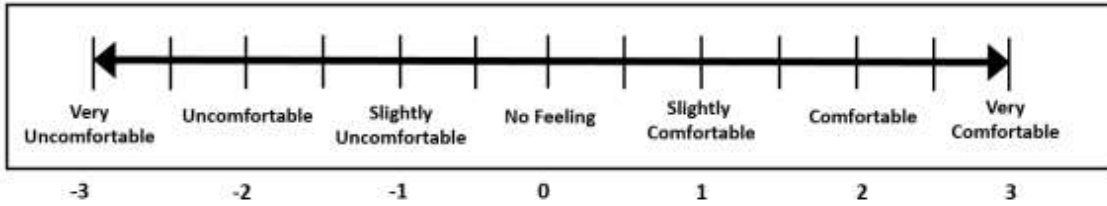
c) Torso Back



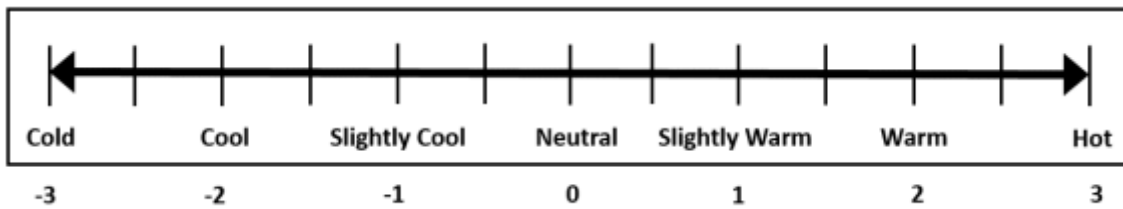
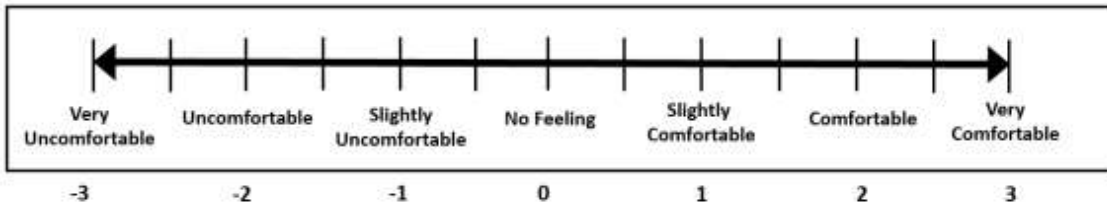
d) Hand



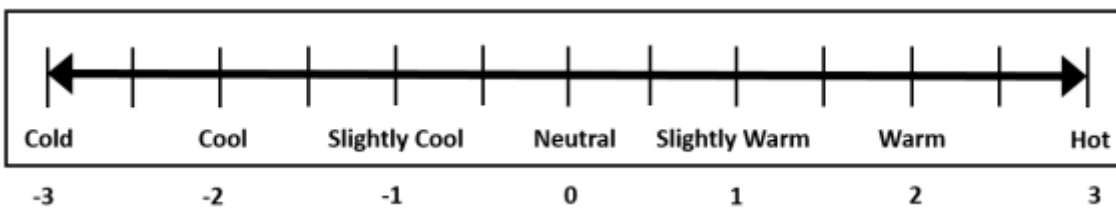
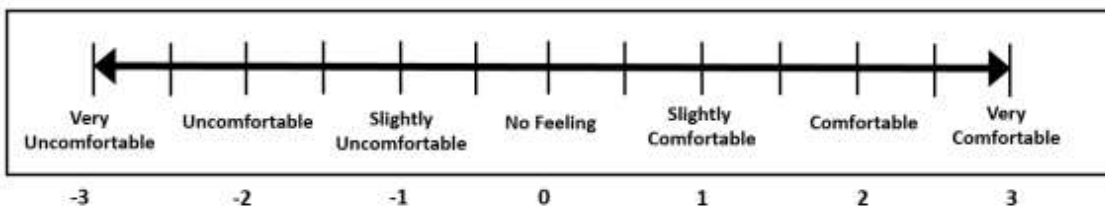
e) Thigh Front



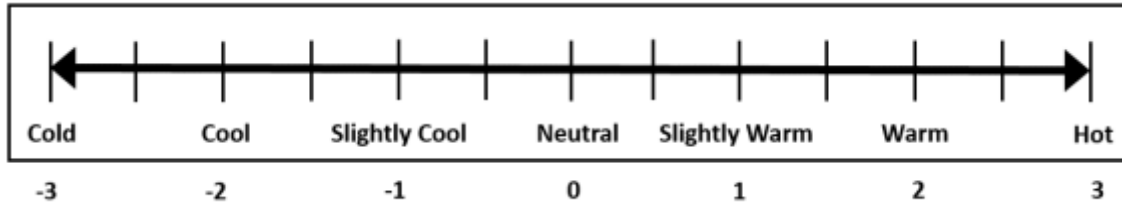
f) Thigh Back



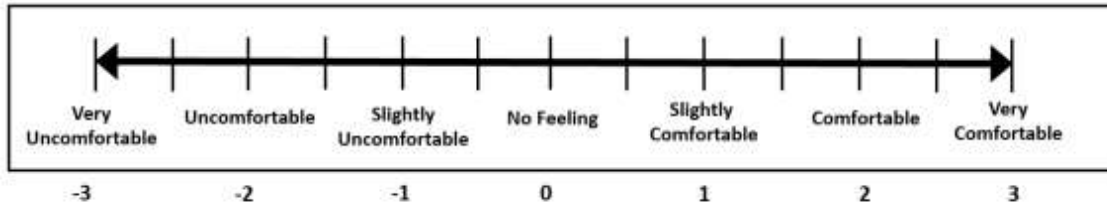
g) Feet



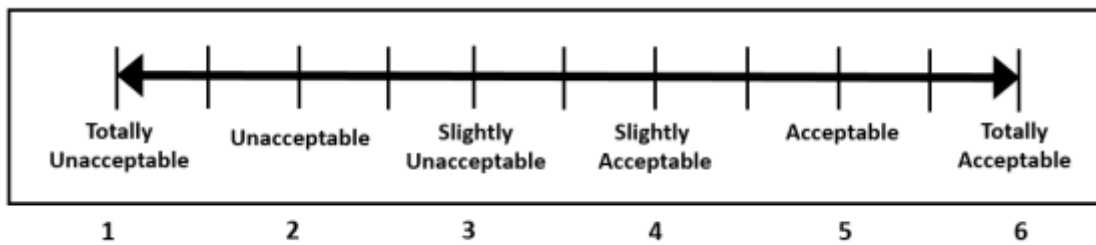
2) Rate your overall thermal sensation at this moment:



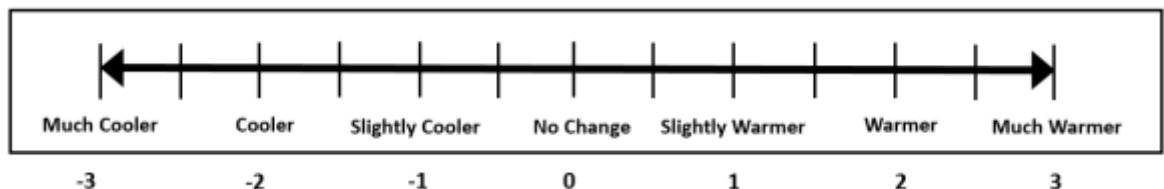
3) Rate your overall thermal comfort at this moment:



4) How acceptable is the thermal environment at this moment?



5) Would you like the environment to be:



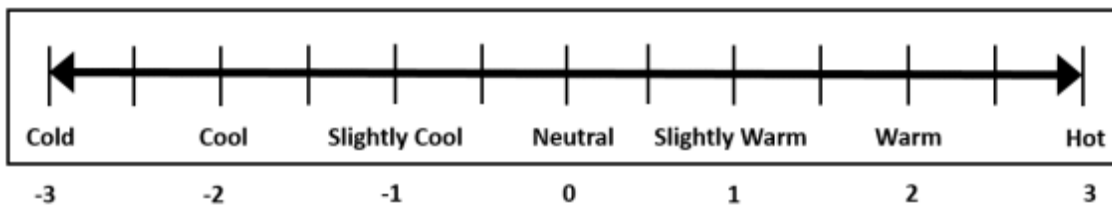
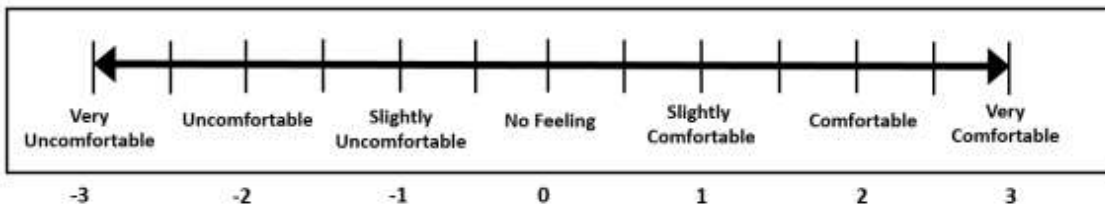
Appendix B: Second Questionnaire (Environmental Condition at the Time)

Date:

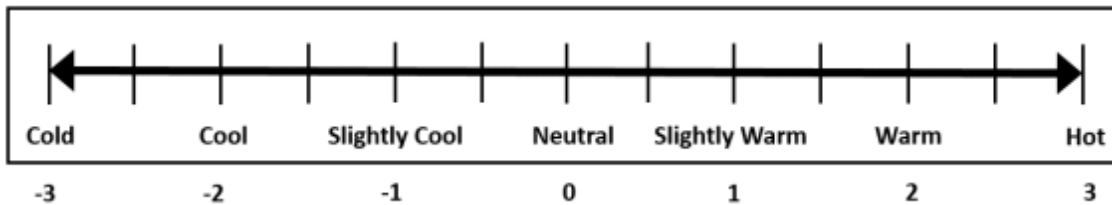
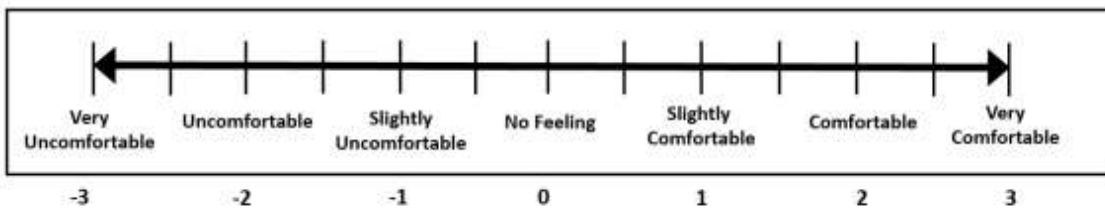
Subjects' code:

1) Rate your thermal sensation and thermal comfort at each parts:

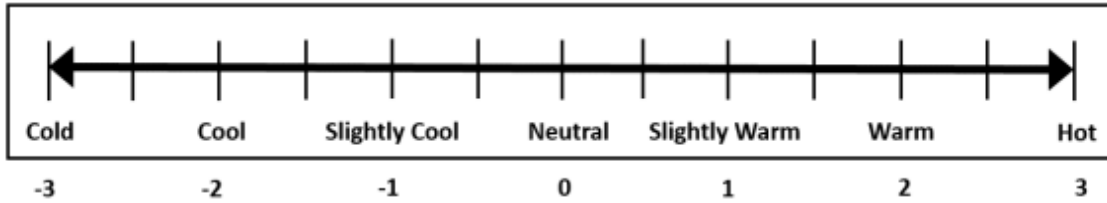
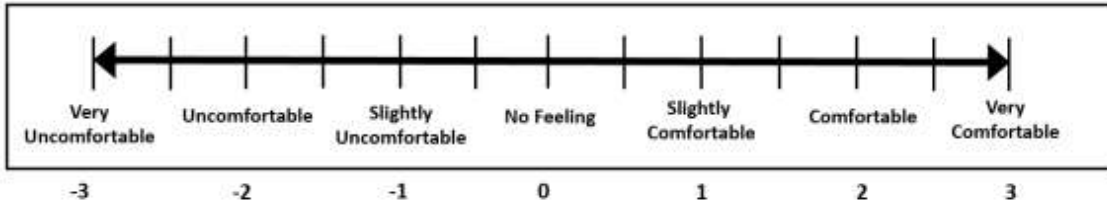
h) Forehead



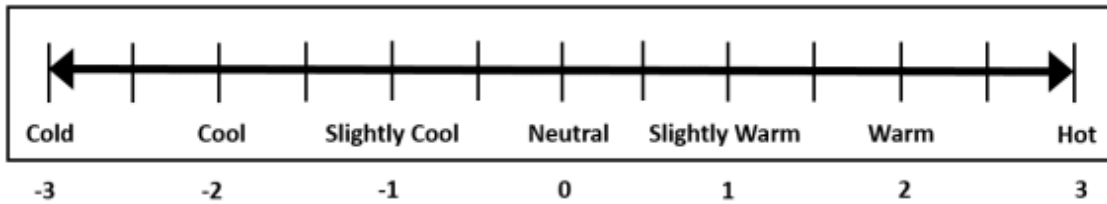
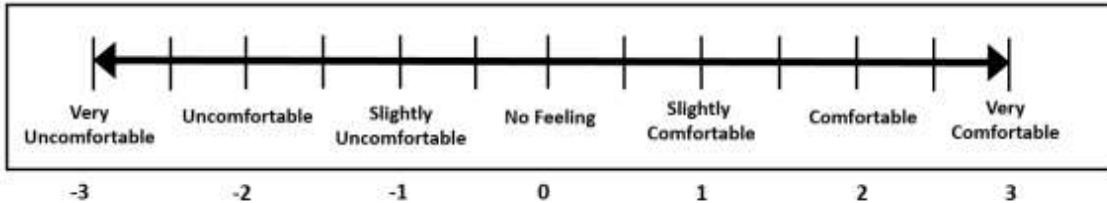
i) Torso Front



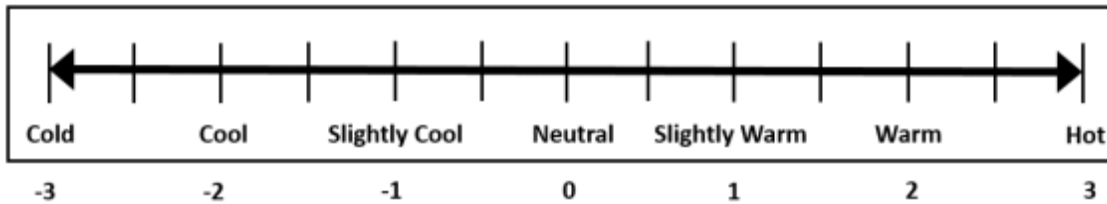
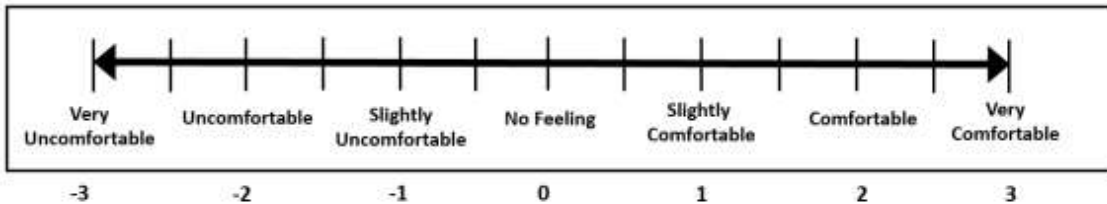
j) Torso Back



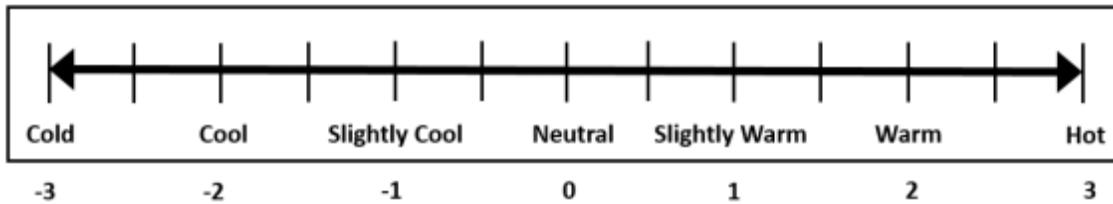
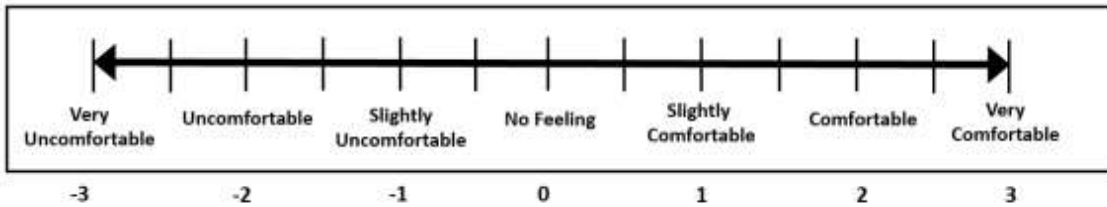
k) Hand



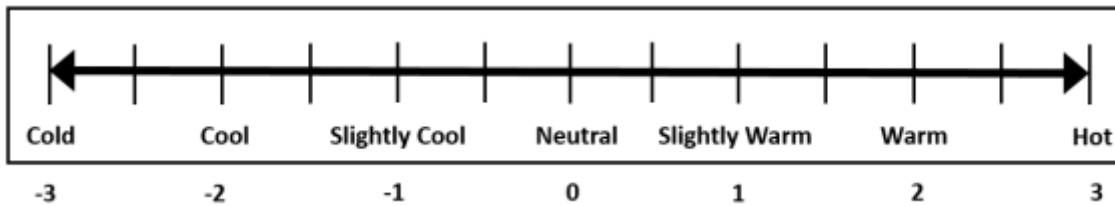
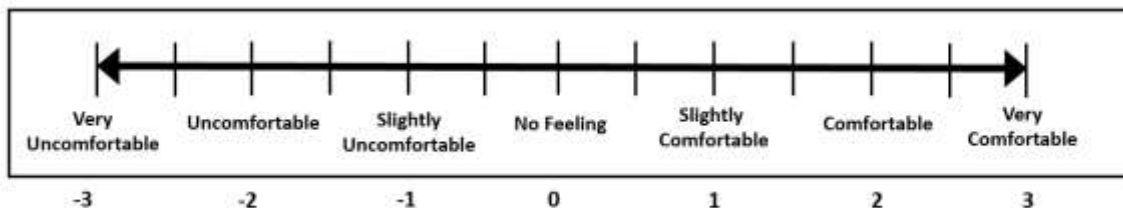
l) Thigh Front



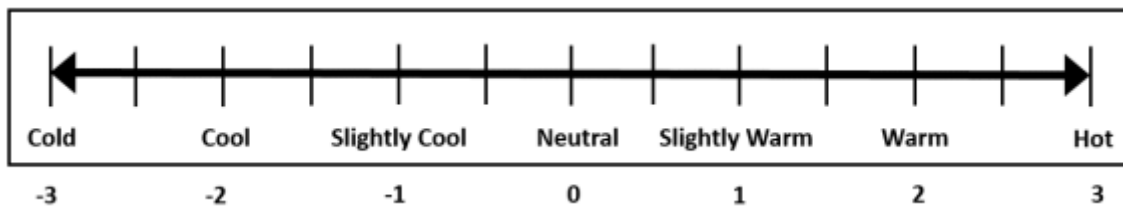
m) Thigh Back



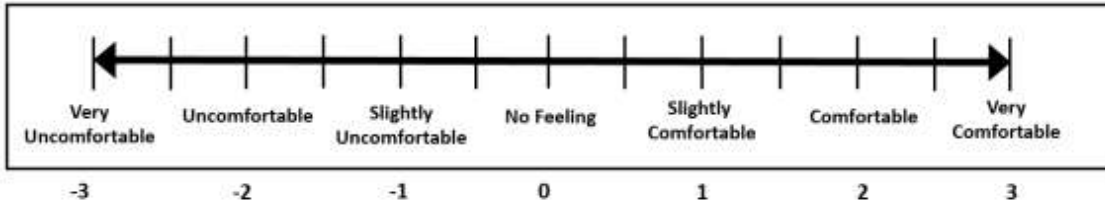
n) Feet



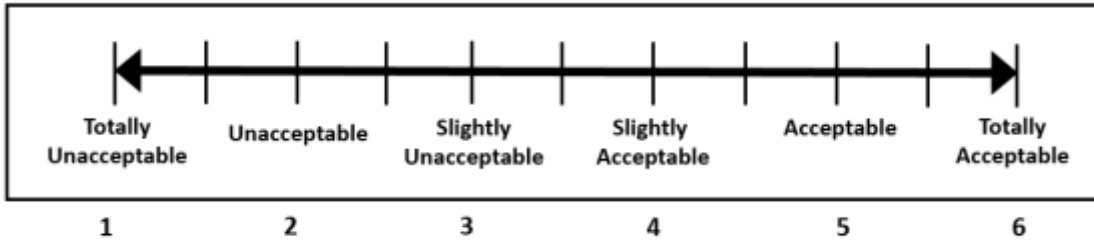
2) Rate your overall thermal sensation at this moment:



3) Rate your overall thermal comfort at this moment:



4) How acceptable is the thermal environment at this moment?

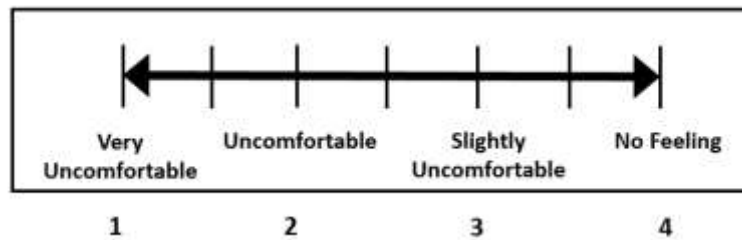


5) Would you like the environment to be:

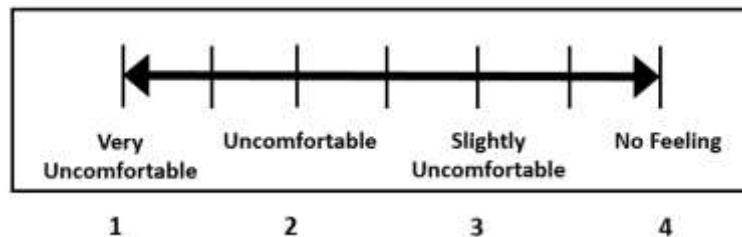


6) Rate any other discomfort:

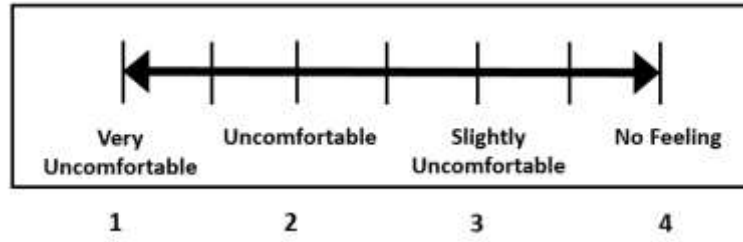
Humid skin



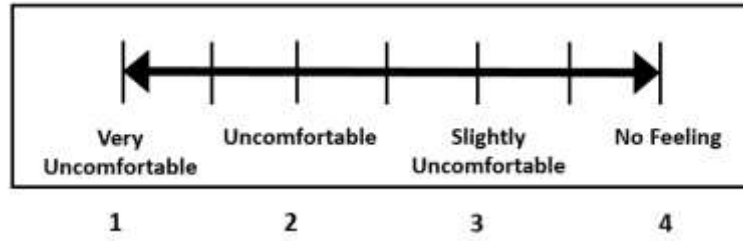
Dry skin



Itchy skin:



Burnt skin:



Appendix C: Request for ethical approval

Request for ethical approval for research undertaken by staff, post-graduate research and post-graduate professional students

Please submit your completed form to the chair of your college research ethics committee (CREC)

Your Name	Zohreh Soleimani	
College	Engineering and Technology	
College Research Ethics Committee		
Staff ID		
Student ID	"Removed due to Data protection"	
Unimail address	"Removed due to Data protection"	
Programme name / code	Traditional PhD	
Name of supervisor(s)	Prof. Stamatis Zoras	
Title of proposed research study		
<p>Research on Powering a Personal Heating Garment with a Hybrid Power Supply</p>		
Background information		
Has this research been funded by an external organisation (e.g. a research council or public sector body) or internally (such as the RLTF fund)? If yes, please provide details.	<p>YES</p> <p>THIS RESEARCH WILL BE FUNDED BY RLTF.</p>	
Have you submitted previous requests for ethical approval to the Committee that relate to this research project? If yes please provide details.	<p>NO</p>	

Are other research partners involved in the proposed research? If yes please provide details.	NO
Signatures	
<p>The information supplied is, to the best of my knowledge and belief, accurate. I clearly understand my obligations and the rights of the participants. I agree to act at all times in accordance with University of Derby Policy and Code of Practice on Research Ethics: http://www.derby.ac.uk/research/uod/ethics/</p>	
Signature of applicant	Zohreh Soleimani
Date of submission by applicant	
Signature of supervisor (if applicable)	
Date of signature by supervisor (if applicable)	
<p><u>For Committee Use</u> Reference Number (Subject area initials/year/ID number)</p> <p>Date received Date considered ...</p> <p>Committee decision Signed</p>	

<p>1. What is the aim of your study? What are the objectives for your study?</p> <p>The aim of this research is to produce a self-sustained wearable personal heating system powered by human body heat to aid the maximization of building energy efficiency, and individual thermal comfort. A thermoelectric generator is going to be used to convert the body heat into electricity for powering the heating unit.</p> <p>The objectives of this research are:</p> <ul style="list-style-type: none"> • To investigate the current research on attributes and features of the existing wearable thermoelectric generators (TEG; thermal energy harvesters). • To explore the most suitable TE material in terms of thermoelectric efficiency and life cycle sustainability for making a wearable TEG in the Lab.

- To pre-evaluate the thermoelectric performance of the designed prototype in a computational simulation tool (COMSOL).
- To make a prototype in the lab and checking its performance under different ambient conditions (temperature, air velocity).
- To explore the performance of the prototype with measuring tools such as a multimeter and a data logger to measure and record the relevant data.
- To test the performance of the produced prototype in the actual condition (Offices) by recruiting some individuals.

2. Explain the rationale for this study (refer to relevant research literature in your response).

To meet thermal comfort requirements in offices, employees can wear personal heating garments including heated socks, heated shoulder pad and heated gloves (Knecht et al., 2016). These devices provide the users to have control on the temperature profile and deploy the conditioned air just around the individual's body (Wang et al., 2010). Therefore, apart from addressing individuals' thermal preferences, personal heating garments save energy through distributing the heated air just around the human body (Newsham, 1997). However, the main practical issues related to wearable personal heating systems are their big dimension, heavy weight, rigidity and above all requirement for recharging every couple of hours (Knecht et al., 2016). As a result, these devices have the potential to cause cumbersome for their users throughout the working hours. The major aim of this study is overcoming these problems through powering the personal heating garments with a wearable thermoelectric generator (TEG). Thermoelectric generator is a viable energy harvester that uses the temperature difference between any living body and surrounding environment to convert it into an electrical output (Wang et al., 2018). Similarly, a wearable TEG, worn on the human skin, generates electricity through the temperature difference between body skin and ambient (Leonov and Vullers, 2009). Although, wearable TEGs are used for powering different portable electronic systems (Siddique et al., 2017) such as motion detection and powering health monitoring (Liu et al., 2017). However, there have been no studies on using them for powering personal heating garments. Therefore, this study examines previous works and proposes a new design of wearable TEG for powering wearable personal heating garments.

REFERENCES

- 1- Katja Knecht, Nick Bryan-Kinns, Karen Shoop, "Usability and Design of Personal Wearable and Portable Devices for Thermal Comfort in Shared Work Environments," in Proceedings of British HCI 2016 Conference Fusion, Bournemouth, 2016.
- 2- Faming Wang, Chuansi Gao, Kalev Kuklane, Ingvar Holmér, "A review of technology of personal heating garments.," International Journal of Occupational Safety and Ergonomics, vol. 16, no. 3, pp. 387-404, 2010.
- 3- Guy R. Newsham , "Clothing as a thermal comfort moderator and the effect on energy consumption," Energy and Buildings, vol. 26, pp. 283-291, 1997.
- 4- Katja Knecht, Nick Bryan-Kinns, Karen Shoop, "Usability and Design of Personal Wearable and Portable Devices for Thermal Comfort in Shared Work Environments," in *British HCI 2016 Conference Fusion*, Bournemouth, UK, 2016.

- 5- Yancheng Wang, Yaoguang Shi, Deqing Mei, Zichen Chen, "Wearable thermoelectric generator to harvest body heat for powering a miniaturized accelerometer," *Applied Energy*, pp. 690-698, 2018.
- 6- Vladimir Leonov, Ruud J. M. Vullers, "Wearable electronics self-powered by using human body heat: The state of the art and the perspective," *Journal of Renewable and Sustainable Energy*, vol. 1, p. 062701, 2009.
- 7- Abu Raihan Mohammad Siddique, Shohel Mahmud, Bill Van Heyst, "A review of the state of the science on wearable thermoelectric powergenerators (TEGs) and their existing challenges," *Renewable and Sustainable Energy Reviews*, vol. 73, pp. 730-744, 2017.
- 8- Haiyan Liu, Yancheng Wang, Deqing Mei, Yaoguang Shi, Zichen Chen, "Design of a Wearable Thermoelectric Generator for Harvesting Human Body Energy," *Wearable Sensors and Robots*, vol. 399, pp. 55-66, 2017.

3. Provide an outline of your study design and methods.

1) Literature Review:

- Exploring the literature in the field of wearable TEG.
- Critically analysing different types of thermoelectric materials to find the most suitable one for this study.
- Finding out the potentials in improving the design of wearable TEG to achieve higher electric potential.

2) Developing Computational Simulations:

- Using commercial software COMSOL to evaluate the performance of the designed prototype (designed TEG) in terms of power potential.
- Evaluating the performance of the device under different ambient condition (temperature, air velocity).
- Using the simulation tool for finding the amount of heat that can be generated by the prototype when it is coupled with a heating unit.

3) Carrying out Experimental Works:

- Making the prototype in the laboratory and connecting it to a multimeter and a data logger to measure and record the relevant data, including the electric potential. As this is a rig test, the prototype would be placed on a hot plate resembling the temperature of the human skin.
- The TEG performance would be investigated under different air velocity and temperature.
- Integrating the designed TEG with a flexible heater in order to measure the power level and thermal output of the whole device.

4) Conducting Fieldworks:

- Finally, the produced prototype, which is coupled with a heating unit, will be mounted on the wrist of some individuals to evaluate its performance under the real condition. The output power of the TEG and thermal power of the heater will be recorded via a thermometer and a multimeter.

- A questionnaire will pass over the individuals during the test to evaluate their comfort, thermal sense, and satisfaction.
- In addition, a thermal camera can be utilized to scan temperature distribution of individuals' wrist while wearing the device in order to verify the obtained results from the former two approaches.

4. If appropriate, please provide a detailed description of the study sample, covering selection, sample profile, recruitment and inclusion and exclusion criteria.

Description of Test Sites and Subjects: An office room in university of Derby will be considered as test site for the field study. Within this room, two distinct groups of subjects will be selected to participate in the study: (1) a TEG group, consisting of workers who originally occupied workstations. This group will mount the prototype on their wrists at the test time, while seated at their desks. (2) a control group, defined as a group of staffs in the same room seated at their desks, but will not mount the prototype on their wrist. By collecting and comparing measurement data from these two groups, it is anticipated that the impact of installing the prototype can be most meaningfully evaluated.

Occupant Survey:

- Questions on environmental condition right now:** A survey will be used to assess the response of both groups to their 'environmental condition right now'. The occupants are asked for their feelings and level of acceptability at the time they are filling out the survey. They are also asked a short series of questions describing their clothing level and food and beverage consumption.
- Questions on satisfaction from the prototype performance:** After mounting the prototype on the wrist of the TEG group, a survey will be done to assess the response of this group about their thermal sensation and their comfort for installation of the prototype.

Field Measurement Procedures:

- Measurement of the room:** physical measurements of different points of the office room will be made using a thermometer and an air velocity meter. These measurements will be generally completed when the occupants also answered survey questions about "environmental conditions right now," described above. The data are used to correlate the occupants' subjective responses with their actual physical environment and to characterize the influence of the prototype on their thermal sensation.
- Measurement of the prototype:** After the occupants finished the survey about 'environmental condition right now', the prototype will be installed on the wrist of the TEG group. After a while, some physical measuring tools will be used to measure the skin temperature, air temperature, electric potential and power output of the prototype. These measurements will be generally completed when the participants also answered survey questions about 'satisfaction from the prototype performance'.

**5. Are payments or rewards/incentives going to be made to the participants? No
If so, please give details.**

6. Please indicate how you intend to address each of the following ethical considerations in your study. If you consider that they do not relate to your study please say so.

Guidance to completing this section of the form is provided at the end of the document.

a. Consent

The researcher will ensure that participants give their consent to participate on this research prior to data collection. Full details about the aim of the research, how the collected data is to be used and how participants can withdraw from the investigation will be provided to all participants prior to signing the informed consent form. The researcher will ensure that the participants understand that all financial or other information will be handled sensitively and in confidence. Consent letter will be provided to the participants.

b. Deception

The research ensures that there is no any kind of deception, distraction, or false misleading information given to participants.

c. Debriefing

Full transparency will be ensured for both research collaborates and participants through providing verbal/printed relevant information at every stage of this research. Where possible the researcher will send a summary of findings that show how the information given has been used. All possible harmful after-effects of the experiment will be concerned to participants. Debriefing letter will be provided to the participants.

d. Withdrawal from the investigation

All participants or collaborators possess full rights to withdraw from the research at any time without giving a reason and without a prejudice.

e. Confidentiality

Participant confidentiality and anonymity will be maintained throughout the time of this research except where written permission is obtained prior to the research being carried out. All information will be treated as confidential and will be locked away securely and/or encrypted.

f. Protection of participants

Participants will be informed that all information given will remain anonymous throughout the study and in publications. Participants' names, and other things that can lead to the identification of people will not be disclosed to anyone or included in the study report and publications. Therefore, all information collected from all participants and participants in on online survey will not be linked in any way to the individual. Participants will be cleared that their involvement in the procedure(s) is voluntary. They will also be notified what they are expected to do, the level of confidentiality offered, their right to pass over a question, and their right to decline to participate. Utmost care will be taken during experiment tests

such as participants rest time and any possible risk of harm. Participants will be noted who has access to their data and what is being done with it.

g. Observation research

The privacy and physical well-being of the participants will be respected. Particular account would be taken of the privacy of individuals who accepts to wear the device.

h. Giving advice

The researcher will not give any advice to the participants, if the need arise the researcher will refer participants to suitably qualified and appropriate professionals.

i. Research undertaken in public places

The well-being, safety and preferences of the people who are taking part in the research will be ensured, and any possible annoyance for other staffs who are not taking part in the research are avoided.

j. Data protection

The researcher will ensure all information collected are protected in accordance with the Data Protection Act and any other legal issues are addressed and clarify well-in-advance prior to data collection. The research will be going carried out in concurrence with the GDPR considerations. Also the research will be conducted in line with the University of Derby's Research Ethics policies

Animal Rights

Not applicable.

k. Environmental protection

Are there other ethical implications that are additional to this list? No

7. Have / do you intend to request ethical approval from any other body/organisation? No

If 'Yes' – please give details

8. Do you intend to publish your research? Yes

If 'Yes', what are your publication plans?

Results will be published in highly ranked, peer-reviewed international scientific journals. My specific publication plans, including probable authors, title, and possible publication outlet, for the next two years are as follows:

Year 2019-2020

- Zohreh Soleimani, Stamatis Zoras, Boris Ceranic, Sally Shahzad. A review of thermoelectric materials. Sustainable and Renewable Energy Review. [will be ready to submit Winter 2019].
- Zohreh Soleimani, Stamatis Zoras, Boris Ceranic, Sally Shahzad. Numerical evaluation of the performance of a novel designed wearable TEG. Energy Conservation and Management. [will be ready to submit Summer 2019].

Year 2020-2021

- Zohreh Soleimani, Stamatis Zoras, Boris Ceranic, Sally Shahzad. Performance of a personal heating system powered by a TEG. Applied Energy. [will be ready to submit summer 2020].

9. Have you secured access and permissions to use any resources that you may require?

(e.g. psychometric scales, equipment, software, laboratory space). **Yes**

If Yes, please provide details.

Restriction on access to laboratory is required. It needs to manage keyed access to laboratory space and restrict the lab to authorized personnel only.

10. Have the activities associated with this research project been risk-assessed? Yes

This prototype supplies a voltage in a range between 5-12V, which is a low voltage and there is no risk of dangerous electrical shock. But to improve safety, following measures will be taken:

- 1- Visual inspections of the TEG prior to use.
- 2- The TEG will be electrically tested before participants wearing them.
- 3- Checking the skin of the participants to be dry.

Which of the following have you appended to this application?

- | | |
|--|--|
| <input type="checkbox"/> Focus group questions | <input type="checkbox"/> Psychometric scales |
| <input checked="" type="checkbox"/> Self-completion questionnaire | <input type="checkbox"/> Interview questions |
| <input checked="" type="checkbox"/> Other debriefing material | <input type="checkbox"/> Covering letter for participants |
| <input type="checkbox"/> Information sheet about your research study | <input checked="" type="checkbox"/> Informed consent forms for participants |
| <input type="checkbox"/> Location consent form | <input type="checkbox"/> Other (please describe) |

PLEASE SUBMIT THIS APPLICATION WITH ALL APPROPRIATE DOCUMENTATION

Participant Debriefing and Withdrawal Letter

Dear Participant,

PhD Engineering and Technology-Participant Debriefing and Withdrawal Letter

Thank you for agreeing to participate in my research, your help was much appreciated and I can confirm the following:

- The information I collected from you will be used in my dissertation for University of Derby, as part of my PhD Engineering and Technology at the University of Derby.
- The aim of the dissertation research is to design a wearable personal heating system, which harvests energy from human body heat, to make current wearable personal heating systems self-sustained and lightweight. The information you will be asked to provide will be used to help to assess the performance of the prototype in terms of providing thermal comfort.
- The data you provided will remain anonymous throughout the study and publications. Participants' names, and other things that can lead to the identification of people will not be disclosed to anyone or included in the study report or publications.
- The data you provided will only be used for the dissertation, and will not be disclosed to any third party, except as part of the dissertation findings, or as part of the supervisory or assessment processes of the University of Derby, or as part of data for publishing in journals.
- The information you provided will only be used for the dissertation, and will not be disclosed to any third party, except as part of the dissertation findings, or as part of the supervisory or assessment processes of the University of Derby.
- The data you provided will be kept until 30th April 2022, so that it is available for security by the University of Derby as part of the assessment process.
- If you later decide that you wish to withdraw from the study, please email me at "Removed due to Data protection" before 30th May 2021 and I will be able to remove your response from my analysis and findings, and destroy your response.

Please do not hesitate to contact me if you have any queries relating to this study.

Kind Regards

Date

Zohreh Soleimani

Briefing and consent of Participants-Questionnaire

Dear Participant,

PhD Engineering and Technology-Participant Briefing and Consent Letter

I am Zohreh Soleimani and I am collecting data from you which will be used in my dissertation for the university of Derby, as the part of my PhD Engineering and Technology at the university of Derby.

The aim of the dissertation research is to design a wearable personal heating system, which harvests energy from human body heat, to make current wearable personal heating systems self-sustained and lightweight. The information you will be asked to provide will be used to help to assess the performance of the prototype in terms of providing thermal comfort.

The data you provided will remain anonymous throughout the study and publications. Participants' names, and other things that can lead to the identification of people will not be disclosed to anyone or included in the study report or publications.

The data you provided will only be used for the dissertation, and will not be disclosed to any third party, except as part of the dissertation findings, or as part of the supervisory or assessment processes of the University of Derby, or as part of data for publishing in journals.

The data you provided will be kept until 30th April 2022, so that it is available for security by the University of Derby as part of the assessment process.

If you feel uncomfortable with any of the questions being asked, you may decline to answer specific questions. You may also withdraw from the study completely, and your answers will not be used.

Moreover, if you later decide that you wish to withdraw from the study, please email me at "Removed due to Data protection" before 30th May 2021 and I will be able to remove your response from my analysis and findings, and destroy your response.

I have read and understood the contents of this consent and briefing form, and freely and voluntarily agree to participate in the research.

I am happy to be identified as a participant in the research as subject code-----.

Signed

Please print name

Date-----

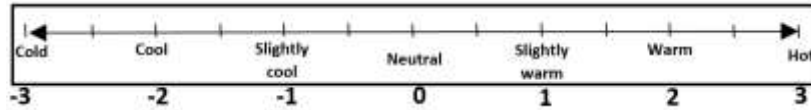
Questions on satisfaction from the prototype performance:

Date:

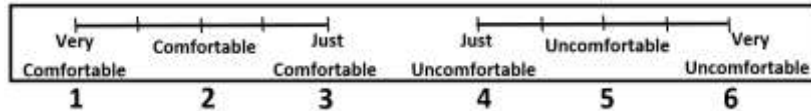
Subjects' code:

Age:

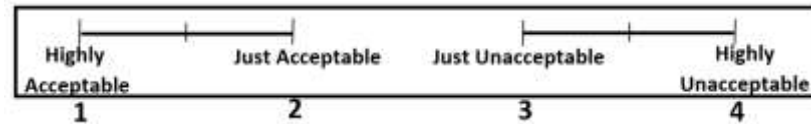
- 1) Rate your thermal sensation at this moment:



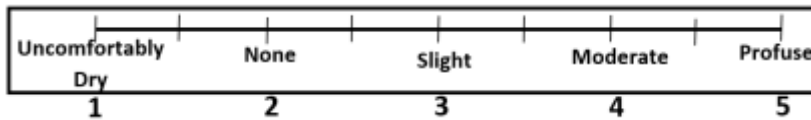
- 2) Rate your overall thermal comfort sensation at this moment:



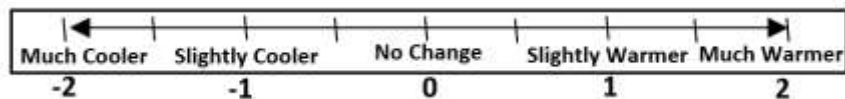
- 3) How acceptable is the thermal environment at this moment?



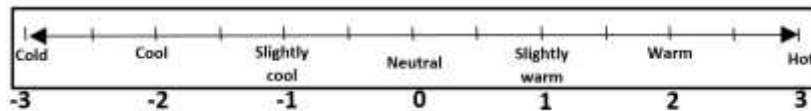
- 4) Rate your body moisture level (sweating) on your wrist:



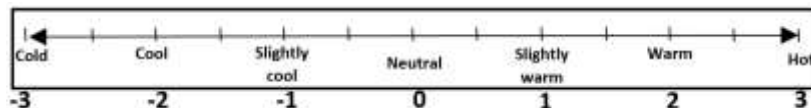
- 5) Would you like the environment to be



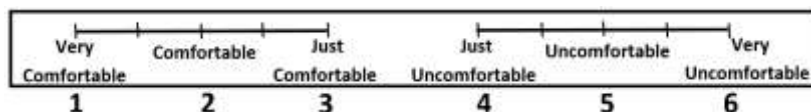
- 6) At this moment, how does your wrist feel?



- 7) At this moment, how does your forearm feel?



- 8) Rate your overall comfort sensation for wearing the prototype at this moment:



Appendix D: Ethics_application_ETH1819-0044_Decision

Kedleston Road, Derby

DE22 1GB, UK

T: +44 (0)1332 591060

E: researchoffice@derby.ac.uk

Sponsor License No: QGN14R294

Dear Zohreh

Thank you for submitting your application to the College of Engineering and Technology Research Ethics Committee, which has now been reviewed and considered.

The outcome of your application is:

approved.

If any changes to the study described in the application are necessary, you must notify the Committee and may be required to make a resubmission of the application.

On behalf of the Committee, we wish you the best of luck with your study.

Yours sincerely

Stuart Wain

